Characterization, classification, and mechanisms for mineralization of critical metal-bearing occurrences in southwestern Meguma Terrane, Canadian Appalachians

By
Naomi Welt

A Thesis Submitted to Saint Mary's University, Halifax, Nova Scotia in Partial Fulfillment of the Requirements for the Degree of Master of Science in Applied Science

April 2022, Halifax, Nova Scotia

Approved: Dr. Erin Adlakha
Supervisor
Department of Geology
Saint Mary's University

Approved: Dr. Jacob Hanley
Supervisory Committee
Department of Geology
Saint Mary's University

Approved: Dr. Geoff Baldwin
Supervisory Committee
Department of Natural Resources and Renewables,
Government of Nova Scotia

Approved: Dr. Danielle Tokarz
Supervisory Committee
Department of Chemistry
Saint Mary's University

Approved: Dr. Mathias Burisch
External Supervisor
Institut für Mineralogie
Technische Universität Bergakademie Freiberg

Date: April 11, 2022

Characterization, classification, and mechanisms for mineralization of critical metal-bearing occurrences in southwestern Meguma Terrane, Canadian Appalachians

by Naomi Welt

Abstract

Multiple polymetallic vein-type occurrences with a suspected but unconfirmed genetic relationship and polymetallic critical metal-bearing assemblages occur in the Meguma Terrane metasediments in southwestern Nova Scotia. A multi-analytical approach integrating results from detailed petrography, scanning electron microscopy (SEM), Re-Os geochronology of arsenopyrite, U-Pb geochronology of apatite, Al-in-chlorite thermometry via electron probe micro-analyzer (EPMA), in-situ secondary ion mass spectrometry (SIMS) of sulfur isotopes in sulfides, and fluid inclusion systematics has allowed for the characterization and interpretation of mineralization at the Lansdowne (Sb-Pb-Zn-Co-Ag) and Cape St. Mary's (Sb-Pb-As-Co-Ni-Bi-Au-REE) occurrences, and comparisons with the Nictaux Falls Dam occurrence (Co-Ni-As-Bi-Au). These results suggest a complex multi-stage mineralizing history for both occurrences due to reactivation of Neoacadian structures. Critical metal mineralization of the Lansdowne occurrence represents a newly classified occurrence type in Nova Scotia related to extensional tectonics from the breakup of Pangea in the Late-Triassic.

April 11, 2022

Acknowledgments

I would firstly like to thank my supervisor Dr. Erin Adlakha for her continued support, vigilant edits, insightful meetings, and cute dog. I would also like to thank my paper co-authors, Jacob Hanley, Mitchell Kerr, Geoff Baldwin, Robert Creaser, Mostafa Fayek, and Ryan Sharpe, for their knowledge and conversations. A big thank you to Joshua Jackman who collected all the fluid inclusion data used for my project, as his work has been invaluable to this thesis. I thank you all for making me smarter, even when I feel like the opposite.

I would like to recognize the work of George O'Reilly, whose preliminary research and field work with the Nova Scotia government over the years brought this project into being, as well as the excellent undergraduate theses by Natalie McNeil and Nicole Kennedy who really laid the foundation for my work. Thank you as well to my glamorous field assistants Kerstin Landry, Ryan Parsons, and Aidan Buyers for their help in lugging around my buckets full of rocks. This project was generously funded by the Mineral Resource Development Fund (MRDF) under the Government of Nova Scotia, as well as the Nova Scotia Graduate Scholarship (NSGS). Thank you to Xiang Yang at Saint Mary's University, Brandon Boucher from the laser ablation laboratory at the University of New Brunswick, and Yanan Liu at the University of Toronto for their help with my analyses.

I need to sincerely thank my family for their unwavering love and support, and for always encouraging me to keep learning. A million thanks to my partner Sam, my best friend and #1 fan, and an excellent geologist to boot. Finally, I want to thank the people who kept me sane over these last two (plus) years: Gabriel, Priyal, Andree, Logan, and all the other students from the Adlakha Lab group. You have made this whole degree worthwhile, and I will miss our daily office banter dearly. And to Kerstin, you have been my rock throughout this whole thing, and I am so lucky we found each other. I need to thank Erin again for putting us side by side, because this would have been impossible without you. We did it!

Table of Contents

Abstract 2
Acknowledgments 3
Table of Contents 4
List of Figures 7
List of Tables 9
List of Appendices 10
Chapter 1: Introduction 12
1.1 Structure of thesis 12
1.2 Previous work 13
1.3 Objectives of thesis 15
References 16
Chapter 2: Late-Triassic hydrothermal polymetallic Sb-Pb-As-Zn veins, Meguma Terrane, Canadian Appalachian Orogen; a new critical metal deposit type in Nova Scotia 17
Abstract 17
2.1 Introduction 18
2.2 Background 21
2.2.1 Geology of the Meguma Terrane 22
2.2.2 Lansdowne 25
2.3 Methodology 26
2.3.1 Field work and petrography 26
2.3.2 Geochronology 26
2.3.3 Chlorite thermometry 28
2.3.4 Fluid inclusion analysis 29
2.3.5 Sulfur isotopes 30
2.3.6 Whole rock geochemistry 31
2.4 Results 31
2.4.1 Field observations and petrography 31
2.4.2 Geochronology 36
2.4.3 Chlorite thermometry 37
2.4.4 Fluid inclusion systematics 38
2.4.5 Sulfur isotopes 45
2.4.6 Whole rock geochemistry 46
2.5 Discussion 47

2.5.1 Paragenesis and timing 47
2.5.2 Pressure-temperature conditions and sources (fluid, S, metal) for critical metal mineralization 50
2.5.3 Classification of the Lansdowne occurrence 56
2.5.4 Exploration vectors 59
2.6 Conclusion 60
2.7 References 61
Chapter 3: Antimony and REE mineralization at the Cape St. Mary's polymetallic (Sb-REE-As-Co-Ni-Au-Ag-Bi-Pb) occurrences, Meguma Terrane, southwest Nova Scotia 69
Abstract 69
3.1 Introduction 70
3.2 Background 72
3.2.1 Regional Geology – The Meguma Terrane 73
3.2.2 Local Geology – Cape St. Mary's 74
3.3 Methodology 75
3.3.1 Field work and petrography 75
3.3.2 Sulfur isotopes 76
3.3.3 Whole rock geochemistry 76
3.4 Results 77
3.4.1 Field observations and petrography 77
3.4.2 Sulfur isotopes 86
3.4.3 Whole rock geochemistry 87
3.5 Discussion 87
3.5.1 Rare earth element mineralization 88
3.5.2 Antimony mineralization 90
3.6 Conclusion 96
References 97
Chapter 4: The genetic relationship between Lansdowne, Cape St. Mary's, and Nictaux Falls 101
4.1 Introduction 101
4.2 Methods 103
4.3 Results 104
4.3.1 Chlorite petrography and thermometry 104
4.3.2 Geochronology 107
4.4 Discussion 108
4.5 Conclusion 112

References 114
Chapter 5: Summary of conclusions and suggestions for future work 116
5.1 Key conclusions from Chapter 2 116
5.2 Key conclusions from Chapter 3 117
5.3 Key conclusions from Chapter 4 117
5.4 Suggestions for future work 118
Appendix I 120
Appendix II 146
Appendix III 154

List of Figures

***In* Chapter 1**

Figure 1-1 Simplified geological map from NSDNR archives showing the general locations and metal assemblages of the three polymetallic occurrence study areas involved in this project

***In* Chapter 2**

Figure 2-1 Geologic map of the of the Meguma Terrane outlining the location of the Lansdowne study area. The Lansdowne map shows location and details of drill core.

Figure 2-2 Mineralized hand samples from Lansdowne

Figure 2-3 Photomicrographs and BSE images of sulfide and sulfosalt mineralization in mineralized veins at Lansdowne

Figure 2-4 Paragenesis of mineralized veins at Lansdowne, subdivided into three stages by associated mineralogy

Figure 2-5 Petrography of type-1 fluid inclusions at Lansdowne

Figure 2-6 Box and whisker plots representing results of microthermometry experiments conducted on type-1 and type-2 fluid inclusions. Isochores representative of microthermometry results of fluid inclusion assemblages with endmember compositions and indicate trapping conditions

Figure 2-7 Ternary diagrams illustrating the composition of decrepitate mounds from type-1 inclusions

Figure 2-8 Isocon plots based on whole rock geochemical data collected from most and least altered samples of mafic sill and metasedimentary rock at Lansdowne

Figure 2-9 Regional geological history of the Meguma Terrane compiled from geochronological data and results of Re-Os geochronology from Lansdowne

Figure 2-10 Sulfur isotope values of major lithologies and select ore deposits within the Meguma Terrane compared to sulfur isotopes of sulfides at Lansdowne

Figure 2-11 Model curve indicating fraction of S into sulfate at different temperatures, based on sulfur isotope values of early and late stage arsenopyrite

Figure 2-12 Sketch illustrating the mechanisms for mineralization in the rifting environment at the time of sulfide deposition

***In* Chapter 3**

Figure 3-1 Geologic map of the of the Meguma Terrane outlining the location of the Cape St. Mary's study area and associated occurrences

Figure 3-2 Photos from outcrop and hand sample, as well as photomicrographs and BSE images of the Deerfoot Trail Sb occurrence at Cape St. Mary's

Figure 3-3 Paragenesis of mineralization at the Deerfoot Trail Sb occurrence

Figure 3-4 Photos and photomicrographs of the Galena and Cormorant Rock occurrences

Figure 3-5 Photos and BSE images of outcrop and representative mineralization at the Ankerite Breccia occurrence at the Cape St. Mary's shear zone

Figure 3-6 Photos and BSE images of outcrop and representative mineralization at the Mavillette Beach occurrence

Figure 3-7 Venn diagram showing overlap in critical metals between the occurrences at Cape St. Mary's

Figure 3-8 Ternary diagrams showing compositional variation in different mineral types from Lansdowne and Cape St. Mary's occurrences

Figure 3-9 Sulfur isotope values of sulfides at Cape St. Mary's compared to sulfur isotope values of sulfides from other Meguma sulfide deposits.

***In* Chapter 4**

Figure 4-1 Geology of the Nictaux Falls spillway with location of mineralization and analyzed samples

Figure 4-2 Photomicrographs and BSE image of chlorite types analyzed at Cape St. Mary's and Nictaux Falls

Figure 4-3 Discordia plot of data collected from U-Pb analyses of sample GB-1, Nictaux Falls gabbro

Figure 4-4 Composition of chlorite types at Lansdowne, Cape St. Mary's and Nictaux Falls, based on proportion of Fe, Mg, and Al (vi)

Figure 4-5 Composition of sulfarsenides at Nictaux Falls, Lansdowne, and the Deerfoot Trail Sb occurrence at Cape St. Mary's, based on proportion of Fe, Co, and Ni

Figure 4-6 Comparisons of major ore stages at the Lansdowne, Cape St Mary's, and Nictaux Falls

List of Tables

***In* Chapter 2**

Table 2-1 Re-Os geochronology results of arsenopyrite in sample LAN2-3. Mixed spike.

Table 2-2 Re-Os geochronology results of arsenopyrite and jamesonite from sample 7157. Mixed double-Os spike

Table 2-3 Abundance of major oxides in chlorite in wt.%, their atomic proportions, and calculated temperatures

Table 2-4 Summary of fluid inclusion types and characteristics at Lansdowne

Table 2-5 Summary of S-isotope data for sulfide minerals determined by SIMS.

***In* Chapter 3**

Table 3-1 Summary of S-isotope data for sulfide minerals at three Cape St. Mary's occurrences, determined by SIMS

***In* Chapter 4**

Table 4-1 Abundance of major oxides in chlorite in wt.% and their atomic proportions from Cape St. Mary's and NFDO

List of Appendices

***In* Appendix I**

Table A1-1 Sample list of samples from Lansdowne

Table A1-2 SEM data of sulfides in mineralized Lansdowne samples

Table A1-3 Analyses of U-Pb in apatite by LA-ICP-MS in mafic sill samples from Lansdowne

Figure A1-1 Terra-Wasserberg plot of U-Pb in apatite geochronology – sample LAN4-3

Figure A1-2 Terra-Wasserberg plot of U-Pb in apatite geochronology – sample LAN4-2

Figure A1-3 Terra-Wasserberg plot of U-Pb in apatite geochronology – Phalaborwa apatite

Figure A1-4 Terra-Wasserberg plot of Re-Os in arsenopyrite geochronology – sample LAN2-3

Table A1-4 Re-Os data from arsenopyrite and jamesonite replicates in samples LAN2-3 and 7157

Table A1-5 EPMA results of chlorite analyses in unmineralized and mineralized samples

Table A1-6 Site assignment of elements in chlorite, based on 14 oxygen

Table A1-7 Fluid inclusion data from Lansdowne mineralized samples LAN4-2 and 7157

Table A1-8 SEM results of decrepitate mound analyses in samples LAN4-2 and 7157

Table A1-9 Sulfur isotope results of in-situ SIMS analyses of sulfides at Lansdowne

Table A1-10 Whole rock geochemistry results of unmineralized Lansdowne samples

Table A1-11 Whole rock geochemistry results of mineralized Lansdowne samples

***In* Appendix II**

Table A2-1 Sample list of samples from the Cape St. Mary's occurrences

Table A2-2 SEM data collected from the Cape St. Mary's occurrences

Table A2-3 Sulfur isotope data collected from sulfides at the Deerfoot Trail Sb, Galena, and Mavillette Beach occurrences

Table A2-4 Whole rock geochemical data of mineralized samples from the Cape St. Mary's occurrences

Table A2-5 Whole rock geochemical data of mineralized samples from the Cape St. Mary's study area

***In* Appendix III**

Table A3-1 Sample list of NFDO samples analyzed in Chapter 4

Table A3-2 EPMA analyses of chlorite from unmineralized samples at Cape St. Mary's and a mineralized sample from Nictaux Falls

Table A3-3 Site assignments of elements in chlorite, based on 14 oxygen

Table A3-4 Analyses of U-Pb in apatite by LA-ICP-MS in sample GB-1

Figure A3-1 Terra-Wasserberg plot of U-Pb in apatite geochronology – Phalaborwa apatite

Chapter 1: Introduction

1.1 Structure of thesis

This thesis is a "thesis by manuscript" and consists of five chapters, two of which are stand alone manuscripts aimed to be submitted to peer-reviewed scientific journals. Chapter 1 outlines the thesis, provides background on previous work and motivations for the project, and introduces the objectives of the thesis.

Chapter 2 presents results of petrographic observations, geochronology, mineral chemistry, and fluid inclusion systematics of the critical metal bearing polymetallic vein-type Lansdowne occurrence, with the aim of interpreting paragenesis, timing for mineralizing stages, fluid and sulfur sources, and mechanisms for mineralization. Chapter 2 is for submission to the *Journal of Economic Geology*. I conducted field work, petrography, data collection (including using electron probe micro-analyzer and scanning electron microscope), data compilation and interpretation, production of tables/figures, calculation of fluid inclusion isochores, and writing of the manuscript. Fluid inclusion analyses of mineralized samples from Lansdowne (including sample petrography, Raman spectra analyses, microthermometry experiments, and decrepitate mound analyses) were conducted by honours student Joshua Jackman. Robert Creaser collected Re-Os data for geochronological interpretation. Mostafa Fayek and Ryan Sharpe collected in-situ S-isotope data by secondary ion mass spectrometry (SIMS). All co-authors provided edits and commented on interpretations of data and the written manuscript.

Chapter 3 covers the mineralogy and mineral chemistry of the Cape St. Mary's occurrences and their geologic context, in order to determine processes for mineralization of important critical metals. Chapter 3 is for submission to the Society of Atlantic Geology's special publication "Developments in mineral resources research in the northern Appalachians" under the guidelines of the *Journal of Atlantic Geoscience*. I conducted field work, sample collection, petrography, data collection by scanning electron microscope, data interpretation, production of tables and figures, and writing of the manuscript. Mostafa

Fayek and Ryan Sharpe collected in-situ S-isotope data of sulfides by SIMS. Co-authors provided comments for the manuscript.

Chapter 4 introduces new data for the Nictaux Falls Dam occurrence, and compares the genetic relationship between the Lansdowne, Cape St. Mary's, and Nictaux Falls Dam occurrences. Chapter 5 summarizes the key conclusions from each chapter and provides suggestions for future work to continue investigating these unique critical metal sources in Nova Scotia.

1.2 Previous work

This project came about from the discovery of multiple polymetallic (Sb-Pb-As-Zn-Co-Ni-Bi-Ag-Au-REE) quartz ± carbonate vein hosted occurrences in the southwestern Meguma Terrane of Nova Scotia by George O'Reilly, a geologist with the NSDNR (Nova Scotia Department of Natural Resources, now Nova Scotia Department of Natural Resources and Renewables) in the 1980s and 1990s. O'Reilly (1995) describes a possible genetic relationship between these occurrences as they share mineralogical characteristics and a spatial relationship to the metasedimentary and metavolcanic rocks of the Rockville Notch Group (White Rock, Kentville, and New Canaan Formations), which only outcrops in a few regions in the northwestern Meguma Terrane west of the South Mountain Batholith (**Figure 1-1**). All of these occurrences are also related spatially to mafic intrusions/sills. These occurrences include the Nictaux Falls Dam occurrence (NFDO; Co-Ni-As-Bi-Au), the Lansdowne Prospect (or Lansdowne occurrence; Sb-Pb-Zn-Ag-Au), and the Cape St. Mary's occurrences (Sb-Pb-Ni-Co-Ag-Au; **Figure 1-1**). O'Reilly (1995) suggests that these occurrences have characteristics reminiscent of "five-element deposits", which are primarily defined by their metallogeny (Ni-Co-As-Bi-Ag; Kissin, 1992) as the models for their formation are largely debated (Kissin, 1992; Markl et al., 2016; Burisch et al., 2017; Burke, 2018). Five-element deposits are often spatially associated with mafic intrusive bodies and are distributed worldwide (see summary in Kissin, 1992). They have historically been an important source of Co, Ni, and Ag, and the

discovery of this deposit type in Nova Scotia would be an important addition to the mineral resource profile of the province.

The Nictaux Falls Dam occurrence (NFDO) was considered to share the most similarities with five-element style deposits, considering mineralogy and host rocks (O'Reilly, 1995). McNeil (2019) indicates that mineralization at the NFDO could be a variant of five-element vein mineralization in Nova Scotia; however, several critical defining characteristics of five-element deposits are missing at the NFDO such as a lack of native Ag or Bi, di- and tri- arsenide complexes, changes in metal zonation, differences in paragenesis, and lack of skeletal or dendritic textures. Since five-element deposits form at generally shallow paleo-depths (<1.5 km; Markl et al., 2016), Kennedy (2019) suggests that the NFDO may be an expression of a five-element occurrence type at much higher depths of emplacement (4 – 11 km), based on fluid inclusion systematics.

Although the Cape St. Mary's and Lansdowne occurrences were thought to be related to the NFDO, the metal assemblages hosted in these occurrences do not possess sufficient overlap to classify them as five-element deposits. I hypothesize that they are likely an example of a different polymetallic vein deposit type or may represent as yet unclassified expressions of vein-hosted critical metal mineralization.

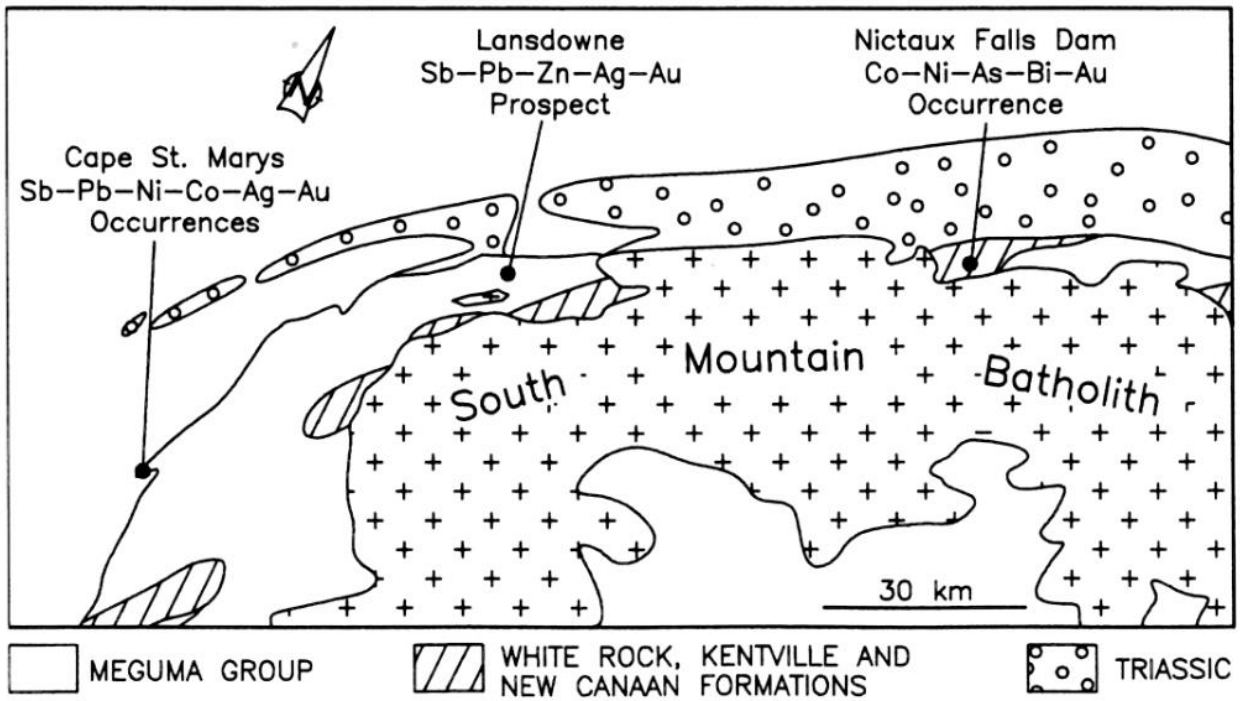

Figure 1-1 - Map by O'Reilly (1995) outlining locations and metal assemblages of the Nictaux Falls Dam occurrence, Lansdowne Prospect, and Cape St. Mary's occurrence after their initial discovery. Meguma Group is now called Meguma Supergroup (which includes the Halifax and Goldenville Groups). The White Rock, Kentville, and New Canaan Formations form the Rockville Notch Group. On this map, Triassic rocks represent the Fundy Group.

1.3 Objectives of thesis

The primary objectives of this thesis are to describe the mineralogy, textures, paragenesis, mineral chemistry, and bulk rock chemistry of the Lansdowne and Cape St. Mary's occurrences. These results are applied to determine paragenesis and timing of critical metal mineralization and potential sources of fluids, metals, and sulfur. The broader objective is to classify these occurrences within the framework of existing deposits in the Meguma Terrane and at a global scale by finding proxies for mineralization in other deposits worldwide. This project will also compare the combined results from the Lansdowne and Cape St. Mary's occurrences with previously collected and new results from the NFDO to evaluate a genetic relationship

between the three study areas and identify vectors for continued exploration of critical metal mineralization in Nova Scotia.

References

Burisch, M., Gerdes, A., Walter, B. F., Neumann, U., Fettel, M., and Markl, G., 2017, Methane and the origin of five-element veins: Mineralogy, age, fluid inclusion chemistry and ore forming processes in the Odenwald, SW Germany: Ore Geology Reviews, v. 81, p. 42–61.

Burke, J. S., 2018, The origin of polymetallic Ni-Co-As-Bi-Sb (-Ag-U) veins in the East Arm Basin and southern Slave Province, Northwest Territories: 162 p.

Kennedy, N., 2019, Fluid inclusion systematics of the polymetallic (Co-Ni-As-Au ± Bi, Ag) veins of the Nictaux Falls Dam Occurrence, Annapolis Valley, Nova Scotia: Saint Mary's University.

Kissin, S. A., 1992, Five Element (Ni-Co-As-Ag-Bi) Veins: Geoscience Canada, v. 19, p. 113–124.

McNeil, N. C., 2019, The mineralogy, petrography, and paragenesis of the polymetallic (Co-Ni-As-Au) veins of the Nictaux Falls Dam Occurrence, Annapolis Valley, Nova Scotia: Saint Mary's University: 98 p.

Markl, G., Burisch, M., and Neumann, U., 2016, Natural fracking and the genesis of five-element veins: Mineralium Deposita, v. 51, p. 703–712.

O'Reilly, G. A., 1995, Little Known Ni-Co-Bi-Sb-Ag-Au Association in the Annapolis Valley, accessed at Minerals Update, Nova Scotia Department of Natural Resources

Chapter 2: Late-Triassic hydrothermal polymetallic Sb-Pb-As-Zn veins, Meguma Terrane, Canadian Appalachian Orogen; a new critical metal deposit type in Nova Scotia

Naomi Welt*[1], Joshua Jackman[1], Erin Adlakha[1], Jacob Hanley[1], Mitchell Kerr[1], Robert Creaser[2], Geoffrey Baldwin[3], Mostafa Fayek[4], Ryan Sharpe[4]

1. Saint Mary's University, Department of Geology, Halifax, Nova Scotia B3H 3C3
2. University of Alberta, Department of Earth and Atmospheric Sciences, Edmonton, Alberta T6G 2R3
3. Nova Scotia Department of Natural Resources and Renewables, Halifax, Nova Scotia B3J 2T9
4. University of Manitoba, Department of Geological Sciences, Winnipeg, Manitoba R3T 2N2
*corresponding author email address: naomi.welt@smu.ca

Submitted to Journal of Economic Geology

Abstract

The Lansdowne occurrence is a poorly understood and little-known polymetallic (As-Sb-Zn-Pb-Fe-Cu-Co-Au-Ag) vein-hosted occurrence in southwestern Nova Scotia, selected to further understand critical metal endowment of the Meguma Terrane, the farthest outboard terrane of the Canadian Appalachians. Detailed petrography along with Re-Os geochronology of arsenopyrite identified two distinct periods of mineralization: i) an early stage (~365 Ma) of massive arsenopyrite mineralization associated with the Devonian Neoacadian orogen and assembly of Pangea, and ii) a late stage (~214 Ma) of critical metal sulfide mineralization (e.g., sphalerite, pyrrhotite, arsenopyrite, chalcopyrite, jamesonite, boulangerite, galena, pyrite) associated with Late-Triassic rifting during the opening of the Bay of Fundy and Atlantic Ocean. Assays of samples hosting critical metals indicate >10 wt.% As, ~2 wt.% Sb, ~2 wt.% Zn, ~0.6 wt.% Pb. Results from Al-in-chlorite thermometry indicate formation of Fe-Zn-Cu minerals of the late stage at ~360 °C. Quartz and carbonate hosted fluid inclusions indicate mingling of a variably high salinity brine ($NaCl_{equiv}$ = ~6 – 27 wt.%) and methane for Sb-Pb mineralizing fluid, with temperature and pressure constraints from fluid inclusion isochores indicate low temperature-low pressure conditions at ~165 ˚C and ~15 bar. Sulfur isotopes indicate that the Devonian stage of arsenopyrite mineralization ($\delta^{34}S$ = ~15.3‰) was partially dissolved under oxidized conditions and provided sulfur to form the late stage sulfides ($\delta^{34}S$

= ~24.0‰). Comparison of whole rock geochemistry between altered and least altered host rocks [altered mafic sills (437 ± 6.3 Ma from U-Pb in apatite geochronology), metamudstone of the Bear River Formation (Ordovician)], indicate that critical metals (Zn, Pb, Co, Cu, and Fe) were likely leached from country rock. The critical mineral stage of the Lansdowne occurrence is the first polymetallic vein-type deposit in Nova Scotia whose formation is linked to the Late-Triassic rifting from the breakup of Pangea, and exhibits overlapping characteristics with epithermal Sb-Au polymetallic deposits of the European Variscan Belt.

2.1 Introduction

"Critical metals" (e.g., Sb, Co, Ni, REE, etc.) are high priority for mineral exploration due to their demand and role in the transition to greener infrastructure (Natural Resources Canada, 2020). In the Meguma Terrane of southwestern Nova Scotia, the farthest outboard terrane of the Canadian Appalachians, multiple polymetallic vein occurrences endowed in Sb ± Au, as well as significant amounts of As, Co, Ni, Pb, Zn, Cu. Ag, and REE exist hosted in Meguma Terrane metasediments. Gold mineralization in the Meguma Terrane is not unusual; however, so called "traditional Meguma Au" deposits, which form throughout the eastern Meguma Terrane and are an important mineral resource for Nova Scotia, rarely form with other sulfides, especially those of complex metal endowment (Sangster and Smith, 2007). Although generally unrecognized in Nova Scotia, polymetallic Sb-Au deposits are widespread globally [e.g., the Cerro de Pasco deposit, Peru (Rottier et al., 2016), the Laqiong Sb-Au deposit in Tibet (Cao et al., 2019), and the Allchar deposit in Macedonia (Palinkaš et al., 2019)], and include abundant deposits in the European Variscan Belt (e.g., Munoz et al., 1992; Marignac and Cuney, 1999; Wagner and Cook, 2000; Seifert and Sandmann, 2006; Pochon et al., 2016; Krolop et al., 2019). Variscan Sb-Au deposits are related to late-Variscan extensional tectonic processes and form in shallow epithermal conditions (see summary in Wagner and Cook, 2000). Polymetallic Sb-Au mineralization in Nova Scotia has yet to be recognized as a mineralization type.

For this study, a multi-analytical approach has been applied to characterize the Lansdowne occurrence; a polymetallic vein occurrence from the Digby area of southwestern Nova Scotia which hosts abundant Sb, Pb, As and Zn and minor Co, Ag, and Au (**Figure 2-1A**). Mineralized quartz-carbonate veins are hosted in mafic sills of unknown age that intrude Ordovician metasedimentary rocks of the Halifax group. These sills are proximal to the Devonian Ellison Lake Pluton of the South Mountain Batholith, and south of the Triassic sedimentary and volcanic rocks of the Fundy rift basin (**Figure 2-B**). Proposed mechanisms for mineralization by O'Reilly (1978, 1995) include a primitive, deep crustal source for metals, with mafic intrusives as a possible source of heat and/or a conduit for mineralizing fluids. No previous detailed study has been conducted to understand the processes which formed these mineralized veins and to determine if tectonic activity in the region may have triggered mineralization. The Lansdowne occurrence, along with mineralization at Cape St Mary's (Sb-As-Co-Ni-Ag-Au-Bi-REE) to the southwest, and the Nictaux Falls prospect (As-Co-Ni-Au) to the northeast (**Figure 2-A**), represent critical metal-rich polymetallic mineralization in southwestern Nova Scotia and support further exploration for this mineralization style in this region. This study is the first to characterize the Lansdowne occurrence in an attempt to evaluate the economic potential of these deposits.

This paper presents the results of i) petrography and mineral chemistry, ii) U-Pb geochronology of apatite in mafic rocks and Re-Os geochronology of arsenopyrite, iii) Al-in-chlorite thermometry, iv) fluid inclusion analyses, including: petrography, micro-Raman spectroscopy, microthermometry, and decrepitated mound analyses, v) sulfur isotope analyses of sulfides, and vi) whole rock geochemistry of the host rocks of the Lansdowne occurrence. These results are used to interpret i) field relationships, mineralization styles, and occurrence characteristics such as mineralogy, mineral paragenesis and ore distribution, ii) timing and regional context of mineralization, iii) conditions of formation (including pressure, temperature, and fluid chemistry), iv) possible fluid and metal sources, v) classification of this occurrence at a global scale (i.e., Variscan epithermal Sb-Au, Meguma Au, or other), and vi) exploration

criteria for similar deposits in Nova Scotia. This study is the first to examine this occurrence and its place in the mineral resource economy and geological history of Nova Scotia.

2.2 Background

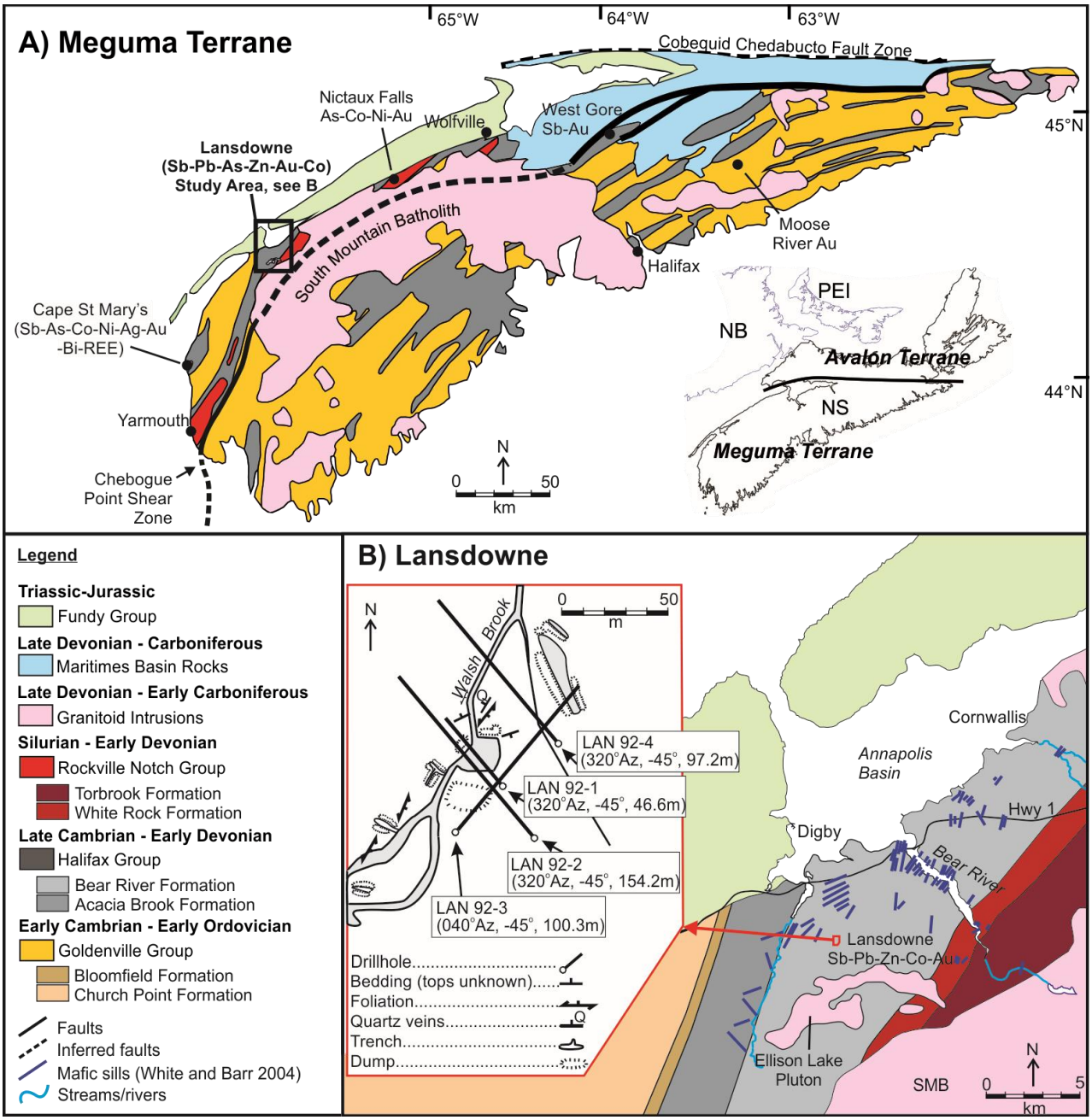

Figure 2-1 - A) Simplified geological map of the Meguma Terrane, with a box outlining the location of the Lansdowne study area, shown in B). Modified from White and Barr (2012). **B)** Local geology of the Lansdowne area. Inset map shows location and details of sampled drill core. Inset and regional map modified from MacIsaac et al. (2017). The locations of mafic sills are from White and Barr (2004).

2.2.1 Geology of the Meguma Terrane

The Meguma and Avalon terranes of mainland Nova Scotia accreted during the latter stages of the assembly of the mid-Paleozoic Appalachian orogen, when the paleo-continents Laurentia (modern North America) and Gondwana (modern Africa and South America) collided to form the supercontinent Pangea (**Figure 2-A**). The Appalachian orogen extends for more than 3000 km along the eastern margin of North America and is considered contemporaneous with the Caledonide and Variscan orogens of western Europe (Murphy and Keppie, 2005; Martínez Catalán et al., 2009). Prior to the final assembly of Pangea, closure of the Rheic and Iapetus Oceans resulted in i) the collision of Avalon into eastern Laurentia, followed by ii) the collision of the Meguma Terrane onto the Avalon Terrane during the mid- to late Devonian Acadian Orogeny, (Williams et al., 1999; Murphy and Keppie, 2005; Shellnutt et al., 2019a). The Meguma and Avalon terranes are separated by the east-west trending Cobequid-Chedabucto fault zone (**Figure 2-A**), the suture zone where the Meguma Terrane was dextrally accreted against the Avalon Terrane (Murphy et al., 2011) which swings into a southeasterly dipping normal fault in the Bay of Fundy (Keppie and Dallmeyer, 1987; Wade et al., 1996).

The Lansdowne occurrence is hosted in the metasedimentary rocks of the Meguma Supergroup along the northwestern margin of the Meguma Terrane (**Figure 2-A**). Metasedimentary rocks of the Meguma Supergroup compose the majority of Meguma Terrane basement rocks and were deposited in a major rift setting along the Gondwanan margin (White, 2010). The Meguma Supergroup consists of thick (up to 11 km; White and Barr, 2010) sequences of interbedded metaturbidites and metasandstones locally interlayered with metasiltstones and black slate of the Cambrian Goldenville Group, and the overlying metasiltstone and metamudstone units of the late Cambrian to middle Ordovician Halifax Group (Raeside and Hill, 1988; White, 2010; White and Barr, 2012). The Silurian Rockville Notch Group unconformably overlies the Meguma Supergroup rocks and consists of slate and quartzite, deposited in a shallow continental shelf setting, along with contemporaneous bimodal metarhyolite and metabasalt (White and Barr, 2017). The Rockville Notch Group has limited surface extent in the Meguma Terrane, occurring only

in the northwest where it is intruded by early Cambrian to early Devonian mafic sills (**Figure 2-1**; White et al., 2003; White and Barr, 2004). These mafic sills formed coevally with deposition of the Meguma Supergroup and the basal unit of the Rockville Notch Group (White Rock Formation; White and Barr, 2004).

The early to middle Devonian Neoacadian Orogeny (ca. 405-365 Ma; Benn et al., 1999; White and Barr, 2012) deformed and variably metamorphosed the Meguma Supergroup, Rockville Notch Group, and mafic sills to sub-greenschist to amphibolite facies. Deformation of the Meguma Supergroup and Rockville Notch Group sediments resulted in NE-SW to N-S trending folds with axial planar cleavage (Horne and Culshaw, 2001). As a result of Acadian deformation, the Meguma Supergroup is cross-cut by the NW-SE striking Chebogue Point Shear Zone (CPSZ), which is interpreted to strike the length of the Meguma Terrane, but is crosscut by the South Mountain batholith (**Figure 2-A**; White and Barr, 2012). The South Mountain batholith and related granitoids were emplaced in the Meguma Terrane at 6 – 10 km depth (Campbell and Raeside, 1999) during the waning stages of the Neoacadian orogeny, between 380 and 370 Ma (Keppie et al., 1993; Kontak and Reynolds, 1994; Reynolds et al., 2004). The granitoid rocks crosscut Neoacadian deformation and faulting (Horne and Culshaw, 2001). The emplacement of these rocks occurred over a period of less than 10 Ma (Benn et al., 1999; Reynolds et al., 2004) and is contemporaneous with widespread lode and disseminated Au mineralization in Goldenville Group metasediments (Kontak et al., 1990a; Kontak et al., 1990b). Clasts of Meguma rocks in the Devonian Horton Group, basal unit of the Maritimes Basin, suggest rapid uplift after the emplacement of the South Mountain batholith (Murphy and Keppie, 2005)

The sedimentary rocks of Maritimes Basin exposed in central Nova Scotia (**Figure 2-A**) are part of a complex package of marine and subaerial sedimentary rocks up to 12 km thick, which were deposited during the final stages of assembly of the supercontinent Pangea over a period of about 120 million years (Gibling et al., 2019). The basin was deposited between the landmasses of Laurentia and Gondwana at an equatorial latitude (Gibling et al., 2019). The Maritimes Basin comprises evaporitic, carbonate, and

siliciclastic rocks, deposited in both marine and fluvio-lacustrine environments (Thomas Martel and Gibling, 1996; Keppie, 2000). In Nova Scotia, the basal units of the Maritimes Basin include the fluvial-lacustrine siliciclastic sedimentary rocks of the Horton Group and evaporitic and shallow marine sedimentary rocks of the Windsor Group (see summary in Keppie, 2000). The Horton Group unconformably overlies Meguma Supergroup metasediments (Thomas Martel and Gibling, 1996). Maritimes Basin rocks are associated with MVT deposits, such as the Gays River carbonate-hosted lead-zinc deposit in Nova Scotia (Akande and Zentilli, 1984). The CPSZ and other similar shear zones along the southwestern Meguma Terrane are suggested to have been re-activated by basin tectonics during the Carboniferous (Culshaw and Reynolds, 1997; Culshaw and Dickson, 2015; Waldron et al., 2015).

By the early Mesozoic, the compressional forces from the closing of the Iapetus and Rheic oceans were replaced by extensional forces that resulted in the breakup of Pangea and the opening of the Atlantic Ocean. These extensional forces caused the opening of the Fundy Rift Basin and a number of other generally northeast trending rift basins along the coast of eastern North America (Kontak, 2008). The Fundy Rift Basin is the largest of this series of failed rift basins, forming the Bay of Fundy between Nova Scotia and New Brunswick, where the Cobequid-Chedabucto fault zone strikes southeast as a normal fault (**Figure 2-A**). Four formations comprise the Middle Jurassic to Lower Triassic Fundy Group in and around the Annapolis Valley of Nova Scotia: The Wolfville Formation, the Blomidon Formation, the North Mountain Basalt (202 ± 1 Ma; Hodych and Dunning, 1992), and the Scots Bay Formation (Wade et al., 1996; Kontak, 2001). The sedimentary sequences of the Fundy Group unconformably overlie the Maritimes Basin and the Meguma Terrane, and represent the initial phase of continental rift sedimentation, subsequent deep lacustrine strata from syn-rift sedimentation, and minor terrestrial facies (Wade et al., 1996).

2.2.2 Lansdowne

The Lansdowne study area is located in Digby County, southwestern Nova Scotia. The local geology at the Lansdowne property consists of laminated metamudstone of the Bear River Formation (Halifax Group) and multiple unnamed carbonate and chlorite altered mafic sills, proximal to the Ellison Lake Pluton, a small granitic intrusion of the South Mountain batholith (**Figure 2-B**). The orientation and abundance of altered mafic sills at the Lansdowne property suggest they are part of a series of mafic sills which are syn-depositional to the Meguma Supergroup and Rockville Notch Group sediments, as established by White and Barr (2003, 2004).

Exploration projects conducted by junior exploration companies in the 1950s and the Nova Scotia government geological survey established the Lansdowne occurrence as a potential prospect for antimony, lead, zinc, arsenic, cobalt, and gold (Conwest Exploration, 1951; O'Reilly, 1995). In 1992, a small diamond drill program conducted by the Nova Scotia government intersected multiple quartz-calcite veins hosting sulfide and sulfosalt mineralization (O'Reilly, 1992). Drill holes LAN92-2 and LAN92-4 (**Figure 2-B** inset) intersected small cm-scale, highly altered mineralized zones within intervals of altered mafic sill, containing quartz-calcite veins hosting considerable jamesonite, arsenopyrite, sphalerite and pyrrhotite. Assays of mineralized samples from drill core indicated elevated Pb (2 – 10 wt.%), Sb (1 – 4 wt.%), Zn (1 – 2 wt.%), Co (up to 640 ppm), and Au (up to 821 ppb; O'Reilly, 1995). Little subsequent work occurred at the Lansdowne prospect until 2016, when a magnetometer survey was carried out. This work established the presence of two large northwest-trending structural features of which one is thought to crosscut the occurrence (MacIsaac et al., 2017). These structural features offset the magnetic anomalies produced by mafic sills in the region (MacIsaac et al., 2017).

2.3 Methodology

2.3.1 Field work and petrography

Representative mineralized veins of the Lansdowne occurrence, and barren samples of the Bear River Formation, altered mafic sills, and quartz-carbonate veins, were collected from available drill core from Nova Scotia government archives at the Stellarton core library. Thin section petrography allowed for characterization of primary and secondary mineralogy and textures, identification of mineral paragenesis, and selection of targets for micro-analytical work. Samples were examined with a TESCAN MIRA 3 LMU Variable Pressure Schottky LEO1450VP field emission scanning electron microscope (SEM) at Saint Mary's University, Halifax, Nova Scotia, equipped with a/an: i) electron dispersive spectroscope (EDS) for semi-quantitative compositional analysis and mineral identification, ii) back-scattered electron (BSE) detector for textural imaging, and iii) cold cathodoluminescence (CL) camera to discriminate zoning and dissolution fractures in quartz and carbonate.

2.3.2 Geochronology

Uranium and lead concentrations in apatite were measured from two samples of altered mafic sills (LAN4-3 and LAN4-2) from Lansdowne for U-Pb dating by laser ablation inductively coupled plasma mass spectrometry (LA-ICP-MS) at the University of New Brunswick's laser ablation facility. Target grains were mapped in thin sections using micro-X-ray fluorescence (XRF). Analyses were performed on a 193 nm excimer laser attached to an Agilent 7700x single quad ICP-MS, following the method of McGregor et al. (2018). Every 15 analyses of unknowns were bracketed by analyses of a primary external standard (Madagascar apatite; Thomson et al., 2012), NIST610 glass standard, and a secondary external standard (Phalaborwa apatite; McGregor et al., 2018). Each apatite grain was analyzed once with a 45 µm beam. Ratios of $^{238}U/^{206}Pb$ and $^{207}Pb/^{206}Pb$ (± 2σ) were plotted, unanchored, on Tera-Wasserburg diagrams to determine intercept ages using the online program IsoplotR (Vermeesch, 2018). The Phalaborwa standard gave a lower intercept age of 2068 ± 15 Ma (n = 10; MSWD = 1.6). This age is within range of the Phalaborwa apatite age determined by McGregor et al. (2018; 2048 ± 16 Ma), as well as ion-microprobe

ages of zircon (2050 ± 13 Ma) and baddeleyite (2060 ± 2 Ma) from the same area and confirm the accuracy of measurements obtained for unknowns of this study.

Two rock samples were submitted for Re-Os isotopic analysis and age dating. Initially, these separates were tested for Re content by isotope dilution and negative thermal ionization mass spectrometry (NTIMS) methods to verify existing Re abundance results, with two samples (LAN2-3 and 7157) yielding ppb level Re abundances suitable for Re-Os dating. Sample LAN2-3 is a representative sample of massive arsenopyrite hosted in calcite and quartz. Sample 7157 is a representative sample of euhedral arsenopyrite and jamesonite hosted in quartz.

A full Re-Os analysis of each sample was undertaken using a small amount of sample, to establish the nature of the Os present, and determine which spike is best suited for each sample. Aliquots of each mineral separate are weighed and transferring to a thick-walled, borosilicate glass Carius tube, with a conventional mixed ^{185}Re + ^{190}Os spike such that the amount of common ^{188}Os, and radiogenic ^{187}Os can be determined. Spiked samples are dissolved at 220 ˚C for 48 hours, followed by chemical separation and purification of Os and Re using procedures described by Shirey and Walker (1995), Cohen and Waters (1996), and Birck et al. (1997), as described in detail by Morelli et al. (2005) and Hnatyshin et al. (2020). These trial analyses showed that sample 7157 contained > 99.9% radiogenic ^{187}Os, and < 0.1% common Os. As such, Re-Os ages are best determined using a mixed double-Os spike containing ^{185}Re + ^{188}Os + ^{190}Os, which allows for accurate mass bias corrections for Os that is purely radiogenic ^{187}Os (described in Markey et al., 2007). Sample LAN2-3 contained > 1% common Os and was analyzed with the conventional mixed ^{185}Re + ^{190}Os spike. Mass spectrometry details are presented by Hnatyshin et al. (2020). Total procedural blanks were measured to be less than 1 picogram Re and 0.2 picogram Os (< 0.01 picograms ^{187}Os). The decay constant used for ^{187}Re is that of Smoliar et al. (1996) of $\lambda = 1.666e^{-11}.a^{-1}$, a value which is cross-calibrated to the U-Pb system (^{238}U and ^{235}U) to better than ~ ± 0.3% (Selby et al., 2007). The Reference Material 8599 Henderson molybdenite (Markey et al., 2007) is routinely analyzed, and during the past 6 years returned an

average Re-Os date of 27.78 ± 0.07 Ma (n = 32), indistinguishable from the reference age value of 27.66 ± 0.1 Ma (Wise and Watters, 2011).

2.3.3 Chlorite thermometry

Major and minor elements of chlorite, in mineralized and unmineralized veins, were collected to identify the chlorite mineral species and calculate temperatures of formation by electron probe microanalyzer (EPMA). Chlorite is a common mineral indicative of low-temperature hydrothermal or metamorphic environments. The wide range of compositions and the non-stoichiometric behaviour of chlorite enables this mineral to be an effective geothermometer (de Caritat et al., 1993). Using an empirical calibration of tetrahedral (Al^{IV}) aluminium in the crystal structure of chlorite, the temperature at which the chlorite crystallized can be determined (de Caritat et al., 1993). Many geothermometers for chlorite exist applicable to certain conditions of chlorite formation, such as a chlorite which forms with a low (< 0.6) Fe/(Fe + Mg) ratio (Jowett, 1991), or when chlorite forms in Al-saturated environments (Kranidiotis and MacLean, 1987). For this project, the empirical equation developed by Cathelineau (1988), which relates *T* (°C) and Al^{IV} composition, is used to calculate the temperature of chlorite formation since the value of Al^{IV} in chlorite appears to be independent of rock lithology and can be applied as a general thermometer in diagenetic, hydrothermal, and metamorphic settings:

$$T = -61.92 + 321.98\,(Al^{IV})$$

Analyses were performed with a JEOL JXA8230 5-WDS EPMA at the University of Toronto using carbon-coated polished thin sections. Measurements were taken with a 10 µm beam, beam current of 10 nA, and accelerating voltage of 15 kV. The major oxides measured, along with their respective quantification reference material in brackets include SiO_2 (chlorite from Smith, 1969), TiO_2 (TiO_2), Al_2O_3 (chlorite from Smith, 1969), Cr_2O_3 (Cr_2O_3), NiO (pentlandite), FeO (hematite), MnO (bustamite), MgO (chlorite from Smith, 1969), CaO (bustamite), Na_2O (albite glass), K_2O (sanidine glass), and SrO ($SrTiO_3$)

as well as anions F (MgF_2) and Cl (tugtupite). The Kα energy line was used for detection of all elements, except for Sr (Lα).

2.3.4 Fluid inclusion analysis

Fluid inclusions in quartz and carbonate were characterized from two mineralized samples at Lansdowne. Fluid inclusion samples were prepared as doubly polished 150 µm thick sections. Petrography was conducted with an optical microscope to identify fluid inclusion assemblages (FIA) and describe other fluid inclusion characteristics, such as phase types and ratios, as well as origin (primary and/or secondary trails). Laser Raman Microscopy (LRM) was used to determine the vapor phase composition of the inclusions and quantify their molar ratios where more than a single vapour phase was analyzed. Analyses used a Jobin-Yvon Horiba LabRam HR confocal Raman microscope with an 800 mm spectrograph at Saint Mary's University, following the method of Kerr et al. (2018). Spectra were collected using an accumulation of three, 45 s acquisitions with a laser spot size of < 5 µm at 80 mV laser output at aperture (2 mV at 100x objective) , and a 600 grooves/mm grating (spectral resolution of approximately ± 2 cm^{-1}).

Chips containing target FIA from fluid inclusion sections were separated for fluid inclusion microthermometry experiments. Analyses were performed using a Linkham FTIR600 heating-freezing stage mounted on an Olympus BX51 microscope at Saint Mary's University. Synthetic fluid inclusions of pure H_2O (melting at 0 °C and homogenization at critical point of 374.1 °C) and pure CO_2 (melting at -56.6 °C) were used as standards for calibration of the instrument. Reproducibility of standards indicated uncertainties ranging from ± 2 to 3°C near the extremes of the working conditions (-190 and 560 °C) and ± 0.1°C near 0°C. Freezing experiments were performed prior to heating experiments to minimize the risk of decrepitation. Salinity of the inclusions was calculated from final ice melting temperatures (Tm_{Ice}; Bodnar 1993). Homogenization temperatures (Th) were determined from heating of inclusions until all phases homogenized. Isochores of aqueous dominated inclusions were determined from homogenization temperatures and salinity using the SoWat software package (Driesner and Heinrich, 2007). Isochores of

vapour dominated inclusions were calculated using the BULK and ISOC fluid inclusion software packages (Bakker, 2003).

To produce decrepitate mounds, mineralized samples containing arsenopyrite and jamesonite (7157) and sphalerite, pyrrhotite, boulangerite, and galena (LAN4-2) were first cleaned with methanol to reduce contamination. The samples were then placed in the Linkham FTIR600 heating-cooling stage and heated to 500 °C at a rate of 40 °C/min to decrepitate the inclusions and produce salt mounds on the sample surface. After decrepitation, the chips were mounted on a glass slide using carbon tape and then carbon coated. The salt mounds were imaged and compositional analyses were collected using the SEM. The EDS was set to a beam voltage of 20 kV in raster mode, and a 45 s count time was allowed for each analysis. The Si and O values were removed from the collected data as quartz contamination.

2.3.5 Sulfur isotopes

Sulfur isotope data were obtained for pyrite, pyrrhotite, arsenopyrite, and chalcopyrite at the Manitoba Isotope Research Facility (MIRF), using a CAMECA 7f secondary ion mass spectrometry (SIMS) instrument, following the methods of McDivitt et al. (2021). Pyrite, pyrrhotite, and chalcopyrite reference material from Crowe and Vaughan (1996) and arsenopyrite reference material from Hastie et al. (In review) were used. Spot to spot reproducibility of the reference material varied: 0.3‰ for apy-1 and post-ore stage pyrite, 0.2‰ for apy-2 and late-stage pyrite, and 0.4‰ for pyrrhotite and chalcopyrite. Analyses were conducted with a ~2ηA beam of Cs^+ accelerated at 10.0 kV. The beam was focused to a ~15 µm spot size using a 700 µm aperture in the primary column. A sample accelerating voltage of -8.7 kV was used with the secondary column set to accept -9.0 kV, the resulting 300 V offset was used to suppress isobaric interferences. The entrance slit was set to 225 µm with a mass resolving power of 350 to obtain flat-topped peaks. Ions were detected using an electron multiplier, with one second of counting on ^{32}S and five seconds on ^{34}S per cycle, a single analysis consisted of 50 cycles. Data are represented in units of per mil (‰) relative to Vienna Canyon Diablo troilite (VCDT). Within spot uncertainties were 0.3‰ (1σ) for all analyses.

2.3.6 Whole rock geochemistry

Whole rock geochemical data were collected from representative most and least altered host rock (Bear River Formation and altered mafic sills), as well as sulfide mineralization. Samples were sent to Actlabs Ancaster, Ontario, Canada, for preparation and analysis. All samples were crushed to a nominal 2 mm and mechanically split to obtain a representative sample and pulverized to 105 µm. To obtain major oxides of unmineralized samples, crushed samples were prepped using lithium borate fusion, and were analyzed with X-ray fluorescence. For minor and trace elements, unmineralized crushed samples were subject to closed vessel multi-acid microwave digestion and measured with ICP-MS. For mineralized samples, minor and trace elements were measured using peroxide total fusion for total metal recovery. Analyses were conducted using ICP-MS and ICP-OES. The concentrations of Au and Ag were also measured in mineralized samples via Au cyanide extraction and ICP-MS for Ag.

Geochemical data were used to quantitatively determine the mass balance of metals from hydrothermal alteration in mafic sills and metasediments. Mass balances were calculated using the method of Gresens (1967), as modified by Grant (1986). Immobile elements aluminum and titanium (TiO_2) were used to define an isocon line, by comparing the mass of the original samples against the mass of the altered samples (M^o/M^a). Elements that plot above the reference isocon were enriched during alteration, whereas elements that plot below were depleted (Grant, 1986).

2.4 Results

2.4.1 Field observations and petrography

The Bear River Formation laminated metamudstone country rock consists of alternating mm to cm wide laminations composed of very fine-grained quartz- and muscovite-rich layers. Dark green carbonate-altered mafic sills, ranging in width from 2-3 cm up to 10 m, crosscut the metamudstone and display chilled margins (**Figure 2-2A, C**). These sills consist of primary plagioclase, augite, hornblende, and apatite, with abundant secondary chlorite, ilmenite, and minor pyrite and calcite. Some sills are pervasively altered by calcite, destroying primary igneous textures. Abundant quartz ± calcite veins (1-10 cm wide) crosscut the

metamudstone and the altered mafic sills. Some of these veins, observed only in the altered mafic sills, contain sulfide mineralization with calcite and overprint quartz (**Figure 2-2A, C**).

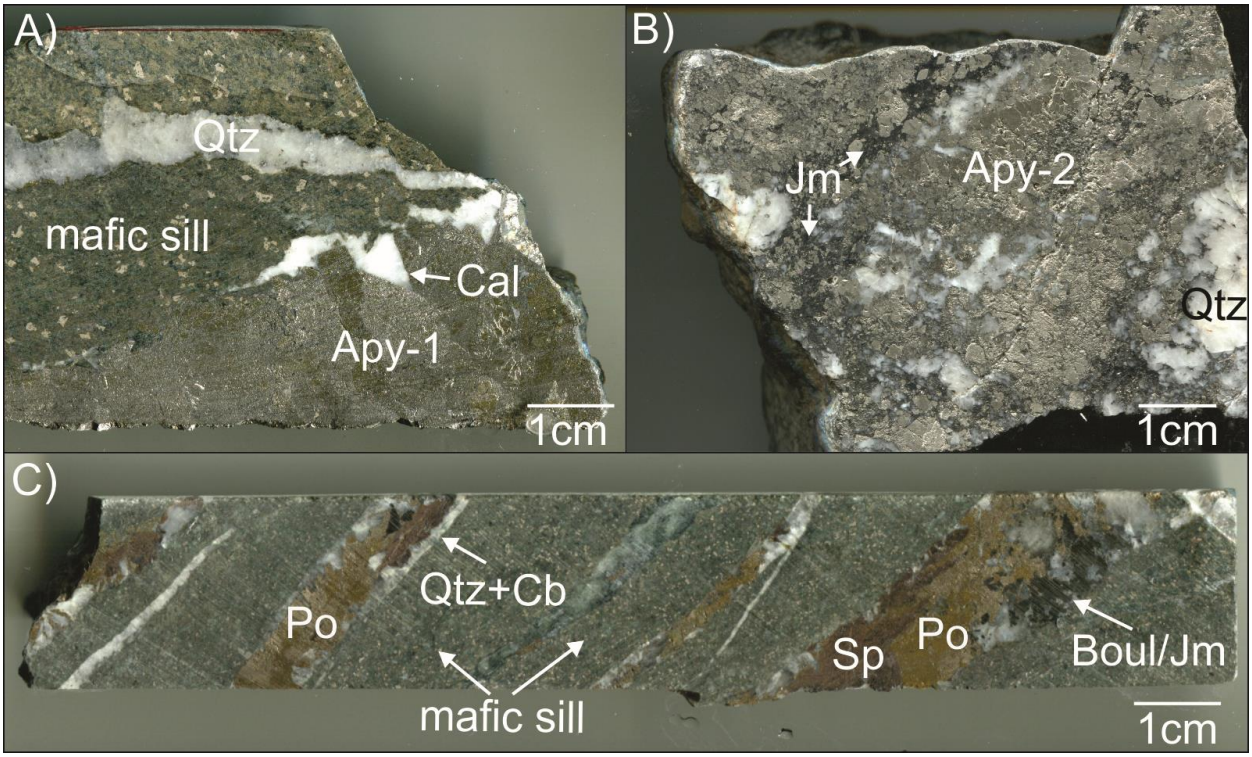

Figure 2-2 - Mineralized hand samples from Lansdowne. **A)** Massive arsenopyrite (Apy-1) with calcite (Cal) crosscutting an altered mafic sill, adjacent to a barren quartz (Qtz) vein. **B)** Euhedral arsenopyrite (Apy-2) and interstitial jamesonite (Jm) crosscutting quartz. **C)** Quartz-calcite veins crosscutting a mafic sill. Mineralized veins host massive pyrrhotite (Po), sphalerite (Sp), and boulangerite (Boul)/jamesonite.

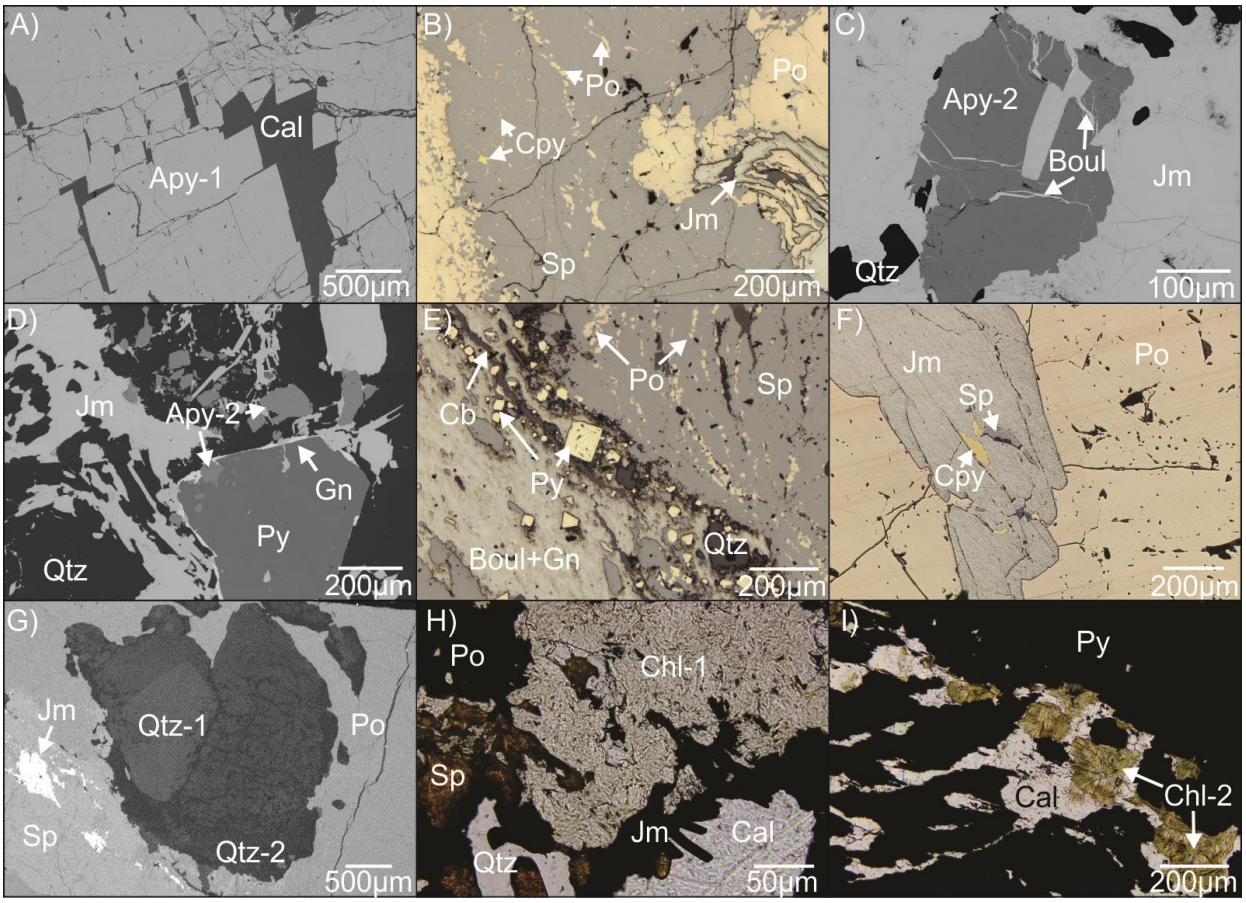

Figure 2-3 – Photomicrographs and BSE images of mineralized veins at Lansdowne. **A)** Photomicrograph (RL): first-generation arsenopyrite (Apy-1) hosted in a calcite (Cal) vein. **B)** Photomicrograph (RL); earlier pyrrhotite (Po) is replaced by later sphalerite (Sp), which exhibits chalcopyrite (Cpy) disease texture. Pyrrhotite and chalcopyrite islands are arranged along grain boundaries and within grains of sphalerite by internal structures. Pyrrhotite and sphalerite are replaced and crosscut by later jamesonite (Jm). **C)** BSE image; subhedral arsenopyrite (Apy-2) is replaced by jamesonite in a quartz (Qtz) vein. Boulangerite (Boul) forms small veinlets cutting only across the arsenopyrite and occasionally along arsenopyrite grain boundaries in with jamesonite. **D)** BSE image; arsenopyrite (Apy-2) and acicular interstitial jamesonite hosted in quartz. Galena reaction rim formed between late euhedral pyrite (Py) and jamesonite. **E)** Photomicrograph (RL); sphalerite with pyrrhotite islands crosscut by later boulangerite, with galena (Gn) exsolution, and euhedral pyrite. Euhedral pyrite often contains inclusions of sphalerite. **F)** Photomicrography (RL); pyrrhotite replaced by jamesonite showing cusp carrie texture. Jamesonite

contains inclusions of chalcopyrite and sphalerite. **G)** CL image; quartz of a mineralized vein. Two generations of quartz visible: Early higher fluorescence quartz (Qtz-1) and later lower fluorescence quartz (Qtz-2). Sulfide minerals adjacent to quartz include pyrrhotite, sphalerite and jamesonite. Qtz-2 coeval with jamesonite. **H)** Photomicrograph (PPL); first-generation chlorite (Chl-1) is formed coevally with sphalerite along the margin of a mineralized quartz and calcite vein. **I)** Photomicrograph (PPL); calcite overprinted by late pyrite. Dark green radial aggregates of second-generation chlorite (Chl-2) are formed between grains of the pyrite.

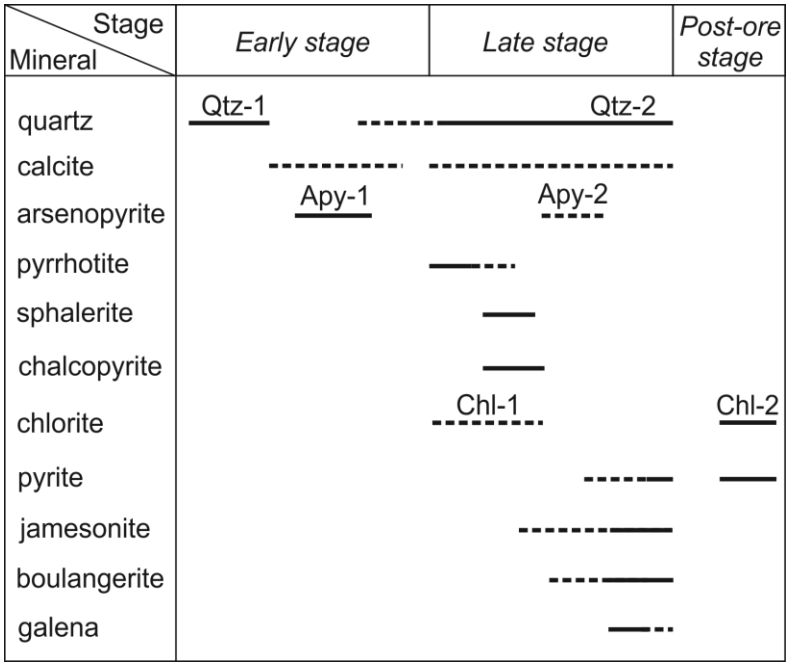

Figure 2-4 - Paragenesis of mineralized veins at Lansdowne, subdivided into three stages by associated mineralogy. Dashed lines indicate uncertainty in the paragenesis.

Mineralization consists of arsenopyrite, pyrrhotite, sphalerite, chalcopyrite, pyrite, boulangerite (ideal formula: $Pb_5Sb_4S_{11}$), jamesonite (ideal formula: $Pb_4FeSb_6S_{14}$) and galena. Gangue minerals include quartz, calcite, chlorite, and pyrite. These minerals can be subdivided into an early, late, and post-ore stage, as outlined in **Figure 2-4**. Massive, early stage arsenopyrite (Apy-1) occurs with interstitial calcite, crosscutting an altered mafic sill (**Figure 2-3A**). Early stage arsenopyrite is compositionally homogenous

and is not observed forming with any other sulfides, however, a single grain shows minor Co-enrichment along fractures (up to 8 wt.%; **Table A2-2**).

Massive pyrrhotite dominates much of the mineralized veins (**Figure 2-2C**) and displays island-mainland texture along grain boundaries with sphalerite, where pyrrhotite occurs as islands (inclusions) distributed along intragrain structures of the sphalerite **(Figure 2-3B, E**). Honey-colored sphalerite is Fe-poor (5-7 wt.%), contains up to 4 wt.% Cd, and exhibits chalcopyrite disease textures with both chalcopyrite and pyrrhotite inclusions (**Figure 2-3B, E**). Late stage arsenopyrite (Apy-2) forms as large (100 µm – 1 mm) euhedral crystals alongside acicular jamesonite. This stage of arsenopyrite is compositionally homogenous. The textural relationship between arsenopyrite and jamesonite is sometimes ambiguous, as some grains of arsenopyrite show jamesonite inclusions, but are also often brecciated by jamesonite (**Figure 2-3C**). Overall, these minerals appear coeval or arsenopyrite formed slightly earlier. Boulangerite often forms along arsenopyrite and jamesonite grain boundaries, and as veinlets in the arsenopyrite (**Figure 2-3C**). Both pyrrhotite and sphalerite are replaced by massive-to-acicular jamesonite, where jamesonite appears to preferentially replace the pyrrhotite (**Figure 2-3B, F**). Massive boulangerite with galena exsolution also crosscuts sphalerite and pyrrhotite, displaying islands of sphalerite in the boulangerite (**Figure 2-3E**). Euhedral pyrite grains (10 – 300 µm) form alongside sulfosalts jamesonite and boulangerite, and contain inclusions of sphalerite, jamesonite, and arsenopyrite (**Figure 2-3D, E**). Where pyrite is in contact with jamesonite, a rim of galena can sometimes be visible along grain boundaries (**Figure 2-3D**). Cathodoluminescence (CL) of mineralized quartz-calcite veins indicate that multiple quartz generations exist in mineralized veins. Early quartz (Qtz-1) is overgrown by later quartz (Qtz-2) and calcite (**Figure 2-3G**). Qtz-2 and calcite are coeval with late-stage Sb-Pb minerals boulangerite and jamesonite.

Late ore stage sphalerite and pyrrhotite form coevally with pale green to colorless fine-grained chlorite, with first order grey to anomalous Berlin blue interference colors, known as type-1 chlorite (Chl-1; **Figure 2-3H**). Chlorite of the same color and characteristics, but coarser grained, also forms in barren veins as radial aggregates. In veins where calcite is replaced by post-ore stage gangue pyrite, spaces between

the pyrite grains are filled with radial crystals of a second-generation dark green chlorite with 1st order grey-green interference colors (Chl-2; **Figure 2-3I**).

2.4.2 Geochronology

Apatite in two samples of altered mafic sills adjacent to mineralized veins were selected for U-Pb geochronology. The first apatite sample (LAN4-3) yielded an upper intercept age of 423 ± 21 Ma (MSWD = 1.08; **Table A1-3**; **Figure A1-**) based on 43 measurements. The second sample (LAN4-2) yielded an intercept age of 437 ± 6.3 Ma (MSWD = 1.5; **Table A1-3**; **Figure A1-2**) based on 53 measurements. These rocks are Silurian in age.

Table 2-1 - Re-Os geochronology results of arsenopyrite in sample LAN2-3. Mixed spike.

Sample ID[a]	Mineral[b]	Re (ppb)	± 2σ	Total Os (ppt)	± 2σ	$^{187}Re/^{188}Os$	± 2σ	$^{187}Os/^{188}Os$	± 2σ	rho	**Model Age (Ma)**
LAN2-3	Apy-1	0.355	0.003	4.2	0.3	702	69	5.59	0.55	0.992	**365.4 ± 4.8**
LAN2-3 R1	Apy-1	0.438	0.001	1.9	0.6	10317	2511	64.95	15.84	0.998	
LAN2-3 R2	Apy-1	0.361	0.002	1.5	0.5	12072	3226	74.09	19.87	0.996	
LAN2-3 R3	Apy-1	0.558	0.003	2.3	0.7	15840	3622	97.44	22.39	0.994	

[a] R = replicate
[b] Apy-1 = early stage arsenopyrite

Table 2-2 - Re-Os geochronology results from sample 7157. Mixed double-Os spike.

Sample ID[a]	Mineral[b]	Total Re (ppm)	± 2σ	^{187}Re (ppb)	± 2σ	^{187}Os (ppb)	± 2σ	Total common Os (pg)	**Model Age (Ma)**	± 2σ
7157 *NM07*	Apy-2	0.716	0.002	449.7	1.3	1.6	0.01	0.3	**214.6**	1.2
7157-R1 *NM07*	Apy-2	0.710	0.002	446.5	1.2	1.6	0.00	0.4	**213.9**	1.1
7157 *M05*	Jm	0.149	0.0004	93.8	0.3	0.4	0.00	0.3	226.6	1.5
7157-R1 *MO5*	Jm	0.177	0.0005	111.6	0.3	0.4	0.00	0.9	228.7	1.4

[a] R = replicate, NM07 = non-magnetic 0.7A on Frantz, M05 = magnetic 0.5A on Frantz
[b] Apy-2 = late stage arsenopyrite, Jm = jamesonite

Samples containing early and late stage arsenopyrite (Apy-1 and Apy-2, respectively) were selected as targets for Re-Os geochronology. Sample LAN2-3 contains massive early stage arsenopyrite hosted in a

quartz and calcite vein. Four replicates of this sample were analyzed (**Table 2-1**), yielding a model age of 365.4 ± 4.8 Ma (MSWD = 1.4; **Figure A1-4**). Sample 7157 contains euhedral late stage arsenopyrite and interstitial jamesonite. Two replicate analyses from the arsenopyrite separate yielded a model age of between 213.9 ± 1.2 Ma and 214.6 ± 1.1 Ma (**Table 2-2**). Since there was sufficient Re content in the jamesonite, two replicates were also run from the jamesonite separate and yielded a model age between 226.6 ± 1.5 Ma and 228.7 ± 1.4 Ma (**Table 2-2**). However, considering the systematics of Re-Os geochronology in jamesonite are unknown, and these ages conflict with the textural evidence for jamesonite with late stage arsenopyrite (**Figure 2-3C-D**), the age of the jamesonite is not considered reliable.

2.4.3 Chlorite thermometry

Chlorite in quartz-carbonate veins has been classified into two generations based on petrographic characteristics such as color, texture, and mineral association/paragenesis. All chlorite examined can be classified as Mg-rich chamosite, based on the proportions of octahedral Al (Al^{VI}), Fe, and Mg (**Table A1-5**). Type-1 chlorite (Chl-1) formed alongside mineralization and barren quartz-carbonate veins. Type-1 chlorite has relatively less Fe than type-2 chlorite (Chl-2; **Table A1-5**). Additionally, the Fe# (Fe/ Fe+Mg)) of type-1 chlorite varies between different samples (0.55 to 0.68; **Table A1-6**) but the proportion of Al is similar (**Table 2-3**). Type-1 chlorite associated with sulfide minerals exhibits the lowest Fe#. Using the equation by Cathelineau (1988) based on the Al^{IV} content of chlorite, type-1 chlorite has temperatures ranging from 350 – 400 °C (**Table A1-6**). Type-2 chlorite has temperatures ranging from 125 – 160 °C (**Table A1-6**). Fe# of type-2 chlorite is higher than type-1, ranging between 0.72 to 0.80 (**Table A1-6**).

Table 2-3 – Abundance of major oxides in chlorite in wt.% and their atomic proportions based on 14 oxygen.

	Chlorite type	Type-1 (mineralized [a])		Type-1 (unmineralized)		Type-2	
	Associated metal stage [b]	Late stage		---		Post-ore stage	
	# of grains/points	4/8		8/12		4/8	
		x̄	1σ	x̄	1σ	x̄	1σ
O14	SiO_2	26.03	0.28	24.55	0.19	30.52	0.51

	TiO_2	0.13	0.02	0.10	0.03	0.07	0.02
	Al_2O_3	23.14	0.66	24.65	0.50	12.77	0.52
	Cr_2O_3	0.01	0.01	0.01	0.01	0.00	0.01
	NiO	0.01	0.01	0.01	0.01	0.01	0.01
	FeO	26.46	1.35	31.21	1.25	38.83	1.69
	MnO	0.23	0.05	0.20	0.05	0.18	0.03
	MgO	12.90	0.75	8.94	0.58	5.82	1.31
	CaO	0.18	0.32	0.02	0.02	0.56	0.22
	Na_2O	0.03	0.02	0.02	0.03	0.06	0.03
	K_2O	0.01	0.02	0.01	0.04	0.03	0.02
	SrO	0.01	0.02	0.01	0.03	0.01	0.03
	F	0.06	0.07	0.05	0.07	0.05	0.07
	Cl	0.01	0.01	0.01	0.01	0.01	0.01
apfu [c]							
T	Si	2.70		2.59		3.40	
	Al	1.30		1.41		0.60	
	sum	4.00		4.00		4.00	
O	Al	1.52		1.66		1.07	
	Fe	2.29		2.76		3.61	
	Mg	1.99		1.41		0.96	
	Mn	0.02		0.02		0.02	
	sum	5.83		5.84		5.67	
	vac	0.17		0.16		0.33	
OH	F	0.01		0.01		0.01	
	Cl	0.00		0.00		0.00	
	OH*	7.97		7.97		7.97	
Fe #		**0.53**		**0.66**		**0.79**	
T (°C) [e]		**357.23**		**391.33**		**132.21**	

[a] Chlorite associated with late stage mineralization in mineralized samples
[b] Determined by paragenesis in section 2.4.1
[c] Atomic proportions of elements in each crystallographic site (T= tetrahedral, O = octahedral, OH = OH site)
[e] Calculated using equation by Cathelineau (1988) in section 2.3.3

2.4.4 Fluid inclusion systematics

Fluid inclusion assemblages (FIA) are concentrated within the second-generation of quartz (Qtz-2) associated with late-stage mineralization. Early quartz (Qtz-1) is FIA poor. Considering the FIA do not crosscut earlier quartz, they are likely primary to the second-generation of quartz. Only one generation of calcite was observed using cathodoluminescence, and it contains abundant fluid inclusion assemblages that are similar to those hosted in the second-generation of quartz.

Two types of fluid inclusion assemblages in the quartz and carbonate are classified based on petrographic observations, composition as determined by LRM, and microthermometry measurements (**Table 2-4**). Type-1 assemblages are subdivided into three distinct subtypes based on phases, all of which can be found in single inclusion trails. Type-1a inclusions are commonly liquid-rich two- (L + V) or three-phase (L + L + V) inclusions. The main liquid phase comprises 80-99% of the total volume (**Figure 2-5**). In the three phase inclusions, a second minor CO_2 liquid phase is observed. Type-1b are vapour-rich two-phase (L + V) inclusions, with the vapour phase comprising 20-99% of the total volume. Type-1a and 1b inclusions show wide H_2O peaks with LRM, which confirms the predominate liquid phase as aqueous, whereas methane is the dominant vapour phase. A small portion of type-1a and -1b inclusions also show the additional presence of CO_2 in the vapour phase. Quantification of methane and CO_2 peaks of type-1 inclusions indicate that when CO_2 is present in the inclusion, the vapour phase will contain 75-95% CO_2. Type-1b inclusions most commonly contain CO_2. Type 1c are single-phase vapour inclusions of methane. Type-2 inclusions are single phase aqueous inclusions, which occur as assemblages in secondary trails (**Figure 2-5**). These are composed of mainly H_2O, with minor or no methane.

Table 2-4 - Summary of fluid inclusion types and characteristics

Properties	FI types			
	Type 1: aqueous methane			Type 2: aqueous
Representative inclusion appearance at 20°C	1a 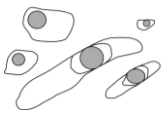	1b 	1c 	2 
Phases present at 20°C	$L_{H2O + NaCl} + V_{CH4 \pm CO2} \pm L_{CO2}$	$V_{CH4 \pm CO2} + L_{H2O + NaCl}$	V_{CH4}	$L_{H2O + NaCl}$
Occurrence/Mineral	Common: clusters in Qtz-2 and calcite	Common: clusters in Qtz-2 and calcite	Uncommon: linear assemblages and clusters in Qtz-2 and calcite	Uncommon: linear assemblages in quartz
Total # of inclusions analyzed	132 (in 23/37 total FIA)	40 (in 12/37 total FIA)	21 (in 9/37 total FIA)	34 (in 9/37 total FIA)
Size (µm)	< 30	< 15	< 40	< 10
% Vapor	1-20	20-99	99-100	0
Tm_{ice} (°C)	-27.9 to -3.8; *n* = 90	ND	ND	-44.8 to -20.4; *n* = 17

Salinity (wt.% NaCl equiv.)	6.16 – 27.35	ND	ND	22.65 – 41.12
Th (°C)	120.5 to 297.0; *n* = 82	ND	-110.3 to -90.2; *n* = 5	ND

White = liquid phase, grey = vapor phase, ND = no data

Microthermometry cooling experiments for the final ice melting (Tm_{Ice}) temperature of each of the inclusion types were used to calculate salinity. The Tm_{Ice} for type-1a ranged from -27.9 °C to -3.8 °C, and salinity ranged from 6.16 to 27.35 wt.% eq. NaCl. Type-1a is therefore a brine with a wide range in salinity. Most FIA containing type-1a exhibit relatively low salinity (6 – 12 wt.% eq. NaCl), and highest salinity (12 – 27 wt.% eq. NaCl) inclusions occur together in a single sample. Most type-1b, -1c and type-2 inclusions did not freeze at or before the limit of liquid nitrogen cooling (~ 180 °C). Those type-2 inclusions which were able to record Tm_{Ice} ranged from -44.8 °C to -20.4 °C, with salinities from 22.65 to 41.12 wt.% eq. NaCl (**Figure 2-6A**).

Microthermometry heating experiments determined temperature of homogenization (Th) for inclusion types -1a and -1c. Type-1b inclusions contain a large vapour phase and decrepitated without ever reaching homogenization. Many of the type-1a inclusions also decrepitated. Many type-1c inclusions never reached homogenization in the temperature range of the instrumentation. The majority of Th data was collected from type-1a dominant FIA. Temperature of homogenization to liquid of type-1a inclusions range from 120.5 °C to 297.0 °C, and for type-1c inclusions range from -110.3 °C to -90.2 °C (**Figure 2-6B**).

Isochores for endmember fluid inclusions representing each of the fluids (nearly 100% aqueous fluid as observed in type-1a two-phase inclusions and nearly 100% methane, as observed in type-1c inclusions) were plotted on a pressure vs temperature plot (**Figure 2-6C**). Entrapment conditions of the fluids are defined where the endmember isochores intersect, at 165 °C and 15 bars (**Figure 2-6C**). Pressure at 15 bars is roughly equivalent to 60 m under lithostatic conditions, and 150 m under hydrostatic conditions.

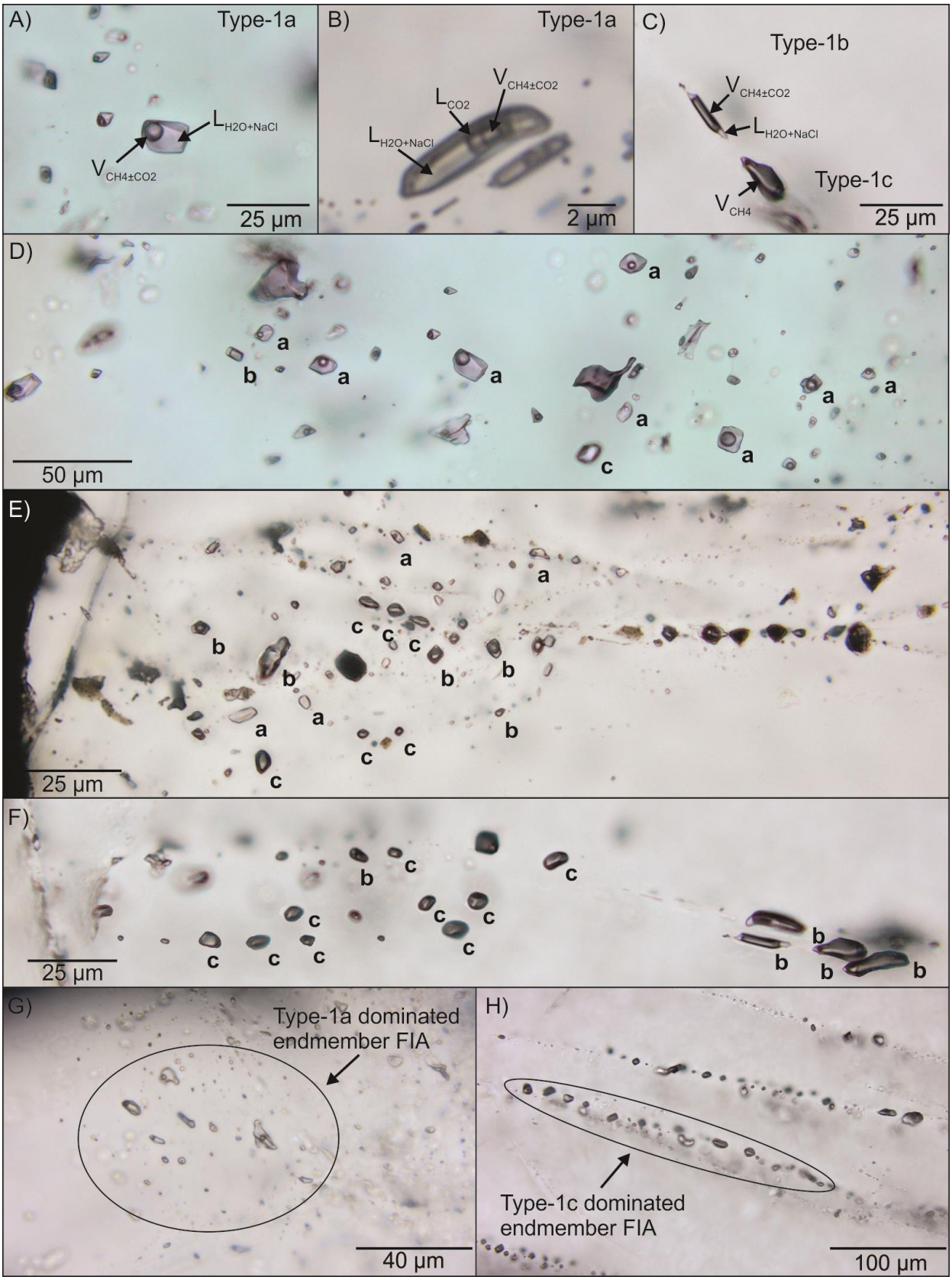
A)
Type-1a
$L_{H2O+NaCl}$
$V_{CH4±CO2}$
25 µm
B)
Type-1a
$V_{CH4±CO2}$
L_{CO2}
$L_{H2O+NaCl}$
2 µm
C)
Type-1b
$V_{CH4±CO2}$
$L_{H2O+NaCl}$
Type-1c
V_{CH4}
25 µm
D)
50 µm
E)
25 µm
F)
25 µm
G)
Type-1a dominated endmember FIA
40 µm
H)
Type-1c dominated endmember FIA
100 µm

Figure 2-5 - Petrography of type-1 fluid inclusions at Lansdowne. Images D-F are manipulated to show inclusions in one depth-plane. **A)** Two-phase liquid rich type-1a inclusions in a cluster FIA in quartz. **B)** Three-phase liquid-rich type-1a inclusions. The second liquid phase is CO_2 liquid. **C)**. Two-phase vapour-rich type-1b inclusion and single-phase vapour type-1c inclusion in same FIA. **D)** A single cluster heterogenous assemblage shows type-1a (**a**), -1b (**b**), -1c (**c**) inclusions. **E)** A sublinear assemblage shows types -1a, -1b, and -1c inclusions. Note that aqueous inclusions with no visible vapour phase contain a very small (~ 0.1% total volume) vapour phase, which could not be resolved in this image. **F)** A linear assemblage shows type-1b and -1c inclusions. **G)** Type-1a dominated cluster FIA hosted in quartz. Representative of endmember type-1a fluid inclusions. **H)** Type-1c dominated linear FIA hosted in quartz. Representative of endmember type-1c inclusions.

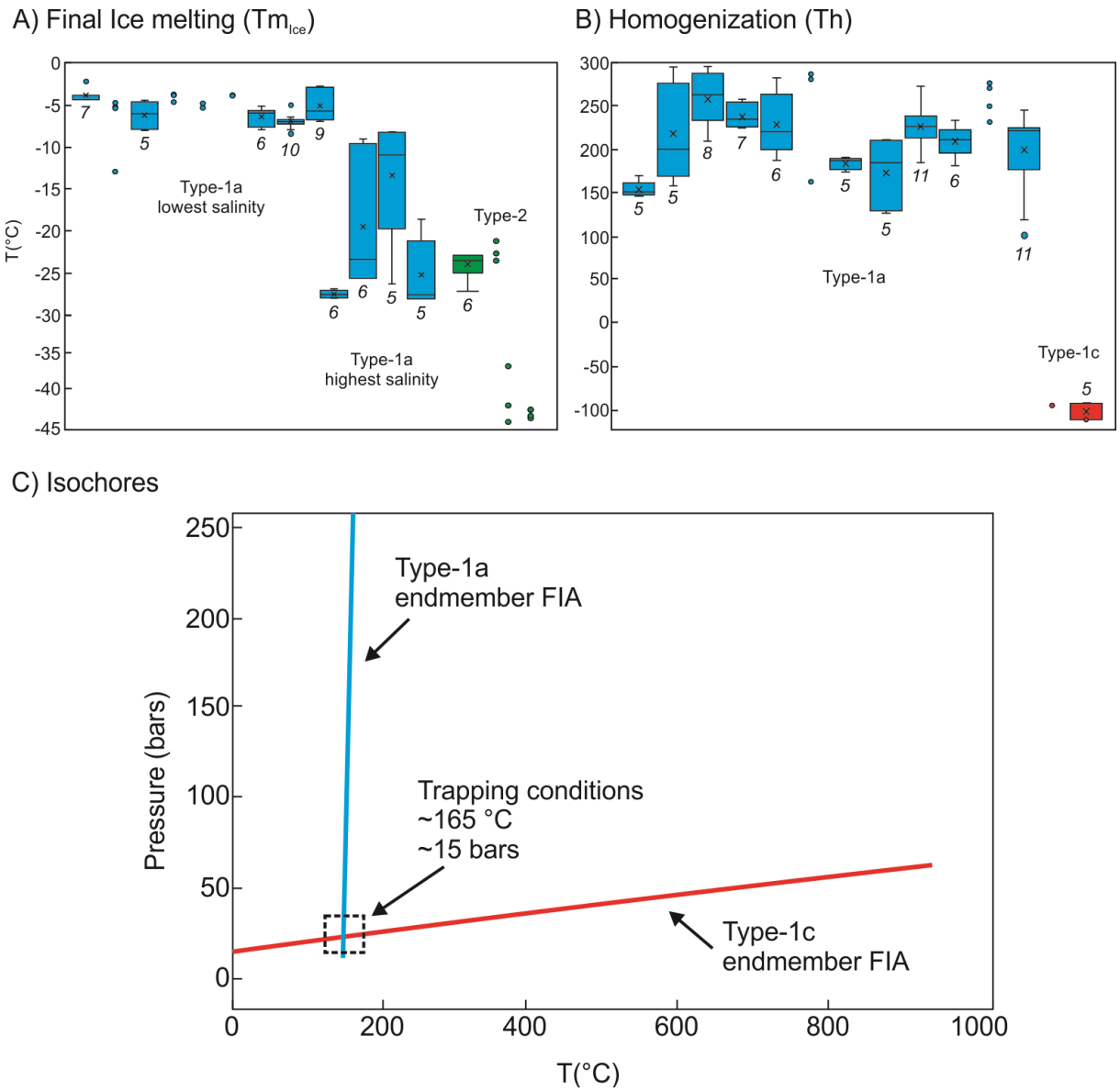

Figure 2-6 - Microthermometry experiments based on FIA from Lansdowne. Each box and whisker plot represents a different FIA. The number in italics below each plot represents the number of analyses per plot. **A)** Cooling experiments determined final ice melting temperatures (Tm_{ice}). **B)** Heating experiments determined temperature of homogenization (Th) to liquid (Type-1a) and to vapour (Type-1c). **C)** Isochores representative of microthermometry results of FIA with endmember compositions, as observed in **Figure 2-5**. Trapping conditions exist where isochores intersect.

2.4.4.1 Decrepitated mound analysis

Decrepitated mounds from two fluid inclusion samples at Lansdowne were analyzed. Sample 7157 is composed of late stage arsenopyrite and jamesonite mineralization. Sample LAN4-2 is associated with late-stage sphalerite, pyrrhotite, and boulangerite mineralization. Salts were composed primarily of Na and Ca cations, with minor K in 86 of 245 total analyses (averaging 2.1 wt.%; **Table A1-8**). Antimony was present in 65 analyses (averaging 37.4 wt.%), arsenic in 90 analyses (averaging 26.5 wt.%), and lead in 10 analyses (averaging 2.3 wt.%; **Table A1-8**). Arsenic was predominantly present in sample 7157 (**Figure 2-7**). Antimony and lead were equally present in the two samples, which both contained Sb-Pb sulfosalt mineralization. Manganese was also detected in 56 analyses, averaging 0.8 wt.% (**Table A1-8**). Other metals were detected in only a small number of analyses (< 10 of 245 total analyses), including Ni, Fe, Mg, Al, and Ti (**Table A1-8**). Plots comparing metal content to Na and Ca content of decrepitated mounds show that metal content generally increases with increasing Ca content (**Figure 2-7**).

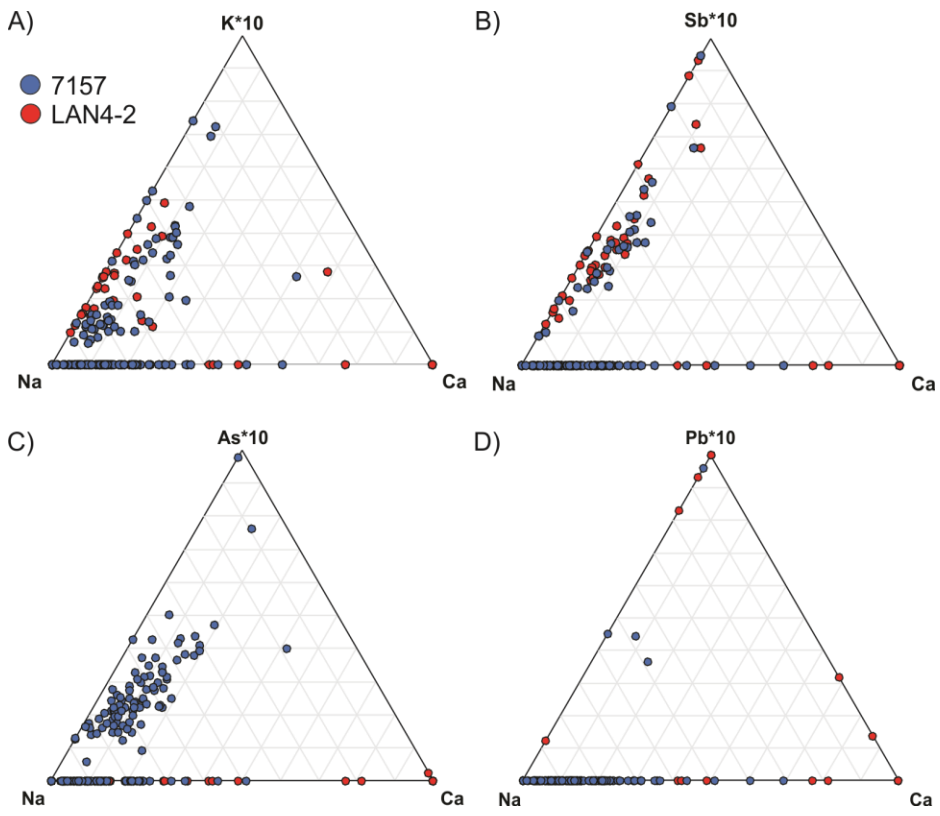

Figure 2-7 – Ternary diagrams illustrating the ratio in compositions of decrepitated mounds. Potassium and metal cation values are multiplied by ten to better show spread in data. Sample 7157 analyses presented in blue. Sample LAN4-2 analyses presented in red. **A)** Na – Ca – K (x10) **B)** Na – Ca – Sb (x10) **C)** Na – Ca – As (x10) **D)** Na – Ca – Pb (x10).

2.4.5 Sulfur isotopes

Sulfur isotope values were measured from four different sulfide minerals: arsenopyrite, pyrrhotite, chalcopyrite, and pyrite. Two separate stages of arsenopyrite and pyrite were analyzed. All minerals analyzed demonstrated high positive S-isotope values, ranging from + 14.7‰ to + 25.1‰. Intrasample variation within a single mineral was relatively small (< 2‰) for all minerals, except for post-ore stage pyrite, which varied from + 17.1‰ to + 23.1‰ over nine points (**Table 2-5**).

The $\delta^{34}S$ of the fluid can be calculated using the formula $\Delta\delta^{34}S = \delta^{34}S_{FLUID} - \delta^{34}S_{SULFIDE}$, where $\Delta\delta^{34}S$ is the fractionation factor between the sulfide and the fluid at a given temperature (*1000 ln α*). $\delta^{34}S_{FLUID}$

assumes SO_4^{2-} is the predominant sulfur species of the fluid due to high positive $\delta^{34}S$ values of sulfides, and that $\delta^{34}S_{SULFIDE}$ represents each individual mineral. This calculation assumes a pure $SO_4^{2-} \Leftrightarrow H_2S$ exchange for all minerals (Eldridge et al., 2016), where H_2S acts as a proxy for the fractionation of sulfur into sulfides. Since appropriate mineral-fluid fractionation factors were not available for these minerals, these results are semi-quantitative. The fractionation factors were calculated using temperatures determined from chlorite thermometry in section 2.4.3 and fluid inclusion isochores of endmember FIA associated with late-stage mineralization in section 2.4.4. At 360 °C, $1000 \ln \alpha = 16.4$ (Eldridge et al., 2016). The $\delta^{34}S$ values of the sulfate dominated fluid associated with the late stage of mineralization ranged from 31.2‰ to 40.4‰. At 165 °C, $1000 \ln \alpha = 32.7$ (Eldridge et al., 2016). The $\delta^{34}S$ values of the sulfate dominated fluid associated with the late stage of mineralization ranged from 47.5‰ to 56.7‰. At 130 °C, $1000 \ln \alpha = 37.9$ (Eldridge et al., 2016). The $\delta^{34}S$ value of the sulfate dominated fluid for post-ore stage pyrite is 57.2‰.

Table 2-5 - Summary of S-isotope data for sulfide minerals determined by SIMS.

Mineral[a]	Associated metal stage[b]	$\delta^{34}S_{SULFIDE}$ (‰)				$\delta^{34}S_{FLUID}$ (‰)[d]		
		# of grains/points [c]	$\bar{x}$	±1σ	T (°C)	360 [e]	165 [f]	130 [g]
arsenopyrite	Early stage (Apy-1)	2/8	**+15.3**	0.59		--	--	--
arsenopyrite	Late stage (Apy-2)	3/5	**+24.0**	0.76		40.4	56.7	--
pyrrhotite	Late stage	3/4	**+15.8**	0.51		32.2	48.5	--
chalcopyrite	Late stage	3/3	**+19.3**	0.30		35.7	52.0	--
pyrite	Late stage	3/3	**+14.8**	0.20		31.2	47.5	--
pyrite	Post ore stage	3/9	**+19.3**	2.66		--	--	57.2

[a] Minerals eligible for SIMS analysis in Lansdowne mineralized samples based on available reference materials
[b] Determined from observed paragenesis in section 4.1
[c] Number of spots analyzed per mineral
[d] Calculated via fractionation factor between H_2S and SO_4^{2-} as determined by Eldridge et al. (2016).
[e] Temperature from chlorite thermometry, determined from Type-1 chlorite in mineralized samples
[f] Temperature from fluid inclusion isochores, determined from Type-1a and Type-1c endmember isochores in equilibrium with late-stage Sb-Pb mineralization
[g] Temperature from chlorite thermometry, determined from Type-2 chlorite in mineralized samples

2.4.6 Whole rock geochemistry

Bulk Au and Ag concentrations were measured from two mineralized samples at Lansdowne. The first sample contained primarily sphalerite, pyrrhotite, boulangerite, jamesonite, and galena. This sample

contained 167 ppb Au and 3520 ppb Ag (**Table A1-11**). The second sample contained only massive arsenopyrite mineralization (Apy-1) and contained 5.45 ppb Au and 1390 ppb Ag (**Table A1-11**).

Mass balance calculated from most and least altered Bear River Formation metasediments and mafic sills indicate depletion of Ni, Zn, Pb, Co, Cu, and Fe, and enrichment in Sb and As from alteration processes (**Figure 2-8**). Both the mafic sills and the metasediments show similar enrichment and depletion patterns (**Figure 2-8**).

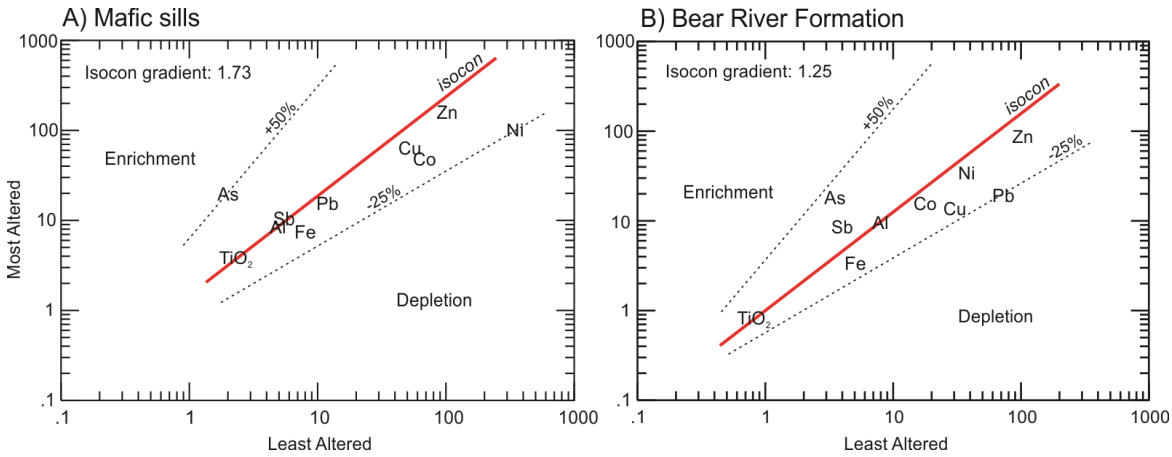

Figure 2-8 - Isocon plots based on whole rock geochemical data collected from most and least altered samples of **A)** mafic sill and **B)** metasedimentary rock at Lansdowne. Isocon gradient determined from concentrations of immobile elements TiO_2 and Al.

2.5 Discussion

2.5.1 Paragenesis and timing

Deposition of the major sedimentary units of the Meguma Terrane during the Cambrian to Silurian occurred prior to any sulfide mineralization at Lansdowne. The results of U-Pb dating of apatite in mafic sills indicate their emplacement at ~ 440 Ma (**Table A1-*3***), which is at least 75 Ma earlier than the earliest stage of mineralization, ruling them out as a possible heat source for mineralization. The age of the sills is similar to those identified by White and Barr (2003, 2004) throughout the metasedimentary rocks of the Halifax, Goldenville, and Rockville Notch Groups, north of the CPSZ (**Figure 2-B**). These mafic sills were

interpreted to have formed from extensional tectonics during and after deposition of the Meguma Supergroup and Rockville Notch Group sediments (White et al., 2003; White and Barr, 2004).

The age of Apy-1 defines the early-stage of mineralization at 365.4 ± 4.8 Ma (**Table 2-1**), which is contemporaneous with the waning stages of the Neoacadian orogeny (Benn et al., 1997). No other sulfides are associated with this early stage of arsenopyrite mineralization. The timing of Apy-1 is also contemporaneous with the youngest orogenic Au deposits of the eastern Meguma Terrane (Kontak et al., 1990a; Sangster and Smith, 2007). Traditional Meguma Au vein deposits formed episodically between 405 to 362 Ma (Kontak et al., 1990a; Morelli et al., 2005). Meguma Au veins are structurally associated with the hinges of anticlinal structures hosted in the meta-sandstone and shale dominated sequences of the Cambrian Goldenville Group (Kontak et al., 1990b; Sangster and Smith, 2007). The overlying Halifax Group, which hosts the Lansdowne occurrence, hosts few Meguma Au occurrences (see distribution map in Sangster and Smith, 2007). Lack of outcrop and drill core precludes detailed structural analysis of Lansdowne at this time.

Rhenium content in early stage arsenopyrite at Lansdowne is very low, averaging less than 0.5 ppb Re (**Table 2-1**). Similar low levels of Re (~1 – 9 ppb) are common for arsenopyrite in Meguma metasediments (Morelli et al., 2005) and are typical of arsenopyrite collected from orogenic gold environments (e.g., Morelli et al., 2010; Lawley et al., 2015; Zoheir et al., 2015). In contrast, late stage arsenopyrite and associated jamesonite of the Lansdowne occurrence show very high levels of Re (up to 700 ppb; **Table 2-2**), and low common Os. Considering the similar age and Re content of Apy-1, it is possible that Apy-1 formed from similar tectonic processes and conditions for mineralization as traditional Meguma Au deposits. However, there is a lack of Au present at Lansdowne (**Table A1-11**). This may be explained by high sulfide content of the occurrence, which generally indicates lower gold content for these deposits (Sangster and Smith, 2007).

Late-stage critical metal mineralization can be subdivided into three sub-stages:

1. Fe-Zn-Cu stage: Chalcopyrite and pyrrhotite disease in Fe-poor sphalerite (**Figure 2-3B**) indicate that these minerals might have formed as replacement of an earlier Fe-rich sphalerite (Barton and Bethke, 1987). Chlorite associated with this stage exhibits temperatures of formation at 350 – 390 ˚C (**Figure 2-3H, Table 2-3**).
2. Fe-As stage: The Re-Os age of late-stage arsenopyrite (Apy-2) defines the timing of critical metal mineralization at ~ 214 Ma (**Table 2-2**). This age is coeval with the deposition of the Fundy Group and failed rifting of the Bay of the Fundy during the initial stages of the opening of the Atlantic Ocean (Withjack et al., 1995; Wade et al., 1996).
3. Sb-Pb stage: Sb-Pb minerals are last to appear in the paragenesis and are coeval with second-generation quartz (Qtz-2; **Figure 2-3G**). The Sb-Pb sulfosalt mineralogy varies depending on precursor sulfides and reaction rims are common between Sb-Pb sulfosalts and sulfide minerals (**Figure 2-3D**). Where boulangerite with galena exsolution occurs interstitial to sphalerite, pyrite forms euhedral crystals in the boulangerite along the margins with sphalerite (**Figure 2-3E**). Where jamesonite forms interstitial to arsenopyrite, pyrite forms with galena reaction rims, separating the pyrite from jamesonite. Boulangerite often forms along grain boundaries between arsenopyrite and jamesonite (**Figure 2-3C**). Therefore, the fluids that produced the Sb-Pb stage were not in equilibrium with the sulfides produced during the previous mineralization stages. Fluid inclusion isochores indicate that this ore-stage formed at 165 °C and at low hydrostatic pressure conditions (15 bar; **Figure 2-6C**).

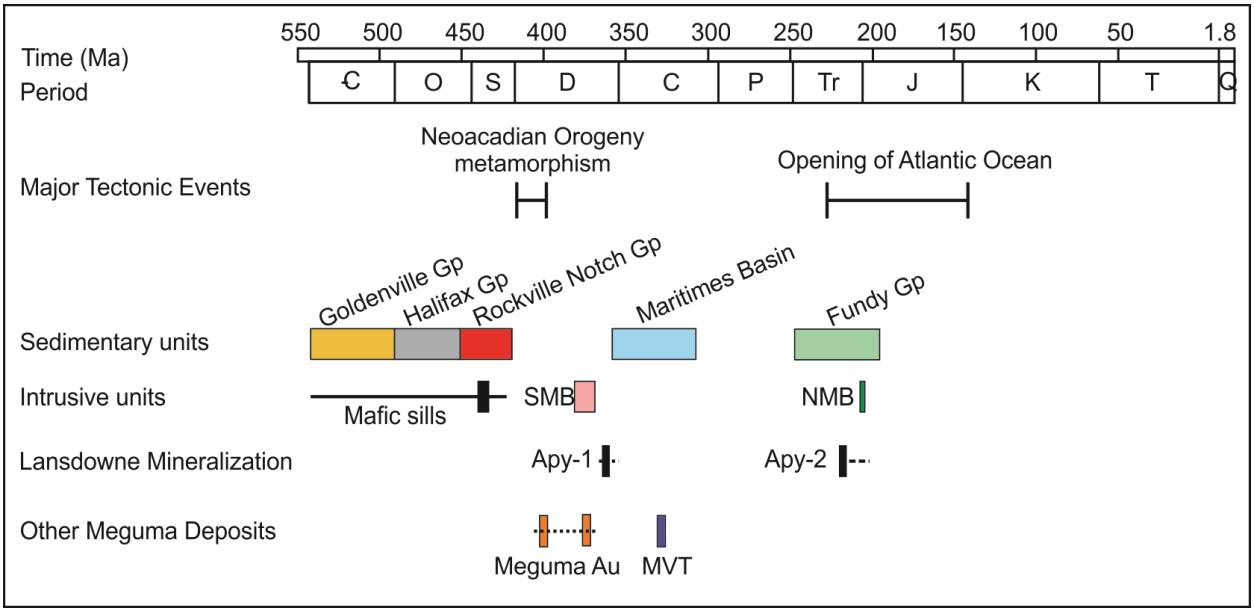

Figure 2-9 - Regional geological history of the Meguma Terrane (compiled from geochronological data in Kontak et al., 1990b; Hodych and Dunning, 1992; Sangster et al., 1998; Kontak, 2001; Reynolds et al., 2004; White and Barr, 2004; Morelli et al., 2005; White et al., 2018; Gibling et al., 2019). Solid line associated with mafic sills indicates suggested spread in timing of formation for other mafic sills in the region (White and Barr, 2004). Ages determined in this study are in black boxes. Dashed lines represent possible range in timing for mineralizing events.

2.5.2 Pressure-temperature conditions and sources (fluid, S, metal) for critical metal mineralization

Temperature constraints from chlorite associated with Fe-Zn-Cu mineralization in the late ore stage (**Table 2-3**), and from fluid inclusion isochores associated with Sb-Pb mineralization in the late ore stage (**Figure 2-6**), indicate cooling over the late stage from 360 °C to 165 °C.

Type-1 fluid inclusion assemblages are hosted in Qtz-2 and calcite, which brecciate Qtz-1 and form coevally with Sb-Pb mineralization of the late stage (**Figure 2-3G**). Decrepitate mound analysis confirms that type-1 inclusions are representative of late-stage mineralizing fluids, considering their significant enrichment in Sb, Pb, and As (**Figure 2-7**). Type-1 fluid inclusions are composed of two distinct but coeval fluids, as they are entrapped in the same assemblages (**Figure 2-5**) – an aqueous NaCl-CaCl-dominate brine

of high but variable salinity (6 – 27 wt.% NaCl equiv.) and methane (**Table 2-4**). These fluids are considered to have been mingling at the time of crystallization, as the inclusions exhibit a large variety of L:V phase ratios trapped within a single assemblage. These fluids likely did not experience unmixing or boiling, as they would have had to unmix along a solvus and have complimentary phase ratios. Most inclusions decrepitated before homogenization, suggesting two immiscible fluids. There is no evidence of post-entrapment modification, considering that similar inclusion types in a single FIA exhibit similar microthermometric characteristics.

High positive sulfur isotope values of late-stage sulfides (~ 15 - 25‰, **Table 2-5**) indicate a sulfate source for sulfur as ^{34}S fractionates preferentially into sulfate. A sulfate source would also be consistent with low-pressure surficial conditions of mineralization as suggested by fluid inclusions, as surface conditions would be oxidizing in the Triassic. When compared to the average isotope values of sulfur reservoirs, marine sulfates typically carry the highest positive values (Hammerli et al., 2021 and references therein). However, global average sulfur isotope values of marine sulfates at ~ 214 Ma were at an all time low (~ 13‰; Claypool et al., 1980). The calculated $\delta^{34}S_{SULFATE}$ required for the formation of late-stage Lansdowne sulfides ranges from ~ 30 – 60‰ (**Table 2-5**). Although there can be significant local variations in marine sulfates, we suggest it is unlikely that Late Triassic seawater sulfate provided the high values recorded at Lansdowne.

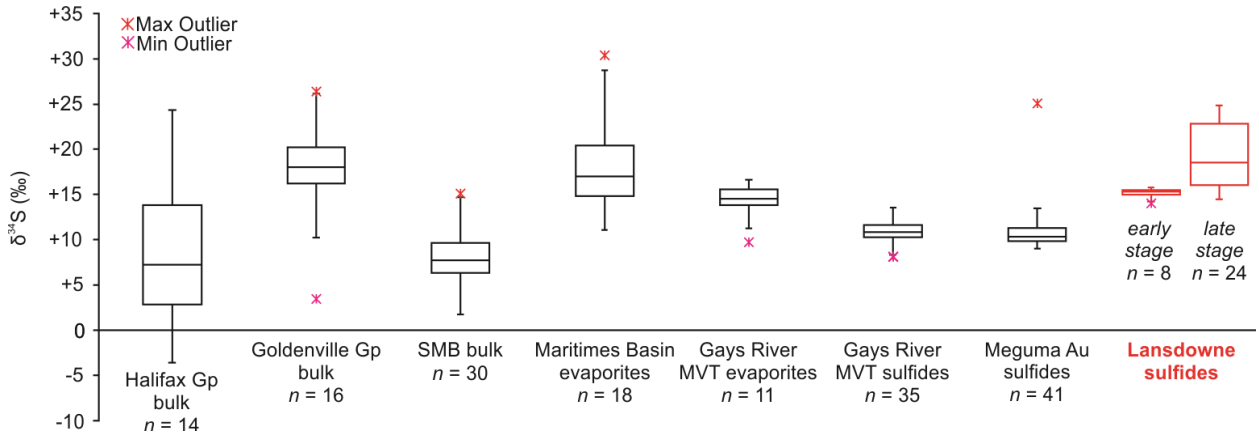

Figure 2-10 - Sulfur isotope values of major lithologies and select ore deposits within the Meguma Terrane (compiled from sulfur isotope data in Kontak and Smith, 1989; Poulson et al., 1991; Sangster et al., 1998). The Lansdowne occurrence sulfide values are highlighted in red. Early stage sulfides include arsenopyrite. Late stage sulfides include arsenopyrite, pyrrhotite, pyrite, and chalcopyrite.

Alternatively, the source of heavy sulfur could be the evaporite minerals of the Maritimes Basin. The Maritimes Basin evaporite minerals would have recorded seawater sulfate signatures from their time of deposition, which was higher in the Carboniferous (~ 15 - 20‰) than the Triassic (Claypool et al., 1980). Dissolution of evaporite minerals would also explain the high salinity of the fluid inclusions found at Lansdowne. However, due to the fractionation factor of $SO_4^{2-} \Leftrightarrow H_2S$ at the temperatures of the late stage and the corresponding high values of the sulfate-dominated liquid, the sulfur isotope values of evaporite minerals of the Gays River MVT deposit and the Maritimes Basin are generally too low, suggesting these evaporite minerals are not the likely source of sulfur (**Figure 2-10**; Akande and Zentilli, 1984).

The Late Triassic – Early Jurassic Blomidon Formation was deposited contemporaneously with the formation of critical metal mineralization at Lansdowne (Ackermann et al., 1995; Leleu and Hartley, 2010). The Blomidon Formation is characterized by shallow lacustrine deposits formed during arid to semi-arid conditions (Ackermann et al., 1995). Detailed bedrock mapping indicates rare evaporite beds in the Blomidon Formation (White et al., 2019). Considering the depositional environment, these evaporites likely had a nonmarine sulfate source, meaning they may record different sulfur isotope signatures than Triassic

seawater sulfate. The dissolution of evaporitic minerals from the Blomidon Formation may have contributed to the high sulfur isotope values recorded in Lansdowne sulfides. Unfortunately, a lack of sulfur isotope data on the evaporite beds of the Blomidon Formation make this comparison difficult, as sulfur isotope values for these minerals are unknown.

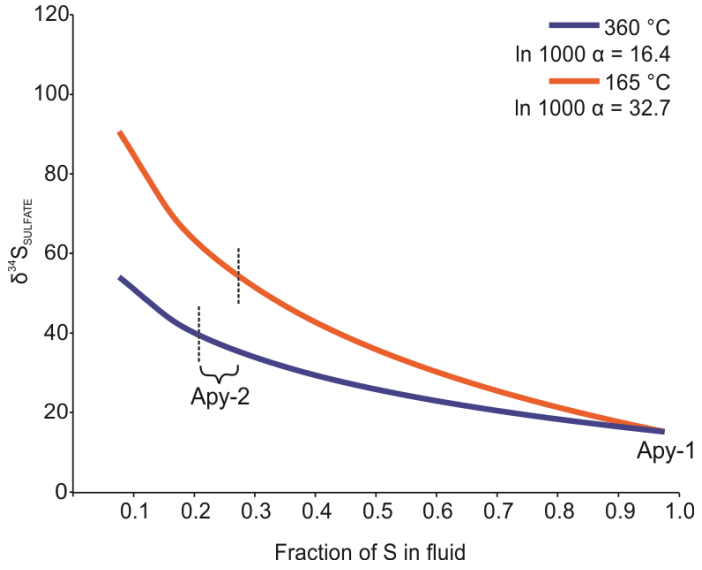

Figure 2-11 - Model curve indicating approximate fraction of S into sulfate at different temperatures, based on sulfur isotope values of early and late stage arsenopyrite (Apy-1 and Apy-2, respectively; **Table 2-5**)

A scenario that might explain the high sulfur isotope values is that late-stage mineralizing fluids sourced sulfur through oxidation and partial dissolution of pre-existing sulfides across the region, such as those in the Goldenville and Halifax groups, as represented by Apy-1 in this study, or in the Maritimes Basin Mississippi Valley-type (MVT) deposits (**Figure 2-10**). Assuming the fractionation factor ($\Delta^{34}S \approx \ln 1000\ \alpha$) between $SO_4^{2-} \Leftrightarrow H_2S$ at 360 °C (temperature of late stage Fe-Zn-Cu mineralization; **Table 2-5**) and 165 °C (temperature of late stage Sb-Pb mineralization, **Table 2-5**), the dissolved fraction of sulfides with a similar composition as Apy-1 (mean $\delta^{34}S$ value of 15.3‰) required by the late-stage mineralizing fluid to locally precipitate the sulfur values observed in Apy-2 can be roughly modelled (**Figure 2-11**). Considering there is no direct arsenopyrite to sulfate fractionation factor, this is a semi-quantitative result. However, it

does demonstrate that between ~ 20 - 30% Apy-1 could have been dissolved under oxidizing conditions to precipitate Apy-2 with a mean $\delta^{34}S$ value of ~ 24‰ (**Figure 2-11**). Therefore, we suggest that sulfur was sourced from Late Devonian Meguma sulfides or possibly the Maritimes Basin.

Considering the high Na and Ca in late-stage mineralizing fluids (**Figure 2-7**), it is likely that the oxidizing saline brine had a seawater source, possibly from the Fundy Rift Basin. We suggest this brine proceeded to mingle with methane, which likely created a reducing environment in which critical metal-bearing sulfides were able to form. Trace CO_2 trapped in some inclusions was likely produced from this redox reaction. It is unclear if methane was of abiogenic or biogenic origin, but a possible source for the methane is the methanogenesis of carbonate-rich rocks or organic-rich shale layers in the Meguma Terrane, or Maritimes or Fundy Basin sediments via heat from rift magmatism at the time (e.g., see mechanism proposed in Berndt et al., 2016; **Figure 2-12**).

The mafic sills associated with mineralization at the Lansdowne occurrence may have played an important role in mineralization (O'Reilly, 1995). Although the age of the sills (~ 440 Ma; **Table A1-3**.), rules them out as a source of heat for the mineralizing fluids, it is possible that these mafic sills may have contributed a metal component to mineralized veins. Isocon plots of most and least altered mafic sills indicate that the mafic sills, as well as the surrounding Bear River formation metasediments, were depleted in Zn, Cu, Fe, Pb, Ni, and Co from alteration of primary mafic minerals augite and plagioclase (**Figure 2-8**). These primary minerals were altered to chamosite, calcite, and minor ilmenite at low temperature (~ 360 °C). Considering the chamosite is coeval with the Fe-Zn-Cu sulfides (**Figure 2-3H**), sulfides would preferentially incorporate metals that may have been hosted in primary mafic minerals. Arsenic and antimony, however, must have had different sources, considering wall rock enrichment in these elements due to alteration (**Figure 2-8)**. A common source of As and Sb for sulfide mineralization are black shales (e.g., Wagner and Boyce, 2003; Hanley, 2007). Black shales are present in the Meguma Terrane as horizons in Halifax Group metasedimentary rocks and show enrichment in As and Sb (Fyffe and Pickerill, 1993). It

is possible that interaction of mineralizing fluids with these shale horizons may have provided As and Sb to the mineralizing fluid (**Figure 2-12**).

Combining the aforementioned data, including the paragenesis, timing, fluid chemistry, and temperature-pressure conditions of critical metal mineralization, a model can be proposed to explain the mechanisms for mineralization (**Figure 2-12**). Considering the timing and spatial association with the rifting of the Bay of Fundy, it is likely that rift tectonics and associated structures are responsible for the migration of fluids through the wallrock, allowing for the mingling of the saline brine and methane (**Figure 2-12**). Methane migration was likely triggered by mantle upwelling providing a considerable heat source. Possible interaction of the Fundy saline brine with the Fundy group or Maritimes basin sediments and evaporites caused the high salinity of the fluid, as well as local alteration hydration reactions (**Figure 2-12**).

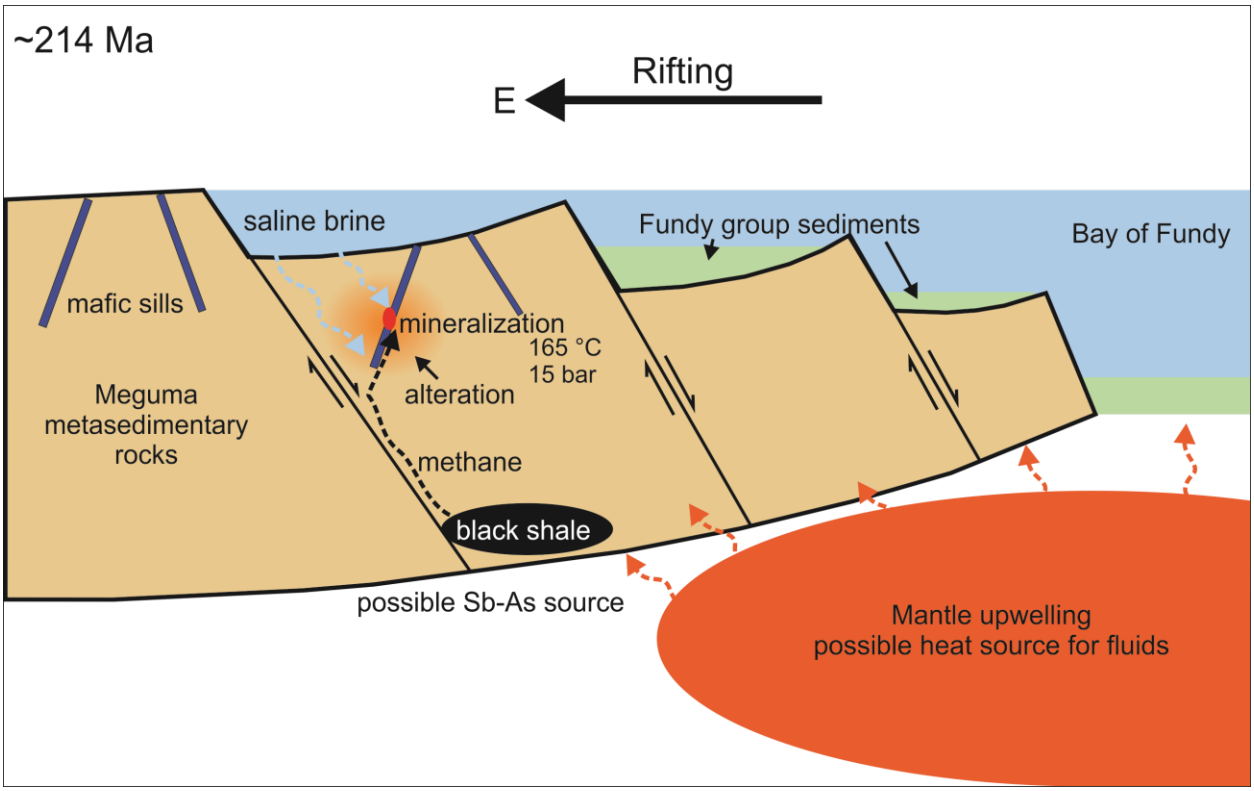

Figure 2-12 – Sketch illustrating the mechanisms and conditions for mineralization based on data collected from this project at the time of critical metal mineralization (~214 Ma)

2.5.3 Classification of the Lansdowne occurrence

Two mineralizing events, separated by approximately 150 Ma, formed the Lansdowne occurrence: i) the early stage arsenopyrite (~365 Ma; **Table 2-1**) and ii) the late stage (~214 Ma; **Table 2-2**), which was responsible for the endowment of critical metals. We suggest that the formation of Apy-1 is related to processes responsible for the formation of Meguma Au deposits because of similarities in age, host rocks, structure, and mineralogy, as outlined in section 2.5.1. Late stage critical metal mineralization is unrelated to processes that formed Meguma Au deposits. We classify the critical metal stage at Lansdowne as a rift-related hydrothermal polymetallic vein mineralization event, triggered by local extensional tectonics from the rifting of the Bay of Fundy and the subsequent migration and mingling of critical metal-bearing mineralizing fluids.

There are other deposits in the Meguma Terrane that share similarities with critical metal mineralization at Lansdowne; for instance, the West Gore Sb-Au deposit in East Hants, Nova Scotia. This deposit is hosted in the Halifax Group and is located along the contact between the Meguma Supergroup and the Maritimes Basin, proximal to the Fundy Group (**Figure 2-A**). Kontak et al. (1996) classified the West Gore Sb-Au deposit as a variant of Meguma Au deposits due to its timing (~ 370 Ma, determined from Ar/Ar ages of muscovite along margins of mineralized veins), structural characteristics (hinges of anticlinal folds), and native gold mineralization (Kontak et al., 1996). It is different than typical Meguma Au deposits due to the high abundance of base metal sulfides and Sb minerals (Kontak et al., 1996), which are unusual in Meguma Au deposits (Sangster and Smith, 2007). Base metal sulfides arsenopyrite, sphalerite, pyrite, and pyrrhotite form prior to Sb mineralization, which is latest in the paragenesis (Kontak et al., 1996), similar to the paragenesis observed in late stage mineralization at Lansdowne. Antimony minerals include stibnite, as well as sulfosalts boulangerite and berthierite ($FeSb_2S_4$), and native Sb and Sb-Au alloys (Kontak et al., 1996). Chlorite thermometry at West Gore is nearly identical to the temperatures identified for Zn-Cu mineralization of the late stage at Lansdowne, between 350 – 390 ˚C (Kontak et al., 1996). As well, Fe-rich sphalerite surrounded by Fe-poor sphalerite (D.J. Kontak, p. comm. 2021), suggests possible replacement

of early sulfide mineralization with a later stage of mineralization, such as the late Sb-rich mineralization at Lansdowne. Although the West Gore Sb-Au deposit was classified as a Meguma Au deposit variant and early muscovite provides a late Devonian age (Kontak et al., 1996), it is possible that this occurrence is overprinted by a Triassic-aged Sb-critical metal stage, as observed at Lansdowne.

Epithermal polymetallic Sb-Au critical metal deposits are widespread across the European Variscan belt (e.g., The Armorican Massif and Massif Central in France; Munoz et al., 1992; Marignac and Cuney, 1999; Pochon et al., 2018), the Mari Rosa deposit in western Spain (Ortega et al., 1996), the Rheinisches Schiefergebirge in NW Germany (Wagner and Cook, 2000), the Saxo-Thuringia zone in central Germany (Krolop et al., 2019), and the Cornubian Orefield in SW England (Clayton and Spiro, 2000). These deposits are primarily hosted in metasedimentary Variscan rocks from paleo-basins; however, a wide variety of host rocks exist (e.g., volcanics, black shales, gneisses, granites, and schists; see summary in Wagner and Cook, 2000). For example, in the Berga Antiform of eastern Germany, antimoniferous vein mineralization forms massive sulfide-sulfosalt-quartz-carbonate veins (Krolop et al., 2019). Assemblages of Zn-Fe-As sulfides (e.g., arsenopyrite, Fe-rich sphalerite, and pyrite) are replaced by Sb-Pb-Zn sulfides (e.g., stibnite, boulangerite and other Pb-Sb sulfosalts, Fe-poor sphalerite, and galena) and pressure-temperature conditions of Sb-Pb mineralization have been constrained to 220 ˚C and 700 – 750 bars apparent pressure (Krolop et al., 2019). In the Rheinisches Schiefergebirge, in northwest Germany, stibnite, Pb-Sb sulfosalts [e.g., zinkenite ($Pb_9Sb_{22}S_{42}$), plagionite ($Pb_5Sb_8S_{17}$), semseyite ($Pb_9Sb_8S_{21}$), and boulangerite], and Fe-poor sphalerite form the latest stages of polymetallic mineralization and show drastic cooling from 390 to 440 °C at 0.6 - 0.1 kbar pressure at the onset of mineralization, with minimum temperatures of 150 to 220 ˚C during the latest stages of stibnite and Sb-Pb sulfosalts mineralization (Wagner and Cook, 2000).

At the Bournac polymetallic vein deposit in southern France, ore paragenesis identifies three related and sequential stages: the Fe-As stage, Zn stage, and Pb-Sb stage (Munoz and Shepherd, 1987). Gangue minerals include carbonates and minor quartz. This deposit is host to boulangerite and jamesonite, as well as rarer Sb-Pb sulfosalt species such as plagionite and meneghinite ($Pb_{13}CuSb_7S_{24}$; Munoz and Shepherd,

1987). The Bournac deposit is part of the Massif Central of France, which is host to numerous Sb-Au polymetallic deposits, many of which share characteristics with Lansdowne, such as Sb mineralization forming at low temperatures (~ 150 ˚C) and low pressures (~ 0.1 kbar; Munoz et al., 1992). Stibnite and other antimony minerals in these deposits always crystallize in the final stages of the polymetallic paragenesis at the lowest temperatures (Munoz et al., 1992; Pochon et al., 2018).

For all the aforementioned deposits, mineralizing fluids are considered to have been triggered by Late Variscan extensional tectonics from the Late-Devonian to Permian following the Variscan orogeny (Munoz et al., 1992; Wagner and Cook, 2000; Pochon et al., 2018), Variscan orogenic uplift caused the formation of extensional shear zones that served as important pathways to bring mineralizing fluids to surface (Munoz et al., 1992). Precipitation mechanisms for mineralization are credited to a combination of drastic cooling and fluid unmixing (see summary in Wagner and Cook, 2000), which are considered requirements for antimony deposition. Many sources for antimony have been suggested, such as granitic intrusive events (Munoz et al., 1992; Ortega et al., 1996), influx of deep-sourced fluids from basement rocks (Wagner and Cook, 2000), and mafic intrusives (e.g., Pochon et al. 2016).

Although the similarities in mineralogy, fluids characteristics, and conditions of formation between the mineralization at Lansdowne and late-orogenic Sb (±Au) polymetallic mineralization in the European Variscan belt are numerous, deposits related to the actual breakup of the North Atlantic and which correspond temporally with the mineralization at Lansdowne show very different mineralogical characteristics. These European Mesozoic hydrothermal deposits host the majority of the world's fluorite and barite resources and host significant Ag, Co, Zn, Pb, Ni, and Cu (Bauer et al., 2019; Burisch et al., 2022). Mineralization is attributed to the mixing of a basement derived metal enriched brine with a sediment derived brine of a distinctly different composition, triggered by crustal thinning and mantle upwelling (Burisch et al., 2022). This sedimentary brine requires the interaction with evaporitic rocks to reach very high salinities (Walter et al., 2016; Burisch et al., 2022). There is a marked lack of antimony mineralization associated with these hydrothermal rift deposits, whose presence at Lansdowne sets the occurrence apart

from many other rift-related hydrothermal systems. Therefore, the standard mineralization style triggered by the Mesozoic rifting of the North Atlantic does not appear responsible for the mineralizing processes at Lansdowne.

The Lansdowne occurrence can, therefore, be considered to belong to a common and globally widespread mineralization style related to the onset of late-Variscan brittle extensional tectonics. Acknowledging the link between these deposits and mineralization in Nova Scotia offers the opportunity to understand more about the formation and origin of these newly classified vein types.

2.5.4 Exploration vectors

The region in which the Lansdowne occurrence was discovered is poorly explored, primarily due to the lack of outcrop and extensive overburden (MacIsaac et al., 2017; Nova Scotia Department of Natural Resources, 2021). This project hopes to highlight this region of Nova Scotia as an area with economic potential for critical minerals. There are multiple criteria which appear to define the Lansdowne occurrence and can be applied to future exploration efforts:

i) Considering the spatial and chronological ties this occurrence shares with the rifting of the Bay of Fundy, we suggest that these two events are intrinsically linked. More occurrences are likely located within reasonable proximity of the Fundy rift in nearby Meguma stratigraphy, such as the Rockville Notch Group or Halifax Group, west of the South Mountain batholith (**Figure 2-**).

ii) Mineralization is concentrated primarily within or adjacent to Silurian mafic sills which crosscut the host metasediments (**Figure 2-2**) and provide metals (**Figure 2-8**). It is possible that mineralization can only form with the metal input from the alteration of these mafic bodies. These sills are well mapped in the Lansdowne region and would be ideal starting points for exploration.

iii) At the outcrop scale, there is obvious pervasive carbonate and chlorite alteration of host rock (both the metasediments and altered mafic sills) around mineralized veins (**Figure 2-2**).

2.6 Conclusion

Early stage arsenopyrite mineralization formed at ~ 365 Ma, coeval with waning stages of Neoacadian orogeny and contemporaneous with youngest Meguma Au deposits. Late-stage mineralization – which deposited critical minerals– formed at ~ 214 Ma. This is contemporaneous with the rifting of the Bay of Fundy and deposition of Fundy Group sediments, a period of major extensional tectonics and mantle upwelling.

Chlorite thermometry records a cooling trend from 360 °C, related to Fe-Zn-Cu mineralization, to 165 °C, related to Sb-Pb mineralization. An oxidizing saline brine which likely interacted with evaporitic rocks and dissolved pre-existing sulfides (up to 30%) mingled with methane, creating a reducing environment where sulfides could re-precipitate. Most metals were likely sourced from alteration of wallrock, however sources of As and Sb are currently unknown.

Critical metal mineralization is reminiscent of late-orogenic epithermal Sb (±Au) polymetallic mineralization in the European Variscan belt. This is a common and widespread deposit style which formed from brittle extensional tectonics. The critical metal stage at Lansdowne likely formed from brittle extensional tectonics from the rifting of the Bay of Fundy and subsequent fluid migration, following structural conduits in the host rock from rift tectonics and the older mafic sills. Although critical metal mineralization appears unrelated to traditional Meguma Au deposits, the West Gore Sb-Au deposit and other Meguma polymetallic occurrences, such as Cape St Mary's (Sb-As-Co-Ni-Ag-Au-Bi-REE) and Nictaux Falls (As-Co-Ni-Au; **Figure 2-A**), suggest that there may be other deposits of this style in the Meguma terrane with similar characteristics. Exploration in the Meguma Terrane for this newly classified occurrence type should focus on the proximity to the Fundy Rift Basin, presence of mafic intrusions, and pervasive host rock alteration.

2.7 References

Ackermann, R. V., Schlische, R. W., and Olsen, P. E., 1995, Synsedimentary collapse of portions of the lower Blomidon Formation (late Triassic), Fundy rift basin, Nova Scotia: Canadian Journal of Earth Sciences, v. 32, p. 1965–1976.

Akande, S. O., and Zentilli, M., 1984, Geologic, fluid inclusion and stable isotope studies of the Gays River lead-zinc deposit, Nova Scotia, Canada.: Economic Geology, v. 79, p. 1187–1211.

Bakker, R. J., 2003, Package FLUIDS 1. Computer programs for analysis of fluid inclusion data and for modelling bulk fluid properties: Chemical Geology, v. 194, p. 3–23.

Barton, P. B., and Bethke, P. M., 1987, Chalcopyrite disease in sphalerite: pathology and epidemiology.: American Mineralogist, v. 72, p. 451–467.

Bauer, M. E., Burisch, M., Ostendorf, J., Krause, J., Frenzel, M., Seifert, T., and Gutzmer, J., 2019, Trace element geochemistry of sphalerite in contrasting hydrothermal fluid systems of the Freiberg district, Germany: insights from LA-ICP-MS analysis, near-infrared light microthermometry of sphalerite-hosted fluid inclusions, and sulfur isotope geochemi: Mineralium Deposita, v. 54, p. 237–262.

Benn, K., Pignotta, G. S., Evans, N. G., Horne, R. J., and Kontak, D. J., 1997, Syn-Acadian emplacement model for the South Mountain Batholith, Meguma Terrane, Nova Scotia: Magnetic fabric and structural analyses: GSA Bulletin, v. 109, p. 1279–1293.

Benn, K., Roest, W. R., Rochette, P., Evans, N. G., and Pignotta, G. S., 1999, Geophysical and structural signatures of syntectonic batholith construction: The South Mountain Batholith, Meguma Terrane, Nova Scotia: Geophysical Journal International, v. 136, p. 144–158.

Birck, J. L., Roy Barman, M., and Capmas, F., 1997, Re-Os isotopic measurements at the femtomole level in natural samples: Geostandards Newsletter, v. 21, p. 19–27.

Bodnar, R. J., 1993, Revised equation and table for determining the freezing point depression of H2O-Nacl solutions: Geochimica et Cosmochimica Acta, v. 57, p. 683–684.

Burisch, M., Markl, G., and Gutzmer, J., 2022, Breakup with benefits - hydrothermal mineral systems related to the disintegration of a supercontinent: Earth and Planetary Science Letters, v. 580, 117373.

Campbell, B., and Raeside, R., 1999, The contact metamorphic aureole of the South Mountain Batholith in the Bear River-Clements area, Nova Scotia - Abstract: Atlantic Geology, v. 35.

Cao, H. W., Zou, H., Bagas, L., Zhang, L. K., Zhang, Z., and Li, Z. Q., 2019, The Laqiong Sb-Au deposit: Implications for polymetallic mineral systems in the Tethys-Himalayan zone of southern Tibet, China: Gondwana Research, v. 72, p. 83–96.

Cathelineau, M., 1988, Cation site occupancy in chlorites and illites as a function of temperature: Clays and Clay Minerals, v. 23, p. 471–485.

Claypool, G. E., Holser, W. T., Kaplan, I. R., Sakai, H., and Zak, I., 1980, The age curves of sulfur and oxygen isotopes in marine sulfate and their mutual interpretation: Chemical Geology, v. 28, p. 199–260.

Clayton, R. E., and Spiro, B., 2000, Sulphur, carbon and oxygen isotope studies of early Variscan mineralisation and Pb-Sb vein deposits in the Cornubian orefield: Implications for the scale of fluid movements during Variscan deformation: Mineralium Deposita, v. 35, p. 315–331.

Cohen, A., and Waters, F. G., 1996, Separation of osmium from geological materials by solvent extraction for analysis by thermal ionisation mass spectrometry: Analytica Chimica Acta, v. 332, p. 269–275.

Conwest Exploration, 1951, Lansdowne Antimony-Lead Prospect, Walsh Brook, Digby Co., Nova Scotia.:

Crowe, D. E., and Vaughan, R. G., 1996, Characterization and use of isotopically homogeneous standards for in situ laser microprobe analysis of 34S/32S ratios: American Mineralogist, v. 81, p. 187–193.

Culshaw, N., and Dickson, C., 2015, Cape st. Marys shear zone and the halifax group – rockville notch group disconformity, southwestern nova scotia: Structural development and tectonic significance: Canadian Journal of Earth Sciences, v. 52, p. 921–937.

Culshaw, N., and Reynolds, P. H., 1997, 40Ar/39Ar age of shear zones in the southwest Meguma Zone between Yarmouth and Meteghan, Nova Scotia: Canadian Journal of Earth Sciences, v. 34, p. 848–853.

Driesner, T., and Heinrich, C. A., 2007, The system H2O-NaCl. Part I: Correlation formulae for phase relations in temperature-pressure-composition space from 0 to 1000 °C, 0 to 5000 bar, and 0 to 1 XNaCl: Geochimica et Cosmochimica Acta, v. 71, p. 4880–4901.

Eldridge, D. L., Guo, W., and Farquhar, J., 2016, Theoretical estimates of equilibrium sulfur isotope effects in aqueous sulfur systems: Highlighting the role of isomers in the sulfite and sulfoxylate systems: Geochimica et Cosmochimica Acta, v. 195, p. 171–200.

Fyffe, L. R., and Pickerill, R. K., 1993, Geochemistry of Upper Cambrian-Lower Ordovician black shale along a northeastern Appalachian transect: Geological Society of America Bulletin, v. 105, p. 897–910.

Gibling, M. R., Culshaw, N., Pascucci, V., Waldron, J. W. F., and Rygel, M. C., 2019, The maritimes basin of atlantic canada: Basin creation and destruction during the paleozoic assembly of pangea: 267–314 p.

Grant, J. A., 1986, The isocon diagram - A simple solution to Gresens' equation for metasomatic alteration: Economic Geology, v. 81, p. 1976–1982.

Gresens, R. L., 1967, Composition-volume relationships of metasomatism: Chemical Geology, v. 2, p. 47–65.

Hammerli, J., Greber, N. D., Martin, L., Bouvier, A. S., Kemp, A. I. S., Fiorentini, M. L., Spangenberg, J. E., Ueno, Y., and Schaltegger, U., 2021, Tracing sulfur sources in the crust via SIMS measurements of sulfur isotopes in apatite: Chemical Geology, v. 579, p. 120242.

Hanley, J. J., 2007, The role of arsenic-rich melts and mineral phases in the development of high-grade Pt-Pd mineralization within komatiite-associated magmatic Ni-Cu sulfide horizons at Dundonald Beach South, Abitibi subprovince, Ontario, Canada: Economic Geology, v. 102, p. 305–317.

Hnatyshin, D., Creaser, R. A., Meffre, S., Stern, R. A., Wilkinson, J. J., and Turner, E. C., 2020a, Understanding the microscale spatial distribution and mineralogical residency of Re in pyrite: Examples from carbonate-hosted Zn-Pb ores and implications for pyrite Re-Os geochronology: Chemical Geology, v. 533, p. 119427.

Hnatyshin, D., Creaser, R. A., Meffre, S., Stern, R. A., Wilkinson, J. J., and Turner, E. C., 2020b, Understanding the microscale spatial distribution and mineralogical residency of Re in pyrite: Examples from carbonate-hosted Zn-Pb ores and implications for pyrite Re-Os geochronology: Chemical Geology, v. 533, p. 119427.

Hodych, J. P., and Dunning, G. R., 1992, Did the Manicouagan impact trigger end-of-Triassic mass extinction? Geology, v. 20, p. 51–54.

Horne, R. J., and Culshaw, N., 2001, Flexural-slip folding in the Meguma Group, Nova Scotia, Canada: Journal of Structural Geology, v. 23, p. 1631–1652.

Jowett, E. C., 1991, Fitting Iron and Magnesium into the Hydrothermal Chlorite Geothermometer: SSRN Electronic Journal.

Keppie, J. D., 2000, Geological Map of the Province of Nova Scotia; Nova Scotia Department of Natural Resources, Minerals and Energy Branch, Map ME 2000-1, scale 1:500 000.:

Keppie, J. D., and Dallmeyer, R. D., 1987, Dating transcurrent terrane accretion: An example from the Meguma and Avalon composite terranes in the Northern Appalachians.: Tectonics, v. 6, p. 831–847.

Keppie, J. D., Dallmeyer, R. D., Krogh, T. E., and Aftalion, M., 1993, Dating mineralization using several isotopic methods: an example from the South Mountain Batholith, Nova Scotia, Canada: Chemical Geology, v. 103, p. 251–270.

Kerr, M. J., Hanley, J. J., Kontak, D. J., Morrison, G. G., Petrus, J., Fayek, M., and Zajacz, Z., 2018, Evidence of upgrading of gold tenor in an orogenic quartz-carbonate vein system by late magmatic-hydrothermal fluids at the Madrid Deposit, Hope Bay Greenstone Belt, Nunavut, Canada: Geochimica et Cosmochimica Acta, v. 241, p. 180–218.

Kontak, D. J., 2001, Internal Stratigraphy of the Jurassic North Mountain Basalt , Southern Nova Scotia: NSDNR Report of Activities, p. 69–79.

Kontak, D. J., 2008, On the edge of CAMP: Geology and volcanology of the Jurassic North Mountain Basalt, Nova Scotia: Lithos, v. 101, p. 74–101.

Kontak, D. J., and Reynolds, P. H., 1994, 40Ar/39Ar dating of metamorphic and igneous rocks of the Liscomb Complex. Meguma Terrane, southern Nova Scotia, Canada: Canadian Journal of Earth Sciences, v. 31, p. 1643–1653.

Kontak, D. J., and Smith, P. K., 1989, Sulphur isotopic composition of sulphides from the Beaver Dam and other Meguma-Group-hosted gold deposits, Nova Scotia: implications for genetic models: Canadian Journal of Earth Sciences, v. 26, p. 1617–1629.

Kontak, D. J., Smith, P. K., Reynolds, P., and Taylor, K., 1990a, Geological and 40Ar/39Ar geochronological constraints on the timing of quartz vein formation in Meguma Group lode-gold deposits, Nova Scotia: Atlantic Geology, v. 26, p. 201–227.

Kontak, D. J., Smith, P. K., Kerrich, R., and Williams, P. F., 1990b, Integrated model for Meguma Group lode gold deposits, Nova Scotia, Canada: Geology, v. 18, p. 238–242.

Kontak, D. J., Horne, R. J., and Smith, P. K., 1996, Hydrothermal Characterization of the West Gore Sb-Au Deposit, Meguma Terrane, Nova Scotia, Canada: Economic Geology, v. 91, p. 1239–1262.

Kranidiotis, P., and MacLean, W. H., 1987, Systematics of chlorite alteration at the Phelps Dodge massive sulfide deposit, Matagami, Quebec: Economic Geology, v. 82, p. 1898–1911.

Krolop, P., Burisch, M., Richter, L., Fritzke, B., and Seifert, T., 2019, Antimoniferous vein-type mineralization of the Berga Antiform, Eastern-Thuringia, Germany: A fluid inclusion study: Chemical Geology, v. 508, p. 47–61.

Lawley, C. J. M., Creaser, R. A., Jackson, S. E., Yang, Z., Davis, B. J., Pehrsson, S. J., Dubé, B., Mercier-Langevin, P., and Vaillancourt, D., 2015, Unraveling the Western Churchill Province Paleoproterozoic Gold Metallotect: Constraints from Re-Os Arsenopyrite and U-Pb Xenotime Geochronology and LA-ICP-MS Arsenopyrite Trace Element Chemistry at the BIF-Hosted Meliadine Gold District, Nunavut, Canada: Economic Geology, v. 110, p. 1425–1454.

Leleu, S., and Hartley, A. J., 2010, Controls on the stratigraphic development of the Triassic Fundy Basin, Nova Scotia: Implications for the tectonostratigraphic evolution of Triassic Atlantic rift basins: Journal of the Geological Society, v. 167, p. 437–454.

MacIsaac, J., O'Reilly, G. A., and Chaput, M., 2017, Exploration of the Lansdowne Sb-Pb-Zn-Cu-Ag-Au Prospect, Digby County, Nova Scotia by Blackfly Exploration & Mining under the Nova Scotia Mineral Incentive Program.:

Marignac, C., and Cuney, M., 1999, Ore deposits of the French Massif Central: Insight into the metallogenesis of the Variscan collision belt: Mineralium Deposita, v. 34, p. 472–504.

Markey, R., Stein, H. J., Hannah, J. L., Zimmerman, A., Selby, D., and Creaser, R. A., 2007, Standardizing Re-Os geochronology: A new molybdenite Reference Material (Henderson, USA) and the stoichiometry of Os salts: Chemical Geology, v. 244, p. 74–87.

Martínez Catalán, J. R., Arenas, R., Abati, J., Martínez, S. S., García, F. D., Suárez, J. F., Cuadra, P. G., Castiñeiras, P., Barreiro, J. G., Montes, A. D., Clavijo, E. G., Pascual, F. J. R., Andonaegui, P., Jeffries, T. E., et al., 2009, A rootless suture and the loss of the roots of a mountain chain: The Variscan belt of NW Iberia: Comptes Rendus - Geoscience, v. 341, p. 114–126.

McDivitt, J. A., Kontak, D. J., Lafrance, B., Petrus, J. A., and Fayek, M., 2021, A trace metal, stable isotope (H, O, S), and geochronological (U-Pb titanite) characterization of hybridized gold orebodies in the

Missanabie-Renabie district, Wawa subprovince (Canada): Mineralium Deposita, v. 56, p. 561–582.

McGregor, M., McFarlane, C. R. M., and Spray, J. G., 2018, In situ LA-ICP-MS apatite and zircon U–Pb geochronology of the Nicholson Lake impact structure, Canada: Shock and related thermal effects: Earth and Planetary Science Letters, v. 504, p. 185–197.

Morelli, R. M., Creaser, R. A., Selby, D., Kontak, D. J., and Horne, R. J., 2005, Rhenium-osmium geochronology of arsenopyrite in Meguma group gold deposits, Meguma terrane, Nova Scotia, Canada: Evidence for multiple gold-mineralizing events: Economic Geology, v. 100, p. 1229–1242.

Morelli, R. M., Bell, C. C., Creaser, R. A., and Simonetti, A., 2010, Constraints on the genesis of gold mineralization at the Homestake Gold Deposit, Black Hills, South Dakota from rhenium-osmium sulfide geochronology: Mineralium Deposita, v. 45, p. 461–480.

Munoz, M., and Shepherd, T. J., 1987, Fluid inclusion study of the bournac polymetallic (Sb-As-Pb-Zn-Fe-Cu...) vein deposit (montagne noire, France): Mineralium Deposita, v. 22, p. 11–17.

Munoz, M., Courjault-Radé, P., and Tollon, F., 1992, The massive stibnite veins of the French Palaeozoic basement: a metallogenic marker of Late Variscan brittle extension: Terra Nova, v. 4, p. 171–177.

Murphy, J. B., and Keppie, J. D., 2005, The acadian orogeny in the northern appalachians: International Geology Review, v. 47, p. 663–687.

Murphy, J. B., Waldron, J. W. F., Kontak, D. J., Pe-Piper, G., and Piper, D. J. W., 2011, Minas Fault Zone: Late Paleozoic history of an intra-continental orogenic transform fault in the Canadian Appalachians: Journal of Structural Geology, v. 33, p. 312–328.

Natural Resources Canada, 2020, The Canadian minerals and metals plan: Update to action plan:, accessed at https://www.nrcan.gc.ca/sites/www.nrcan.gc.ca/files/CMMP/CMMP_The_Plan-EN.pdf.

Natural Resources Canada, 2021, Canada's Critical Minerals List:, accessed at https://www.canada.ca/en/natural-resources-canada/news/2021/03/canada-announces-critical-minerals-list.html.

Nova Scotia Department of Natural Resources, 2021, Mineral Production in 2019 and Exploration in 2020 - Report ME 2021-001.:

O'Reilly, G. A., 1992, NSDNR Field Notes - 1992:

O'Reilly, G. A., 1995, Little Known Ni-Co-Bi-Sb-Ag-Au Association in the Annapolis Valley:, accessed at Minerals Update. Nova Scotia Department of Natural Resources

Ortega, L., Oyarzun, R., and Gallego, M., 1996, The Mari Rosa late Hercynian Sb-Au deposit, western Spain: Geology and geochemistry of the mineralizing processes: Mineralium Deposita, v. 31, p. 172–187.

Palinkaš, S. S., Hofstra, A. H., Percival, T. J., Šoštarkć, S. B., Palinkaš, L., Bermanec, V., Pecskay, Z., and Boev, B., 2019, Comparison of the Allchar Au-As-Sb-Tl Deposit, Republic of Macedonia, with Carlin-Type Gold Deposits: Diversity in Carlin-Style Gold Deposits, p. 335–363.

Pochon, A., Gapais, D., Gloaguen, E., Gumiaux, C., Branquet, Y., Cagnard, F., and Martelet, G., 2016, Antimony deposits in the Variscan Armorican belt, a link with mafic intrusives? Terra Nova, v. 28, p. 138–145.

Pochon, A., Gloaguen, E., Branquet, Y., Poujol, M., Ruffet, G., Boiron, M. C., Boulvais, P., Gumiaux, C., Cagnard, F., Gouazou, F., and Gapais, D., 2018, Variscan Sb-Au mineralization in Central Brittany (France): A new metallogenic model derived from the Le Semnon district: Ore Geology Reviews, v. 97, p. 109–142.

Poulson, S. R., Kubilius, W. P., and Ohmoto, H., 1991, Geochemical behavior of sulfur in granitoids during intrusion of the South Mountain Batholith, Nova Scotia, Canada: Geochimica et Cosmochimica Acta, v. 55, p. 3809–3830.

Raeside, R. P., and Hill, J. D., 1988, Metamorphism of Meguma Group metasedimentary rocks, Whitehead Harbour Area, Guysborough County, Nova Scotia: Maritime Sediments and Atlantic Geology, v. 24, p. 1–9.

Reynolds, P. H., Clarke, D. B., and Bogutyn, P. A., 2004, 40Ar/39Ar laser dating of zoned white micas from the Lake Lewis leucogranite, South Mountain Batholith, Nova Scotia, Canada: Canadian Mineralogist, v. 42, p. 1129–1137.

Rottier, B., Kouzmanov, K., Wälle, M., Bendezú, R., and Fontboté, L., 2016, Sulfide replacement processes revealed by textural and LA-ICP-MS trace element analyses: Example from the early mineralization stages at Cerro de Pasco, Peru: Economic Geology, v. 111, p. 1347–1367.

Sangster, A. L., and Smith, P. K., 2007, Metallogenic Summary of the Meguma Gold Deposits, Nova Scotia, in Goodfellow, W. D. ed., Mineral Deposits of Canada: A Synthesis of Major Deposit-Types, District Metallogeny, the Evolution of Geological Provinces, and Exploration Methods: Geological Association of Canada, Mineralogical Association of Canada, Special Publication, p. 723–732.

Sangster, D. F., Savard, M. M., and Kontak, D. J., 1998, A genetic model for mineralization of Lower Windsor (Visean) carbonate rocks of Nova Scotia, Canada: Economic Geology, v. 93, p. 932–952.

Scott, S. D., 1983, Chemical behaviour of sphalerite and arsenopyrite in hydrothermal and metamorphic environments: Mineralogical Magazine, v. 47, p. 427–435.

Seifert, T., and Sandmann, D., 2006, Mineralogy and geochemistry of indium-bearing polymetallic vein-type deposits: Implications for host minerals from the Freiberg district Eastern Erzgebirge, Germany: Ore Geology Reviews, v. 28, p. 1–31.

Shellnutt, J. G., Owen, J. V., Yeh, M. W., Dostal, J., and Nguyen, D. T., 2019, Long-lived association between Avalonia and the Meguma terrane deduced from zircon geochronology of metasedimentary granulites: Scientific Reports, v. 9, p. 1–11.

Shirey, S. B., and Walker, R. J., 1995, Carius Tube Digestion for Low-Blank Rhenium-Osmium Analysis: Analytical Chemistry, v. 67, p. 2136–2141.

Simmons, S. F., White, N. C., and John, D. A., 2019, Geological Characteristics of Epithermal Precious and Base Metal Deposits: One Hundredth Anniversary Volume, p. 485–522.

Smith, D. G. W., 1969, Pyrometamorphism of phyllites by a dolerite plug: Journal of Petrology, v. 10, p. 20–55.

Smoliar, M. I., Walker, R. J., and Morgan, J. W., 1996, Re-Os ages of group IIA, IIIA, IVA, and IVB iron meteorites: Science, v. 271, p. 1099–1102.

Thomas Martel, A., and Gibling, M. R., 1996, Stratigraphy and tectonic history of the Upper Devonian to Lower Carboniferous Horton Bluff Formation, Nova Scotia: Atlantic Geology, v. 32, p. 13–38.

Thomson, S. N., Gehrels, G. E., Ruiz, J., and Buchwaldt, R., 2012, Routine low-damage apatite U-Pb dating using laser ablation-multicollector- ICPMS: Geochemistry, Geophysics, Geosystems, v. 13, p. 1–23.

Vermeesch, P., 2018, IsoplotR: A free and open toolbox for geochronology: Geoscience Frontiers, v. 9, p. 1479–1493.

Wade, J. A., Brown, D. E., Traverse, A., and Fensome, R. A., 1996, The Triassic-Jurassic Fundy Basin, eastern Canada: Regional setting, stratigraphy and hydrocarbon potential: Atlantic Geology, v. 32, p. 189–231.

Wagner, T., and Boyce, A. J., 2003, Sulphur isotope geochemistry of black shale-hosted antimony mineralization, Arnsberg, northern Rhenish Massif, Germany: Implications for late-stage fluid flow during the Variscan orogeny: Journal of the Geological Society, v. 160, p. 299–308.

Wagner, T., and Cook, N. J., 2000, Late-Variscan antimony mineralisation in the Rheinisches Schiefergebirge, NW Germany: Evidence for stibnite precipitation by drastic cooling of high-temperature fluid systems: Mineralium Deposita, v. 35, p. 206–222.

Waldron, J. W. F., Barr, S. M., Park, A. F., White, C. E., and Hibbard, J., 2015, Late Paleozoic strik-slip faults in Maritime Canada and their role in the reconfiguration of the northern Appalachian orogen: Tectonics, v. 34, p. 1661–1684.

Walter, B. F., Burisch, M., and Markl, G., 2016, Long-term chemical evolution and modification of continental basement brines – a field study from the Schwarzwald, SW Germany: Geofluids, v. 16, p. 604–623.

White, C. E., 2010, Stratigraphy of the Lower Paleozoic Goldenville and Halifax groups in the western part of southern Nova Scotia: Atlantic Geology, v. 46, p. 136–154.

White, C. E., and Barr, S. M., 2004, Age and Petrochemistry of Mafic Sills in Rocks of the Northwestern Margin of the Meguma Terrane , Bear River - Yarmouth Area of Southwestern Nova Scotia: Mineral Resources Branch, Report of Activities 2003; Nova Scotia Department of Natural Resources, p. 97–117.

White, C. E., and Barr, S. M., 2010, Lithochemistry of the Lower Paleozoic Goldenville and Halifax groups, southwestern Nova Scotia, Canada: Implications for stratigraphy, provenance, and tectonic setting of the Meguma terrane: 347–366 p.

White, C. E., and Barr, S. M., 2012, Meguma Terrane Revisited; Stratigraphy, Metamorphism, Paleontology, and Provenance, in GAC-MAC 2012 Post Meeting Field Trip: St-John's, NF.

White, C. E., and Barr, S. M., 2017, Stratigraphy and depositional setting of the Silurian–Devonian Rockville Notch group, Meguma Terrane, Nova Scotia, Canada: Atlantic Geology, v. 53, p. 337–365.

White, C. E., Barr, S. M., and Gould, R. C., 2003, Gabbroic Intrusions in the Meteghan - Yarmouth the Meguma Terrane , Southern Nova Scotia Field Relations and: Mineral Resources Branch, Report of Activities 2003; Nova Scotia Department of Natural Resources, p. 147–162.

White, C. E., Barr, S. M., and Linnemann, U., 2018, U-Pb (zircon) ages and provenance of the White Rock Formation of the Rockville Notch Group, Meguma terrane, Nova Scotia, Canada: evidence for the "Sardian gap" and West African origin: Canadian Journal of Earth Sciences, v. 55, p. 589–603.

White, C. E., Marshall, L., and Allen, E., 2019, Nova Scotia Department of Energy and Mines Bedrock Geology Map of the Central Annapolis Valley Area , Nova Scotia.

Williams, H., Dehler, S. A., Grant, A. C., and Oakey, G. N., 1999, Tectonics of Atlantic Canada: Geoscience Canada, v. 26, p. 51–70.

Wise, S. A., and Watters, R. L., 2011, Reference Material 8599 Henderson Molybdenite.:

Withjack, M. O., Olsen, P. E., and Schlische, R. W., 1995, Tectonic evolution of the Fundy rift basin, Canada: Evidence of extension and shortening during passive margin development: Tectonics, v. 14, p. 390–405.

Zoheir, B. A., Creaser, R. A., and Lehmann, B., 2015, Re-Os geochronology of gold mineralization in the Fawakhir area, Eastern Desert, Egypt: International Geology Review, v. 57, p. 1418–1432.

Chapter 3: Antimony and REE mineralization at the Cape St. Mary's polymetallic (Sb-REE-As-Co-Ni-Au-Ag-Bi-Pb) occurrences, Meguma Terrane, southwest Nova Scotia

Naomi Welt*[1], Erin Adlakha[1], Geoffrey Baldwin[3], Mostafa Fayek[4], Ryan Sharpe[4]

1. Saint Mary's University, Department of Geology, Halifax, Nova Scotia B3H 3C3
3. Nova Scotia Department of Natural Resources and Renewables, Halifax, Nova Scotia B3J 2T9
4. University of Manitoba, Department of Geological Sciences, Winnipeg, Manitoba R3T 2N2

Submitted to Atlantic Geoscience Society Special Publication "Developments in mineral resources research in the northern Appalachians" under the guidelines of the Journal of Atlantic Geoscience

Abstract

Multiple critical metal bearing occurrences occur in the Cape St. Mary's area of southwestern Nova Scotia, hosted in the metasedimentary rocks of the Halifax and Rockville Notch Groups of the Meguma Terrane and are associated with multiple unnamed mafic sills. These occurrences include the Deerfoot Trail Sb (± As-Co-Ni-Cu-Bi-Ag-REE) occurrence (formally known as the Stibnite occurrence), the Galena and Cormorant Rock Pb occurrences, the Ankerite Breccia shear zone REE occurrence, and the Mavillette Beach Sb-Pb-Au occurrence. This project combines a multi-analytical approach involving detailed petrography, field observations, semi-quantitative mineral chemistry, sulfur isotopes of sulfides, and whole rock geochemical analysis of mineralized samples. The REE mineralization (florencite, monazite, and xenotime) of the Ankerite Breccia occurrence and arsenopyrite (containing up to 8 wt.% Co and 20 wt.% Ni) related florencite mineralization at the Deerfoot Trail Sb occurrence are related to Alleghenian deformation in the Mid-Carboniferous from the reactivation of the Cape St. Mary's shear zone at 320 Ma. The Deerfoot Trail Sb occurrence (5.62 wt.% Sb, 3.32 wt.% Cu, 2620 ppm Bi) shows evidence of an injection of a Sb-Cu (±Pb-Bi) bearing mineralizing fluid along a small fault in the host metasedimentary rock, replacing siderite. Chalcostibite reacts with Fe to form tetrahedrite and Bi-rich stibnite, and a further reaction forms chalcopyrite with Sb-Bi alloys. These transitions are representative of an increase in sulfur fugacity and decrease in temperature. At Mavillette Beach, Sb-Au mineralization (>1 ppm Au) is

reminiscent of the Late-Triassic extension-related critical metal mineralization of the Lansdowne occurrence, discovered only ~ 80 km north of Cape St. Mary's and hosted in the same metasedimentary host rocks.

3.1 Introduction

Southwestern Nova Scotia is host to numerous polymetallic vein occurrences (e.g., the Cape St. Mary's occurrences, Lansdowne occurrence, Nictaux Falls Dam occurrence, West-Gore Sb-Au deposit; **Figure 3-1A**) which host unique critical metal assemblages (e.g., Sb-Cu-Bi-Co-Ni-REE) and are suspected to share a genetic relationship (O'Reilly, 1995). The Lansdowne occurrence, Nictaux Falls Dam occurrence, and Cape St. Mary's occurrences are all hosted in or are adjacent to the sparsely distributed Rockville Notch Group and/or a series of pre- and syn-depositional mafic sills, which only form to the west of the South Mountain Batholith. Although the Meguma Terrane is endowed in many mineral resources, such as orogenic gold deposits (e.g. Smith and Kontak, 1996; Sangster and Smith, 2007), MVT related Pb-Zn deposits (e.g. Akande and Zentilli, 1984; Carew et al., 2020), and granitoid related polymetallic Sn deposits (e.g. Kontak et al., 2009; Gowans et al., 2018;), there has not been a concerted effort to understand the mineralization style of unique critical metal-bearing vein hosted occurrences in southwestern Meguma Terrane.

The Cape St. Mary's area has been selected for this study due to a high concentration of polymetallic occurrences in a small area (five documented over < 2 km^2) and the complex important metal assemblages they host (Sb-As-Pb-Co-Ni-Cu-Bi-Ag-Au-REE). Host rocks include the Ordovician-aged Bear River Formation and the unconformably overlying Silurian-aged White Rock Formation (**Figure 3-1B**). The contact between these units is the Cape St. Mary's shear zone, part of a series of NE-SW shear zones spanning the southwestern coast of Nova Scotia between Yarmouth and Digby (Culshaw and Reynolds, 1997; Culshaw and Dickson, 2015) that also include the Chebogue Point Shear Zone (**Figure 3-1A**).

Few documented occurrences of antimony and REE mineralization exist in Nova Scotia. Rare earth element mineralization in Nova Scotia is usually associated with granitoid intrusions related to late hydrothermal circulation of REE-bearing fluids from Alleghenian reactivation of the Cobequid Chedabucto Fault Zone (CCFZ; **Figure 3-1A**) in the Cobequid Highlands of Nova Scotia, north of the CCFZ (Kontak et al., 2008; Papoutsa and Pe-Piper, 2013; Papoutsa and Pe-Piper, 2014; Ersay, 2020). Antimony mineralization is only documented in two other known occurrences within the Meguma Terrane; the West Gore Sb-Au deposit in East Hants County, and the Lansdowne prospect in Digby County. Both of these occurrences host Sb and other critical metals and are generally along strike with Cape St. Mary's along the western flank of the Meguma Terrane (**Figure 3-1A**). The West Gore Sb-Au deposit and the Lansdowne occurrence are hosted in the metasedimentary host rocks of the Halifax Group and have similar parageneses (Welt et al., In review); however, the West Gore Sb-Au deposit is considered a variation of typical Meguma gold deposits, unlike Lansdowne which has little Au content (Welt et al., In review; Kontak et al., 1996).

This paper combines the results of detailed petrography, semi-quantitative mineral compositional analyses, sulfur isotopes of sulfides, and whole rock geochemistry, to determine paragenesis, timing, and conditions of formation for each of the Cape St. Mary's occurrences. Considering the endowment of critical metals at Cape St. Mary's, conditions for REE and antimony mineralization are compared to other similar mineralization styles in Nova Scotia and globally to support interpretations and determine mechanisms for mineralization.

3.2 Background

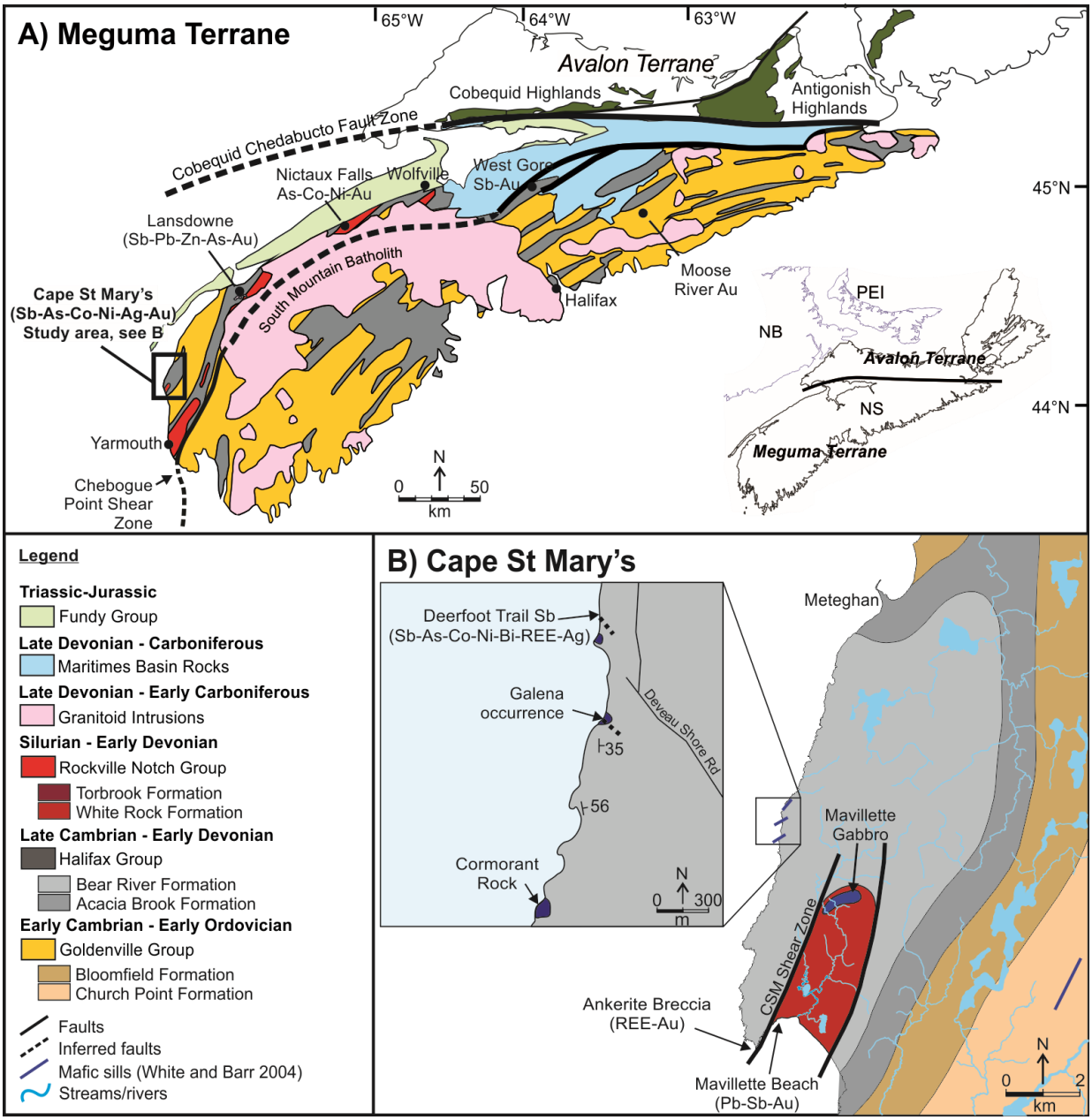

Figure 3-1 - A) Simplified geological map of the Meguma Terrane in southern Nova Scotia with a box outlining the location of the Cape St. Mary's study area, shown in B). Modified from White and Barr (2012). **B)** Local geology of the Cape St. Mary's area with the five occurrences indicated. Inset and regional map modified from White (2010). The locations of mafic sills are from White and Barr (2004) and White et al. (2003).

3.2.1 Regional Geology – The Meguma Terrane

The Cape St. Mary's occurrences are hosted in the metasedimentary rocks of the Meguma Supergroup and Rockville Notch Group along the northwestern margin of the Meguma Terrane (**Figure 3-1**). The Meguma Supergroup composes the majority of the Meguma Terrane and constitutes thick turbiditic successions (up to 11km; White and Barr, 2010) deposited on the continental slope of a peri-Gondwanan passive margin (White, 2010). These sequences include metaturbidites and metasandstones, locally interlayered with metasiltstones and black slate, of the Cambrian Goldenville Group, and the overlying metasiltstone and metamudstone units of the late Cambrian to middle Ordovician Halifax Group (Raeside and Hill, 1988; White, 2010; White and Barr, 2012). The Silurian Rockville Notch Group unconformably overlies the Meguma Supergroup rocks and consists of slate and quartzite, deposited in a shallow continental shelf setting, along with contemporaneous metabasalt and metarhyolite. The volcanic units formed as a response to periods of minor extensional rift volcanism in the Early Silurian (White and Barr, 2017). The Rockville Notch Group has limited surface exposure in the Meguma Terrane, occurring only in the northwest where it is intruded by Early Cambrian to Early Devonian mafic sills (**Figure 3-1A**; White et al., 2003; White and Barr, 2004). These mafic sills formed in multiple stages, first coevally with deposition of the Meguma Supergroup and subsequently with the basal unit of the Rockville Notch Group (White Rock Formation; White and Barr, 2004).

The early to middle Devonian Neoacadian Orogeny (ca. 405-365 Ma; Benn et al., 1999; White and Barr, 2012) deformed and variably metamorphosed the Meguma Supergroup, Rockville Notch Group, and mafic sills under sub-greenschist to amphibolite facies conditions. Widespread deformation occurred from the accretion of the Meguma Terrane onto to the Avalon Terrane (**Figure 3-1A**), including the formation of the NE-SW striking Chebogue Point shear zone (CPSZ) and related smaller shear zones in the southwest of the province, such as the Cape St. Mary's shear zone (**Figure 3-1B**). The CPSZ acts as a lithological boundary between the Meguma Supergroup units of the southeast and northwest Meguma Terrane, and is interpreted to strike the length of the Meguma Terrane, crosscut by the South Mountain batholith (**Figure**

3-1A; White and Barr, 2012). The South Mountain batholith and other related granitoids were emplaced within the upper crust of the Meguma Terrane between 380 – 370 Ma. The emplacement of these rocks is contemporaneous with widespread lode and disseminated Au mineralization in Goldenville Group metasediments (Sangster and Smith, 2007).

3.2.2 Local Geology – Cape St. Mary's

The Cape St. Mary's study area is located in Digby County, southwestern Nova Scotia. Local geology consists of laminated metamudstone of the Bear River Formation (Halifax Group), as well as unconformably overlying quartzite of the White Rock Formation, the basal unit of the Rockville Notch Group. The Mavillette Gabbro (426.4 ± 2.0 Ma; Warsame et al., 2017), a large mafic intrusive body, crosscuts the White Rock Formation, while multiple unnamed mafic sills intrude into the Bear River Formation along the western shore of Cape St. Mary's (**Figure 3-1B**). These sills were formed in an intra-plate extensional environment (White and Barr, 2004). Multiple periods of sill emplacement are believed to be coeval with the deposition of turbiditic sequences of the Goldenville and Halifax Groups over a span of 70 million years between the Cambrian and Ordovician, followed by another episode in the Silurian where the sills formed contemporaneously with the White Rock Formation and synchronous volcanic activity (White and Barr, 2004).

The NE-SW Cape St. Mary's shear zone defines the contact between the Bear River Formation and White Rock Formation at Cape St. Mary's (**Figure 3-1B**). This contact represents an angular unconformity overprinted by a ductile shear zone (Culshaw and Dickson, 2015), as there is a 30 Ma gap between deposition of the Bear River and White Rock formations (White et al., 2018). The Cape St. Mary's shear zone, along with other NE-SW trending shear zones in southwestern Nova Scotia, exhibits dextral strike-slip motion and formed from deformation during the Neoacadian orogeny. These shear zones were subsequently reactivated by Alleghenian-Variscan deformation in the Mid-Carboniferous (320 Ma; Culshaw and Reynolds, 1997) as a response to the collision of Gondwana with Laurentia causing

transpressional movement along the Cobequid-Chedabucto fault zone, which acts as the structural boundary between the Meguma and Avalon terranes (Culshaw and Liesa, 1997).

Prospecting and field work conducted by the Nova Scotia Department of Natural Resources (NSDNR; now Nova Scotia Department of Natural Resources and Renewables) in the 1980s and 1990s uncovered mineralized quartz-carbonate veins, found to be richly argentiferous (up to 1230 ppm Ag) and to contain anomalous Co, Ni and Au (O'Reilly and Mills, 2011) across five distinct occurrences. The five occurrences at Cape St. Mary's are distributed along the coast (from north to south): The Deerfoot Trail Sb occurrence, the Galena occurrence, the Cormorant Rock occurrence, the Ankerite Breccia occurrence, and the Mavillette Beach occurrence (**Figure 3-1B**). The Deerfoot Trail Sb occurrence has previously been described as the Cape St. Mary's Stibnite occurrence due to high Sb in assays; however, this study shows that stibnite is not the main Sb mineral at this location and will henceforth be referred to as the Deerfoot Trail Sb occurrence. The Deerfoot Trail Sb occurrence and the Mavillette Beach occurrence host the most significant sulfide mineralization at Cape St. Mary's. Assays indicated a combined elemental assemblage of Sb-Pb-As-Cu-Ni-Co-Bi-Ag-Au-REE from mineralized quartz-carbonate veins, mineralized samples of ankerite breccia, and stringer zones (O'Reilly, 1995).

3.3 Methodology

3.3.1 Field work and petrography

Representative samples of barren host rocks (including the Bear River Formation metamudstone, White Rock Formation quartzite, and unnamed altered mafic sills) were collected; however, mineralization is sparse due to coastal erosion and oversampling. Samples with sufficient mineralization for further analytical work were recovered from NSDNR archives. Thin section petrography allowed for characterization of primary and secondary mineralogy and textures, identification of mineral paragenesis, and selection of targets for micro-analytical work. Samples were examined with a TESCAN MIRA 3 LMU Variable Pressure Schottky LEO1450VP field emission scanning electron microscope (SEM) at Saint Mary's University, Halifax, Nova Scotia, equipped with an electron dispersive spectroscope (EDS) for

semi-quantitative compositional analysis and mineral identification and a back-scattered electron (BSE) detector for textural imaging.

3.3.2 Sulfur isotopes

Sulfur isotope data were obtained for pyrite, arsenopyrite, and chalcopyrite at the Manitoba Isotope Research Facility (MIRF), using secondary ion mass spectrometry (SIMS), following the methods of McDivitt et al. (2021). Pyrite and chalcopyrite reference material sourced from Crowe and Vaughan (1996) and arsenopyrite reference material from Hastie et al. (In review) indicated uncertainties (1σ) of 0.3‰ for all analyses. Spot to spot reproducibility on the reference material varied: 0.2‰ for arsenopyrite, 0.4‰ for chalcopyrite, and 0.3‰ for pyrite. Analyses were conducted with a ~15 µm spot size, entrance slit of 225 µm, and accelerating voltage of -8.7 kV for 50 cycles. Counts were collected for one second for ^{32}S and five seconds for ^{34}S per cycle. Data are represented as per mil (‰) ^{34}S relative to ^{32}S ($\delta^{34}S$) relative Vienna Cañon Diablo Troilite (VCDT).

3.3.3 Whole rock geochemistry

Whole rock geochemical data of major oxides and trace elements were collected from three mineralized samples from Cape St. Mary's containing Cu-Sb-Fe sulfide mineralization in siderite breccia, massive galena with pyrite mineralization in a mafic intrusion, and massive pyrite mineralization in quartz. Samples were sent to Actlabs Ancaster, Ontario, Canada, for preparation and analysis. All samples were crushed to a nominal 2 mm and mechanically split to obtain a representative sample and pulverized to 105 µm. Major oxides were obtained from crushed samples which were prepped using lithium borate fusion and were analyzed with X-ray fluorescence. For minor and trace elements, unmineralized crushed samples were subject to closed vessel multi-acid microwave digestion and measured with ICP-MS. For mineralized samples, minor and trace elements were measured using peroxide total fusion for total metal recovery. Analyses were conducted using ICP-MS and ICP-OES. The concentrations of Au and Ag were also measured in mineralized samples via Au cyanide extraction and ICP-MS for Ag.

3.4 Results

3.4.1 Field observations and petrography

The Cape St. Mary's area spans from north to south from Deveau Shore Rd to Mavillette Beach Provincial Park (**Figure 3-1B**). The Bear River Formation metamudstone is predominantly composed of quartz, muscovite, chlorite, and ilmenite. Cleavage is defined by fine-grained muscovite and a perpendicular crenulation. Mafic intrusives are present along the Cape St. Mary's coastline and are associated with the Deerfoot Trail Sb occurrence, Galena occurrence, and Cormorant Rock occurrence. The Mavillette Gabbro is a large mafic intrusive body that has been exploited as a quarry inland, hosted in the White Rock Formation (**Figure 3-1B**). Quartz veining is abundant through all host rocks, and at least three generations of quartz veining are present. The most dominant quartz veins form as en-echelon and conjugate veins oblique to the cleavage of the host rock. Mineralization at Cape St. Mary's has been subdivided into five occurrences as follows.

3.4.1.1 Deerfoot Trail Sb occurrence

The Deerfoot Trail Sb occurrence is hosted in Bear River Formation metamudstone at the northernmost point of the Cape St. Mary's study area in a fault which strikes southeast through the host rock (**Figure 3-1B**). About 20 m south of the fault, a ~3m wide rounded mafic intrusion crosscuts the metamudstone host rock. The mafic intrusive is fine-grained and altered by chlorite and calcite, which erase primary igneous textures. Strongly chlorite altered wallrock clasts of the Bear River Formation are hosted in the siderite breccia. Mineralization occurs as large grains or aggregates (up to 20 mm) of sulfides disseminated within the breccia (**Figure 3-2B**). Euhedral rhomb-shaped arsenopyrite with high Co and Ni concentrations along grain margins (up to 8 wt.% Co and 20 wt.% Ni) truncate the siderite. This arsenopyrite is overprinted by aggregates of < 1-5 µm size grains of the REE-rich aluminium phosphate-sulfate (APS) mineral florencite (ideal formula: $(REE)Al_3(PO_4)_2(OH)_6$) as well as minor ~ 10 µm subhedral grains of pyrite (**Figure 3-2C-D**). In general, APS minerals have the formula $AB_3(XO_4)_2(OH)_6$, where a large cation in 12-fold coordination occupies the *A* site (e.g., Ca, Sr, Ba, Pb, REE, etc.), Al, Fe, Cu and/or Zn

occupy the *B* site in octahedral coordination, and P or S anions occupy the *X* site (Dill, 2001). Semi-quantitative EDS analyses of the aluminum-phosphate mineral florencite from The Deerfoot Trail occurrence indicate that Sr, LREE (Ce, La, Th, and Nd), and Ca occupy the *A* site, while Fe and Al occupy the *B* site, as part of the crandallite solid-solution-series (Dill, 2001). Florencite is compositionally zoned (**Figure 3-2D**), where there is higher Ce (9.68 to 10.02 wt.%) and Nd (2.90 to 3.51 wt.%) and lower Sr (2.34 to 1.95 wt.%), Th (1.84 to 0.73 wt.%), Ca (1.61 to 0.86 wt.%), and Fe (1.81 to 0.72 wt.%) from rim to cores (**Table A2-2**).

Disseminated throughout the siderite breccia and rarely occurring alongside arsenopyrite are large (up to 2 cm) anhedral masses of Cu-Sb sulfosalts, Cu-sulfides, Sb-sulfides, and Sb-Bi alloys. Chalcostibite (ideal formula: $CuSbS_2$) is replaced by Fe-tetrahedrite (ideal formula: $Cu_{10}Fe_2Sb_4S_{13}$), as evidenced by tetrahedrite forming along the rims of chalcostibite grains and extensive cusp-carrie textures. Tetrahedrite forms with anhedral masses of disseminated Bi-rich stibnite ($(Sb, Bi)_2S_3$), and occasionally with rare Sb-Pb sulfosalt plagionite (ideal formula: $Pb_5Sb_4S_{11}$; **Figure 3-2F-G**). In a single sample, Ag substitutes for Fe and Cu in tetrahedrite, forming Ag-bearing tetrahedrite, known as freibergite (ideal formula: $(Ag,Cu,Fe)_{12}Sb_4S_{13}$; **Figure 3-2H)**. Chalcopyrite forms as large rims around the chalcostibite/tetrahedrite/freibergite grains, along with small, disseminated grains of native Sb-Bi (75-90 wt.% Sb, 10-25 wt.% Bi).

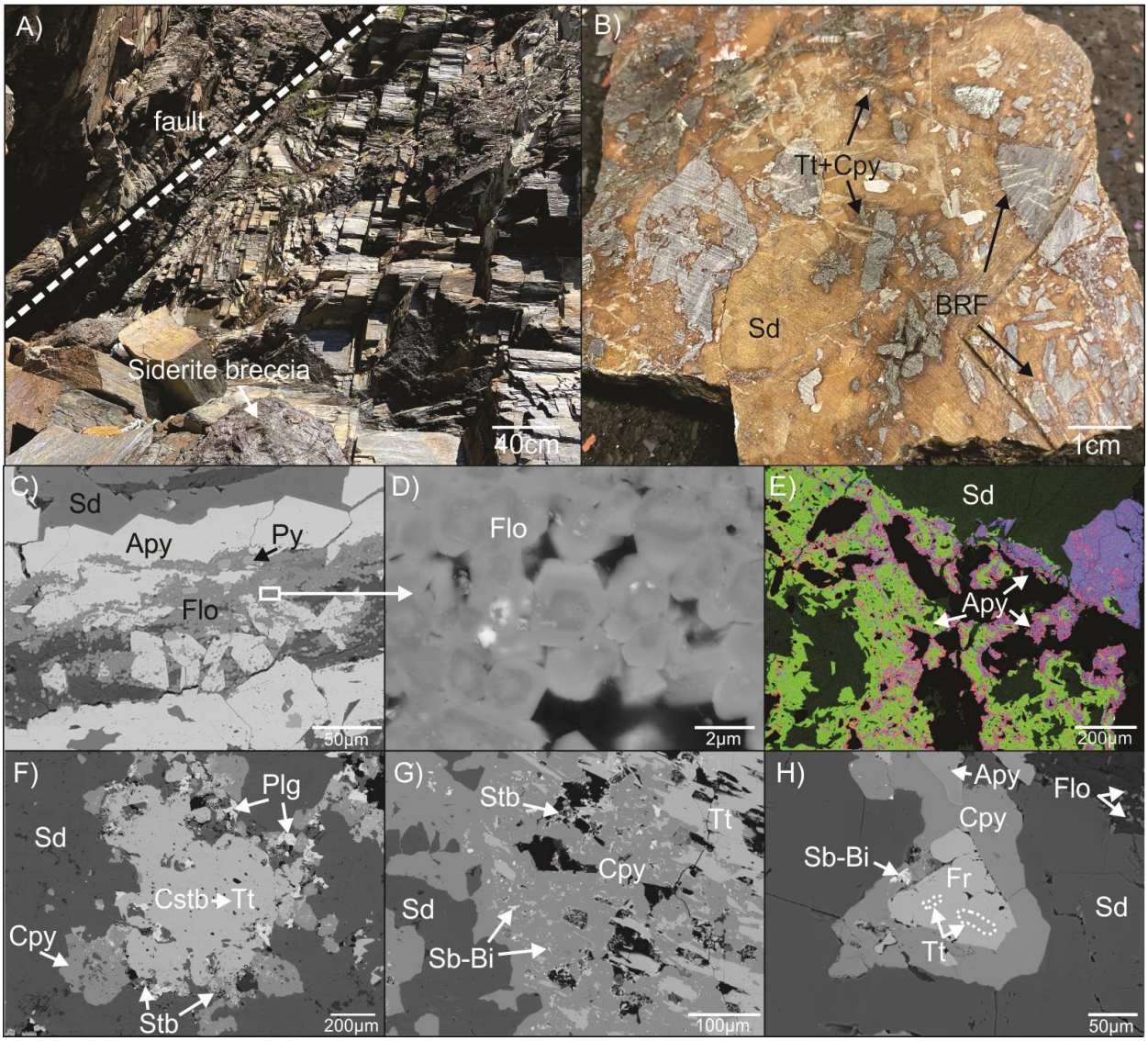

Figure 3-2 – **A)** The fault at the Deerfoot Trail Sb occurrence. Siderite breccia outcrops at the base of the fault. **B)** Mineralized hand sample of siderite breccia from the Deerfoot Trail Sb occurrence, collected from the base of the fault by NSDNR. Bear River Formation. (BRF) metamudstone clasts are brecciated by siderite (Sd). Tetrahedrite (Tt) with chalcopyrite (Cpy) rims cut across the siderite. **C)** BSE image; euhedral arsenopyrite (Apy) is hosted in siderite and forms with altered wall rock clasts. Florencite (Flo) overprints arsenopyrite as aggregates of zoned hexagonal grains along with rounded grains of pyrite (Py). **D)** BSE image; zoned florencite grains with darker cores with higher Sr, Th, Ca, and Fe concentrations and lighter rims with higher Ce and Nd concentrations. **E)** False colour elemental distribution map by EDS showing Fe (green), Co (red), and Ni (blue) distribution in arsenopyrite. **F)** BSE image; chalcostibite (Ctsb) grain

with Fe-tetrahedrite (Tt) in siderite. Tetrahedrite occurs with Bi-rich stibnite (Stb) and plagionite (Plg). Chalcopyrite (Cpy) forms with small, disseminated grains of Sb-Bi alloys. **G)** BSE image; chalcopyrite is pitted and contains fragments of tetrahedrite and Bi-rich stibnite, as well as anhedral rounded grains of Sb-Bi alloys. **H)** BSE image; arsenopyrite in contact with the chalcopyrite rim of freibergite (Fr), which replaces Fe-tetrahedrite. Large grains of an Sb-Bi alloy occur in the chalcopyrite.

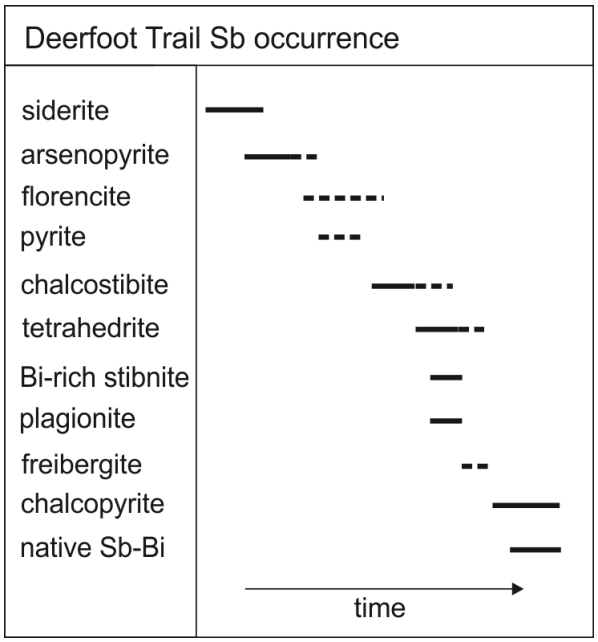

Figure 3-3 - Paragenesis of mineralization at the Deerfoot Trail Sb occurrence. Dashed lines indicate uncertainty in the paragenesis.

3.4.1.2 Galena occurrence and Cormorant Rock occurrence

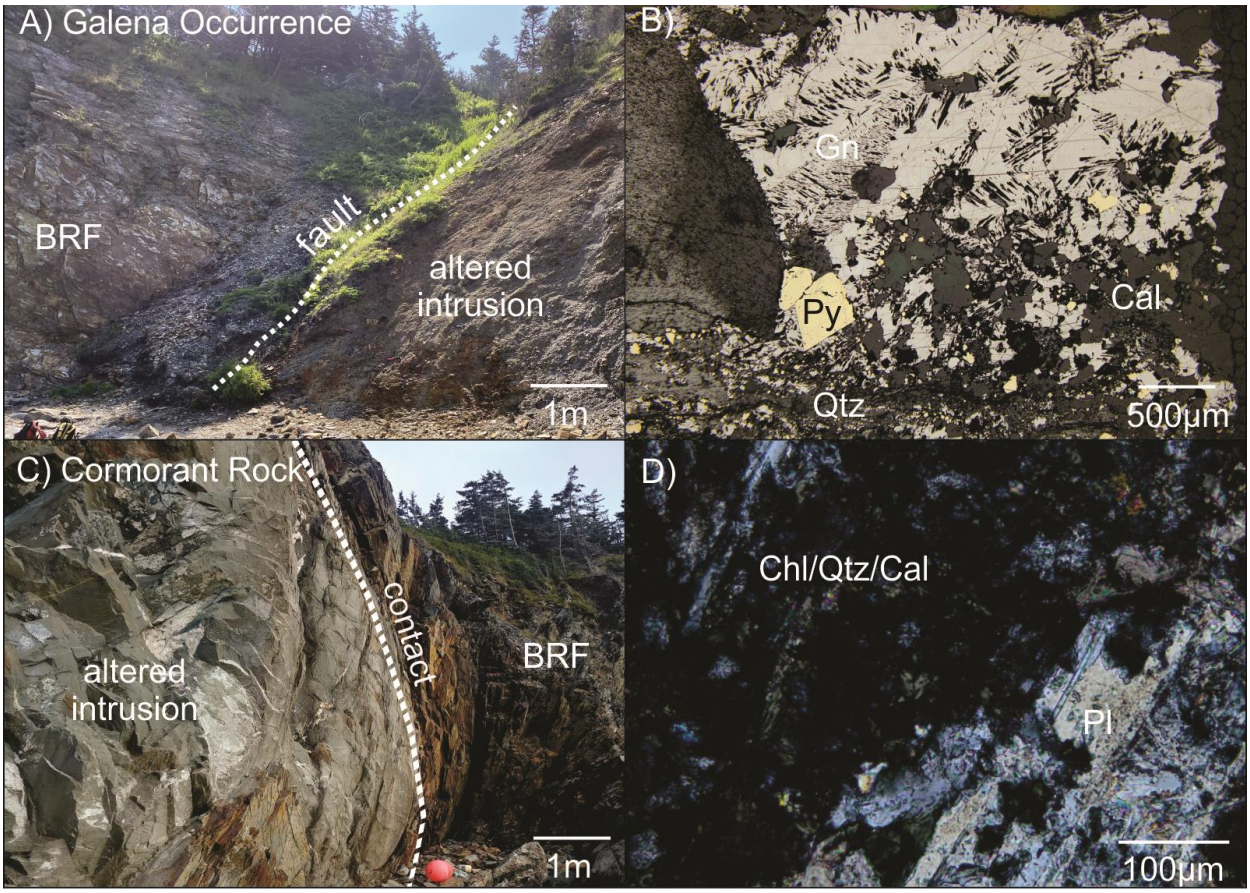

Figure 3-4 - A) Photograph of the Galena occurrence. An unnamed altered mafic intrusion is separated from the Bear River Formation (BRF) country rock by a fault gouge. **B)** Photomicrograph in reflected light shows massive galena (Gn) and minor euhedral pyrite (Py) hosted in a quartz (Qtz) calcite (Cal) vein. **C)** Photograph of the Cormorant Rock occurrence. The Cormorant Rock mafic intrusion displays a sharp contact with the Bear River Formation. **D)** Photomicrograph (XPL) demonstrates fine grained chlorite (Chl), quartz (Qtz), and calcite (Cal), which replace and overprint primary plagioclase (Pl) in the Cormorant Rock intrusion.

Mineralization of the Galena and Cormorant Rock occurrences was not observed *in situ*; however, NSDNR archived field notes describe mineralization as being hosted in quartz-calcite veins crosscutting the large mafic intrusions outcropping at both locations. At the Galena occurrence, the intrusion is fine-grained and heavily altered, with a crumbling texture. A fault gouge separates the intrusion at the Galena

occurrence from the Bear River Formation metasediments to the north (**Figure 3-4A**). The sediments directly adjacent to the fault gouge are bleached white and fine-grained (**Figure 3-4A**). An archived polished thin section of mineralization from the Galena occurrence shows galena with characteristic triangle pit pattern and minor euhedral pyrite hosted in a quartz and calcite vein (**Figure 3-4B**). Heavily altered wallrock fragments in the vein are composed of chlorite and mica and are adjacent to mineralization.

At the Cormorant Rock occurrence, another large altered mafic intrusion cuts through the Bear River Formation (**Figure 3-4C**). The Cormorant Rock intrusion is less altered than the Galena occurrence intrusion and displays primary plagioclase overprinted by a fine-grained chlorite, quartz, and calcite matrix (**Figure 3-4D**). The intrusion displays chilled margins on its southern contact with the Bear River Formation. Barren quartz and calcite veins cut across the intrusion; however, no mineralized veins were uncovered by recent field work and no archived samples for this occurrence exist. From archived field notes, mineralization was documented as galena and minor possible sphalerite hosted in quartz-carbonate veins within the intrusion (O'Reilly, 1992).

3.4.1.3 Ankerite Breccia shear zone occurrence

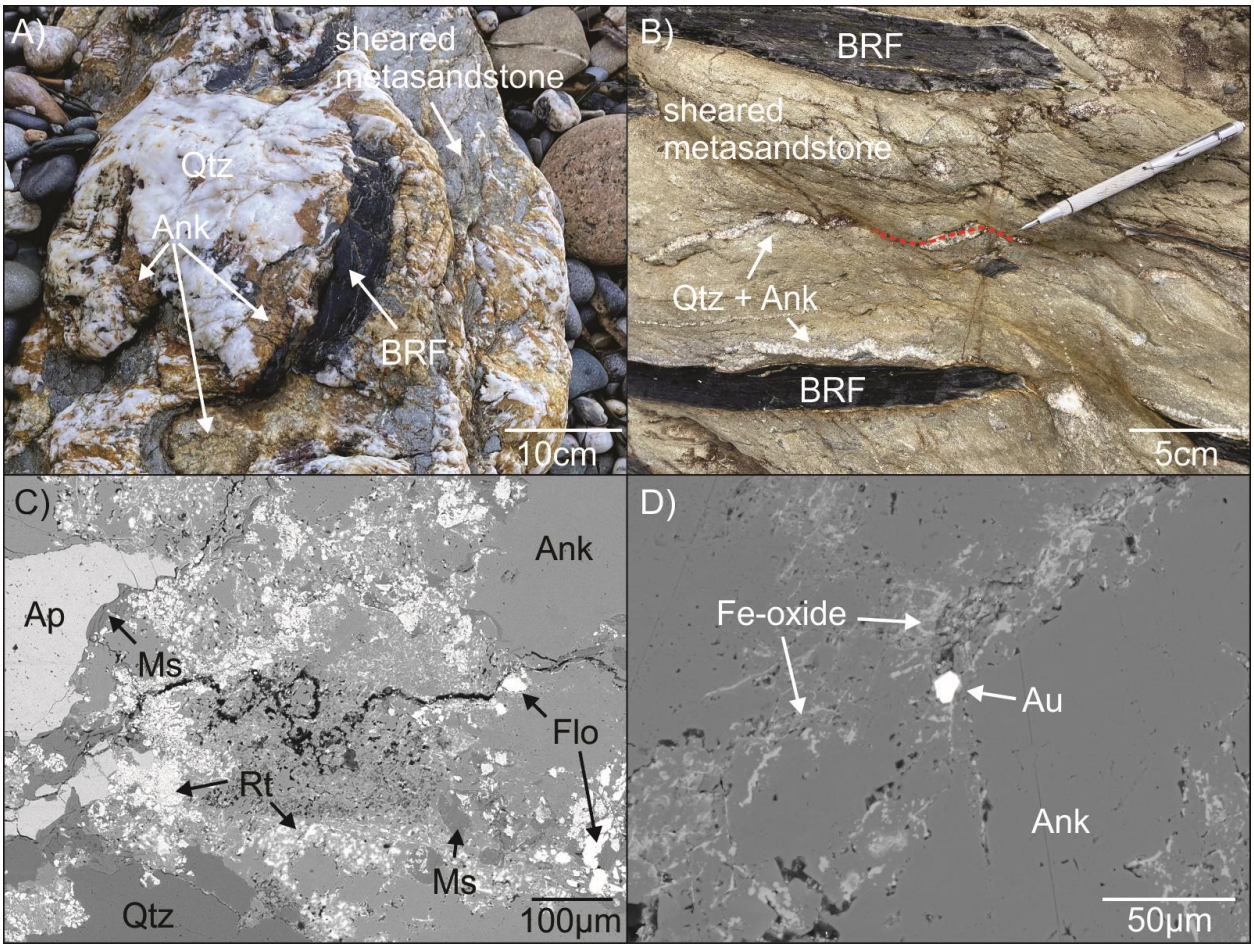

Figure 3-5 - Ankerite Breccia shear zone occurrence. **A)** Sheared beige-coloured metasandstone hosting xenoliths of Bear River Formation (BRF) metamudstone, white quartz (Qtz), and pale yellow ankerite (Ank). **B)** Boudinaged quartz-ankerite veins hosted in sheared metasandstone and adjacent to Bear River formation metamudstone xenoliths. Red dashed line represents inferred rotational direction of boudinaged quartz-ankerite vein. **C)** BSE image: Disseminated rutile (Rt), muscovite (Ms), florencite (Flo), and a large anhedral grain of apatite (Ap) form in ankerite along the grain boundary between quartz and ankerite. **D)** BSE image: native Au bleb with Fe-oxide infilled fractures in ankerite.

The Ankerite Breccia occurrence is hosted within sheared metasandstone at the promontory of the Cape St. Mary's shear zone (**Figure 3-1A**). This shear zone marks the boundary between the Bear River Formation and the White Rock Formation (Culshaw and Dickson, 2015). The area features clasts of Bear

River Formation metasediments, sometimes rotated, and rounded or boudinaged veins/veinlets of yellow Mg-rich ankerite, displaying distinct rhombic cleavage, and milky white quartz form in the sheared metasandstone (**Figure 3-5**A). Some boudinaged quartz-ankerite veins and Bear River Formation metamudstone clasts in the sheared metasandstone show ambiguous rotational indicators, as some veins exhibit dextral motion, whereas others show sinistral motion (**Figure 3-5B**).

Mineralization at the Ankerite Breccia occurrence is only observed in ankerite along quartz and ankerite grain boundaries, and consists of important metals Au, Ti, and REE. Iron-oxide forms a cross-hatching pattern overprinting the ankerite, forming along ankerite cleavage planes (**Figure 3-5C-D**). In some areas, large grains of anhedral apatite (up to 500 µm), along with subhedral to anhedral rutile, elongate grains of muscovite, and massive anhedral aggregates of florencite form along and adjacent to fractures in the ankerite (**Figure 3-5C**). The paragenesis of this mineralization is unclear; however, anhedral apatite likely formed relatively early as it is infilled by muscovite in some fractures. Muscovite is abundant and forms coevally with rounded anhedral florencite and rutile along grain boundaries and fractures in the ankerite (**Figure 3-5C**). Monazite also forms anhedral aggregates with muscovite, although they are less abundant and smaller than florencite. Monazite hosts LREEs Nd (21.57 wt.%), Ce (11.53 wt.%), Sm (10.54 wt.%), Gd (3.7 wt.%), and La (2.48 wt.%; **Table A2-2**). Florencite at the Ankerite Breccia occurrence is different in composition and habit from the Deerfoot Trail occurrence, as florencite forms subhedral-anhedral grains that show no compositional zoning and contain no Fe or Th, as well as lower Sr values (~ 0.5 – 0.9 wt.%; **Table A2-2**).

Native Au forms as small (< 20 µm) disseminated blebs in Fe-oxide infilled fractures in the ankerite (**Figure 3-5D**). Rare xenotime is rounded (~ 30 µm in diameter) and hosts 32.1 wt.% Y and ~ 16 wt.% middle REE (6.82 wt.% Gd, and 6.24 wt.% Dy, 2.67 wt.% Sm; **Table A2-2**). Xenotime occurs as a small bleb along Fe-oxide fractures, like gold mineralization.

3.4.1.4 Mavillette Beach occurrence

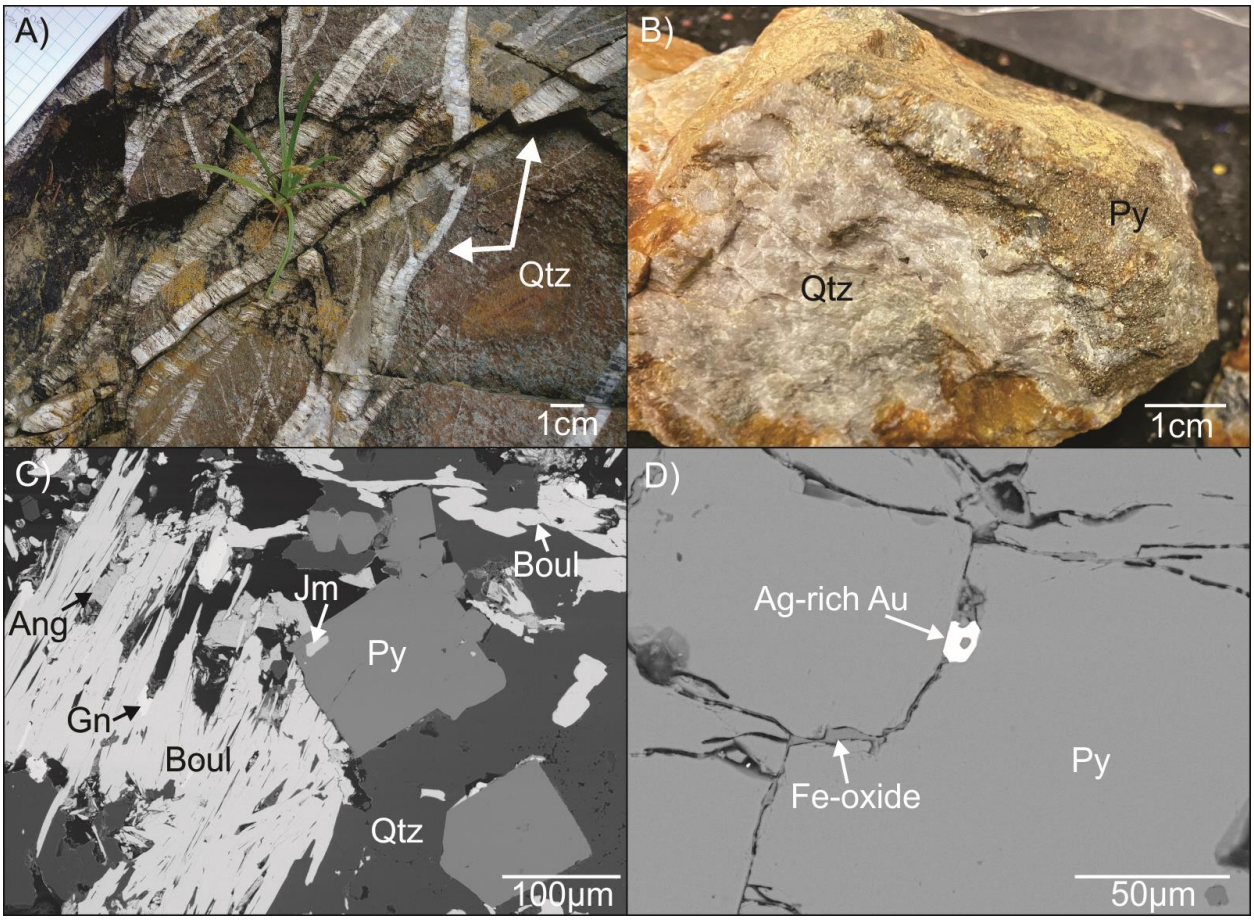

Figure 3-6 - Mavillette Beach occurrence. **A)** Conjugate veins of barren quartz (Qtz) hosted in White Rock Formation quartzite; representative of barren quartz veins abundant at the Mavillette Beach occurrence. **B)** Massive pyrite mineralization hosted in a large quartz vein, from NSDNR archives. **C)** BSE image: euhedral pyrite (Py) forms with needle-like boulangerite (Boul) and jamesonite (Jm), along with minor galena (Gn), in a quartz vein. Thin section collected from NSDNR archives. **D)** BSE image: Ag-rich Au forms as disseminated blebs between pyrite grains from hand sample observed in B. Silver-rich Au and Fe-oxide form as small veinlets between the grains of pyrite aggregate.

The Mavillette Beach occurrence is hosted in the White Rock Formation quartzite, proximal to the Cape St. Mary's shear zone. The White Rock Formation quartzite is host to abundant barren quartz veins, often forming as conjugate vein systems (**Figure 3-6A**). These veins range in width from a few mm to up

to 30 cm. Quartz grains in the veins are elongate and show evidence of undulose extinction. Veins also show minor, green-coloured chlorite with first order grey-green interference colours forming between quartz grains. The elongate quartz grains form perpendicularly to the strike of the vein, creating a unique erosional pattern where quartz was preferentially eroded along grain boundaries (**Figure 3-6A**).

Mineralized samples were collected by O'Reilly in the 1980's and 1990's and were retrieved from NSDNR archives. The exact distance and placement of the original mineralized veins from the Cape St. Mary's shear zone is unknown; however, field notes indicate that the occurrence was close to the White Rock Formation and Bear River Formation contact (O'Reilly, 1992). Two archived NSDNR samples showed evidence of mineralization. The first was a hand sample of a massive quartz vein with a large aggregate of pyrite (**Figure 3-6**B). In fractures and interstitial spaces between pyrite in the pyrite aggregates, a few disseminated Ag-rich (~ 13 wt.%) Au blebs (~10 µm) form with Fe-oxide (**Figure 3-6D**). Another thin section recovered from archived samples showed sparse euhedral pyrite grains forming with silver coloured acicular boulangerite and jamesonite (Sb-Pb sulfosalts), along with minor galena along sulfosalt grain margins. Petrographically, it is unclear if the massive pyrite mineralization and euhedral pyrite-sulfosalt mineralization formed from the same mineralizing event, but archived field notes confirm they were found in approximately the same area (O'Reilly, 1992).

3.4.2 Sulfur isotopes

Sulfur isotope values were measured from arsenopyrite, chalcopyrite, and pyrite in samples from three of the Cape St. Mary's occurrences: arsenopyrite and chalcopyrite from the Deerfoot Trail occurrence, and pyrite from the Galena occurrence and Mavillette Beach occurrence. All minerals analyzed demonstrate positive S-isotope values, ranging from 7.8 ‰ to 12.7 ‰ (**Table 3-1**). Intrasample variation within a single mineral is relatively small (< 2‰) for all minerals (**Table A2-3**).

Table 3-1 - Summary of S-isotope data for sulfide minerals determined by SIMS.

Mineral[a]	Occurrence		$\delta^{34}S_{SULFIDE}$ (‰)	
		# of grains/points [b]	$\bar{x}$	±1σ
arsenopyrite	Deerfoot Trail Sb	5/6	**+12.06**	0.72
chalcopyrite	Deerfoot Trail Sb	4/5	**+11.06**	0.38
pyrite	Galena Occurrence	3/5	**+11.07**	0.22
pyrite	Mavillette Beach	5/7	**+8.94**	0.58

[a] Minerals eligible for SIMS analysis in CSM mineralized samples based on available reference materials
[b] Total number of grains and spots analyzed

3.4.3 Whole rock geochemistry

Sample B1-92-G015, hosting chalcostibite-tetrahedrite-stibnite-chalcopyrite mineralization from siderite breccia at the Deerfoot Trail Sb occurrence shows 5.62 wt.% Sb, 3.32 wt.% Cu, 2.34 wt.% Al, 1.03 wt.% Mn, and 2620 ppm Bi. This sample also exhibits Au below detection limits and negligible amounts of Ag. Up to 26 ppm As, 3.2 ppm Co, and 40 ppm Ni were recovered from this sample indicating no arsenopyrite mineralization present (**Table A2-4**). Sample B1-97-G005, hosting galena and pyrite in a mafic sill from the Galena occurrence, shows 7.85 wt.% Pb, 1.31 wt.% Mn, 1.8 ppb Au and 202 ppb Ag, as well 633 ppm Cu and 451 ppm Sb (**Table A2-4**). Sample B1-97-G010, hosting massive pyrite in a quartz vein from the Mavillette Beach occurrence shows > 1 ppm Au and 817 ppb Ag, as well as 2.65 wt.% Fe, 1420 ppm Pb, 854 ppm As, and 319 ppm Sb (**Table A2-4**).

3.5 Discussion

Of the five occurrences at Cape St. Mary's, an abundance of important critical and economically significant metals can be found, including Sb, Pb, Ag, Co, Ni, As, Bi, Cu, REE, as well as native Au. However, the distribution of these metals is not the same between occurrences (**Figure 3-7**). The Galena occurrence and Cormorant rock occurrences appear to host only Pb mineralization. Considering that both these occurrences are hosted in highly chlorite and carbonate altered mafic intrusions, Pb may have been derived from replacement of calcic plagioclase, although Pb-isotope analyses would be required to confirm

the source of Pb in galena. It is unclear how these occurrences tie into the mineralizing events that formed the other occurrences at Cape St. Mary's.

The Deerfoot Trail Sb occurrence, the Ankerite Breccia occurrence, and the Mavillette Beach occurrence show the most critical metal mineralization, expressed by different mineralogy and parageneses. Antimony, REE, and gold mineralization link these three occurrences; however, Sb is only present at the Deerfoot Trail Sb and Mavillette Beach occurrences, Au is only present at the Ankerite Breccia and Mavillette Beach occurrences, and REE are only present at the Deerfoot Trail Sb and Ankerite Breccia occurrences (**Figure 3-7**). This likely represents multiple distinct mineralizing events. The Sb mineralization at the Deerfoot Trail occurrence formed later than REE mineralization, suggesting the REE mineralizing event occurred first. Since Au mineralization forms as late interstitial disseminated blebs at both the Ankerite Breccia and Mavillette Beach occurrence, it is reasonable to infer that Au formed as the last mineralizing event.

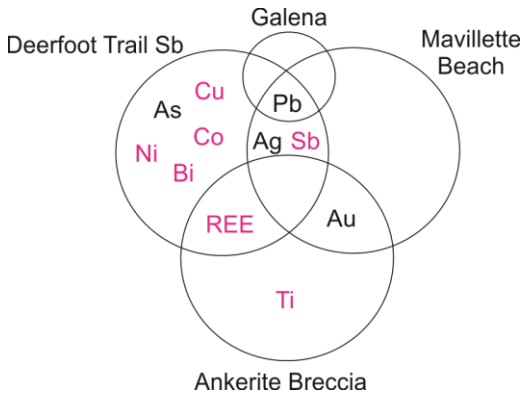

Figure 3-7 - Venn diagram showing overlap in metals of interest between the occurrences at Cape St. Mary's. Critical metals highlighted in pink text (as defined by Natural Resources Canada, 2021)

3.5.1 Rare earth element mineralization

Rare earth element mineralization at Cape St. Mary's is associated with clusters of the APS mineral florencite, as well as rare disseminated grains of monazite and xenotime, occurring in fractures at the Ankerite Breccia occurrence, and as zoned euhedral florencite aggregates associated with arsenopyrite

mineralization at the Deerfoot Trail Sb occurrence. At both occurrences, REE mineralization is associated with local structural features (i.e., the Cape St. Mary's shear zone and Deerfoot Trail fault). The latest movement along the Cape St. Mary's and associated shear zones in southwestern Nova Scotia is considered to have occurred in the Mid-Carboniferous (ca. 320 Ma; Culshaw and Reynolds, 1997) in order to accommodate stress from the reactivation of basement structures along the CCFZ in northern Meguma (Culshaw and Liesa, 1997).

Rare earth element mineralization associated with the Cobequid-Chedabucto Fault Zone (CCFZ), formed from the remobilization of REE from REE-rich granites by hydrothermal fluids during a late-magmatic stage at ~360 Ma and a "post-magmatic stage" at ~320 Ma (Ersay, 2020). We note that there are A-type granites of "post-magmatic stage" age associated with IOCG deposits in the Cobequid and Antigonish highlands, north of the CCFZ hosted in the Avalon Terrane (Wisen, 2020; **Figure 3-1A**). Iron-oxide-copper-gold (IOCG) mineralization associated with REE minerals occurs along the CCFZ (e.g. the Copper Lake IOCG deposit; Kontak et al., 2008). . Although IOCG deposits include a wide variety of deposit characteristics, all IOCG mineralization is related to widespread carbonate and iron-oxide alteration of host rocks by magmatic-hydrothermal fluids, is structurally controlled, and hosts significant brecciation (Groves et al., 2010). Many IOCG deposits worldwide also exhibit associations with high levels of light-REE (La, Ce, Nd, Sm) concentrations (e.g., Groves and Vielreicher, 2001; Ismail et al., 2014; Weng et al., 2014; Day et al., 2016), as exhibited by the Olympic Dam IOCG deposit in Australia where abundant florencite and monazite occur as fine grained crystals and aggregates in copper-bearing mineralized host rocks (Schmandt et al., 2019).

Rare earth element minerals associated with IOCG mineralization at Copper Lake was dated to ~320 Ma (Kontak et al., 2008), consistent with other REE mineralization in the Cobequid and Antigonish highlands (Ersay, 2020), and coeval with Alleghenian deformation and movement along the CCFZ (Faure et al., 1996; Murphy et al., 2011; Piper and Pe-Piper, 2020). We speculate that mineralization along the Cape St. Mary's shear zone at the Ankerite Breccia occurrence is a result of Alleghenian stress reactivating

the Cape St. Mary's shear zone at 320 Ma, causing brecciation of the host rock by Fe bearing carbonate, and producing Fe-oxide alteration with REE mineralization, resulting in similar processes which formed the REE-bearing IOCG deposits in the Cobequid highlands. This same period of deformation is possibly responsible for faulting, brecciation, and REE mineralization at the Deerfoot Trail Sb occurrence. However, sources for REEs remain unclear, as no REE-rich granites or other clear REE sources are documented in the region.

3.5.2 Antimony mineralization

Antimony mineralization at Cape St. Mary's occurs at the Deerfoot Trail Sb occurrence and at the Mavillette Beach occurrence, expressed by two distinct Sb mineralization styles. The antimony mineral species at the Deerfoot Trail Sb occurrence are complex and occur with metals of interest Cu, Bi, Pb, and Ag, hosted in a siderite breccia. Mineralogy at the Deerfoot Trail Sb occurrence exhibits a transition marking changes in fluid composition and pH conditions: Chalcostibite ($CuSbS_2$) is replaced by Fe-tetrahedrite ($Cu_{10}Fe_2Sb_4S_{13}$), which forms with Bi-rich stibnite (up to ~27 wt.% Bi; **Table A2-2**; **Figure 3-2G-H**). The transition from chalcostibite to tetrahedrite requires the addition of Fe from the dissolution siderite and an addition of Bi to form Fe-tetrahedrite and Bi-rich stibnite, as modelled by the reaction:

$$10CuSbS_{2(chalcostibite)} + 2FeCO_{3(siderite)} + 6Bi_{(aq)} + 2H_2S$$
$$\rightarrow Cu_{10}Fe_2Sb_4S_{13(Fe-Tetrahedrite)} + 3(SbBi)_2S_{3(Bi-rich\ stibnite)} + 2HCO_3^- + 2H^+$$

The sulfur species represented in the reaction is the reduced form H_2S, although the exact sulfur species involved in the reaction is unknown. When assuming H_2S as the sulfur species, this reaction produces excess H^+ ions, indicating an increase in acidity for the system. In some instances, rare Sb-Pb sulfosalt plagionite ($Pb_5Sb_4S_{11}$) forms coevally with Bi-rich stibnite and tetrahedrite (**Figure 3-2F**). In a sample which hosts both Cu-Sb-Fe-Bi mineralization and Co-Ni rich arsenopyrite at the Deerfoot Trail Sb occurrence, tetrahedrite is replaced by freibergite [$(Ag, Cu, Fe)_{12}Sb_4S_{13}$] before the reaction to form chalcopyrite and native Sb-Bi takes place (**Figure 3-2H**). The Cu – Fe + Zn – Ag ternary in **Figure 3-8D**

shows how the composition of tetrahedrite changes with the addition of Fe and Ag to follow the curve from endmember chalcostibite to tetrahedrite to freibergite. Chalcopyrite and a native Sb-Bi alloy (75 – 85 wt.% Sb, 15 – 25 wt.% Bi) form as a rim around tetrahedrite and Bi-rich stibnite from the further dissolution of siderite:

$$Cu_{10}Fe_2Sb_4S_{13_{(Fe-Tetrahedrite)}} + 2(SbBi)_2S_{3_{(Bi-rich\ stibnite)}} + 8FeCO_{3_{(siderite)}} + 4H_2S_{(aq)}$$
$$\rightarrow 10CuFeS_{2_{(Chalcopyrite)}} + 6(SbBi)_{(s)} + 8HCO_3^-$$

A decrease in temperature could also produce the reactions seen here, as shown in the Cu-Fe-Sb-(As)-S system as defined by Mateus and Figueiras (2005) and the Cu_2S-FeS-Sb_2S_3 system as defined by Krismer and Tropper (2013). Both these systems assume a generally low temperature for the breakdown reactions of chalcostibite and tetrahedrite, occurring between 70 – 350 °C (Mateus and Figueiras, 2005; Krismer and Tropper, 2013). Therefore, it is likely that cooling and dissolution of siderite from the mineralizing fluid contributed to the transition of antimony mineral species at the Deerfoot Trail Sb occurrence.

Antimony mineralization is also present at Cape St. Mary's at the Mavillette Beach occurrence, hosted in the White Rock Formation quartzite. At the Mavillette Beach occurrence, Sb is deposited as Sb-Pb sulfosalts boulangerite and jamesonite, which form alongside euhedral pyrite and galena, distinctly different from the mineralization at the Deerfoot Trail occurrence. Additionally, the Mavillette Beach occurrence is hosted in quartz veins, not a carbonate breccia. The mineralization at Mavillette Beach bears many resemblances to Sb-Pb mineralization observed at the Lansdowne occurrence, a polymetallic (Sb-Pb-As-Zn) vein deposit hosted in the Bear River Formation, proximal to the South Mountain Batholith and Fundy rift basin in southwestern Nova Scotia (**Figure 3-1A**). This occurrence is only ~ 80 km north of the Cape St. Mary's study area.

Mineralization at Lansdowne is hosted in quartz-carbonate veins, which crosscut host metasediments and altered mafic sills (Welt et al., In review; O'Reilly and Mills, 2011). Sulfide mineralization forms in

two stages: an early arsenopyrite stage that occurred in the Late Devonian, and a late critical metal stage that formed during the Late Triassic, composed of Fe-poor sphalerite, pyrrhotite, chalcopyrite, arsenopyrite, jamesonite, boulangerite, galena, and pyrite (Welt et al., In review). The latest stage of critical metal mineralization, composed of boulangerite, jamesonite, and pyrite, formed at 165 ºC and 15 bar pressure, based on fluid inclusion isochores of mineralizing fluids (Welt et al., In review). Antimony mineralization at Lansdowne has been attributed to Triassic rifting and extensional tectonics of the Fundy rift basin and opening of the Atlantic Ocean (Welt et al., In review). Using Re-Os geochronology, arsenopyrite associated with the critical metal stage yields an age of approximately 214 Ma (Welt et al., In review).

The Mavillette Beach occurrence shares the most mineralogical similarities to the Lansdowne occurrence of any of the Cape St. Mary's occurrences. The Mavillette Beach occurrence sulfosalts boulangerite and jamesonite form with galena and euhedral pyrite, exactly as the Sb-Pb stage at Lansdowne, and reflect the same compositions (**Figure 3-8B**). However, many critical metals present at Lansdowne and stages of mineralization are missing from the paragenesis at Mavillette Beach. Although the Deerfoot Trail Sb occurrence hosts extensive critical metal mineralization, mineral species are completely different than mineralization observed at the Lansdowne occurrence (Welt et al., In review). The only sulfide that appears at both occurrences is arsenopyrite, but these arsenopyrite species vary drastically in composition (**Figure 3-8C**), with arsenopyrite at Deerfoot Trail exhibiting compositional zoning and significantly higher Co and Ni values (up to 8 wt.% Co and 15 wt.% Ni; **Table A2-2**) than at Lansdowne (up to 7 wt.% Co; Welt et al., In review). Structurally, the Cape St. Mary's study area shows consistent evidence of an extensional environment, including abundant conjugate veining of quartz, and en-echelon boudinaged quartz vein systems (**Figure 3-6A**); however, the timing and relationship between antimony mineralization at the Deerfoot Trail Sb and Mavillette Beach occurrences and this extensional environment is unclear.

Antimony mineralization is very rare in the Meguma Terrane. There are only two other occurrences which indicate elevated Sb: the aforementioned Lansdowne occurrence and the West Gore Sb-Au occurrence (Kontak et al., 1996; **Figure 3-1A**). The Lansdowne and Cape St. Mary's occurrences, as well

as the West Gore Sb-Au deposit, lie along strike of the Fundy Rift basin, and the only other documented Sb occurrence in Nova Scotia also lies along this strike line (**Figure 3-1A**). At both Lansdowne and the West Gore Sb-Au deposit, sources of Sb are unclear and are not considered to have come from alteration of wallrock (Welt et al., In review; Kontak et al., 1996); therefore, this work speculates that antimony mineralization in Nova Scotia may be related to a widespread Sb mineralizing event along reactivated Acadian structures, triggered by extensional tectonics during opening of the Fundy rift basin in the Mesozoic.

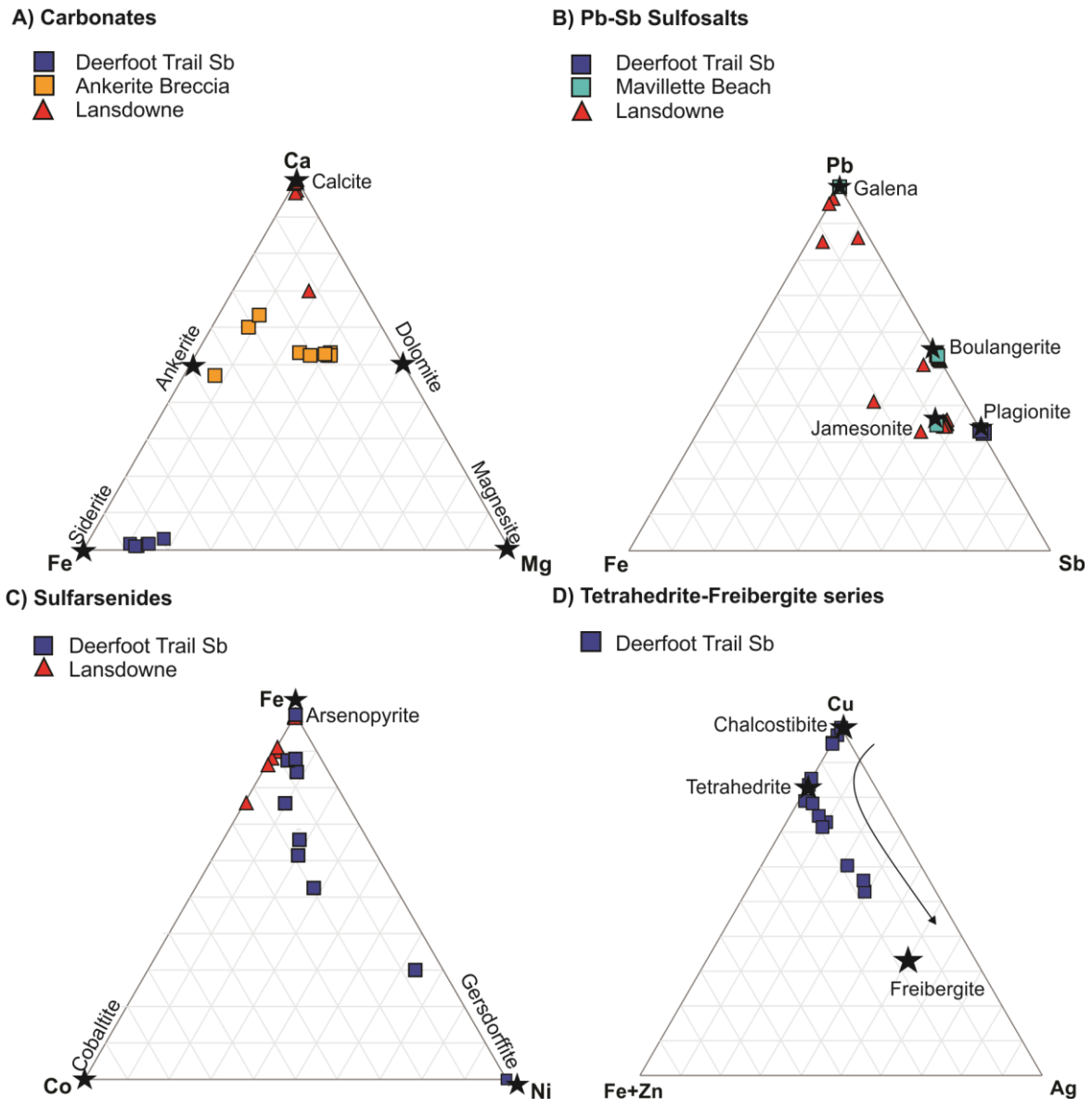

Figure 3-8 - Compositional variation in different mineral types from Lansdowne and Cape St. Mary's occurrences. Stars indicate ideal composition for indicated mineral. A) Carbonate species by Ca – Fe – Mg ternary. B) Pb-Sb sulfosalt species by Pb – Fe – Sb ternary. C) Sulfarsenide species by Fe – Co – Ni ternary. D) Tetrahedrite-freibergite series by Cu – Fe + Zn – Ag ternary

Sulfur isotope data collected from pyrite at the Mavillette Beach occurrence, and arsenopyrite and chalcopyrite from the Deerfoot Trail Sb occurrence show a small range in sulfur isotope values ($\delta^{34}S$ = ~8 – 12 ‰; **Table 3-1**), much lower than the $\delta^{34}S$ values of sulfides from Lansdowne (Welt et al., In review; **Figure 3-9**), but similar to the $\delta^{34}S$ values of sulfides from Meguma Au deposits (Kontak and Smith, 1989). The Gays River MVT deposit, which formed from metal-rich brines in the Carboniferous Maritimes Basin, also shows very similar $\delta^{34}S$ values as Cape St. Mary's and Meguma Au sulfides (**Figure 3-9**). In Meguma Au deposits, reduced sulfur (H_2S) is representative of mineralizing fluids (Kontak and Smith, 1989), rather than at the Gays River deposit, where the mineralizing fluid was sulfate-dominated and required a different sulfur source (Akande and Zentilli, 1984). Since the temperature for mineralization of the Cape St. Mary's sulfides are unknown, fractionation between H_2S and SO_4 cannot be determined, and an accurate comparison between the sulfur isotope values of sulfides in different deposits and their sulfur sources cannot be made. The contrast in sulfur isotope values of sulfides from the Lansdowne and Cape St. Mary's occurrences suggests that sulfides at these occurrences were formed from different sulfur sources.

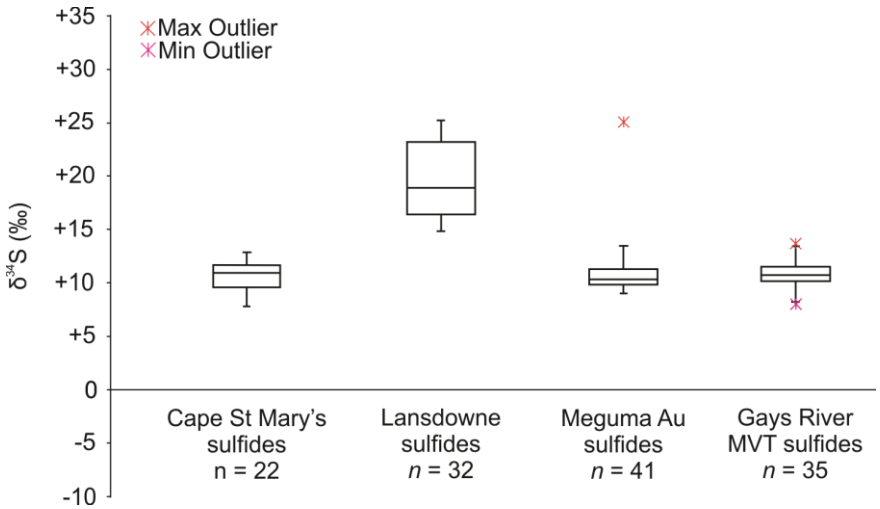

Figure 3-9 - Sulfur isotope values of sulfides at Cape St. Mary's (Deerfoot Trail Sb and Ankerite Breccia occurrence) and other sulfides from Meguma deposits. Sulfur isotope values collected from (Welt et al., In review; Akande and Zentilli, 1984; Kontak and Smith, 1989)

3.6 Conclusion

The occurrences at Cape St. Mary's represent a wide variety of critical metal mineralizing events in a small area with little overlapping mineralogy. Paragenesis of the Deerfoot Trail Sb occurrence, where both REE mineralization and antimony mineralization occur, indicates early REE mineralization followed by a Cu-Sb (±Pb-Bi) stage. The Ankerite Breccia occurrence is hosted by the Cape St. Mary's shear zone, which was reactivated at 320 Ma by Alleghenian deformation along the CCFZ, and mineralization is reminiscent of IOCG mineralization in the Cobequid highlands. Therefore, we suggest that the Ankerite Breccia occurrence (and likely the Deerfoot Trail Sb occurrence) is related to reactivation of the Cape St. Mary's shear zone and circulating of REE-enriched magmatic-hydrothermal fluids.

The paragenesis of Sb minerals at the Deerfoot Trail Sb occurrence indicates dissolution of siderite by a metal bearing fluid, possibly triggered by a decrease in temperature. Antimony mineralization at the Mavillette Beach occurrence cannot be constrained by timing, however mineralization is very similar to the Sb-Pb mineralizing stages of the Lansdowne occurrence, ~80 km north of Cape St. Mary's, which was determined to have formed from Late-Triassic extensional tectonics from the rifting of the Bay of Fundy. Although sulfur isotope values of sulfides related to antimony mineralization at Cape St. Mary's are like those of Meguma Au deposits and the Gays River MVT deposit, a lack of temperature data makes a direct comparison of the mineralizing fluids which formed the different occurrences impossible.

References

Akande, S. O., and Zentilli, M., 1984, Geologic, fluid inclusion and stable isotope studies of the Gays River lead-zinc deposit, Nova Scotia, Canada.: Economic Geology, v. 79, p. 1187–1211.

Benn, K., Roest, W. R., Rochette, P., Evans, N. G., and Pignotta, G. S., 1999, Geophysical and structural signatures of syntectonic batholith construction: The South Mountain Batholith, Meguma Terrane, Nova Scotia: Geophysical Journal International, v. 136, p. 144–158.

Carew, T., Gilman, T., Raponi, T. R., and Hannon, P., 2020, Scotia Mine Pre-Feasibility Study Technical Report For ScoZinc Limited - NI 43-101 TECHNICAL REPORT.:

Crowe, D. E., and Vaughan, R. G., 1996, Characterization and use of isotopically homogeneous standards for in situ laser microprobe analysis of 34S/32S ratios: American Mineralogist, v. 81, p. 187–193.

Culshaw, N., and Dickson, C., 2015, Cape st. Marys shear zone and the halifax group – rockville notch group disconformity, southwestern nova scotia: Structural development and tectonic significance: Canadian Journal of Earth Sciences, v. 52, p. 921–937.

Culshaw, N., and Liesa, M., 1997, Alleghanian reactivation of the Acadian fold belt, Meguma Zone, southwest Nova Scotia: Canadian Journal of Earth Sciences, v. 34, p. 833–847.

Culshaw, N., and Reynolds, P. H., 1997, 40Ar/39Ar age of shear zones in the southwest Meguma Zone between Yarmouth and Meteghan, Nova Scotia: Canadian Journal of Earth Sciences, v. 34, p. 848–853.

Day, W. C., Slack, J. F., Ayuso, R. A., and Seeger, C. M., 2016, Regional geologic and petrologic framework for iron oxide ± apatite ± rare earth element and iron oxide copper-gold deposits of the mesoproterozoic St. Francois Mountains Terrane, Southeast Missouri, USA: Economic Geology, v. 111, p. 1825–1858.

Dill, H. G., 2001, The geology of aluminum phosphate and sulphates of the alunite group minerals: A review: Earth Science Reviews, v. 53, p. 35–93.

Ersay, L., 2020, Multistage, magmatic and hydrothermal evolution of the Debert Lake rare earth element (REE) prospect, Nova Scotia, Canada. M.Sc. Thesis, University of British Columbia, The College of Graduate Studies, Earth and Environmental Sciences.

Faure, S., Tremblay, A., and Angelier, J., 1996, Alleghanian paleostress reconstruction in the northern Appalachians: Intraplate deformation between Laurentia and Gondwana: Bulletin of the Geological Society of America, v. 108, p. 1467–1480.

Gowans, R., Jacobs, C., Anderson, D., Spooner, J., Mercer, W., Hains, D. H., and Smith, R., 2018, The East Kemptville tin production and site rememdiation project - Preliminary economic assessment, Nova Scotia, Canada - NI 43-101 Technical Report.:

Groves, D. I., and Vielreicher, N. M., 2001, The Phalabowra (Palabora) carbonatite-hosted magnetite-copper sulfide deposit, South Africa: An end-member of the iron-oxide copper-gold-rare earth element deposit group? Mineralium Deposita, v. 36, p. 189–194.

Groves, D. I., Bierlein, F. P., Meinert, L. D., and Hitzman, M. W., 2010, Iron oxide copper-gold (IOCG) deposits through earth histoiy: Implications for origin, lithospheric setting, and distinction from other epigenetic iron oxide deposits: Economic Geology, v. 105, p. 641–654.

Ismail, R., Ciobanu, C. L., Cook, N. J., Teale, G. S., Giles, D., Mumm, A. S., and Wade, B., 2014, Rare earths and other trace elements in minerals from skarn assemblages, Hillside iron oxide-copper-gold deposit, Yorke Peninsula, South Australia: Lithos, v. 184–187, p. 456–477.

Kontak, D. J., and Smith, P. K., 1989, Sulphur isotopic composition of sulphides from the Beaver Dam and other Meguma-Group-hosted gold deposits, Nova Scotia: implications for genetic models: Canadian Journal of Earth Sciences, v. 26, p. 1617–1629.

Kontak, D. J., Horne, R. J., and Smith, P. K., 1996, Hydrothermal Characterization of the West Gore Sb-Au Deposit, Meguma Terrane, Nova Scotia, Canada: Economic Geology, v. 91, p. 1239–1262.

Kontak, D. J., Archibald, D. A., Creaser, R. A., and Heaman, L. M., 2008, Dating Hydrothermal Alteration Attending IOCG Mineralization Along a Terrane Bounding Fault Zone: The Copper Lake Deposit, Nova Scotia: Atlantic Geology, v. 44, p. 146–166.

Krismer, M., and Tropper, P., 2013, Reactions involving famatinite and Fe-Zn tetrahedrite: thermochemical evaluation of phase relations in the Cu-Fe-Sb-S and Cu-Zn-Sb-S end-member systems: European Journal of Mineralogy, v. 25, p. 155–163.

Mateus, A., and Figueiras, J., 2005, Thermochemical Evolution of Sb-Cu Ores at Ventosa (Beja, Portugal): XIV Semana de Geoquímica/VIII Congresso de Geoquímica dos Países de Língua Portuguesa abstracts, p. 299–303.

McDivitt, J. A., Kontak, D. J., Lafrance, B., Petrus, J. A., and Fayek, M., 2021, A trace metal, stable isotope (H, O, S), and geochronological (U-Pb titanite) characterization of hybridized gold orebodies in the Missanabie-Renabie district, Wawa subprovince (Canada): Mineralium Deposita, v. 56, p. 561–582.

Murphy, J. B., Waldron, J. W. F., Kontak, D. J., Pe-Piper, G., and Piper, D. J. W., 2011, Minas Fault Zone: Late Paleozoic history of an intra-continental orogenic transform fault in the Canadian Appalachians: Journal of Structural Geology, v. 33, p. 312–328.

Natural Resources Canada, 2021, Canada's Critical Minerals List: accessed at https://www.canada.ca/en/natural-resources-canada/news/2021/03/canada-announces-critical-minerals-list.html.

O'Reilly, G. A., 1992, NSDNR Field Notes - 1992:

O'Reilly, G. A., 1995, Little Known Ni-Co-Bi-Sb-Ag-Au Association in the Annapolis Valley: accessed at Minerals Update. Nova Scotia Department of Natural Resources

O'Reilly, G. A., and Mills, R. F., 2011, Selected Mineral Deposits of the Annapolis Valley of Nova Scotia.:

Papoutsa, A., and Pe-Piper, G., 2013, The relationship between REE-Y-Nb-Th minerals and the evolution of an a-type granite, wentworth pluton, nova scotia: American Mineralogist, v. 98, p. 444–462.

Papoutsa, A., and Pe-Piper, G., 2014, Variation of REE-hydrothermal circulation in complex shear zones: The Cobequid Highlands, Nova Scotia: Canadian Mineralogist, v. 52, p. 943–968.

Piper, D. J. W., and Pe-Piper, G., 2020, Evolution of late Paleozoic shearing in the Cobequid Highlands: constraints on the fragmentation of the Appalachian Orogen in Nova Scotia along intra-continental shear zones: Geological Society of London, Special Publications, v. 503, p. 423–442.

Raeside, R. P., and Hill, J. D., 1988, Metamorphism of Meguma Group metasedimentary rocks, Whitehead Harbour Area, Guysborough County, Nova Scotia: Maritime Sediments and Atlantic Geology, v. 24, p. 1–9.

Sangster, A. L., and Smith, P. K., 2007, Metallogenic Summary of the Meguma Gold Deposits, Nova Scotia, in Goodfellow, W. D. ed., Mineral Deposits of Canada: A Synthesis of Major Deposit-Types, District Metallogeny, the Evolution of Geological Provinces, and Exploration Methods: Geological Association of Canada, Mineralogical Association of Canada, Special Publication, p. 723–732.

Schmandt, D. S., Cook, N. J., Ciobanu, C. L., Ehrig, K., Wade, B. P., Gilbert, S., and Kamenetsky, V. S., 2019, Rare earth element phosphate minerals from the olympic dam Cu-U-Au-Ag deposit, South Australia: Recognizing temporal-spatial controls on ree mineralogy in an evolved iocg system: Canadian Mineralogist, v. 57, p. 3–24.

Smith, P. K., and Kontak, D. J., 1996, Gold Deposits in the Meguma Group of Nova Scotia, NSDNR, MEB, IC51: accessed at NSDNR Open-File Report at papers://32862730-33e4-4f24-9997-a2585c9ed6b6/Paper/p118.

Warsame, H. S., McCausland, P. J. A., White, C. E., Barr, S. M., and Dunning, G. R., 2017, Age and preliminary paleomagnetic assessment of the Silurian Mavillette gabbro, Meguma Terrane, Nova Scotia, Canada, in GAC-MAC program with abstracts Vol.40: p. 408.

Welt, N., Jackman, J., Adlakha, E. E., Hanley, J. J., Kerr, M. J., Creaser, R. A., Baldwin, G., Fayek, M., and Sharpe, R., In review, Late-Triassic epithermal polymetallic Sb-Au (-Pb-Zn-Co-Ag) veins, Meguma Terrane, Canadian Appalachian Orogen; a new critical metal deposit type in Nova Scotia: Unpublished Manuscript.

Weng, Z. H., Jowitt, S. M., Mudd, G. M., and Haque, N., 2014, Assessing rare earth element mineral deposit types and links to environmental impacts: Transactions of the Institutions of Mining and Metallurgy, Section B: Applied Earth Science, v. 122, p. 83–96.

White, C. E., 2010, Stratigraphy of the Lower Paleozoic Goldenville and Halifax groups in the western part of southern Nova Scotia: Atlantic Geology, v. 46, p. 136–154.

White, C. E., and Barr, S. M., 2004, Age and Petrochemistry of Mafic Sills in Rocks of the Northwestern Margin of the Meguma Terrane, Bear River - Yarmouth Area of Southwestern Nova Scotia: Mineral Resources Branch, Report of Activities 2003; Nova Scotia Department of Natural Resources, p. 97–117.

White, C. E., and Barr, S. M., 2012, Meguma Terrane Revisited; Stratigraphy, Metamorphism, Paleontology, and Provenance, in GAC-MAC 2012 Post Meeting Field Trip: St-John's, NF.

White, C. E., and Barr, S. M., 2017, Stratigraphy and depositional setting of the Silurian–Devonian Rockville Notch group, Meguma Terrane, Nova Scotia, Canada: Atlantic Geology, v. 53, p. 337–365.

White, C. E., Barr, S. M., and Gould, R. C., 2003, Gabbroic Intrusions in the Meteghan - Yarmouth the Meguma Terrane, Southern Nova Scotia Field Relations and: Mineral Resources Branch, Report of Activities 2003; Nova Scotia Department of Natural Resources, p. 147–162.

White, C. E., Barr, S. M., and Linnemann, U., 2018, U-Pb (zircon) ages and provenance of the White Rock Formation of the Rockville Notch Group, Meguma terrane, Nova Scotia, Canada: evidence for the "Sardian gap" and West African origin: Canadian Journal of Earth Sciences, v. 55, p. 589–603.

Wisen, J., 2020, REE and other minerals in the West Moose River Pluton and associated rocks, Cobequid Highlands , Nova Scotia , and their association with fracturing: University of Quebec in Chicoutimi.

Chapter 4: The genetic relationship between Lansdowne, Cape St. Mary's, and Nictaux Falls

4.1 Introduction

Uranium exploration projects in the Nictaux South area of Annapolis county uncovered the Nictaux Falls Dam occurrence (NFDO; Black, 1978). Reports on mineralization and a small drill program were subsequently conducted in the region (Van Oirschot, 1994; Jensen, 2012), with the occurrence further described by O'Reilly (1998) as a vein-type polymetallic occurrence hosted in the Kentville Formation metasediments of the Rockville Notch Group. Mineralization style, constraints on fluid source, and the relationship between this occurrence and five-element style deposits were investigated by McNeil (2019). Fluid inclusion analyses of mineralized samples were conducted by Kennedy (2019). Mineralization at the NFDO is characterized by quartz-breccia hosting mineralized wallrock clasts and laminated sulfarsenide quartz veins which host arsenopyrite, cobaltite, gersdorffite and a Au-Ag alloy preceded by gangue chlorite, biotite, and rutile (McNeil, 2019). Bulk rock data suggests the Kentville Formation metasediments are the likely source of metals for the NFDO (McNeil, 2019). Fluid inclusion results from mineralized samples and bulk $\delta^{34}S$ values from sulfarsenide minerals indicate that the Carboniferous Maritimes Basin was the most likely source of sulfur and fluids, due to high Ca and Na in inclusions and comparisons with average $\delta^{34}S$ values of Carboniferous seawater (Kennedy, 2019; McNeil, 2019).

O'Reilly (1995) considered the NFDO to bear a likeness to five-element style deposits, as defined by Kissin (1992). Results from McNeil (2019) indicate that indeed some similarities in mineralogy exist between the NFDO and other five-element style deposits, such as the presence of native metals (e.g., Au-Ag alloy), sulfarsenides with high Co and Ni and associated compositional zoning, and late gangue minerals. However, there are too many differences to properly classify the occurrence as this deposit type, including a lack of native Ag and Bi, absence of di- and tri-arsenide minerals, and an opposite zoning pattern of metals in sulfarsenides (McNeil, 2019). O'Reilly (1995) suggests a genetic relationship between the NFDO and the Lansdowne and Cape St. Mary's occurrences. In chapter 3, comparisons between the mineralogy and timing of the Cape St. Mary's and Lansdowne occurrences are discussed, however, their

relationship to the NFDO is as yet unclear. To evaluate the genetic relationship between these occurrences, supplementary data are collected from the NFDO and Cape St. Mary's to determine chlorite thermometry and U-Pb in apatite geochronology of a mafic intrusion at the NFDO, and make comparisons between the NFDO, Lansdowne occurrence, and Cape St. Mary's occurrences. By understanding the relationship between these occurrences, we can evaluate the potential for similar timing, fluid sources, and/or similar processes for formation and deposition of mineralization.

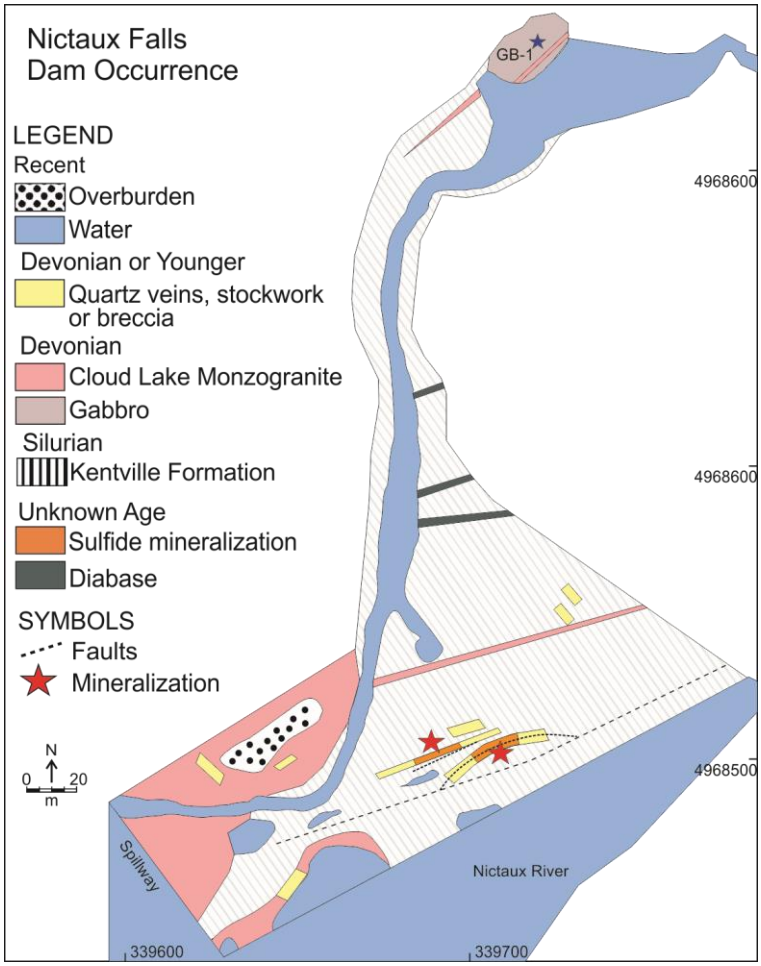

Figure 4-1 - Geologic map of the Nictaux Falls Dam occurrence (modified from McNeil, 2019). Location of the gabbro sample used for U-Pb in apatite geochronology (GB-1) is marked with a blue star. Mineralization is hosted in main zone 1 (MZ1) and main zone 2 (MZ2). Coordinates are UTM zone 20.

4.2 Methods

Major and minor elements of chlorite from the Cape St. Mary's study area and the NFDO were collected to identify chlorite mineral species and calculate temperatures of formation. Using an empirical calibration of tetrahedral (Al^{IV}) aluminium in the crystal structure of chlorite, the temperature at which the chlorite crystallized can be determined (de Caritat et al., 1993). Many geothermometers for chlorite exist applicable to certain conditions of chlorite formation, such as a chlorite which forms with a low (< 0.6) Fe/(Fe + Mg) ratio (Jowett, 1991), or when chlorite forms in Al-saturated environments (Kranidiotis and MacLean, 1987). For this project, the empirical equation developed by Cathelineau (1988), which relates *T* (°C) and Al^{IV} composition, is used to calculate the temperature of chlorite formation since the value of Al^{IV} in chlorite appears to be independent of rock lithology and can be applied as a general thermometer in diagenetic, hydrothermal, and metamorphic settings:

$$T = -61.92 + 321.98\ (Al^{IV})$$

Analyses were performed with a JEOL JXA8230 5-WDS electron probe microanalyzer (EPMA) at the University of Toronto using carbon-coated polished thin sections. Measurements were taken with a 10 µm beam, beam current of 10 nA, and accelerating voltage of 15 kV. The major oxides measured, along with their respective quantification standard in brackets include SiO_2 (chlorite from Smith, 1969), TiO_2 (TiO_2), Al_2O_3 (chlorite from Smith, 1969), Cr_2O_3 (Cr_2O_3), NiO (pentlandite), FeO (hematite), MnO (bustamite), MgO (chlorite from Smith, 1969), CaO (bustamite), Na_2O (albite glass), K_2O (sanidine glass), and SrO ($SrTiO_3$) as well as anions F (MgF_2) and Cl (tugtupite). The Kα energy line was used for detection of all elements, except for Sr (Lα).

Uranium and lead concentrations in apatite were measured from one sample of gabbro (GB-1) from the NFDO for U-Pb dating by LA-ICP-MS at the University of New Brunswick's laser ablation facility. Target grains were mapped in thin sections using micro-XRF. Analyses were performed on a 193 nm excimer laser attached to an Agilent 7700x single quad ICP-MS, following the method of McGregor et al. (2018). Every

15 analyses of unknowns were bracketed by analyses of a primary external standard (Madagascar apatite; Thomson et al., 2012), NIST610 glass standard, and a secondary external standard (Phalaborwa apatite; McGregor et al., 2018). Analyses were conducted with a 45 µm beam once per apatite grain. Ratios of $^{238}U/^{206}Pb$ and $^{207}Pb/^{206}Pb$ (± 2σ) were plotted, unanchored, on Tera-Wasserburg diagrams to determine intercept ages using the online program IsoplotR (Vermeesch, 2018). The Phalaborwa standard gave a lower intercept age of 2068 ± 15 Ma (n = 10; MSWD = 1.6). This age is within range of the Phalaborwa apatite age determined by McGregor et al. (2018; 2048 ± 16 Ma), as well as ion-microprobe ages of zircon (2050 ± 13 Ma) and baddeleyite (2060 ± 2 Ma) from the same area and confirm the accuracy of measurements obtained for unknowns of this study.

4.3 Results

4.3.1 Chlorite petrography and thermometry

Two types of chlorite are present at Cape St. Mary's, associated with different host rocks. Type-1 chlorite is associated with quartz veins that cut across barren Bear River and White Rock Formation host rocks. This chlorite is pale green to colourless and exhibits anomalous berlin blue interference colours (**Figure 4-2**). Grains typically form as radial aggregates along the margins of quartz and/or calcite veins. Type-1 chlorite is not associated with any stages of mineralization. Type-2 chlorite is found as an alteration product of augite and plagioclase in the Mavillette gabbro. The Mavillette Gabbro is a mafic plug in the White Rock Formation that exhibits a dark green colour due to the high chlorite content of the rock. This type-2 chlorite is green in colour and exhibits first order grey-green interference colours (**Figure 4-2**).

At the NFDO, a single chlorite type was identified that forms interstitially and along margins of sulfarsenide (arsenopyrite and cobaltite) grains in quartz veins. Chlorite is very fine grained, and often exhibits a needle like habit (**Figure 4-2**). Chlorite forms with fine grained muscovite, such that they are difficult to distinguish by petrographic observation. Chlorite is dark grey-green in colour and exhibits dark first order interference colours.

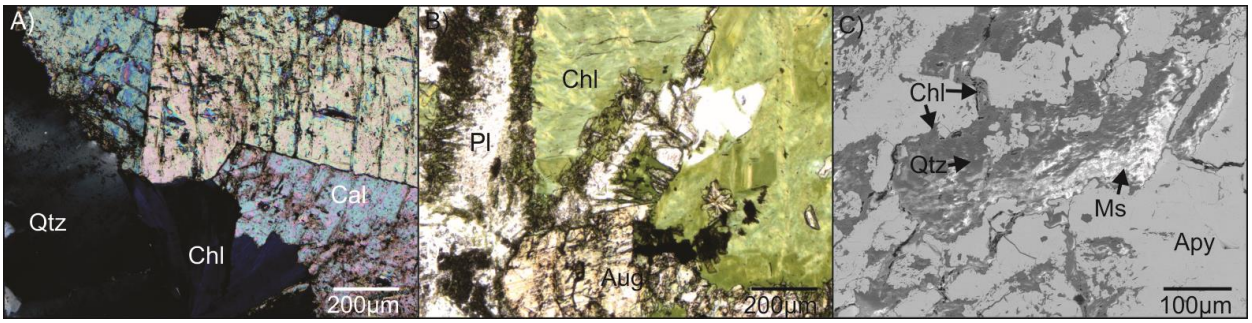

Figure 4-2 - Chlorite types analyzed at Cape St. Mary's and Nictaux Falls. **A)** Photomicrograph XPL: Type-1 chlorite at CSM along grain boundary between quartz and calcite in a barren quartz vein. **B)** Photomicrograph PPL: Type-2 chlorite at CSM forms as reaction rims along plagioclase and augite in a gabbro. **C)** BSE image: Nictaux Falls chlorite forms as needle-like aggregates between and along grain boundaries of Co-rich arsenopyrite along with muscovite (Ms).

Both types of chlorite examined at Cape St. Mary's can be classified as Mg-rich chamosite, based on the proportions of octahedral Al (Al^{VI}), Fe, and Mg (**Figure 4-4**). The NFDO chlorite is clinochlore in composition (**Figure 4-4).** Cape St. Mary's type-1 chlorite has relatively higher Fe than type-2 chlorite (Chl-2; Table 1). Additionally, the Fe # (Fe/(Fe+Mg)) of type-1 chlorite varies between different samples (0.55 to 0.68) but the proportion of Al is similar (**Table A3-2**). Type-1 chlorite yields a mean temperature of approximately 397 °C (**Table 4-1**). Type-2 chlorite has an average temperature of approximately 273 °C (**Table 4-1**). The Fe # of type-2 chlorite is lower than type-1, with a mean of 0.55 (**Table 4-1**). Nictaux Falls chlorite has a Fe # lower than both Cape St. Mary's chlorite types, at 0.40 (**Table 4-1**). Nictaux Falls chlorite has an average temperature of approximately 282 °C (**Table 4-1**).

Table 4-1 - Abundance of major oxides in chlorite in wt.% determined by EPMA and their calculated atomic proportions (based on 14 oxygen) from Cape St. Mary's and NFDO

	Chlorite type	CSM - Type-1		CSM - Type-2		NFDO	
	Chlorite host [a]	Quartz vein, BRF		Mavillette Gabbro		Quartz-Apy vein	
	# of grains/points	3/8		5/9		4/4	
		x̄	1σ	x̄	1σ	x̄	1σ
O14	SiO_2	24.49	0.16	27.54	1.15	29.77	1.78
	TiO_2	0.09	0.03	0.08	0.03	0.08	0.01
	Al_2O_3	25.32	0.16	18.09	1.49	23.25	0.22
	Cr_2O_3	0.01	0.01	0.01	0.02	0.03	0.03
	NiO	0.01	0.01	0.02	0.01	0.02	0.02
	FeO	29.42	0.22	33.36	0.70	19.56	0.54
	MnO	0.14	0.04	0.21	0.03	0.26	0.03
	MgO	9.63	0.25	9.90	0.85	16.17	1.07
	CaO	0.02	0.02	0.11	0.06	0.13	0.06
	Na_2O	0.03	0.05	0.02	0.02	0.03	0.02
	K_2O	0.04	0.07	0.02	0.02	0.15	0.15
	SrO	0.02	0.04	0.01	0.02	0.00	0.01
	F	0.02	0.03	0.03	0.04	0.15	0.01
	Cl	0.01	0.01	0.00	0.00	0.02	0.01
apfu [b]							
T	Si	2.58		2.96		2.93	
	Al	1.42		1.04		1.07	
	sum	4.00		4.00		4.00	
O	Al	1.71		1.25		1.64	
	Fe	2.59		3.00		1.61	
	Mg	1.51		1.59		2.38	
	Mn	0.01		0.02		0.02	
	sum	5.83		5.86		5.65	
	vac	0.17		0.14		0.35	
OH	F	0.00		0.00		0.02	
	Cl	0.00		0.00		0.00	
	OH*	7.99		7.98		7.93	
Fe #		**0.65**		**0.55**		**0.40**	
T (°C) [c]		**396.52**		**273.01**		**281.65**	

[a] Chlorite host or host rock as determined from petrography, BRF = Bear River Formation, Apy = arsenopyrite
[b] Atomic proportions of elements in each crystallographic site (T= tetrahedral, O = octahedral, OH = OH site)
[c] Calculated using equation by Cathelineau (1988)

4.3.2 Geochronology

Apatite from NFDO sample GB-1 gabbro (**Figure 4-**) was selected for U-Pb analyses for geochronology. Sample GB-1 crosscuts Kentville Formation metasediments north of mineralized veins. Sample GB-1 exhibits primary lath-like plagioclase, anhedral augite, and apatite with accessory to trace cobaltite, titanite, pyrite, zircon, and baddeleyite (McNeil, 2019). Augite exhibits significant actinolite alteration with minor biotite and ilmenite alteration. There is no evidence of a significant fabric developed by metamorphic minerals. The results from 36 U-Pb measurements in apatite in this sample yielded an upper intercept age of 393 ± 11 Ma (MSWD = 3.1; **Figure 4-3**; **Table A3-4**).

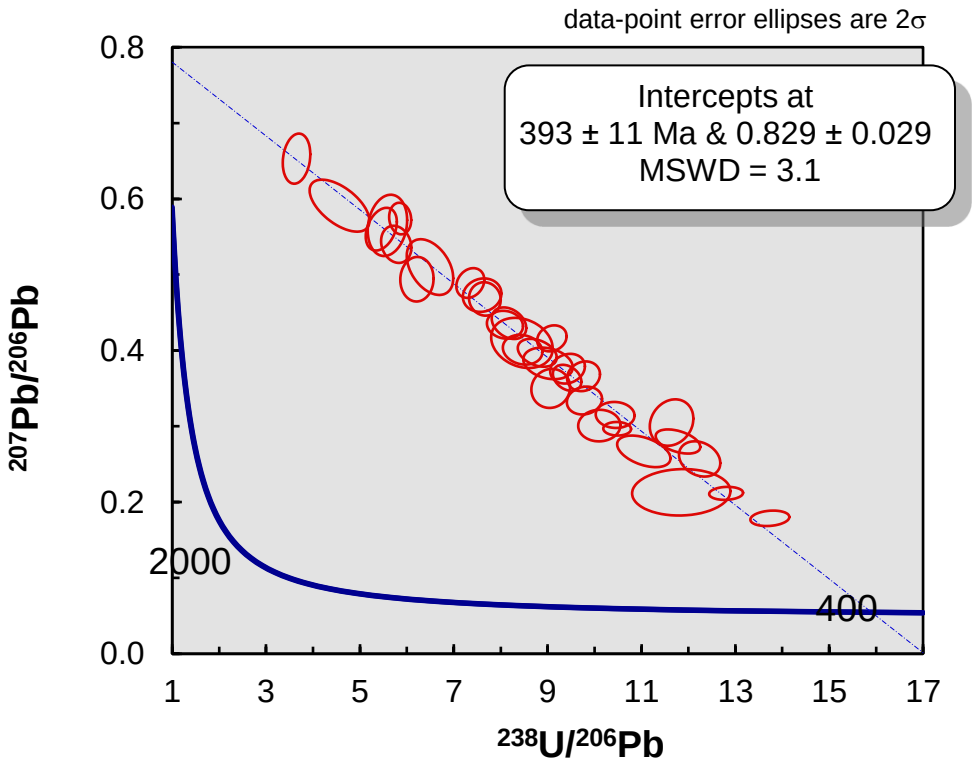

Figure 4-3 -Terra-Wasserberg plot of data collected from U-Pb analyses of sample GB-1, Nictaux Falls gabbro

4.4 Discussion

Based on chlorite associated with arsenopyrite mineralization at the NFDO, the temperature of chlorite formation is constrained to ~ 280 °C (**Table 4-1**). Chlorite at the NFDO is significantly more enriched in Mg when compared to chlorite compositions from Lansdowne and Cape St. Mary's (**Figure 4-4**). Temperatures associated with the Fe-As and Sb-Pb mineralization stages at Lansdowne are constrained to ~165 °C based on fluid inclusion isochores (**Figure 2-6C**). Type-1 chlorite from Cape St. Mary's, associated with barren quartz veining, exhibits very similar characteristics as type-1 chlorite associated with unmineralized veins at Lansdowne, including temperature (~ 390 °C), Fe # (~ 0.65), colour (both pale-green to colourless), habit (coarse grained radial aggregates), and interference colour (anomalous berlin blue). This overlap in similarities suggest that these chlorite types formed from similar hydrothermal processes. The chlorite at the NFDO, however, does not share any significant characteristics with type-1 chlorite at Lansdowne or Cape St. Mary's (**Figure 4-4**).

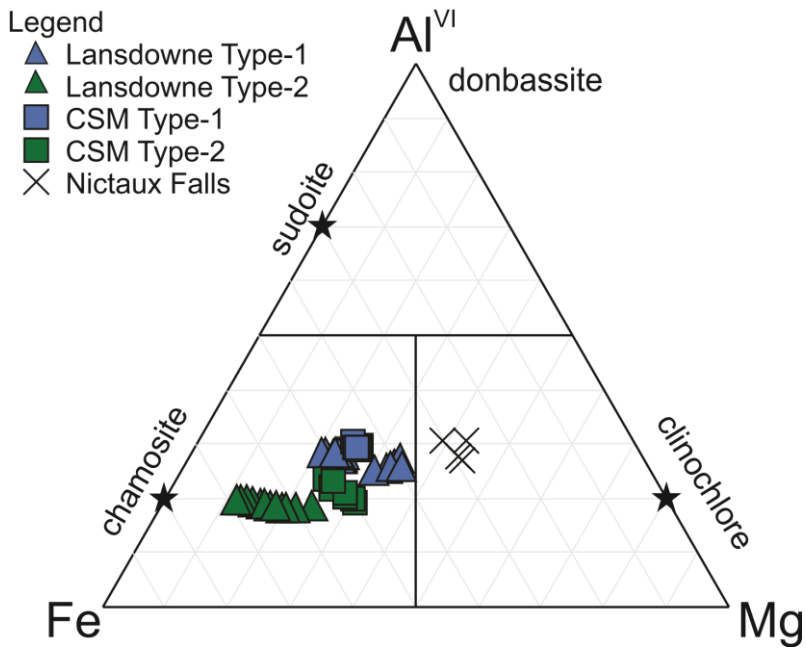

Figure 4-4 - Chlorite composition of chlorite types at Lansdowne, Cape St. Mary's and NFDO, based on proportion of Fe, Mg, and octahedral Al.

The age of the gabbro at the NFDO (393 ± 11 Ma) is just earlier than the timing of the onset of the emplacement of the South Mountain Batholith and related granitoid intrusions (~380-370 Ma; Benn et al., 1997; Shellnutt et al., 2019). Mafic to intermediate porphyritic intrusive bodies have been associated with large peraluminous plutons in the Meguma Terrane (Clarke et al., 1997). This association might explain the provenance of the NFDO gabbro and its proximal location to the Cloud Lake Monzogranite (**Figure 4-**). At Lansdowne and Cape St Mary's, mafic intrusions are related to a series of mafic sills which formed syn-depositionally to the Meguma Supergroup and Rockville Notch Group from the Cambrian to Silurian (White and Barr, 2004). These results confirm the interpretations from McNeil (2019) that mafic magmatism at Nictaux Falls occurred post metamorphism but pre-granitoid emplacement.

Sulfarsenides are the most abundant and significant sulfides at the NFDO. Most can be classified as either arsenopyrite or cobaltite. Sulfarsenides are also present at the Deerfoot Trail Sb occurrence at Cape St. Mary's, and at the Lansdowne occurrence. The mineral chemistry of these sulfarsenide species varies in terms of Co and Ni content, as shown in **Figure 4-5**. Compositional zoning is evident in the sulfarsenides from the NFDO and the Deerfoot Trail Sb occurrence and show a similar pattern of high Fe at the cores of grains, and high Co at the margins of grains. Arsenopyrite from the Deerfoot Trail Sb occurrence shows high Ni and Co forming, on average, in equal amounts, or with higher Ni concentrations along arsenopyrite grain margins, whereas at the NFDO, Ni is sparse and when present appears as another discreet zone which forms after Co mineralization, rather than forming coevally.

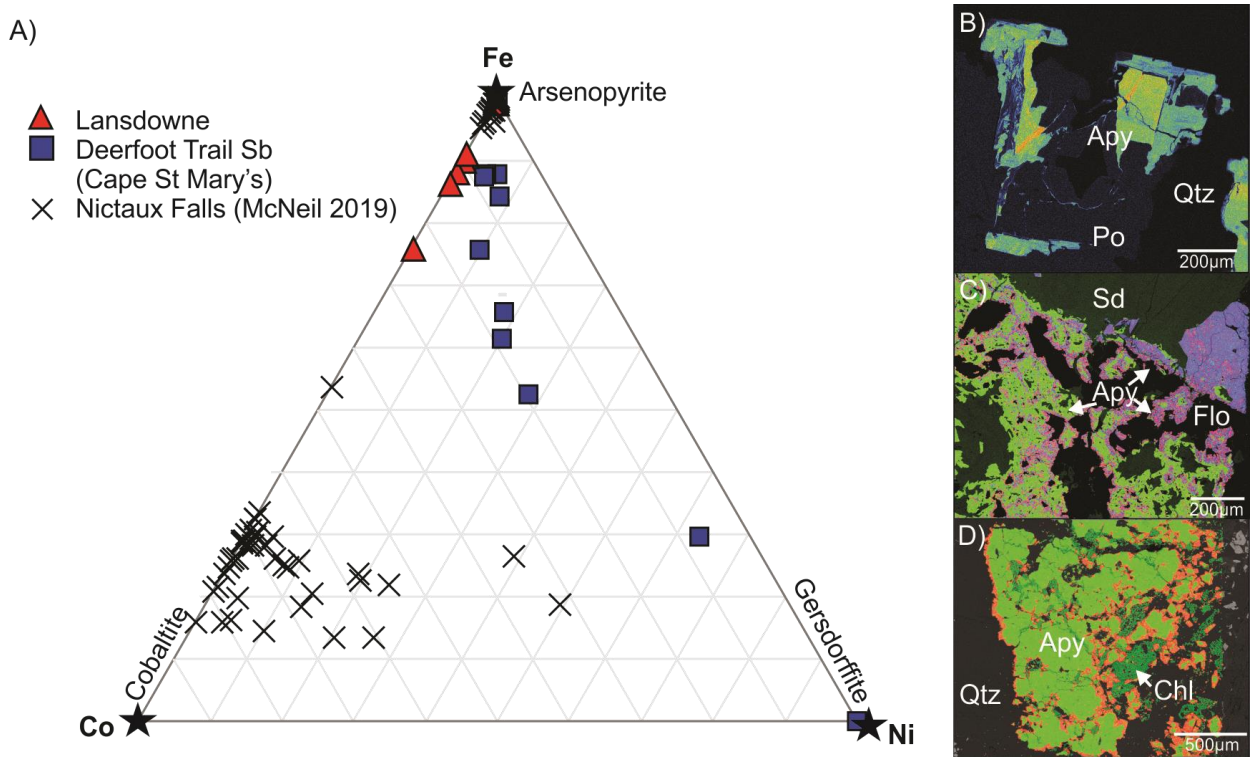

Figure 4-5 - A) Composition of sulfarsenides at the Lansdowne occurrence, the Deerfoot Trail Sb occurrence at Cape St. Mary's, and the NFDO (McNeil, 2019), based on the proportion of Fe, Co, and Ni. **B)** False colour EPMA elemental distribution map of Co content in a Co-rich grain of arsenopyrite at Lansdowne. Highest Co = orange, lowest Co = blue. **C)** False colour EDS elemental distribution map of arsenopyrite hosted in siderite at the Deerfoot Trail Sb occurrence. Fe = green, Co = red, Ni = blue. **D)** False colour EDS elemental distribution map of arsenopyrite hosted in quartz from Nictaux Falls. Fe = green, Co = orange.

The mineralogy of critical metal mineralization at the Lansdowne occurrence, Cape St. Mary's occurrences, and NFDO show few similarities. When simplified into major stages of important metal-bearing minerals, some overlap exists (**Figure 4-6**), specifically between sulfarsenides and native gold mineralization. As previously discussed, sulfarsenide species vary between occurrences in terms of chemistry and texture (**Figure 4-5**), however, Co and Ni mineralization always occurs paragenetically late along the outer margins of the arsenopyrite. Gold at the NFDO is similar to Cape St. Mary's as it forms interstitial to sulfide grains as small disseminated blebs (McNeil, 2019).

The simplified comparison of mineralizing stages at all three study areas indicates that all mineralization starts with an early arsenopyrite stage with associated Co-Ni mineralization. Early stage arsenopyrite at Lansdowne as well as abundant arsenopyrite associated with Meguma Au deposits throughout the Meguma Terrane are associated with mineralizing events triggered by Neoacadian deformation and emplacement of the South Mountain Batholith (**Chapter 2**; Morelli et al., 2005). It is possible that arsenopyrite at Cape St. Mary's and the NFDO are also related to this same period of mineralization. At Lansdowne and Cape St. Mary's, critical metal mineralization is associated with reactivation of Neoacadian structures by later deformational events; Mesozoic rifting and Carboniferous Alleghenian deformation, respectively. Since Co and Ni mineralizing fluids at the NFDO are associated with the marine brines of the Carboniferous Maritimes Basin (Kennedy, 2019; McNeil, 2019), I suggest that Carboniferous deformation from the Alleghenian orogeny, which reactivated the Cobequid-Chedabucto fault zone (**Figure 3-1**) and which I suggest as a trigger for REE and arsenopyrite mineralization at Cape St. Mary's (**Chapter 3**), may be responsible for the critical metal Co-Ni mineralization at Nictaux Falls. After the arsenopyrite-Co-Ni stage, all occurrences underwent different stages of reactivation of previous structures in different tectonic environments, which may account for the wide mineralogical varieties.

	Lansdowne	Cape St Mary's	Nictaux Falls
Early Fe-Pb			Py + Gn
Fe-As (±Co-Ni) Stage	Apy (± Co)	Apy (±Co-Ni)	Apy (±Co-Ni)
REE Stage		Flo + Mnz + Xtm	?
Zn-Cu Stage	Sp + Po + Cpy + Chl		
Pb-Sb Stage	Apy + Boul + Jm + Gn +Py	Boul + Jm + Gn + Ang + Py	
Cu-Sb-Bi Stage		Cstb → Tt (± Ag) + Bi-Stb	
Cu-Fe Stage		Cpy + Bi-Sb alloy	
Native Au stage		Au + Ag	Au + Ag

Figure 4-6 - Simplified comparison of major mineralizing stages at each of the occurrences involved in this project. Mineral abbreviations are consistent with definitions from results sections in Chapter 2, Chapter 3, and Chapter 4. Question mark (?) indicates that REE mineralization at the NFDO is not defined, but REE were detected via SEM analysis in very small anhedral grains interstitial to sulfarsenide mineralization.

4.5 Conclusion

Chlorite from the NFDO is of a significantly different composition, temperature, and habit then the chlorite which forms at Lansdowne or Cape St. Mary's. Although gabbroic rocks are associated with all three study areas, the gabbro at the NFDO is significantly younger in age (~ 45 Ma) then the sills associated with the Lansdowne and Cape St. Mary's occurrences, which are considered part of a series of mafic sills which formed syn-depositionally to Meguma Supergroup and Rockville Notch Group sediments.

Sulfarsenides are the link between the three study areas, and although their composition does vary, high Co and/or Ni hosted along the margins of arsenopyrite grains is present at Lansdowne, Cape St. Mary's, and the NFDO. Arsenopyrite mineralization is widespread across Meguma during the Neoacadian orogeny, and may have been responsible for arsenopyrite mineralization at Nictaux Falls. Reactivation of Neoacadian structures by later deformation (e.g., Alleghenian orogeny or Mesozoic rifting) is associated

with critical metal mineralization at Lansdowne and likely at Cape St. Mary's; therefore, post-Neoacadian orogeny deformation may responsible for the mineralization at the NFDO. Since mineralizing fluids are associated with the Carboniferous Maritimes Basin, Alleghenian deformation in the Carboniferous is the likely trigger of this mineralizing event. Not enough is known about timing at the NFDO to determine if any other stages of mineralization were contemporaneous with any stages at the other occurrences.

References

Benn, K., Pignotta, G. S., Evans, N. G., Horne, R. J., and Kontak, D. J., 1997, Syn-Acadian emplacement model for the South Mountain Batholith, Meguma Terrane, Nova Scotia: Magnetic fabric and structural analyses: GSA Bulletin, v. 109, p. 1279–1293.

Black, D. L., 1978, Uranium, Nictaux South, Annapolis County, Nova Scotia. Report on Geological Mapping, a Soil Geochemical Survey and a Ground Radiometric Survey; Assessment Report ME 21A/14A 54-A-21(01).:

Cathelineau, M., 1988, Cation site occupancy in chlorites and illites as a function of temperature: Clays and Clay Minerals, v. 23, p. 471–485.

Clarke, D. B., MacDonald, M. A., and Tate, M. C., 1997, Late Devonian mafic-felsic magmatism in the Meguma Zone, Nova Scotia, in Sinha, A. K., Whalen, J. B., and Hogan, J. P. eds., The Nature of Magmatism in the Appalachian Orogen: Boulder, Colorado, Geological Society of America Memoir.:

Jensen, L., 2012, Base Metals, Precious Metals, Nictaux South, Annapolis County, Nova Scotia. Drill Program, Nictaux Dam Area, Annapolis Co., N.S. Celtic Tiger Minerals Exploration Inc. NTS: 21A14A [Exploration Licence 09068].:

Jowett, E. C., 1991, Fitting Iron and Magnesium into the Hydrothermal Chlorite Geothermometer: SSRN Electronic Journal.

Kennedy, N., 2019, Fluid inclusion systematics of the polymetallic (Co-Ni-As-Au ± Bi, Ag) veins of the Nictaux Falls Dam Occurrence, Annapolis Valley, Nova Scotia: Saint Mary's University.

Kranidiotis, P., and MacLean, W. H., 1987, Systematics of chlorite alteration at the Phelps Dodge massive sulfide deposit, Matagami, Quebec: Economic Geology, v. 82, p. 1898–1911.

Kissin, S. A., 1992, Five Element (Ni-Co-As-Ag-Bi) Veins: Geoscience Canada, v. 19, p. 113–124.

McGregor, M., McFarlane, C. R. M., and Spray, J. G., 2018, In situ LA-ICP-MS apatite and zircon U–Pb geochronology of the Nicholson Lake impact structure, Canada: Shock and related thermal effects: Earth and Planetary Science Letters, v. 504, p. 185–197.

McNeil, N. C., 2019, The mineralogy, petrography, and paragenesis of the polymetallic (Co-Ni-As-Au) veins of the Nictaux Falls Dam Occurrence, Annapolis Valley, Nova Scotia: Saint Mary's University: 98 p.

Morelli, R. M., Creaser, R. A., Selby, D., Kontak, D. J., and Horne, R. J., 2005, Rhenium-osmium geochronology of arsenopyrite in Meguma group gold deposits, Meguma terrane, Nova Scotia, Canada: Evidence for multiple gold-mineralizing events: Economic Geology, v. 100, p. 1229–1242.

O'Reilly, G. A., 1998, Geological Overview of the Nictaux Falls Dam Co-Ni-As-Au Prospect, Annapolis County, N.S.: Nova Scotia Department of Natural Resources

Van Oirschot, M. L., 1994, Gold, Cobalt, Nictaux South, Annapolis County, Nova Scotia. Report on Prospecting, and Rock and Soil Geochemical Surveys [Nictaux Dam Prospect Area, Report on Investigation Under NSPAP Program]: Assessment Report ME 1995-007.:

Shellnutt, J. G., Owen, J. V., Yeh, M. W., Dostal, J., and Nguyen, D. T., 2019, Long-lived association between Avalonia and the Meguma terrane deduced from zircon geochronology of metasedimentary granulites: Scientific Reports, v. 9, p. 1–11.

Smith, D. G. W., 1969, Pyrometamorphism of phyllites by a dolerite plug: Journal of Petrology, v. 10, p. 20–55.

Thomson, S. N., Gehrels, G. E., Ruiz, J., and Buchwaldt, R., 2012, Routine low-damage apatite U-Pb dating using laser ablation-multicollector- ICPMS: Geochemistry, Geophysics, Geosystems, v. 13, p. 1–23.

Vermeesch, P., 2018, IsoplotR: A free and open toolbox for geochronology: Geoscience Frontiers, v. 9, p. 1479–1493.

White, C. E., and Barr, S. M., 2004, Age and Petrochemistry of Mafic Sills in Rocks of the Northwestern Margin of the Meguma Terrane , Bear River - Yarmouth Area of Southwestern Nova Scotia: Mineral Resources Branch, Report of Activities 2003; Nova Scotia Department of Natural Resources, p. 97–117.

Chapter 5: Summary of conclusions and suggestions for future work

5.1 Key conclusions from Chapter 2

i. Two distinct generations of mineralization exist at the Lansdowne occurrence, defined by Re-Os geochronology of arsenopyrite: (i) an early-stage associated with the waning stage of the Neoacadian orogeny at 365 ± 4.8 Ma, and (ii) a late-stage composed of critical metal mineralization which formed at ~ 214 Ma, contemporaneous with the rifting of the Bay of Fundy and deposition of the Blomidon Formation. Rifting of the Bay of Fundy is associated with the breakup of Pangea and a period of significant extensional tectonics and mantle upwelling.

ii. Based on temperatures recorded from chlorite thermometry and fluid inclusion isochores of late-stage mineralizing fluids, critical metal mineralization experienced drastic cooling between the Fe-Zn-Cu stage at ~ 360 °C and the deposition of the Sb-Pb mineralizing stage at ~ 165 °C occurred under epithermal conditions.

iii. Oxidizing fluids which likely interacted with evaporites locally dissolved pre-existing sulfides (up to 30%) and mingled with methane along ore hosting structures, creating a reducing environment where critical-metal bearing sulfides could precipitate.

iv. Critical metal mineralization is reminiscent of late-orogenic epithermal Sb-Au polymetallic mineralization in the European Variscan Belt, which formed from brittle extensional tectonics and record drastic cooling. Mineralization at Lansdowne is an analogue for this mineralization style in Nova Scotia.

v. Vectors for further exploration of this style of mineralization in Nova Scotia include: i) reasonable proximity to the Fundy rift basin, west of the South Mountain Batholith, ii) association with altered mafic sills found north of the CPSZ in Meguma Supergroup metasediments, and iii) pervasive local carbonate and chlorite alteration of host rocks, including mafic sills and host metasediments.

5.2 Key conclusions from Chapter 3

i. The Cape St. Mary's occurrences exhibit a diverse assemblage of critical metal minerals but show little mineralogical, chemical, or petrographical overlap between occurrences. Their spatial concentration in this region may be related to reactivated Devonian structures. Antimony, REE, and Au mineralization exist across multiple occurrences, suggesting there may have been multiple mineralizing events.

ii. The REE mineralization observed at Cape St Mary's is likely associated with reactivation of the Cape St. Mary's shear zone at 320 Ma, triggered by Alleghenian deformation and transpressional movement along the Cobequid-Chedabucto fault zone at the northern contact of the Meguma Terrane with the Avalon Terrane. This period of deformation is associated with REE-rich IOCG-style mineralization at 320 Ma in the Cobequid Highlands.

iii. At the Deerfoot Trail Sb occurrence, the dissolution of siderite by metal bearing fluids at the Deerfoot Trail fault caused the transition from Sb-Cu mineral chalcostibite to form tetrahedrite and Bi-rich stibnite, and then formed chalcopyrite and native Sb-Bi.

iv. Antimony mineralization at the Mavillette Beach occurrence is reminiscent of the Sb-Pb mineralization stage observed at the Lansdowne occurrence; however, the exact relationship between these occurrences is unknown. The Sb mineral species at the Mavillette Beach occurrence are vastly different than the Sb mineral species than at the Deerfoot Trail Sb occurrence, however considering the rarity of this metal in the Meguma Terrane, it is possible that they were sourced from similar Sb sources under different mineralizing conditions.

5.3 Key conclusions from Chapter 4

i. Chemistry of chlorite discovered at the Lansdowne and Cape St. Mary's study area, and NFDO, show little similarities in composition, habit, colour, or temperature. The timing of the

intrusion of gabbro at the NFDO also distinguishes it from the mafic sills observed at Lansdowne and Cape St. Mary's.

ii. Since critical metal mineralization at Lansdowne and Cape St. Mary's is associated with reactivation of Neoacadian structures by later deformation, the Co-Ni mineralization associated with arsenopyrite at the NFDO may be related to Carboniferous deformation from the Alleghenian orogeny. This is supported by the fact that mineralizing fluids were determined to be sourced from the Carboniferous Maritimes Basin in previous work.

5.4 Suggestions for future work

Additional work is needed to improve the current understanding of these occurrences and their place in the global framework of critical metal deposits, as well as provide tools to accurately search for more critical metal sources in Nova Scotia. Of the occurrences discussed in this project, further constraints on timing of mineralization are needed to give proper geological context, such as Re-Os geochronology of arsenopyrite, which is present at Cape St. Mary's and Nictaux Falls occurrences, in addition to Lansdowne. Since host metasediments and mafic sills were determined as the source of metals at the Lansdowne and Nictaux Falls occurrences, a more detailed comparative host rock analysis should be conducted to better understand metal concentration and distribution in these host rocks. Carbon isotope systematics of carbonate rocks can provide insight into carbon sources and help in determining mantle derivation for mineralizing fluids. The saline brine which interacted with methane can be further characterized by Cl-Br anion isotope analyses, in order to better constrain fluid source.

Structural features in the western Meguma Terrane are not well constrained, primarily due to lack of outcrop. Further structural field work, including possible geophysical approaches, may provide new understanding of structures related to mineralization, and how reactivation of pre-existing faults may have contributed to mineralizing fluids, as determined for REE mineralization at Cape St. Mary's. A clearer

picture of the effect major tectonic events in the region have had on small scale localized structural features is necessary to understand how these occurrences may have formed.

Since the West Gore Sb-Au deposit shares many overlapping characteristics with the Lansdowne occurrence, a re-examination of this deposit would be useful in proving that this Sb-bearing mineralization style does exist across the Meguma Terrane, and that there is the possibility for more to be found. Geochronology of sulfides (e.g., via Re-Os geochronology of pyrite) would help to provide an absolute time for mineralizing events.

Across nearly all the occurrences studied for this project, proxies for mineralization have been found in the European Variscan belt of western Europe. Drawing parallels between these deposits has allowed for a better understanding of the mechanisms for mineralization which formed the polymetallic occurrences of the Meguma Terrane. More research is needed to understand the nature of the connection between the polymetallic deposits of the European Variscan belt and those found in Nova Scotia. Understanding this relationship may provide better tools for the continued exploration of deposit scale critical metal sources in the Meguma Terrane, as have been discovered in Europe. The deposits of the Meguma Terrane and those of the European Variscan Belt may represent mirrored processes from the formation and breakup of Pangea, connecting these terranes which now find themselves thousands of kilometers apart.

Appendix I

Data related to Chapter 2: Late-Triassic hydrothermal polymetallic Sb-Pb-As-Zn veins, Meguma Terrane, Canadian Appalachian Orogen; a new critical metal deposit type in Nova Scotia

Table A1-1 - Sample List and locations, context for sample collection, mineralization, and analyses conducted

Sample ID	year/ month collected	Easting/ Northing	Core ID[b]	Depth (m)	Host rock[c]	Veining	Mineralization	Context for collection	Analyses[d]
7157[a]	1989	283452/ 4939434			BRF	Qtz	Apy-Jm-Boul-Py-Gn	Eu. Apy-2	Pet, SEM, Re-Os, EPMA, FI, SI
LAN2-1	Sep/19		LAN92-2	61.77	BRF			Representative barren vein	Pet, SEM
LAN2-2	Sep/19		LAN92-2	76.63	BRF-MS	Qtz-Cal	Sp-Po-Apy-Jm-Boul-Gn-Py	Representative Sp-Po and Sb-Pb sulfosalt mineralization	Pet, SEM, EPMA, SI
LAN2-3	Sep/19		LAN92-2	82.45	BRF-MS	Qtz-Cal	Apy	Massive Apy-1	Pet, SEM, Re-Os, EPMA, FI, SI
LAN2-5	Sep/19		LAN92-2	121.36	MS			Representative barren mafic sill	Pet, SEM
LAN3-2	Sep/19		LAN92-3	59.84	BRF	Qtz-Cal	Py	Post-ore stage pyrite	Pet, SEM, EPMA, SI
LAN4-2	Sep/19		LAN92-4	69.19	BRF-MS	Qtz-Cal	Sp-Po-Jm-Boul-Gn-Py	Representative Sp-Po and Sb-Pb sulfosalt mineralization	Pet, SEM, U-Pb, EPMA, FI, SI
LAN4-3	Sep/19		LAN92-4	74.06	MS			Representative barren mafic sill	Pet, SEM, U-Pb
LAN2-10	Aug/20		LAN92-2	72.24	MS	Qtz		Barren veins in gabbro	WRG
LAN2-11	Aug/20		LAN92-2	76.8	MS	Qtz-Cal	Sp-Po-Jm	Mineralized vein in gabbro	WRG
LAN2-12	Aug/20		LAN92-2	82.3	BRF-MS	Qtz-Cal	Apy	Apy mineralization	WRG
LAN2-13	Aug/20		LAN92-2	49.4	BRF	Qtz-Cal		Barren vein in metasediments	WRG
LAN2-14	Aug/20		LAN92-2	79.55	MS			Representative altered gabbro	WRG
LAN2-15	Aug/20		LAN92-2	88.3	MS			Representative unaltered gabbro	WRG
LAN2-16	Aug/20		LAN92-2	55.8	BRF			Representative unaltered metasediments, no veins	WRG
LAN2-17	Aug/20		LAN92-2	4.8	BRF			Representative altered sediments	WRG
LAN2-18	Aug/20		LAN92-2	134.7	MS			Silica flooded gabbro	WRG
LAN2-19	Aug/20		LAN92-2	75.9	BRF	Qtz		Qtz veins	WRG
LAN2-20	Aug/20		LAN92-2		BRF		Minor Py	Pyrite in sandy metasediments laminations	WRG

[a] Sample collected by O'Reilly, 1989. Month unknown. Grab sample from surface.
[b] Core ID as indicated in Figure 1 inset map
[c] BRF = Bear River Formation, MS = gabbroic mafic sill
[d] Pet = petrography, SEM = scanning electron microscopy (including EDS and/or BSE), Re-Os = Re-Os geochronology via mass spectrometry, U-Pb = U-Pb geochronology of apatite via LA-ICP-MS, EPMA = electron probe microanalysis of chlorite, FI = fluid inclusion analysis, SI = sulfur isotope analysis via SIMS, WRG = Whole rock geochemical analysis

Table A1-2 - SEM data of sulfides in mineralized Lansdowne samples. All data in wt.%

	S	Fe	Cu	Zn	Cd	Sb	Pb	As	Co
7157									
Arsenopyrite	20.37	29.98						49.65	
	19.89	28.96						49.94	
	21.08	29.93						48.71	
	20.72	30.57						48.7	
	20.78	29.37						49.54	
	20.99	28.41						50.61	
Jamesonite	22.05	2.46				35.3	35.48		
	18.66	2.49				36.97	38.68		
	18.94	2.42				36.6	38.64		
	19.42	2.4				36.7	38.35		
	19.28	2.26				36.81	38.77		
	18.06	2.34				34.94	38.34		
	19.26	2.41				36.94	39.31		
	19.61	2.35				37.67	40.37		
	19.78	2.07				37.94	40.21		
	19.78	2.26				37.94	40.01		
	20.05	2.3				38.46	39.19		
	20.02	2.24				38.17	39.58		
	19.91	3.03				37.5	39.56		
	20.12	2.08				38.44	39.36		
	19.43	2.35				37.08	39.65		
Boulangerite	17.06					28.79	54.15		
	17.01					27.84	55.14		
	17.35					28.27	54.38		
	17.26					27.34	55.4		
	20.56					26.91	52.53		
Pyrite	56.75	43.25							
	56.82	43.18							
	55.2	43.86							
Galena	15.61						84.39		
	15.32						84.68		
	15.33						84.67		
	12.24	0.81					86.95		
Sphalerite	37.34			61.38	1.28				
	36.38			62.32		1.3			
LAN2-2									
Sphalerite	32.23	5.33		60.29	2.14				
	32.55	6.25		58.71	2.49				
	33.14	17.33		48.08	1.45				
	31.95	7.17		58.23	2.65				
	38.15	4.66		54.73	2.46				
	38.49	7.05		51.22	3.25				
	38.85	6.39		52.37	2.4				
	39.05	6.02		52.35	2.57				
	38.58	5.08		52.92	3.06				
Pyrrhotite	46.53	51.99		1.48					
	46.38	52		1.63					
	46.71	52.45		0.83					
	39.79	60.21							
	40.19	59.81							
	40.34	59.66							
	39.68	58.98		1.35					
	39.59	59.08		1.33					
	39.99	58.19		1.82					
	40.24	59.76							
	39.82	58.69		1.49					
	39.5	59.01		1.5					
	39.92	58.76		1.32					
Boulangerite	18.97		0.88			20.66	55.11		
	20.59					27.64	51.77		
	19.03					27.93	53.05		
	16.63			1.1		28.13	54.13		
	16.93			1.42		28.11	53.54		
	16.86					28.5	54.64		

	17.12					28.91	53.97		
	16.03		1.26	1.04		22.1	59.57		
	15.81		1.01	1.39		22.77	59.03		
	20.2					27.92	51.88		
Galena	11.95						88.05		
	14.82						85.18		
Pyrite	55.4	44.6							
	55.61	44.39							
	60.38	39.62							
	60.05	39.95							
LAN2-3									
Arsenopyrite	23.66	29.53						46.81	
	23.31	29.34						47.35	
	23.31	29.08						47.61	
	24.39	28.81						46.8	
LAN3-2									
Pyrite	53.99	46.01							
	53.99	46.01							
	53.79	46.21							
	54.02	45.98							
	54.06	45.75							
	53.83	46.17							
	53.7	46.3							
	53.9	46.1							
	53.8	46.2							
	54.06	45.94							
	53.77	46.23							
	53.87	46.13							
	54.02	45.98							
	53.56	45.66							
LAN4-2									
Sphalerite	31.75	7		58.93	2.32				
	31.66	7.67		58.33	2.34				
	31.97	6.87		59	2.16				
	32.04	7.17		58.4	2.4				
	32	7.01		57.54	3.45				
	32.23	6.46		57.33	3.98				
	32.18	7.56		57.09	3.17				
	31.75	8.35		56.96	2.93				
	31.73	8.66		56.73	2.87				
	39.76	6.26		48.53	3.57				
Pyrrhotite	40.54	59.46							
	40.27	59.73							
	39.3	60.7							
	40.11	59.89							
	40.54	59.46							
	40.68	59.32							
	40.84	59.16							
	39.89	60.11							
	39.95	60.05							
Chalcopyrite	40.19	27.07	29.25					3.5	
	42.76	26.47	30.76						
Arsenopyrite	22.91	22.67						47.5	6.92
	23.62	28.7						47.68	
	23.48	25.73						48.39	2.4
	24.11	28.27						47.63	
	24.37	27.73						47.9	
	23.96	27.89						48.15	
	23.55	25.34						48.52	2.59
	24.34	27.77						47.88	
	23.38	24.68						48.85	3.09
	22.99	24.2						48.09	3.71
	23.98	25.2				1.07		49.75	
	23.32	26.99				1.64		48.05	
	24.26	27.48						48.27	
	26.71	26.71						46.58	
	24.26	27.33						48.41	

	23.61	24.92				48.28	2.29
Jamesonite	20.1	2.4		38.7	38.8		
	19.52	4.58		36.98	38.91		
	23.6	2.22		36.36	37.81		
Boulangerite	17.44			28.37	54.2		
	17.17			28.83	54		
	17.64			28.42	53.95		
Galena	12.65				87.35		
	13.55	0.62		6.2	79.64		
	12.55				87.45		
	12.41		2.9		84.69		
	12.14	1.19			86.67		
	12.15				87.85		

Figure A1-1 - Discordia diagram for U-Pb geochronology of apatite in sample LAN4-3

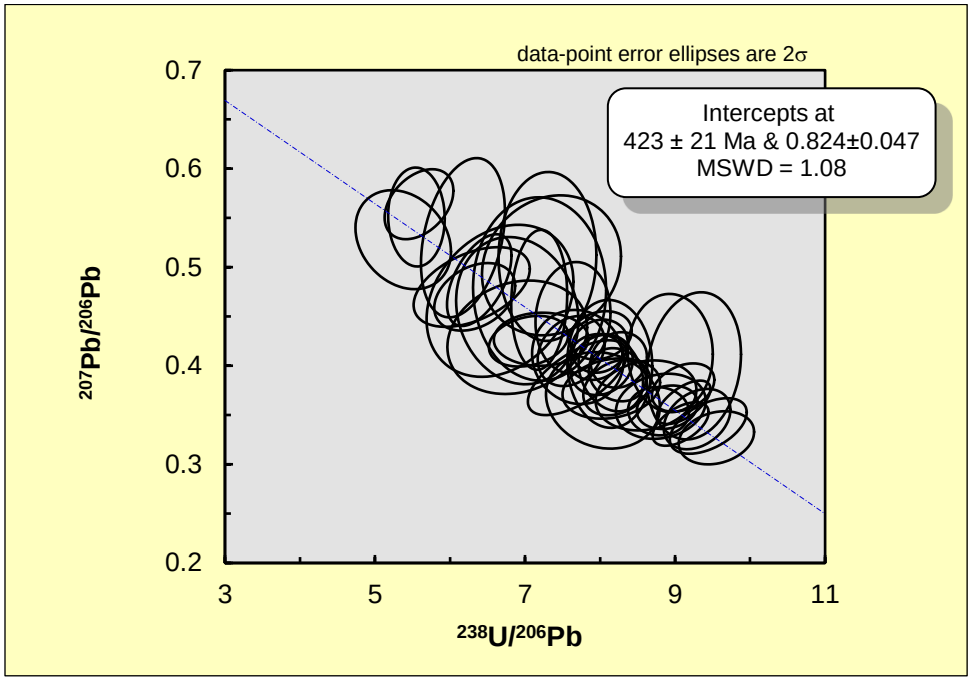

Figure A1-2 - Discordia diagram for U-Pb geochronology of apatite in sample LAN4-2

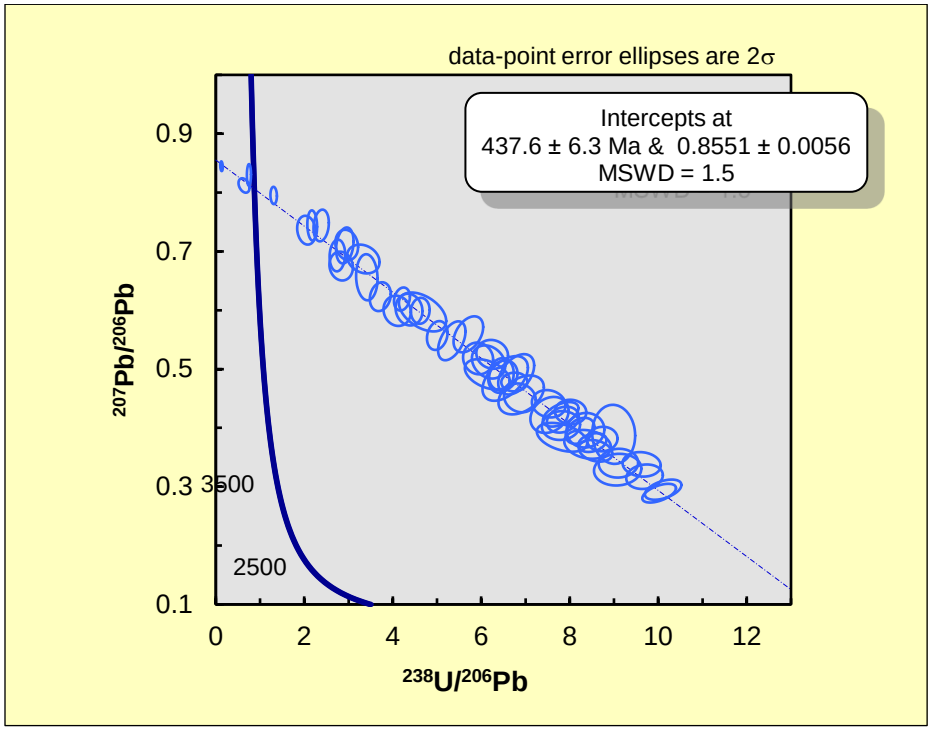

Figure A1-3 - Discordia diagram for U-Pb geochronology of apatite standard Phalaborwa apatite

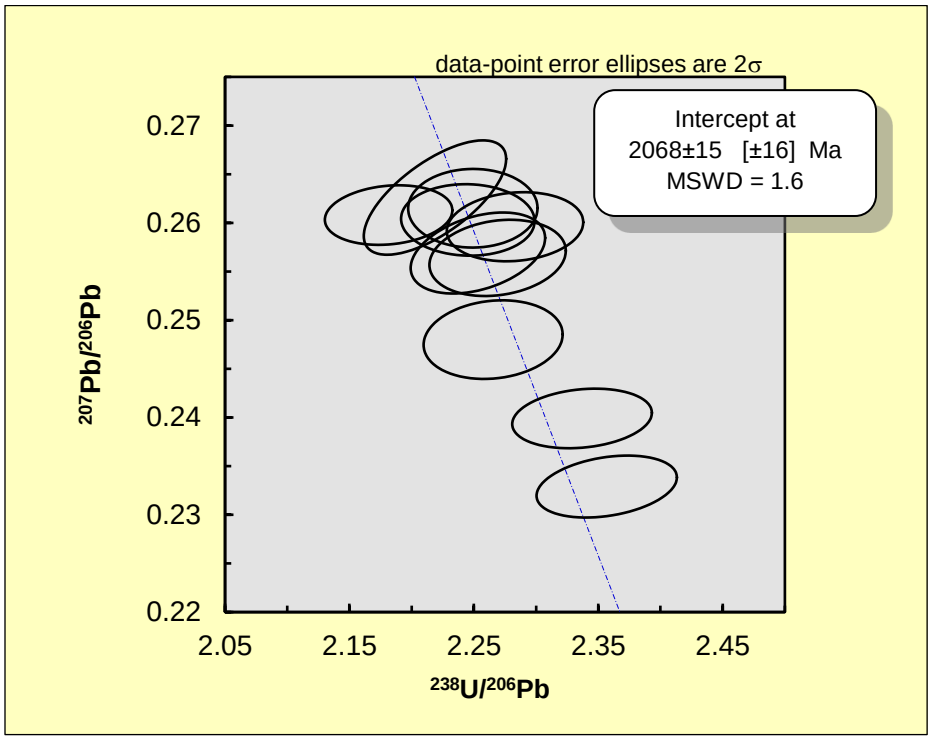

Table A1-3 - U-Pb analyses of apatite in mafic sill samples from Lansdowne

Comments	Pb ppm 204	Pb ppm 206	Final 207_235	Final 207_235 Prop2SE	Final 206_238	Final 206_238 Prop2SE	Error Correlation 6_38 vs 7_35	Final 238_206	Final 238_206 Prop2SE	Final 207_206	Final 207_206 Prop2SE	Error Correlation 38_6 vs 7_6	Age Final 206_238	Age Final 206_238 Prop2SE	Age Final 207_235	Age Final 207_235 Prop2SE	Age Final 208_232	Age Final 208_232 Prop2SE
LAN4-3 - 27	1.96	1.141	6.52	0.7	0.1122	0.0051	0.22187	8.912656	0.4051207	0.433	0.048	0.08926	685	29	1965	75	839	67
LAN4-3 - 52	1.98	0.925	5.9	0.57	0.1068	0.0049	0.093641	9.363296	0.4295894	0.396	0.04	0.17013	647	25	1876	69	734	37
LAN4-3 - 33	1.88	0.948	6.7	1.1	0.1119	0.0058	0.061747	8.93655	0.4631992	0.413	0.049	-0.018528	682	33	1949	78	805	78
LAN4-3 - 45	1.8	1.069	5.61	0.25	0.1098	0.0041	0.3527	9.107468	0.3400785	0.378	0.02	0.32237	671	24	1914	36	783	34
LAN4-3 - 35	2.34	1.118	9.3	1.3	0.137	0.01	0.19473	7.29927	0.5327934	0.511	0.07	0.01658	808	51	2240	100	1017	94
LAN4-3 - 15	2.77	1.78	7.45	0.44	0.1249	0.0053	0.35232	8.006405	0.3397434	0.431	0.02	0.18217	757	30	2151	53	982	51
LAN4-3 - 36	2.03	0.976	6.21	0.84	0.1081	0.006	0.015279	9.250694	0.513452	0.4	0.061	0.15537	660	34	1868	67	759	43
LAN4-3 - 22	2.42	1.07	9.8	1.6	0.136	0.014	0.36581	7.352941	0.7569204	0.502	0.058	0.12851	813	71	2232	92	1020	80
LAN4-3 - 10	3.16	1.84	14.59	0.96	0.179	0.012	0.67536	5.586592	0.3745201	0.564	0.029	0.3832	1062	67	2776	64	1510	120
LAN4-3 - 4	2.16	1.164	5.42	0.19	0.1097	0.0035	0.019458	9.11577	0.2908404	0.363	0.018	0.61413	670	21	1882	30	793	33
LAN4-3 - 48	3.21	2.42	7.56	0.6	0.1251	0.0048	0.029542	7.993605	0.3067091	0.42	0.022	0.12906	759	27	2126	57	909	49
LAN4-3 - 29	2.25	1.418	7.77	0.72	0.1309	0.007	0.023964	7.639419	0.4085251	0.449	0.046	0.084978	783	36	2146	73	928	62
LAN4-3 - 5	3.37	1.641	6.8	0.36	0.1212	0.0045	0.089505	8.250825	0.3063425	0.406	0.023	0.10257	737	26	2063	46	880	41
LAN4-3 - 51	2.43	1.19	9.1	1.8	0.139	0.014	0.14554	7.194245	0.7246002	0.478	0.076	-0.014605	814	63	2123	99	809	47
LAN4-3 - 17	3.89	1.53	11.5	1.3	0.162	0.012	0.045614	6.17284	0.4572474	0.53	0.066	0.32561	963	63	2442	72	1098	91
LAN4-3 - 20	5.56	2.049	14.2	1.6	0.1801	0.01	0.28293	5.552471	0.3082993	0.551	0.041	-0.02901	1063	54	2648	57	1416	85
LAN4-3 - 59	2.68	1.451	9.2	1.2	0.1391	0.0059	0.040165	7.189073	0.3049283	0.467	0.058	0.070686	838	33	2236	66	1016	64
LAN4-3 - 6	1.99	1.156	4.96	0.28	0.1059	0.0047	0.34524	9.442871	0.4190887	0.339	0.023	0.49006	648	28	1816	43	786	37
LAN4-3 - 28	1.84	0.981	5.08	0.31	0.1076	0.0042	0.065337	9.29368	0.3627645	0.346	0.025	0.31065	658	24	1807	50	741	32
LAN4-3 - 19	2.52	0.939	4.76	0.29	0.1047	0.0045	-0.055152	9.551098	0.4105057	0.327	0.022	0.22065	641	26	1752	48	698	32
LAN4-3 - 34	2	0.968	7.7	1.6	0.123	0.007	0.11479	8.130081	0.4626876	0.402	0.053	-0.031957	746	40	1959	77	876	77
LAN4-3 - 41	2.09	1.049	5.54	0.26	0.1124	0.0042	0.030998	8.896797	0.3324426	0.358	0.018	0.16902	686	24	1889	41	742	35
LAN4-3 - 58	1.6	0.983	7.17	0.4	0.126	0.0047	0.48566	7.936508	0.2960443	0.409	0.019	0.12767	764	27	2106	49	899	45
LAN4-3 - 8	1.97	1.001	5.82	0.46	0.1161	0.0074	0.68991	8.613264	0.5489936	0.37	0.029	0.15949	707	43	1931	67	1170	850
LAN4-3 - 55	1.71	1.124	5.51	0.4	0.1135	0.0063	0.46867	8.810573	0.4890445	0.359	0.027	0.15844	691	36	1866	57	835	72
LAN4-3 - 40	2.88	1.183	10.55	0.68	0.1565	0.0086	0.20294	6.389776	0.3511315	0.487	0.038	0.53245	936	48	2467	61	1002	67
LAN4-3 - 49	2.62	1.234	6.59	0.47	0.1215	0.0046	0.6827	8.230453	0.3116056	0.391	0.022	-0.16019	738	26	2002	56	802	36
LAN4-3 - 2	2.28	0.962	6.91	0.48	0.1247	0.0053	0.34859	8.019246	0.3408034	0.401	0.025	0.1641	756	30	2064	59	832	38
LAN4-3 - 53	2.03	1.12	8.3	0.77	0.15	0.018	-0.032607	6.666667	0.8	0.466	0.063	0.2486	884	89	2187	57	957	66
LAN4-3 - 46	3.44	1.98	8.9	1.3	0.145	0.014	0.12782	6.896552	0.6658674	0.456	0.061	-0.13423	864	74	2162	95	938	74
LAN4-3 - 21	3.3	1.509	6.72	0.62	0.1228	0.0053	0.51307	8.143322	0.3514626	0.393	0.032	-0.2376	746	30	2025	65	849	41
LAN4-3 - 60	1.84	1.017	5.07	0.23	0.1102	0.0037	0.16199	9.07441	0.3046762	0.341	0.018	0.54076	674	22	1839	37	772	36
LAN4-3 - 30	3.56	2.29	7.8	1.3	0.1298	0.0084	0.19196	7.70416	0.4985743	0.409	0.039	-0.06734	784	47	2044	73	831	44
LAN4-3 - 56	2.13	1.014	7.61	0.55	0.1313	0.0063	0.33859	7.616146	0.3654358	0.415	0.029	0.24048	793	35	2155	60	895	49
LAN4-3 - 31	2.42	1.3	9.65	0.72	0.159	0.016	0.26911	6.289308	0.6328864	0.48	0.033	0.45297	939	83	2370	69	994	54
LAN4-3 - 42	2.33	2.02	5.38	0.37	0.1139	0.0043	0.46452	8.779631	0.3314523	0.354	0.02	-0.048763	694	25	1857	57	733	50

LAN4-3-25	3.59	1.82	13.4	2.2	0.186	0.018	0.95329	5.376344	0.5202914	0.528	0.041	-0.23958	1064	76	2550	120	1410	200
LAN4-3-57	1.68	0.971	6.25	0.4	0.1216	0.0054	0.26582	8.223684	0.3651965	0.378	0.023	0.26611	738	31	1980	51	844	41
LAN4-3-16	2.21	1.049	6.41	0.53	0.1227	0.008	0.18057	8.149959	0.5313747	0.377	0.025	0.1974	743	44	1980	55	766	40
LAN4-3-37	3.24	1.47	8.4	1.2	0.145	0.016	0.22176	6.896552	0.7609988	0.429	0.047	0.17238	839	72	2152	82	929	77
LAN4-3-9	2.26	1.81	8.13	0.65	0.1386	0.0099	0.26299	7.215007	0.5153577	0.427	0.022	0.02282	834	55	2208	55	912	47
LAN4-3-1	2.99	1.48	10.1	0.69	0.158	0.011	0.084856	6.329114	0.4406345	0.47	0.028	0.32387	924	52	2403	62	1071	68
LAN4-3-24	3.07	2.04	6.69	0.38	0.1299	0.0091	0.090747	7.698229	0.5392909	0.388	0.031	0.6405	785	50	2068	48	957	65
LAN4-3-39	3.71	2.82	7.1	1.6	0.1244	0.0096	0.42634	8.038585	0.620341	0.365	0.04	-0.12992	751	52	1895	68	794	48
LAN4-3-18	2.64	1.337	8.15	0.52	0.1419	0.0087	0.82978	7.047216	0.4320703	0.425	0.021	0.24436	852	48	2216	54	1029	56
LAN4-3-23	2.14	1.092	5.09	0.47	0.1119	0.0061	0.34025	8.93655	0.4871578	0.316	0.024	0.14134	682	35	1774	63	668	36
LAN4-3-43	1.89	1.366	5.65	0.26	0.1186	0.004	0.11837	8.431703	0.2843745	0.343	0.018	0.40141	722	23	1907	39	864	36
LAN4-2-43	1.5	1.46	6.42	0.28	0.1145	0.0039	0.25452	8.733624	0.2974772	0.409	0.02	0.28228	699	23	2031	38	697	36
LAN4-2-27	3.43	3.35	32.4	3.3	0.332	0.03	0.93679	3.012048	0.272173	0.724	0.023	-0.12928	1830	140	3560	100	2680	240
LAN4-2-58	1.26	1.064	4.53	0.27	0.0982	0.0038	0.17572	10.1833	0.3940584	0.335	0.021	0.39126	606	23	1732	46	828	43
LAN4-2-47	22.9	13.59	151.3	7.4	1.336	0.068	0.93772	0.748503	0.03809746	0.83	0.015	0.032546	5450	190	5093	49	10400	490
LAN4-2-16	7.77	7.54	82.5	3.8	0.765	0.035	0.94403	1.30719	0.05980606	0.795	0.012	-0.061929	3640	130	4492	48	5330	250
LAN4-2-18	9.5	8.7	32.8	2.7	0.338	0.024	0.79267	2.95858	0.2100767	0.711	0.021	-0.13943	1860	120	3542	85	2140	120
LAN4-2-33	1.4	1.462	7.27	0.31	0.1247	0.0045	0.87039	8.019246	0.2893874	0.427	0.017	-0.031952	757	26	2131	37	957	44
LAN4-2-55	1.57	1.259	4.95	0.32	0.1039	0.0038	0.34712	9.624639	0.352008	0.338	0.017	-0.096128	637	22	1773	50	755	36
LAN4-2-3	8.2	7.42	42.7	3.1	0.42	0.025	0.72594	2.380952	0.1417234	0.744	0.022	0.16686	2250	110	3830	73	3200	240
LAN4-2-21	2	1.452	6.18	0.88	0.1112	0.0049	0.32412	8.992806	0.3962657	0.389	0.041	-0.04249	683	27	1914	83	818	53
LAN4-2-34	2.1	1.87	11.71	0.67	0.1601	0.0075	0.89725	6.246096	0.2926029	0.525	0.02	-0.083971	956	42	2562	50	1278	65
LAN4-2-62	4.15	2.93	29.4	3	0.3	0.027	0.96142	3.333333	0.3	0.687	0.02	-0.21434	1660	130	3400	97	2650	260
LAN4-2-39	2.48	1.91	13.4	0.67	0.1752	0.0084	0.57291	5.707763	0.2736598	0.559	0.025	0.40531	1038	46	2698	49	1422	74
LAN4-2-59	1.52	1.288	5.94	0.27	0.1145	0.0037	0.54939	8.733624	0.2822219	0.381	0.017	0.039567	698	22	1951	39	911	39
LAN4-2-9	5.24	3.34	34.2	2.2	0.343	0.019	0.59216	2.915452	0.1614973	0.71	0.025	0.22558	1887	91	3592	66	2520	130
LAN4-2-19	6.2	4.05	47.3	1.7	0.459	0.019	0.19809	2.178649	0.09018374	0.744	0.021	-0.08283	2456	77	3934	34	3470	140
LAN4-2-63	2.25	1.494	9.79	0.57	0.1473	0.0072	0.34128	6.788866	0.3318387	0.491	0.028	0.43923	885	41	2400	54	1138	55
LAN4-2-56	1.54	1.368	7.88	0.47	0.1329	0.0055	0.86028	7.524454	0.3113958	0.441	0.019	-0.11843	803	31	2222	52	995	45
LAN4-2-13	1.75	1.353	6.4	0.39	0.1197	0.005	0.21659	8.354219	0.3489649	0.396	0.024	0.036274	728	29	2033	54	932	50
LAN4-2-42	1.2	0.97	4.06	0.16	0.0989	0.0033	0.12569	10.11122	0.3373816	0.295	0.014	0.46786	608	19	1640	34	725	34
LAN4-2-22	1.91	1.347	4.47	0.24	0.1032	0.0036	0.32404	9.689922	0.3380206	0.317	0.017	0.12698	637	21	1693	38	732	30
LAN4-2-2	1.74	1.208	7.33	0.28	0.1283	0.0054	0.38729	7.794232	0.3280503	0.423	0.017	0.49694	777	31	2155	34	966	54
LAN4-2-1	2.65	2.23	17.8	2.1	0.214	0.02	0.87762	4.672897	0.4367194	0.597	0.027	-0.46389	1240	100	2920	120	1600	130
LAN4-2-40	2.36	1.966	17.46	0.65	0.2164	0.0081	0.89563	4.621072	0.1729699	0.599	0.018	0.064743	1260	43	2948	34	1632	76
LAN4-2-26	2.04	1.78	11.31	0.84	0.1622	0.0081	0.55974	6.165228	0.3078813	0.512	0.023	-0.22284	966	45	2517	69	1311	82
LAN4-2-14	3.46	4.01	9.6	0.32	0.1482	0.0053	0.8227	6.747638	0.2413123	0.478	0.013	0.031218	890	30	2390	30	1136	46
LAN4-2-57	1.43	1.253	6.48	0.24	0.1215	0.0039	0.506	8.230453	0.2641874	0.395	0.018	0.32913	739	22	2032	33	922	40
LAN4-2-50	3.72	2.872	20.31	0.7	0.2377	0.0083	0.83549	4.206984	0.1468993	0.619	0.016	0.20308	1377	43	3108	34	1866	77

LAN4-2-24	1.63	1.285	7.26	0.34	0.1275	0.0048	0.65418	7.843137	0.295271	0.414	0.018	0.21971	772	27	2127	40	870	40
LAN4-2-36	1.46	1.289	10.02	0.47	0.1539	0.0062	0.85027	6.497726	0.2617667	0.489	0.021	0.14028	921	35	2423	44	1107	51
LAN4-2-17	2.46	1.533	9.59	0.47	0.1529	0.0098	0.088225	6.540222	0.4191902	0.484	0.031	0.48357	914	53	2382	45	1008	55
LAN4-2-6	2.29	1.769	5.86	0.19	0.1175	0.0036	0.50708	8.510638	0.2607515	0.375	0.013	0.28277	716	21	1947	28	844	36
LAN4-2-49	1.34	1.638	3.99	0.18	0.0998	0.0031	0.11041	10.02004	0.3112437	0.289	0.013	0.54157	613	18	1625	36	672	28
LAN4-2-11	1.82	1.053	5.15	0.31	0.1099	0.0044	0.61211	9.099181	0.3642984	0.34	0.02	0.037916	671	26	1820	44	805	42
LAN4-2-8	3.11	2.51	10.48	0.53	0.1552	0.0057	0.17997	6.443299	0.2366418	0.489	0.024	0.12584	929	32	2456	46	1125	49
LAN4-2-46	2.48	1.91	12.21	0.78	0.1687	0.0079	0.14765	5.927682	0.2775856	0.518	0.022	-0.069967	1002	43	2593	63	1258	70
LAN4-2-20	5.82	5.74	50.9	4.8	0.488	0.041	0.87063	2.04918	0.1721647	0.736	0.02	-0.13815	2510	180	3909	98	2280	260
LAN4-2-4	1.94	1.748	13.88	0.8	0.1875	0.0089	0.18572	5.333333	0.2531556	0.548	0.027	0.48164	1106	48	2726	54	1360	67
LAN4-2-12	3.48	2.66	27.2	2.2	0.293	0.017	0.71913	3.412969	0.1980221	0.656	0.032	-0.061576	1671	86	3346	79	1806	97
LAN4-2-48	1.76	1.251	9.35	0.59	0.1449	0.0088	0.49858	6.901311	0.4191273	0.456	0.027	0.39369	871	49	2356	58	1103	63
LAN4-2-54	1.97	1.316	7.54	0.51	0.1326	0.0062	0.63113	7.541478	0.3526181	0.422	0.025	0.22758	801	35	2163	56	1001	52
LAN4-2-29	3.72	2.84	35.5	2.1	0.364	0.019	0.54592	2.747253	0.1434006	0.693	0.022	0.075258	1991	87	3617	58	2750	120
LAN4-2-32	2.74	2.32	19.4	1.5	0.229	0.013	0.78719	4.366812	0.2478976	0.601	0.022	-0.097136	1321	65	3012	67	1744	98
LAN4-2-52	1.78	1.3	5.75	0.43	0.119	0.0061	0.86288	8.403361	0.4307605	0.372	0.02	-0.20159	723	35	1905	56	911	57
LAN4-2-61	1.3	1.48	6.9	0.43	0.1282	0.0058	0.42868	7.800312	0.3529002	0.404	0.02	0.062804	776	33	2082	52	959	54
LAN4-2-60	0.94	1.082	4.87	0.32	0.1101	0.0053	0.31784	9.082652	0.4372212	0.329	0.022	0.06825	672	31	1781	55	820	46
LAN4-2-23	105	109	880	150	7.8	1.4	0.99857	0.1282051	0.02301118	0.8447	0.0067	-0.18457	12708.08	1.10E+03	6640	210	26343.3783	2.80E+03
LAN4-2-51	1.84	1.383	5.74	0.28	0.1165	0.0042	0.9194	8.583691	0.309455	0.361	0.015	-0.25035	710	24	1921	38	854	45
LAN4-2-7	2.51	2.073	15.16	0.66	0.1998	0.0076	0.69406	5.005005	0.1903806	0.557	0.02	0.19906	1178	42	2824	43	1550	74
LAN4-2-28	1.62	1.298	9.3	0.61	0.1455	0.0062	0.84228	6.872852	0.2928638	0.451	0.02	-0.13682	874	35	2330	60	1085	54
LAN4-2-35	18	18.5	183	31	1.57	0.25	0.99715	0.6369427	0.101424	0.812	0.01	-0.34054	5740	570	5110	150	10602.3344	1.30E+03
LAN4-2-31	2.11	1.95	11.5	1.1	0.163	0.011	0.94364	6.134969	0.4140163	0.491	0.021	-0.40739	968	60	2487	82	1169	78
LAN4-2-37	4.55	3.6	33.8	3	0.353	0.027	0.90312	2.832861	0.2166778	0.675	0.02	-0.095336	1940	130	3532	85	2730	220
LAN4-2-5	10.32	2.601	22.9	1.2	0.269	0.014	0.8416	3.717472	0.1934744	0.623	0.02	0.1714	1543	69	3206	54	2102	99
LAN4-2-45	3.06	2.5	19.6	1.3	0.244	0.015	0.18484	4.098361	0.2519484	0.599	0.021	-0.093668	1399	77	3025	66	1990	120
LAN4-2-53	2.4	1.413	7.09	0.82	0.1278	0.0076	0.92181	7.824726	0.4653202	0.384	0.02	-0.40077	761	34	2015	47	887	46
LAN4-2-30	1.32	1.178	4.94	0.24	0.1135	0.004	0.62184	8.810573	0.3105048	0.326	0.016	-0.011532	693	23	1799	40	721	34
Phalaborwa Apatite																		
Phal - 2	4.05	18.15	15.84	0.22	0.4446	0.0084	0.4813	2.249213	0.04249525	0.2615	0.0033	0.0061673	2371	38	2867	13	2196	59
Phal - 3	3.79	20.87	14.09	0.15	0.4279	0.0084	0.52674	2.336995	0.04587697	0.2399	0.0025	0.18931	2296	38	2754	10	2163	59
Phal - 4	4.49	18.53	15.71	0.2	0.4438	0.0087	0.36489	2.253267	0.04417176	0.2569	0.0034	0.37212	2367	39	2861	12	2222	60
Phal - 5	4.02	20.3	13.64	0.16	0.4243	0.0083	0.34011	2.356823	0.0461033	0.2329	0.0026	0.29637	2279	37	2725	11	2177	59
Phal - 6	4.09	18.12	15.62	0.19	0.438	0.0086	0.53447	2.283105	0.04482809	0.2596	0.0029	0.12793	2341	38	2856	11	2220	61
Phal - 7	4.25	17.27	15.92	0.22	0.4454	0.0087	0.60612	2.245173	0.04385497	0.2603	0.003	-0.033531	2381	38	2872	13	2231	60
Phal - 8	4.25	18.29	15.58	0.21	0.4407	0.0087	0.4713	2.269117	0.04479537	0.2564	0.0032	0.18533	2353	39	2850	13	2228	60
Phal - 9	3.82	19.11	15.19	0.2	0.4414	0.0089	0.4549	2.265519	0.04567992	0.248	0.0033	0.13294	2359	39	2827	12	2213	60

Phal - 10	4.08	18.36	16.59	0.2	0.4584	0.0088	0.58311	2.181501	0.04187873	0.2608	0.0025	0.15815	2432	39	2911	12	2227	61
Phal_1	3.8	17.59	16.33	0.21	0.4507	0.0095	-0.097288	2.218771	0.04676797	0.2626	0.0048	0.67381	2398	42	2896	12	2185	61
Standards																		
MAD - 1	1.65	7.453	0.598	0.022	0.07571	0.0015	0.063189	13.20829	0.2616886	0.0568	0.002	0.20868	470.4	9.3	475	14	469.3	13
MAD - 2	1.71	7.427	0.598	0.028	0.07627	0.0016	-0.13453	13.11132	0.2750505	0.0572	0.003	0.3254	473.8	9.3	475	19	468.2	13
MAD - 3	1.71	7.63	0.612	0.028	0.07699	0.0016	-0.11506	12.9887	0.2699301	0.0576	0.0027	0.27107	478.1	9.7	484	18	476.8	13
MAD - 4	1.4	7.23	0.599	0.023	0.07592	0.0016	-0.14859	13.17176	0.2775924	0.0577	0.0024	0.41131	472.3	9.5	476	15	466.3	13
MAD - 5	1.62	7.342	0.606	0.024	0.07644	0.0016	-0.16015	13.08216	0.2738285	0.058	0.0025	0.39596	474.8	9.6	481	16	475.3	13
MAD - 6	1.54	7.383	0.6	0.027	0.07599	0.0015	-0.09079	13.15963	0.2597636	0.0573	0.0026	0.28777	472.1	8.7	476	17	474.6	13
MAD - 7	1.61	7.283	0.595	0.024	0.076	0.0016	-0.22149	13.15789	0.2770083	0.0563	0.0024	0.43029	472.1	9.5	476	15	473.6	13
MAD - 8	1.83	7.553	0.613	0.041	0.07714	0.0015	-0.24753	12.96344	0.2520763	0.0578	0.0041	0.38899	479	9.1	481	26	486.7	14
MAD - 9	1.29	7.298	0.604	0.024	0.07691	0.0016	-0.067753	13.00221	0.270492	0.0567	0.0023	0.32658	477.6	9.4	478	15	473.5	14
MAD - 10	1.34	7.514	0.587	0.025	0.07485	0.0015	-0.075209	13.36005	0.2677365	0.0559	0.0026	0.25982	465.3	8.9	469	16	466.5	13
MAD - 11	1.54	7.272	0.606	0.026	0.07641	0.0015	0.0038213	13.08729	0.2569158	0.0581	0.0026	0.19033	475.1	9.2	478	16	470.8	13
MAD - 12	1.33	7.692	0.599	0.033	0.07648	0.0015	-0.018052	13.07531	0.2564457	0.057	0.0032	0.19538	475.1	9.2	474	21	478.8	14
MAD - 13	1.34	7.846	0.617	0.029	0.07773	0.0016	-0.12377	12.93661	0.2677694	0.058	0.0029	0.33259	480	9.6	484	19	481.6	14
MAD - 14	1.44	7.588	0.598	0.033	0.07553	0.0015	-0.14781	13.23977	0.2629374	0.0576	0.0032	0.24882	469.3	9	471	21	475.2	13
MAD - 15	1.39	7.461	0.597	0.03	0.07606	0.0016	0.16805	13.14752	0.2765714	0.057	0.003	-0.0056419	472.5	9.3	475	19	469.9	13
MAD - 16	1.29	7.562	0.604	0.028	0.07674	0.0015	-0.11725	13.03101	0.2547511	0.0572	0.0028	0.27956	476.6	8.8	476	18	470.2	13
MAD - 17	1.76	7.751	0.611	0.028	0.07761	0.0016	-0.037616	13.1406	0.2762808	0.0578	0.0028	0.27689	472.8	9.7	481	18	480.4	14
MAD - 18	1.17	7.316	0.592	0.024	0.07566	0.0016	-0.030521	13.21702	0.2795035	0.0562	0.0025	0.30379	470.1	9.3	474	16	463.4	13
MAD - 19	1.33	7.06	0.596	0.023	0.07537	0.0016	-0.022155	13.26788	0.2816586	0.0574	0.0023	0.2888	468.4	9.4	474	15	468.1	13
MAD - 20	1.28	7.58	0.613	0.032	0.0774	0.0016	0.031222	12.9199	0.267078	0.0574	0.0031	0.21719	480.6	9.8	486	21	479.4	14
NIST610 - 1	436.9	438.5	34.7	0.21	0.2756	0.0051	0.89234	3.628447	0.0671447	0.9145	0.0018	0.29503	1569.2	26	3629.9	6.1	9307	210
NIST610 - 2	411.1	414.5	33.25	0.23	0.2637	0.005	0.90094	3.792188	0.0719345	0.9173	0.0024	0.39575	1508.9	25	3588.2	6.8	9051	210
NIST610 - 3	429.9	428.9	33.87	0.23	0.2699	0.005	0.92955	3.705076	0.06863794	0.9125	0.0017	0.17182	1540.3	25	3605.7	6.6	9275	210
NIST610 - 4	426.7	426.6	33.69	0.21	0.2687	0.005	0.9194	3.721623	0.06925237	0.9093	0.0019	0.32228	1534.2	25	3601.4	6.2	9293	210
NIST610 - 5	426.4	426.4	33.06	0.24	0.2648	0.0049	0.91505	3.776435	0.06988116	0.9058	0.002	0.207	1514.5	25	3581.8	7.1	9206	210
NIST610 - 6	429.2	427.5	32.83	0.21	0.2634	0.0049	0.90543	3.796507	0.07062599	0.9079	0.002	0.31557	1506.9	25	3576.6	6.1	9133	210
NIST610 - 7	431.9	427.4	32.57	0.2	0.2619	0.0048	0.89549	3.818251	0.0699794	0.9045	0.0023	0.32973	1499.5	25	3567.4	6.1	9118	210
NIST610 - 8	426.2	428.3	32.23	0.2	0.2595	0.0048	0.86846	3.853565	0.07127981	0.9017	0.0021	0.2176	1487	24	3557.7	6.2	9017	210
NIST610 - 9	427.5	428.9	33.54	0.22	0.2685	0.005	0.92274	3.724395	0.06935558	0.9028	0.0019	0.37049	1533.3	25	3596.3	6.6	9294	210
NIST610 - 10	420.4	422.6	32.82	0.23	0.2621	0.0049	0.91177	3.815338	0.07132833	0.8999	0.0021	0.19878	1500.6	25	3574.6	7	9044	210

Table A1-4 - Re-Os data from arsenopyrite and jamesonite for geochronology

Mixed spike

Sample	Re ppb	± 2s	Total Os ppt	± 2s	187Re/188 Os	± 2s	187/188 Os	± 2s	rho
LAN2-3	0.355	0.003	4.2	0.3	701.6	69.4	5.585	0.554	0.992
LAN2-3-R1	0.438	0.001	1.9	0.6	10317	2511	64.95	15.84	0.998
LAN2-3-R2	0.361	0.002	1.5	0.5	12072	3226	74.09	19.87	0.996
LAN2-3-R3	0.558	0.003	2.3	0.7	15840	3622	97.44	22.39	0.994

5.4.1.1.1.1 Mixed Double-Os spike

Sample	Re ppm	± 2s	187Re ppb	± 2s	187Os ppb	± 2s	Total common Os pg	Model Age (Ma)	±2s with I (Ma)
7157-MD bulk	0.522	0.001	328.4	0.9	1.196	0.003	0.1	218.1	1.0
7157-MD bulk-R1	0.510	0.001	320.3	0.9	1.138	0.001	0.5	212.9	0.9
7157-MD bulk-R3	0.561	0.002	352.6	1.0	1.314	0.006	2.8	223.3	1.4
7157 M05 Jam	0.149	0.0004	93.8	0.3	0.4	0.00	0.3	226.6	1.5
7157-M05 Jam-R1	0.177	0.0005	111.6	0.3	0.4	0.00	0.9	228.7	1.4
7157 NM07 aspy	0.716	0.002	449.7	1.3	1.6	0.01	0.3	214.6	1.2
7157-NM07 aspy-R1	0.710	0.002	446.5	1.2	1.6	0.00	0.4	213.9	1.1

R = replicate

Jam = Jamesonite

Aspy = arsenopyrite

NM07 = non magnetic 0.7A on Frantz

M05 = magnetic 0.5A on Frantz

Figure A1-4 – LAN2-3 isochron from Re-Os geochronology of arsenopyrite.

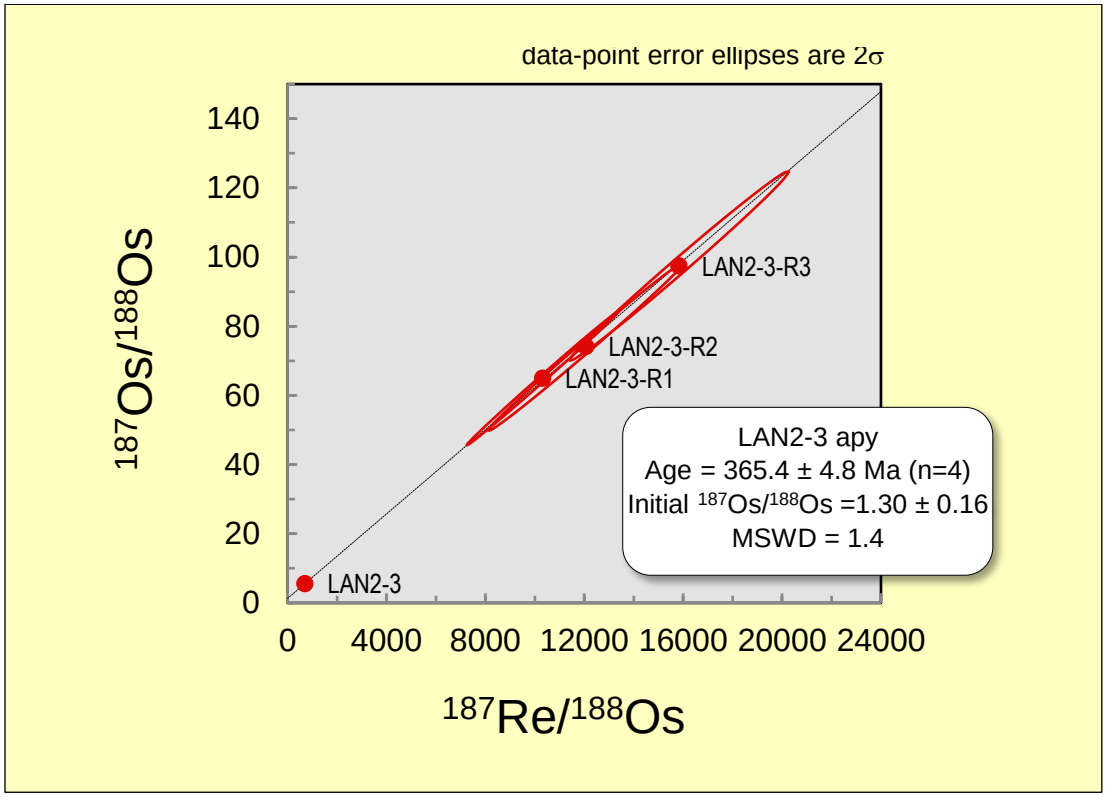

Table A1-5 - EPMA results of chlorite analyses in unmineralized and mineralized samples. All values in wt.%.

Sample Spot	K_2O	SrO	Na_2O	MgO	F	SiO_2	Al_2O_3	FeO	MnO	NiO	Cr_2O_3	Cl	CaO	TiO_2	(OH)	Total
Unmineralized samples																
LAN3-2_spot2.3	< D.L.	< D.L.	< D.L.	9.008	0.125	24.916	24.027	31.786	0.244	< D.L.	< D.L.	0.007	0.01	0.065	9.867	100.055
LAN3-2_spot2.3_top	0.003	< D.L.	< D.L.	9.084	0.229	24.641	23.991	31.682	0.22	0.025	0.002	0.026	< D.L.	0.134	10.065	100.102
LAN3-2_spot2.4_rim	< D.L.	0.077	0.019	8.772	< D.L.	24.229	24.65	32.127	0.219	0.058	0.01	0.009	< D.L.	0.104	9.727	100.001
LAN3-2_spot2.4_center	0.021	0.031	0.045	9.009	< D.L.	24.753	23.897	32.131	0.236	0.011	0.035	0.001	0.005	0.167	9.658	100
LAN3-2_spot2.1_center	0.006	< D.L.	< D.L.	8.829	< D.L.	24.559	24.365	31.824	0.237	< D.L.	< D.L.	< D.L.	0.007	0.129	10.044	100
LAN3-2_spot2.1_side	< D.L.	< D.L.	0.027	9.215	0.125	24.698	24.581	31.523	0.226	< D.L.	0.022	0.011	0.011	0.084	9.533	100.056
LAN3-2_spot2_wPy	0.003	< D.L.	< D.L.	7.924	0.145	24.761	24.305	32.881	0.17	< D.L.	0.01	0.003	0.031	0.089	9.74	100.062
LAN3-2_spot2_wPycenter	< D.L.	< D.L.	0.021	8.795	< D.L.	24.757	24.519	32.221	0.226	0.017	0.002	0.008	< D.L.	0.123	9.312	100.001
LAN3-2_spot2_woPy	< D.L.	< D.L.	0.024	7.665	0.144	24.457	24.554	33.348	0.131	< D.L.	< D.L.	< D.L.	0.022	0.132	9.582	100.059
LAN3-2_spot2_woPy	< D.L.	< D.L.	0.069	8.792	< D.L.	24.562	24.451	31.892	0.272	< D.L.	0.012	0.006	< D.L.	0.071	9.875	100.002
LAN3-2_spot1_center	0.048	0.03	0.085	7.293	0.343	29.601	12.465	35.175	0.215	0.035	< D.L.	0.012	0.727	0.051	14.067	100.147
LAN3-2_spot1_rim	0.006	< D.L.	0.06	7.008	0.134	21.361	7.874	23.106	0.243	< D.L.	0.022	0.011	16.87	0.076	23.289	100.06
LAN3-2_spot1.1_rim	0.01	< D.L.	< D.L.	8.472	0.062	30.075	13.993	35.926	0.101	0.018	< D.L.	< D.L.	0.45	0.051	10.869	100.027
LAN3-2_spot1.1_pyborder	< D.L.	< D.L.	0.014	7.257	0.232	29.796	12.869	35.941	0.169	< D.L.	< D.L.	0.013	1.234	0.062	12.513	100.1
LAN3-2_spot1.2_center	0.002	< D.L.	0.045	8.845	0.174	30.312	10.861	33.74	0.156	0.043	< D.L.	0.007	0.755	0.079	15.058	100.077
LAN3-2_spot1.2_center2	0.027	< D.L.	0.062	8.061	0.41	28.012	11.705	30.8	0.21	0.032	< D.L.	< D.L.	4.2	0.092	16.56	100.171
LAN1-2_spot2.1_center	0.049	< D.L.	0.048	5.402	< D.L.	30.366	12.887	39.714	0.185	< D.L.	< D.L.	0.013	0.44	0.066	10.833	100.003
LAN1-2_spot2.1_center2	0.047	< D.L.	0.089	4.855	< D.L.	30.399	12.786	39.921	0.173	< D.L.	< D.L.	< D.L.	0.504	0.084	11.141	99.999
LAN1-2_spot2.1_smallcenter1	0.04	0.112	0.096	6.687	0.062	31.313	12.024	37.807	0.19	< D.L.	< D.L.	0.009	0.655	0.104	10.929	100.028
LAN1-2_spot2.1_smallcenter2	0.028	0.015	0.068	6.886	0.103	31.388	12.135	37.682	0.199	0.03	0.039	0.002	0.517	0.042	10.911	100.045
LAN1-2_spot2.2_whispy1	0.03	< D.L.	0.094	4.509	< D.L.	30.224	13.117	40.408	0.172	0.006	< D.L.	0.007	0.541	0.081	10.812	100.001
LAN1-2_spot2.2_whispy2	0.006	< D.L.	0.054	5.963	< D.L.	31.077	12.321	39.128	0.198	0.01	0.002	< D.L.	0.394	0.063	10.784	100
LAN1-2_spot2.2_whispy3	0.03	< D.L.	0.049	4.139	< D.L.	30.097	13.045	40.838	0.184	0.013	< D.L.	0.014	0.426	0.067	11.101	100.003
LAN1-2_spot2.2_whispy4	0.016	< D.L.	< D.L.	5.611	< D.L.	30.59	12.73	39.324	0.193	< D.L.	< D.L.	0.004	0.418	0.048	11.067	100.001
LAN1-2_spot2._center3	0.05	< D.L.	0.075	3.849	0.141	30.057	13.093	41.226	0.184	< D.L.	0.01	0.009	0.416	0.059	10.89	100.059
LAN1-2_spot2.1_smallcenter4	0.015	< D.L.	0.096	6.209	0.021	30.88	12.21	38	0.202	0.026	< D.L.	0.048	0.685	0.08	11.547	100.019
LAN1-2_spot1_center2	< D.L.	0.07	< D.L.	8.517	< D.L.	24.508	24.591	32.077	0.247	0.007	< D.L.	0.013	0.025	0.111	9.838	100.004
LAN1-2_spot1_side	0.006	< D.L.	< D.L.	8.575	0.042	24.403	24.329	31.566	0.204	0.016	0.024	< D.L.	0.107	0.083	10.662	100.017
LAN1-2_spot1_center1	0.018	< D.L.	0.005	8.571	< D.L.	24.204	24.819	31.801	0.227	< D.L.	< D.L.	< D.L.	0.011	0.122	10.221	99.999
LAN1-2_spot1_center3	< D.L.	< D.L.	< D.L.	8.423	0.104	24.385	24.213	32.076	0.272	0.009	0.012	0.003	< D.L.	0.11	10.439	100.046
LAN1-2_spot1_smallcenter1	0.013	0.015	< D.L.	8.818	0.042	24.432	24.235	31.605	0.202	< D.L.	< D.L.	< D.L.	0.021	0.102	10.532	100.017
LAN1-2_spot1_smallcenter2	< D.L.	< D.L.	0.058	8.738	0.021	24.662	24.553	31.656	0.242	0.006	0.01	0.02	0.062	0.135	9.849	100.012
LAN1-2_spot1_smallcenter3	0.004	< D.L.	0.003	8.399	0.146	24.652	24.299	32.036	0.167	0.033	0.063	0.001	0.03	0.086	10.142	100.061
LAN1-2_spot1_smallcenter4	< D.L.	0.054	0.021	8.354	< D.L.	24.817	23.95	31.802	0.186	0.013	< D.L.	0.006	0.043	0.123	10.632	100.001
Mineralized sample																
LAN2-2_spot1_1	< D.L.	< D.L.	0.047	12.47	0.258	25.709	22.831	26.913	0.188	< D.L.	< D.L.	0.006	0.076	0.11	11.502	100.11
LAN2-2_spot1_2	< D.L.	0.031	0.08	12.742	0.043	26.125	22.593	26.838	0.174	0.007	0.008	< D.L.	0.023	0.146	11.209	100.019
LAN2-2_spot1_3	0.027	< D.L.	0.034	12.11	< D.L.	25.702	22.386	27.599	0.178	0.026	< D.L.	0.003	0.179	0.126	11.632	100.002
LAN2-2_spot1_4	< D.L.	0.046	0.013	11.487	0.126	26.801	21.703	29.263	0.142	0.017	0.028	0.013	0.046	0.174	10.195	100.054
LAN2-2_spot1_5	< D.L.	0.015	0.067	12.636	< D.L.	26.033	23.241	27.277	0.246	< D.L.	0.002	0.005	0.02	0.111	10.348	100.001
LAN2-2_spot1_6	< D.L.	0.031	0.043	12.828	0.043	26.108	23.773	26.171	0.267	0.024	0.002	< D.L.	0.018	0.133	10.578	100.019
LAN2-2_spot1_7	< D.L.	0.046	0.031	12.442	0.064	25.77	23.167	27.5	0.248	< D.L.	< D.L.	< D.L.	0.013	0.155	10.59	100.026
LAN2-2_spot1_8	< D.L.	< D.L.	0.003	13.157	0.065	26.029	22.668	26.306	0.216	0.013	< D.L.	0.003	0.032	0.137	11.4	100.029
LAN2-2_spot2_1	0.033	< D.L.	0.005	13.433	0.065	25.916	23.855	25.678	0.265	< D.L.	< D.L.	0.011	0.02	0.08	10.669	100.03
LAN2-2_spot2_2	0.003	< D.L.	< D.L.	0.616	< D.L.	< D.L.	0.025	1.349	1.643	< D.L.	0.029	< D.L.	60.055	0.112	36.168	100
LAN2-2_spot2_3	0.046	< D.L.	0.013	13.262	< D.L.	26.039	23.554	25.519	0.252	< D.L.	< D.L.	0.017	0.184	0.125	10.992	100.003
LAN2-2_spot2_4	2.423	< D.L.	0.041	7.6	0.102	31.731	20.347	13.908	0.128	0.01	< D.L.	0.012	0.246	16.519	6.978	100.045
LAN2-2_spot2_5	0.013	< D.L.	0.023	14.761	< D.L.	26.331	23.132	23.303	0.226	0.009	0.004	< D.L.	1.253	0.16	10.786	100.001
LAN2-2_spot2_6	0.135	< D.L.	0.012	1.228	0.195	0.148	0.084	1.888	0.467	0.024	0.046	0.005	59.755	0.124	35.971	100.082
LAN2-2_spot2_7	0.058	< D.L.	< D.L.	13.015	0.107	25.919	23.981	25.886	0.289	< D.L.	0.03	0.005	0.172	0.11	10.475	100.047
LAN2-2_spot2_8	< D.L.	< D.L.	0.02	13.375	0.043	25.875	23.876	25.732	0.305	< D.L.	< D.L.	0.01	0.266	0.109	10.411	100.022

Table A1-6 - Site assignment of elements in chlorite. Temperature (T) based on equation by Cathelineau (1988), as described in section 2.3.3. Sample IDs correspond to grain number and area within the grain analyzed or description of adjacent minerals. Fe# = Fe/(Fe + Mg). Normalized to 14 oxygen. T = tetrahedral site, O = octahedral site, OH = OH anion site.

				LAN3-2_spot2.3	LAN3-2_spot2.3_top	LAN3-2_spot2.4_rim	LAN3-2_spot2.4_center	LAN3-2_spot2.1_center	LAN3-2_spot2.1_side	LAN3-2_spot2_wPy	LAN3-2_spot2_wPycenter	LAN3-2_spot2_woPy	LAN3-2_spot2_woPy	LAN3-2_spot1.1_rim	LAN3-2_spot1.1_pyborder
O	wt.%	cat													
2	60.08	1	SiO2	0.83	0.82	0.81	0.82	0.82	0.82	0.82	0.82	0.81	0.82	1.00	0.99
2	79.88	1	TiO2	0.00	0.00	0.00	0.00	0.00	0.00	0.00	0.00	0.00	0.00	0.00	0.00
3	101.96	2	Al2O3	0.71	0.71	0.73	0.70	0.72	0.72	0.72	0.72	0.72	0.72	0.41	0.38
3	151.99	2	Cr2O3	0.00	0.00	0.00	0.00	0.00	0.00	0.00	0.00	0.00	0.00	0.00	0.00
1	74.692	1	NiO	0.00	0.00	0.00	0.00	0.00	0.00	0.00	0.00	0.00	0.00	0.00	0.00
1	71.844	1	FeO	0.44	0.44	0.45	0.45	0.44	0.44	0.46	0.45	0.46	0.44	0.50	0.50
1	70.94	1	MnO	0.00	0.00	0.00	0.00	0.00	0.00	0.00	0.00	0.00	0.00	0.00	0.00
1	40.3	1	MgO	0.22	0.23	0.22	0.22	0.22	0.23	0.20	0.22	0.19	0.22	0.21	0.18
1	56.08	1	CaO	0.00	0.00	0.00	0.00	0.00	0.00	0.00	0.00	0.00	0.00	0.01	0.02
1	61.98	2	Na2O	0.00	0.00	0.00	0.00	0.00	0.00	0.00	0.00	0.00	0.00	0.00	0.00
1	94.2	2	K2O	0.00	0.00	0.00	0.00	0.00	0.00	0.00	0.00	0.00	0.00	0.00	0.00
1	103.62	1	SrO	0.00	0.00	0.00	0.00	0.00	0.00	0.00	0.00	0.00	0.00	0.00	0.00
1	19	0	F	0.00	0.01	0.00	0.00	0.00	0.00	0.00	0.00	0.00	0.00	0.00	0.01
1	35.45	0	Cl	0.00	0.00	0.00	0.00	0.00	0.00	0.00	0.00	0.00	0.00	0.00	0.00
			Total O:	2.21	2.21	2.20	2.21	2.20	2.22	2.20	2.22	2.20	2.21	2.14	2.08
			CF	6.33	6.35	6.35	6.34	6.35	6.30	6.36	6.31	6.36	6.35	6.55	6.72
			Si	2.63	2.60	2.56	2.61	2.60	2.59	2.62	2.60	2.59	2.59	3.28	3.33
			Ti	0.01	0.01	0.01	0.01	0.01	0.01	0.01	0.01	0.01	0.01	0.00	0.01
			Al	2.98	2.99	3.07	2.97	3.04	3.04	3.03	3.03	3.06	3.04	1.80	1.70
			Cr	0.00	0.00	0.00	0.00	0.00	0.00	0.00	0.00	0.00	0.00	0.00	0.00
			Ni	0.00	0.00	0.00	0.00	0.00	0.00	0.00	0.00	0.00	0.00	0.00	0.00
			Fe	2.80	2.80	2.84	2.84	2.81	2.76	2.91	2.83	2.95	2.82	3.28	3.36
			Mn	0.02	0.02	0.02	0.02	0.02	0.02	0.02	0.02	0.01	0.02	0.01	0.02
			Mg	1.42	1.43	1.38	1.42	1.39	1.44	1.25	1.38	1.21	1.38	1.38	1.21
			Ca	0.00	0.00	0.00	0.00	0.00	0.00	0.00	0.00	0.00	0.00	0.05	0.15
			Na	0.00	0.00	0.00	0.01	0.00	0.01	0.00	0.00	0.00	0.01	0.00	0.00
			K	0.00	0.00	0.00	0.00	0.00	0.00	0.00	0.00	0.00	0.00	0.00	0.00
			Sr	0.00	0.00	0.00	0.00	0.00	0.00	0.00	0.00	0.00	0.00	0.00	0.00
			total	9.86	9.85	9.90	9.89	9.87	9.87	9.83	9.88	9.85	9.88	9.81	9.77
			charge	27.96	27.92	27.99	28.00	28.00	27.96	27.95	28.00	27.95	28.00	27.98	27.92
			F	0.02	0.04	0.00	0.00	0.00	0.02	0.02	0.00	0.02	0.00	0.01	0.04
			Cl	0.00	0.00	0.00	0.00	0.00	0.00	0.00	0.00	0.00	0.00	0.00	0.00
	apfu	T	Si	2.63	2.60	2.56	2.61	2.60	2.59	2.62	2.60	2.59	2.59	3.28	3.33
			Al	1.37	1.40	1.44	1.39	1.40	1.41	1.38	1.40	1.41	1.41	0.72	0.67
			Sum	4.00	4.00	4.00	4.00	4.00	4.00	4.00	4.00	4.00	4.00	4.00	4.00
		O	Al	1.61	1.59	1.63	1.59	1.63	1.63	1.65	1.63	1.65	1.64	1.08	1.03
			Fe	2.80	2.80	2.84	2.84	2.81	2.76	2.91	2.83	2.95	2.82	3.28	3.36
			Mg	1.42	1.43	1.38	1.42	1.39	1.44	1.25	1.38	1.21	1.38	1.38	1.21
			Mn	0.02	0.02	0.02	0.02	0.02	0.02	0.02	0.02	0.01	0.02	0.01	0.02
			sum	5.85	5.84	5.87	5.86	5.86	5.85	5.82	5.86	5.83	5.86	5.75	5.62
			vac	0.15	0.16	0.13	0.14	0.14	0.15	0.18	0.14	0.17	0.14	0.25	0.38
		OH	F	0.02	0.04	0.00	0.00	0.00	0.02	0.02	0.00	0.02	0.00	0.01	0.04
			Cl	0.00	0.00	0.00	0.00	0.00	0.00	0.00	0.00	0.00	0.00	0.00	0.00
			OH	7.94	7.88	7.99	8.00	8.00	7.93	7.93	8.00	7.93	8.00	7.97	7.87
			Fe#	0.66	0.66	0.67	0.67	0.67	0.66	0.70	0.67	0.71	0.67	0.70	0.74
			T	380.48	387.86	401.39	384.74	389.67	392.29	382.69	389.02	392.19	390.69	169.53	152.93

				LAN1-2_spot2.1_center	LAN1-2_spot2.1_center2	LAN1-2_spot2.1_smallcenter1	LAN1-2_spot2.1_smallcenter2	LAN1-2_spot2.2_whispy1	LAN1-2_spot2.2_whispy2	LAN1-2_spot2.2_whispy3	LAN1-2_spot2.2_whispy4	LAN1-2_spot2._center3	LAN1-2_spot2.1_smallcenter4	LAN1-2_spot1_center2	LAN1-2_spot1_side
O	wt.%	cat													
2	60.08	1	SiO2	1.01	1.01	1.04	1.04	1.01	1.03	1.00	1.02	1.00	1.03	0.82	0.81
2	79.88	1	TiO2	0.00	0.00	0.00	0.00	0.00	0.00	0.00	0.00	0.00	0.00	0.00	0.00
3	101.96	2	Al2O3	0.38	0.38	0.35	0.36	0.39	0.36	0.38	0.37	0.39	0.36	0.72	0.72
3	151.99	2	Cr2O3	0.00	0.00	0.00	0.00	0.00	0.00	0.00	0.00	0.00	0.00	0.00	0.00
1	74.692	1	NiO	0.00	0.00	0.00	0.00	0.00	0.00	0.00	0.00	0.00	0.00	0.00	0.00
1	71.844	1	FeO	0.55	0.56	0.53	0.52	0.56	0.54	0.57	0.55	0.57	0.53	0.45	0.44
1	70.94	1	MnO	0.00	0.00	0.00	0.00	0.00	0.00	0.00	0.00	0.00	0.00	0.00	0.00
1	40.3	1	MgO	0.13	0.12	0.17	0.17	0.11	0.15	0.10	0.14	0.10	0.15	0.21	0.21
1	56.08	1	CaO	0.01	0.01	0.01	0.01	0.01	0.01	0.01	0.01	0.01	0.01	0.00	0.00
1	61.98	2	Na2O	0.00	0.00	0.00	0.00	0.00	0.00	0.00	0.00	0.00	0.00	0.00	0.00
1	94.2	2	K2O	0.00	0.00	0.00	0.00	0.00	0.00	0.00	0.00	0.00	0.00	0.00	0.00
1	103.62	1	SrO	0.00	0.00	0.00	0.00	0.00	0.00	0.00	0.00	0.00	0.00	0.00	0.00
1	19	0	F	0.00	0.00	0.00	0.00	0.00	0.00	0.00	0.00	0.00	0.00	0.00	0.00
1	35.45	0	Cl	0.00	0.00	0.00	0.00	0.00	0.00	0.00	0.00	0.00	0.00	0.00	0.00
			Total O:	2.09	2.08	2.11	2.12	2.08	2.10	2.07	2.09	2.07	2.09	2.20	2.19
			CF	6.70	6.73	6.63	6.62	6.72	6.66	6.76	6.70	6.76	6.70	6.35	6.40
			Si	3.38	3.41	3.46	3.46	3.38	3.44	3.39	3.41	3.38	3.44	2.59	2.60
			Ti	0.01	0.01	0.01	0.00	0.01	0.01	0.01	0.00	0.00	0.01	0.01	0.01

			Al	1.69	1.69	1.56	1.58	1.73	1.61	1.73	1.67	1.73	1.60	3.06	3.05
			Cr	0.00	0.00	0.00	0.00	0.00	0.00	0.00	0.00	0.00	0.00	0.00	0.00
			Ni	0.00	0.00	0.00	0.00	0.00	0.00	0.00	0.00	0.00	0.00	0.00	0.00
			Fe	3.70	3.74	3.49	3.47	3.78	3.63	3.84	3.66	3.88	3.54	2.83	2.81
			Mn	0.02	0.02	0.02	0.02	0.02	0.02	0.02	0.02	0.02	0.02	0.02	0.02
			Mg	0.90	0.81	1.10	1.13	0.75	0.99	0.69	0.93	0.65	1.03	1.34	1.36
			Ca	0.05	0.06	0.08	0.06	0.06	0.05	0.05	0.05	0.05	0.08	0.00	0.01
			Na	0.01	0.02	0.02	0.01	0.02	0.01	0.01	0.00	0.02	0.02	0.00	0.00
			K	0.01	0.01	0.01	0.00	0.00	0.00	0.00	0.00	0.01	0.00	0.00	0.00
			Sr	0.00	0.00	0.01	0.00	0.00	0.00	0.00	0.00	0.00	0.00	0.00	0.00
			total	9.77	9.76	9.75	9.74	9.76	9.75	9.75	9.75	9.73	9.75	9.87	9.86
			charge	28.00	28.00	27.97	27.96	28.00	28.00	28.00	28.00	27.95	27.98	27.99	27.99
			F	0.00	0.00	0.01	0.02	0.00	0.00	0.00	0.00	0.03	0.00	0.00	0.01
			Cl	0.00	0.00	0.00	0.00	0.00	0.00	0.00	0.00	0.00	0.00	0.00	0.00
	apfu	T	Si	3.38	3.41	3.46	3.46	3.38	3.44	3.39	3.41	3.38	3.44	2.59	2.60
			Al	0.62	0.59	0.54	0.54	0.62	0.56	0.61	0.59	0.62	0.56	1.41	1.40
			Sum	4.00	4.00	4.00	4.00	4.00	4.00	4.00	4.00	4.00	4.00	4.00	4.00
		O	Al	1.08	1.09	1.02	1.03	1.11	1.05	1.12	1.08	1.11	1.05	1.65	1.65
			Fe	3.70	3.74	3.49	3.47	3.78	3.63	3.84	3.66	3.88	3.54	2.83	2.81
			Mg	0.90	0.81	1.10	1.13	0.75	0.99	0.69	0.93	0.65	1.03	1.34	1.36
			Mn	0.02	0.02	0.02	0.02	0.02	0.02	0.02	0.02	0.02	0.02	0.02	0.02
			sum	5.70	5.66	5.63	5.65	5.66	5.69	5.67	5.70	5.65	5.64	5.85	5.84
			vac	0.30	0.34	0.37	0.35	0.34	0.31	0.33	0.30	0.35	0.36	0.15	0.16
		OH	F	0.00	0.00	0.01	0.02	0.00	0.00	0.00	0.00	0.03	0.00	0.00	0.01
			Cl	0.00	0.00	0.00	0.00	0.00	0.00	0.00	0.00	0.00	0.00	0.00	0.00
			OH	8.00	8.00	7.96	7.94	8.00	8.00	8.00	8.00	7.92	7.98	7.99	7.98
			Fe#	0.80	0.82	0.76	0.75	0.83	0.79	0.85	0.80	0.86	0.77	0.68	0.67
			T	136.12	129.33	112.61	112.96	137.09	116.81	135.22	128.41	137.83	117.74	392.03	389.60

				LAN1-2_spot1_center1	LAN1-2_spot1_center3	LAN1-2_spot1_smallcenter1	LAN1-2_spot1_smallcenter2	LAN1-2_spot1_smallcenter3	LAN1-2_spot1_smallcenter4	LAN2-2_spot1_1	LAN2-2_spot1_2	LAN2-2_spot1_3	LAN2-2_spot1_4	LAN2-2_spot1_5	LAN2-2_spot1_6
O	wt.%	cat													
2	60.08	1	SiO2	0.81	0.81	0.81	0.82	0.82	0.83	0.86	0.87	0.86	0.89	0.87	0.87
2	79.88	1	TiO2	0.00	0.00	0.00	0.00	0.00	0.00	0.00	0.00	0.00	0.00	0.00	0.00
3	101.96	2	Al2O3	0.73	0.71	0.71	0.72	0.71	0.70	0.67	0.66	0.66	0.64	0.68	0.70
3	151.99	2	Cr2O3	0.00	0.00	0.00	0.00	0.00	0.00	0.00	0.00	0.00	0.00	0.00	0.00
1	74.692	1	NiO	0.00	0.00	0.00	0.00	0.00	0.00	0.00	0.00	0.00	0.00	0.00	0.00
1	71.844	1	FeO	0.44	0.45	0.44	0.44	0.45	0.44	0.37	0.37	0.38	0.41	0.38	0.36
1	70.94	1	MnO	0.00	0.00	0.00	0.00	0.00	0.00	0.00	0.00	0.00	0.00	0.00	0.00
1	40.3	1	MgO	0.21	0.21	0.22	0.22	0.21	0.21	0.31	0.32	0.30	0.29	0.31	0.32
1	56.08	1	CaO	0.00	0.00	0.00	0.00	0.00	0.00	0.00	0.00	0.00	0.00	0.00	0.00
1	61.98	2	Na2O	0.00	0.00	0.00	0.00	0.00	0.00	0.00	0.00	0.00	0.00	0.00	0.00
1	94.2	2	K2O	0.00	0.00	0.00	0.00	0.00	0.00	0.00	0.00	0.00	0.00	0.00	0.00
1	103.62	1	SrO	0.00	0.00	0.00	0.00	0.00	0.00	0.00	0.00	0.00	0.00	0.00	0.00
1	19	0	F	0.00	0.00	0.00	0.00	0.00	0.00	0.01	0.00	0.00	0.00	0.00	0.00
1	35.45	0	Cl	0.00	0.00	0.00	0.00	0.00	0.00	0.00	0.00	0.00	0.00	0.00	0.00
			Total O:	2.20	2.19	2.19	2.21	2.20	2.19	2.23	2.23	2.21	2.24	2.25	2.26
			CF	6.37	6.39	6.39	6.33	6.36	6.40	6.29	6.27	6.34	6.26	6.22	6.19
			Si	2.57	2.60	2.60	2.60	2.61	2.64	2.69	2.73	2.71	2.79	2.69	2.69
			Ti	0.01	0.01	0.01	0.01	0.01	0.01	0.01	0.01	0.01	0.01	0.01	0.01
			Al	3.10	3.04	3.04	3.05	3.03	3.01	2.82	2.78	2.78	2.67	2.83	2.89
			Cr	0.00	0.00	0.00	0.00	0.01	0.00	0.00	0.00	0.00	0.00	0.00	0.00
			Ni	0.00	0.00	0.00	0.00	0.00	0.00	0.00	0.00	0.00	0.00	0.00	0.00
			Fe	2.82	2.85	2.81	2.79	2.84	2.83	2.36	2.34	2.43	2.55	2.36	2.26
			Mn	0.02	0.02	0.02	0.02	0.01	0.02	0.02	0.02	0.02	0.01	0.02	0.02
			Mg	1.35	1.34	1.40	1.37	1.33	1.33	1.95	1.98	1.90	1.79	1.95	1.97
			Ca	0.00	0.00	0.00	0.01	0.00	0.00	0.01	0.00	0.02	0.01	0.00	0.00
			Na	0.00	0.00	0.00	0.01	0.00	0.00	0.01	0.02	0.01	0.00	0.01	0.01
			K	0.00	0.00	0.00	0.00	0.00	0.00	0.00	0.00	0.00	0.00	0.00	0.00
			Sr	0.00	0.00	0.00	0.00	0.00	0.00	0.00	0.00	0.00	0.00	0.00	0.00
			total	9.88	9.86	9.87	9.87	9.84	9.85	9.85	9.87	9.89	9.84	9.89	9.85
			charge	28.00	27.96	27.98	27.99	27.95	28.00	27.91	27.98	28.00	27.95	28.00	27.98
			F	0.00	0.02	0.01	0.00	0.02	0.00	0.04	0.01	0.00	0.02	0.00	0.01
			Cl	0.00	0.00	0.00	0.00	0.00	0.00	0.00	0.00	0.00	0.00	0.00	0.00
	apfu	T	Si	2.57	2.60	2.60	2.60	2.61	2.64	2.69	2.73	2.71	2.79	2.69	2.69
			Al	1.43	1.40	1.40	1.40	1.39	1.36	1.31	1.27	1.29	1.21	1.31	1.31
			Sum	4.00	4.00	4.00	4.00	4.00	4.00	4.00	4.00	4.00	4.00	4.00	4.00
		O	Al	1.67	1.63	1.63	1.65	1.64	1.65	1.51	1.50	1.49	1.46	1.53	1.58
			Fe	2.82	2.85	2.81	2.79	2.84	2.83	2.36	2.34	2.43	2.55	2.36	2.26
			Mg	1.35	1.34	1.40	1.37	1.33	1.33	1.95	1.98	1.90	1.79	1.95	1.97
			Mn	0.02	0.02	0.02	0.02	0.01	0.02	0.02	0.02	0.02	0.01	0.02	0.02
			sum	5.86	5.85	5.86	5.83	5.82	5.82	5.83	5.84	5.85	5.81	5.86	5.83
			vac	0.14	0.15	0.14	0.17	0.18	0.18	0.17	0.16	0.15	0.19	0.14	0.17
		OH	F	0.00	0.02	0.01	0.00	0.02	0.00	0.04	0.01	0.00	0.02	0.00	0.01
			Cl	0.00	0.00	0.00	0.00	0.00	0.00	0.00	0.00	0.00	0.00	0.00	0.00
			OH	8.00	7.95	7.98	7.98	7.93	8.00	7.87	7.98	8.00	7.93	8.00	7.98
			Fe#	0.68	0.68	0.67	0.67	0.68	0.68	0.55	0.54	0.56	0.59	0.55	0.53
			T	399.81	390.34	389.84	389.04	385.50	375.14	359.47	348.46	353.03	326.38	358.52	359.67

				LAN2-2_spot1_7	LAN2-2_spot1_8	LAN2-2_spot2_1	LAN2-2_spot2_3	LAN2-2_spot2_5	LAN2-2_spot2_7	LAN2-2_spot2_8
O	wt.%	cat								
2	60.08	1	SiO2	0.86	0.87	0.86	0.87	0.88	0.86	0.86
2	79.88	1	TiO2	0.00	0.00	0.00	0.00	0.00	0.00	0.00
3	101.96	2	Al2O3	0.68	0.67	0.70	0.69	0.68	0.71	0.70
3	151.99	2	Cr2O3	0.00	0.00	0.00	0.00	0.00	0.00	0.00
1	74.692	1	NiO	0.00	0.00	0.00	0.00	0.00	0.00	0.00
1	71.844	1	FeO	0.38	0.37	0.36	0.36	0.32	0.36	0.36
1	70.94	1	MnO	0.00	0.00	0.00	0.00	0.00	0.00	0.00
1	40.3	1	MgO	0.31	0.33	0.33	0.33	0.37	0.32	0.33
1	56.08	1	CaO	0.00	0.00	0.00	0.00	0.02	0.00	0.00
1	61.98	2	Na2O	0.00	0.00	0.00	0.00	0.00	0.00	0.00
1	94.2	2	K2O	0.00	0.00	0.00	0.00	0.00	0.00	0.00
1	103.62	1	SrO	0.00	0.00	0.00	0.00	0.00	0.00	0.00
1	19	0	F	0.00	0.00	0.00	0.00	0.00	0.00	0.00
1	35.45	0	Cl	0.00	0.00	0.00	0.00	0.00	0.00	0.00
			Total	2.24	2.24	2.26	2.26	2.28	2.27	2.27
			O:							
			CF	6.25	6.26	6.18	6.21	6.15	6.18	6.17
			Si	2.68	2.71	2.67	2.69	2.69	2.67	2.66
			Ti	0.01	0.01	0.01	0.01	0.01	0.01	0.01
			Al	2.84	2.79	2.89	2.87	2.79	2.91	2.89
			Cr	0.00	0.00	0.00	0.00	0.00	0.00	0.00
			Ni	0.00	0.00	0.00	0.00	0.00	0.00	0.00
			Fe	2.39	2.29	2.21	2.21	1.99	2.23	2.21
			Mn	0.02	0.02	0.02	0.02	0.02	0.03	0.03
			Mg	1.93	2.04	2.06	2.04	2.25	2.00	2.05
			Ca	0.00	0.00	0.00	0.02	0.14	0.02	0.03
			Na	0.01	0.00	0.00	0.00	0.00	0.00	0.00
			K	0.00	0.00	0.00	0.01	0.00	0.01	0.00
			Sr	0.00	0.00	0.00	0.00	0.00	0.00	0.00
			total	9.88	9.87	9.87	9.87	9.90	9.86	9.88
			charge	27.98	27.98	27.98	28.00	28.00	27.96	27.98
			F	0.01	0.01	0.01	0.00	0.00	0.02	0.01
			Cl	0.00	0.00	0.00	0.00	0.00	0.00	0.00
	apfu	T	Si	2.68	2.71	2.67	2.69	2.69	2.67	2.66
			Al	1.32	1.29	1.33	1.31	1.31	1.33	1.34
			Sum	4.00	4.00	4.00	4.00	4.00	4.00	4.00
		O	Al	1.52	1.50	1.56	1.56	1.48	1.57	1.55
			Fe	2.39	2.29	2.21	2.21	1.99	2.23	2.21
			Mg	1.93	2.04	2.06	2.04	2.25	2.00	2.05
			Mn	0.02	0.02	0.02	0.02	0.02	0.03	0.03
			sum	5.86	5.86	5.86	5.83	5.75	5.82	5.84
			vac	0.14	0.14	0.14	0.17	0.25	0.18	0.16
		OH	F	0.01	0.01	0.01	0.00	0.00	0.02	0.01
			Cl	0.00	0.00	0.00	0.00	0.00	0.00	0.00
			OH	7.97	7.97	7.97	8.00	8.00	7.95	7.98
			Fe#	0.55	0.53	0.52	0.52	0.47	0.53	0.52
			T	363.32	352.25	367.05	359.64	358.77	367.68	369.75

Table A1-7 - Fluid inclusion data from Lansdowne mineralized samples LAN4-2 (LN4-2) and 7157. Qtz-2 indicates second generation quartz. All 7157 samples hosted in quartz, but the generation is undefined. **Eu. = euhedral, Sub. = subhedral, An. = anhedral, Cl. = cluster, elon. = elongate

	Sample	***LN4-2***	***LN4-2***	***LN4-2***	***LN4-2***	***LN4-2***	***LN4-2***	***LN4-2***	***LN4-2***	***LN4-2***	***LN4-2***	***LN4-2***	***LN4-2***	***LN4-2***	***LN4-2***	***LN4-2***
Inclusion ID	Host							Qtz-2	Qtz-2	Qtz-2	Qtz-2	Qtz-2	Qtz-2	Qtz-2	Qtz-2	Qtz-2
	Chip															
	Assemblage	GR1_FIA1	GR1_FIA1	GR1_FIA1	GR1_FIA1	GR1_FIA4	GR1_FIA4	GR1_FIA5	GR1_FIA5	GR1_FIA5	GR1_FIA5	GR1_FIA5	GR1_FIA5	GR1_FIA5	GR1_FIA5	GR1_FIA5
	Type	2	2	2	2	1c	1c	1a	1a	1a	1a	1a	1a	1b	1b	1b
Petrographic characteris	Shape	Sub.	Sub.	Sub.	Sub.	Sub.	Sub.	Sub., elon.	Sub., elon.	Sub., elon.	Sub., elon.	Sub., elon.	Sub., elon.	Sub., elon.	Sub., elon.	Sub., square
	Size (um)	< 7	< 7	< 7	< 7	6	17	< 18	< 18	< 18	< 18	< 18	< 18	6	< 18	6
	Assemblage	Linear	Linear	Linear	Linear	Linear	Linear	Cl.	Cl.	Cl.	Cl.	Cl.	Cl.	Cl.	Cl.	Cl.
Phase proportions	LH2O	100	100	100	100	100	20	90	90	90	90	90	90	40	20	40
	LCO2													40		40
	S															
	V						80	10	10	10	10	10	10	20	80	20
Raman Results	H2O													x	x	x
	CH4					x	x							x	x	x
	CO2														x	
	N2															
Microthermometry Results	Tm(ice)	N/A	N/A	-14.2	-14	N/A		-5.3	-4.8	-5.3	N/A	N/A	N/A	-58.2	-17.5	-4.8
	Tm(s)															
	Tm(calathrate)															
	Th(L)	Decr.	Decr.	Decr.	Decr.			235.9	262.5	295.8	298.9	274.4	212.2	238.0	268.7	
	Th(V)															

	Sample	***LN4-2***	***LN4-2***	***LN4-2***	***LN4-2***	***LN4-2***	***LN4-2***	***LN4-2***	***LN4-2***	***LN4-2***	***LN4-2***	***LN4-2***	***LN4-2***	***LN4-2***	***LN4-2***	***LN4-2***
Inclusion ID	Host	Qtz-2	Qtz-2	Qtz-2	Qtz-2	Qtz-2	Qtz-2	Qtz-2	Qtz-2	Qtz-2	Qtz-2	Qtz-2				
	Chip															
	Assemblage	GR1_FIA5	GR1_FIA5	GR1_FIA6	GR1_FIA6	GR1_FIA6	GR1_FIA6	GR1_FIA6	GR1_FIA6	GR1_FIA6	GR1_FIA6	GR1_FIA8	GR2_FIA1	GR2_FIA1	GR2_FIA1	GR2_FIA1
	Type	1b	2	1a	1a	1a	1a	1a	1a	1b	1b	1a	2	2	2	2
Petrographic characteris	Shape	Sub., square	Sub., elon.	Eu., Sub.	Eu., Sub.	Eu., Sub.	Eu., Sub.	Eu., Sub.	Eu., Sub.	Eu., Sub.	Eu., Sub.	Sub., elon.	Sub., elon.	Sub., elon.	Sub., elon.	Sub., elon.
	Size (um)	6	6	< 12	< 13	< 14	< 15	< 16	< 17	7	7	14	< 14	< 14	< 14	< 14
	Assemblage	Cl.	Cl.	Cl.	Cl.	Cl.	Cl.	Cl.	Cl.	Cl.	Cl.	Cl.	Linear	Linear	Linear	Linear
Phase proportions	LH2O	40	100	95	95	95	95	95	95	20	20	95	100	100	100	100
	LCO2	40														
	S															
	V	20		5	5	5	5	5	5	80	80	5				
Raman Results	H2O	x	x	x						x	x		x			
	CH4	x								x	x					
	CO2			x						x	x					
	N2															
Microthermometry Results	Tm(ice)	-5.3	N/A	-6.1C	-4.9C			-4.5C		-57.6	-57.7	-7.5	-24.4C	-27C	-23.9C	DNF
	Tm(s)															
	Tm(calathrate)					+8.3C	+7.8C		+8.2C							
	Th(L)			183.0	160.0	202.2	297.9	260.0	N/A			N/A	Decr.	Decr.	Decr.	Decr.
	Th(V)															

	Sample	***LN4-2***	***LN4-2***	***LN4-2***	***LN4-2***	***LN4-2***	***LN4-2***	***LN4-2***	***LN4-2***	***LN4-2***	***LN4-2***	***LN4-2***	***LN4-2***	***LN4-2***	***LN4-2***	***LN4-2***
Inclusion ID	Host			Qtz-2	Qtz-2	Qtz-2	Qtz-2	Qtz-2	Qtz-2	Qtz-2	Qtz-2	Qtz-2	Qtz-2	Qtz-2	Qtz-2	Qtz-2
	Chip															
	Assemblage	GR2_FIA1	GR2_FIA1	GR2A_FIA1	GR2A_FIA1	GR2A_FIA1	GR2A_FIA1	GR4B_FIA1	GR4B_FIA1	GR4B_FIA1	GR4B_FIA1	GR4B_FIA1	GR4C_FIA1	GR4C_FIA1	GR4C_FIA1	GR4C_FIA1
	Type	2	2	1a	1a	1a	1a	1a	1a	1a	1a	1a	1a	1a	1a	1a
Petrographic characteris	Shape	Sub., elon.	Sub., elon.	Sub., elon.	Sub., elon.	Sub., elon.	Sub., elon.	Sub., An.	Sub., An.	Sub., An.	Sub., An.	Sub., An.	Sub.	Sub.	Sub.	Sub.
	Size (um)	< 14	< 14	< 12	< 12	< 12	< 12	< 10	< 10	< 10	< 10	< 10	< 13	< 13	< 13	< 13
	Assemblage	Linear	Linear	Linear	Linear	Linear	Linear	Cl.	Cl.	Cl.	Cl.	Cl.	Cl.	Cl.	Cl.	Cl.
Phase proportions	LH2O	100	100	95	95	95	95	95	95	95	95	95	95	95	95	95
	LCO2															
	S															
	V			5	5	5	5	5	5	5	5	5	5	5	5	5
Raman Results	H2O							x					x	x		
	CH4															
	CO2															
	N2															
Microtherm	Tm(ice)	-23.6C	-23.6C	-3.9C	-4C	DNF	-3.9C	-4.9	-5.5	-5	N/A	N/A	-4.4	-3.9	-4.1	-4.4
	Tm(s)															

	Tm(calathrate)															
	Th(L)	Decr.	Decr.	N/A	N/A	N/A	N/A	153.2	171.9	152.7	148.2	154	228.8	227.5	228.3	257
	Th(V)															
	Sample	***LN4-2***	***LN4-2***	***LN4-2***	***LN4-2***	***LN4-2***	***LN4-2***	***LN4-2***	***LN4-2***	***LN4-2***	***LN4-2***	***LN4-2***	***LN4-2***	***LN4-2***	***LN4-2***	***LN4-2***
Inclusion ID	Host	Qtz-2	Qtz-2	Qtz-2									Qtz-2	Qtz-2	Qtz-2	Qtz-2
	Chip															
	Assemblage	GR4C_FIA1	GR4C_FIA1	GR4C_FIA1	GR4D_FIA1	GR4D_FIA1	GR6C_FIA2	GR6C_FIA2	GR6C_FIA2	GR7_FIA1	GR7_FIA1	GR7_FIA1	GR7_FIA2	GR7_FIA2	GR7_FIA2	GR7_FIA4
	Type	1a	1a	1a	1b	1a	2	2	2	1b	1b	1a	1a	1a	1a	1b
Petrographic characteris	Shape	Sub.	Sub.	Sub.	Sub.	Sub.	An., elon.	An., elon.	An., elon.	An.	Sub.	Sub.	Sub.	Sub.	Sub.	Eu., Sub.
	Size (um)	< 13	< 13	< 13	8	15	< 10	< 10	< 10	9	13	11	< 8	< 8	< 8	< 12
	Assemblage	Cl.	Cl.	Cl.	Cl.	Cl.	Linear	Linear	Linear	Linear	Linear	Linear	Cl.	Cl.	Cl.	Linear
Phase proportions	LH2O	95	95	95	20	90	100	100	100	40	20	95	85	85	85	80
	LCO2									40			5	5	5	
	S															
	V	5	5	5	80	10				20	80	5	10	10	10	20
Raman Results	H2O				x	x	x			x	x	x	x			
	CH4				x	x										
	CO2				x	x				x						
	N2															
Microthermometry Results	Tm(ice)	-4.4	-2.2	-3.9	N/A	N/A	-23.8	-23.5	-20.4				-4C	-3.8C	-4.7C	-66.1
	Tm(s)															
	Tm(calathrate)															
	Th(L)	237.6	239.1	260.9			x	x	x				N/A	N/A	N/A	N/A
	Th(V)															
	Sample	***LN4-2***	***LN4-2***	***LN4-2***	***LN4-2***	***LN4-2***	***LN4-2***	***LN4-2***	***LN4-2***	***LN4-2***	***LN4-2***	***LN4-2***	***LN4-2***	***LN4-2***	***LN4-2***	***LN4-2***
Inclusion ID	Host	Qtz-2	Qtz-2	Qtz-2	Qtz-2	Qtz-2	Qtz-2	Qtz-2	Qtz-2	Qtz-2	Qtz-2	Qtz-2	Qtz-2			
	Chip															
	Assemblage	GR7_FIA4	GR7C_FIA1	GR7C_FIA1	GR7C_FIA1	GR7C_FIA1	GR7C_FIA1	GR7C_FIA1	GR8_FIA1	GR8_FIA1	GR8_FIA1	GR8_FIA1	GR8_FIA1	GR8_FIA2	GR8_FIA2	GR8_FIA2
	Type	1b	1a	1a	1a	1a	1a	1a	1c	1c	1c	1c	1c	1c	1b	1b
Petrographic characteris	Shape	Eu., Sub.	Sub., An.	Sub., An.	Sub., An.	Sub., An.	Sub., An.	Sub., An.	Eu., Sub.	Eu., Sub.	Eu., Sub.	Eu., Sub.	Eu., Sub.	Sub.	Sub.	Sub.
	Size (um)	< 12	< 30	< 30	< 30	< 30	< 30	< 30	< 35	< 35	< 35	< 35	< 35	<15	<15	<15
	Assemblage	Linear	Cl.	Cl.	Cl.	Cl.	Cl.	Cl.	Linear	Linear	Linear	Linear	Linear	Cl.	Cl.	Cl.
Phase proportions	LH2O	80	95	95	95	95	95	95						95	20	20
	LCO2															
	S															
	V	20	5	5	5	5	5	5	100	100	100	100	100	5	80	80
Raman Results	H2O								x			x		x	x	x
	CH4								x	x	x	x	x		x	x
	CO2								x						x	x
	N2															
Microthermometry Results	Tm(ice)	-65	-4.8	-1			-5.3	-3.7						-4.5	-60.3	-64.6
	Tm(s)															
	Tm(calathrate)				0.8	2										
	Th(L)	N/A	217.6	227.2	190	259.7	206.8	285.4	-110.3	-110.3	-91.9	-94.2	-94			
	Th(V)															
	Sample	***LN4-2***	***LN4-2***	***LN4-2***	***7157***	***7157***	***7157***	***7157***	***7157***	***7157***	***7157***	***7157***	***7157***	***7157***	***7157***	***7157***
Inclusion ID	Host															
	Chip				3	3	3	3	3	3	4	4	4	4	4	4
	Assemblage	GR12_FIA1	GR12_FIA1	GR12_FIA1	FIA10	FIA10	FIA10	FIA10	FIA10	FIA10	FIA12a	FIA12a	FIA12a	FIA12a	FIA12a	FIA12a
	Type	2	1b	1a	2	2	2	2	2	2	1a	1a	1a	1a	1a	1a
Petrographic character	Shape	Sub.	An.	Sub.	An.	An.	An.	An.	An.	An.	An.	An.	An.	An.	An.	An.
	Size (um)	20	8	5												
	Assemblage	Cl.	Cl.	Cl.	Cl.	Cl.	Cl.	Cl.	Cl.	Cl.	Linear	Linear	Linear	Linear	Linear	Linear
Phase proportions	LH2O	100	20	95	100	100	100	100	100	100	95	95	95	95	95	95
	LCO2															
	S															
	V		80	5							5	5	5	5	5	5
Raman Results	H2O	x		x										x		
	CH4		x													
	CO2															
	N2															
Microthermometry Results	Tm(ice)				-43.6	DNF	DNF	-44.8	-37.3	DNF	-5.9	-8	-6.1	-5.9	-7.6	-5.2
	Tm(s)															
	Tm(calathrate)															
	Th(L)										176.4	193.1	182.2	184.5	N/A	190

	Th(V)															
	Sample	***7157***	***7157***	***7157***	***7157***	***7157***	***7157***	***7157***	***7157***	***7157***	***7157***	***7157***	***7157***	***7157***	***7157***	***7157***
Inclusion ID	Host															
	Chip	4	4	4	4	4	4	4	4	4	4	4	4	4	4	4
	Assemblage	FIA12b	FIA12b	FIA12b	FIA12b	FIA12b	FIA12b	FIA12b	FIA12b	FIA12b	FIA13	FIA13	FIA13	FIA13	FIA13	FIA15
	Type	1a	1a	1a	1a	1a	1a	1a	1a	1c	2	2	2	2	2	1a
Petrographic character	Shape	Sub.	Sub.	Sub.	Sub.	Sub.	Sub.	Sub.	Sub.	Sub.	An.	An.	An.	An.	An.	An.
	Size (um)															
	Assemblage	Cl.	Cl.	Cl.	Cl.	Cl.	Cl.	Cl.	Cl.	Cl.	Cl.	Cl.	Cl.	Cl.	Cl.	Cl.
Phase proportions	LH2O	95	95	95	95	95	95	95	95		100	100	100	100	100	95
	LCO2															
	S															
	V	5	5	5	5	5	5	5	5	100						5
Raman Results	H2O			x							x				x	x
	CH4									x						
	CO2															
	N2															
Microthermnometry Results	Tm(ice)	-5.8	-9	-8.8	-8.9	-7.8	N/A	-8.2	-9.1	N/A	DNF	DNF	DNF	DNF	DNF	DNF
	Tm(s)															
	Tm(calathrate)															
	Th(L)	255.5	173.2	282.9	250.3	293.1	138.8	119.7	263.7	N/A						PEM
	Th(V)															
	Sample	***7157***	***7157***	***7157***	***7157***	***7157***	***7157***	***7157***	***7157***	***7157***	***7157***	***7157***	***7157***	***7157***	***7157***	***7157***
Inclusion ID	Host															
	Chip	4	4	4	4	4	4	4	4	4	4	6	6	6	1	1
	Assemblage	FIA15	FIA15	FIA15	FIA15	FIA15	FIA15	FIA16	FIA16	FIA16	FIA16	FIA19	FIA19	FIA19	FIA2	FIA2
	Type	1a	1a	1a	1a	1a	1a	2	2	2	2	1b	1b	1b	1a	1a
Petrographic character	Shape	An.	An.	An.	An.	An.	An.	An.	An.	An.	An.	Sub.	Sub.	Sub.	An.	An.
	Size (um)															
	Assemblage	Cl.	Cl.	Cl.	Cl.	Cl.	Cl.	Cl.	Cl.	Cl.	Cl.	Cl.	Cl.	Cl.	Cl.	Cl.
Phase proportions	LH2O	95	95	95	95	95	95	100	100	100	100	40	40	40	98	98
	LCO2															
	S															
	V	5	5	5	5	5	5					60	60	60	2	2
Raman Results	H2O											x				
	CH4											x				
	CO2											x				
	N2															
Microthermnometry Results	Tm(ice)	DNF	DNF	DNF	DNF	DNF	DNF	-42.6	-43.6	-43	-43.5	-60.8	-62.7	-94	DNF	DNF
	Tm(s)															
	Tm(calathrate)															
	Th(L)	PEM	134.5	128.8	212.8	186.7	211.5								101	120.5
	Th(V)															
	Sample	***7157***	***7157***	***7157***	***7157***	***7157***	***7157***	***7157***	***7157***	***7157***	***7157***	***7157***	***7157***	***7157***	***7157***	***7157***
Inclusion ID	Host															
	Chip	1	1	1	1	1	1	1	1	1	6	6	6	6	6	6
	Assemblage	FIA2	FIA2	FIA2	FIA2	FIA2	FIA2	FIA2	FIA2	FIA2	FIA20	FIA20	FIA20	FIA20	FIA20	FIA20
	Type	1a	1a	1a	1a	1a	1a	1a	1a	1a	1a	1a	1a	1a	1b	1b
Petrographic character	Shape	An.	An.	An.	An.	An.	An.	An.	An.	An.	Sub.	Sub.	Sub.	Sub.	Sub.	Sub.
	Size (um)															
	Assemblage	Cl.	Cl.	Cl.	Cl.	Cl.	Cl.	Cl.	Cl.	Cl.	Cl.	Cl.	Cl.	Cl.	Cl.	Cl.
Phase proportions	LH2O	95	95	95	95	95	95	95	95	95	95	90	95	90	50	80
	LCO2															
	S															
	V	5	5	5	5	5	5	5	5	5	5	10	5	10	50	20
Raman Results	H2O														x	
	CH4														x	
	CO2														x	
	N2															
Microthermnometry Results	Tm(ice)	-28.1	-23.8	DNF	-18.6	-28.1	-27.6	DNF	DNF	DNF	-7.9	-8.8	-6.9	N/A	-61.8	-8
	Tm(s)															
	Tm(calathrate)															
	Th(L)	226.4	227	226.9	247.8	219	244.1	224.2	205.6	178.9						
	Th(V)										218.6	246.9	243.4	N/A	N/A	N/A
	Sample	***7157***	***7157***	***7157***	***7157***	***7157***	***7157***	***7157***	***7157***	***7157***	***7157***	***7157***	***7157***	***7157***	***7157***	***7157***
In	Host															

	Chip	6	6	6	6	6	6	6	6	6	6	6	6	6	6	7
	Assemblage	FIA21a	FIA21a	FIA21a	FIA21a	FIA21b	FIA21b	FIA21b	FIA22	FIA22	FIA22	FIA22	FIA22	FIA22	FIA22	FIA26
Petrographic character	Type	1c	1c	1c	1c	1a	1c	1c	1b	1b	1b	1b	1b	1b	1b	1a
	Shape	Sub.	Sub.	Sub.	Sub.	Sub.	Sub.	Sub.	Sub.	Sub.	Sub.	Sub.	Sub.	Sub.	Sub.	Sub.
	Size (um)															
	Assemblage	Cl.	Cl.	Cl.	Cl.	Linear	Linear	Linear	Cl.	Cl.	Cl.	Cl.	Cl.	Cl.	Cl.	Cl.
Phase proportions	LH2O	95				95	10	10	30	30	30	30	30	30	30	97
	LCO2															
	S															
	V	5	100	100	100	5	90	90	70	70	70	70	70	70	70	3
Raman Results	H2O					x			x	x					x	
	CH4						x	x	x	x					x	
	CO2						x		x	x					x	
	N2															
Microthermometry Results	Tm(ice)	-13.1	DNF	DNF	DNF	-28.9	-61.9	-94.1	-70	-65	N/A	N/A	-60.3	-66.2	-60.8	-27.8
	Tm(s)															
	Tm(calathrate)															
	Th(L)															
	Th(V)	105.7				Decr.										148.9
	Sample	***7157***	***7157***	***7157***	***7157***	***7157***	***7157***	***7157***	***7157***	***7157***	***7157***	***7157***	***7157***	***7157***	***7157***	***7157***
Inclusion ID	Host															
	Chip	7	7	7	7	8	8	8	8	8	8	8	8	8	8	8
	Assemblage	FIA26	FIA26	FIA26	FIA26	FIA27	FIA27	FIA27	FIA27	FIA28	FIA28	FIA28	FIA28	FIA28	FIA28	FIA28
Petrographic characteris	Type	1a	1b	1c	1c	1a	1c	1c	1c	1a	1a	1a	1a	1a	1a	1a
	Shape	Sub.	Sub.	Sub.	Sub.	Sub., An.	Sub., An.	Sub., An.	Sub., An.	Sub.	Sub.	Sub.	Sub.	Sub.	Sub.	Sub.
	Size (um)															
	Assemblage	Cl.	Cl.	Cl.	Cl.	Linear	Linear	Linear	Linear	Cl.	Cl.	Cl.	Cl.	Cl.	Cl.	Cl.
Phase proportions	LH2O	97	80			97				95	95	95	90	90	95	95
	LCO2		5													
	S															
	V	3	15	100	100	3	100	100	100	5	5	5	10	10	5	5
Raman Results	H2O			x		x						x				
	CH4			x			x					x				
	CO2			x			x					x				
	N2															
Microthermometry Results	Tm(ice)	-27.4	-19.3	-66.3	-68.5	-27.7	-60	-60.2	-60.5	N/A	-3.1	-2.9	-5.9	-5.4	N/A	N/A
	Tm(s)															
	Tm(calathrate)															
	Th(L)									Decr.	164.8	Decr.	284.2	289.2	Decr.	Decr.
	Th(V)	134.6	Decr.			N/A										
	Sample	***7157***	***7157***	***7157***	***7157***	***7157***	***7157***	***7157***	***7157***	***7157***	***7157***	***7157***	***7157***	***7157***	***7157***	***7157***
Inclusion ID	Host															
	Chip	8	8	8	8	8	8	8	8	8	8	8	8	8	8	8
	Assemblage	FIA30	FIA30	FIA30	FIA30	FIA30	FIA30	FIA31a	FIA31a	FIA31a	FIA31a	FIA31a	FIA31a	FIA31a	FIA31a	FIA31a
Petrographic character	Type	2	1b	1b	1b	1b	1b	1a	1a	1a	1a	1a	1a	1a	1a	1a
	Shape	Sub.	Sub.	Sub.	Sub.	Sub.	Sub.	Sub.	Sub.	Sub.	Sub.	Sub.	Sub.	Sub.	Sub.	Sub.
	Size (um)															
	Assemblage	Cl.	Cl.	Cl.	Cl.	Cl.	Cl.	Cl.	Cl.	Cl.	Cl.	Cl.	Cl.	Cl.	Cl.	Cl.
Phase proportions	LH2O	30	30	30	30	30	30	95	95	95	95	95	95	95	95	95
	LCO2															
	S															
	V	70	70	70	70	70	70	5	5	5	5	5	5	5	5	5
Raman Results	H2O	x				x	x	x								
	CH4						x	x								
	CO2					x	x	x								
	N2															
Microthermometry Results	Tm(ice)	DNF	-60.8	-60.5	-60.9	-60.9	-45.5	-7	-5	-7.1	-7.1	-7.1	-8.3	-8	-6.9	-6.5
	Tm(s)															
	Tm(calathrate)															
	Th(L)							Decr.	Decr.	Decr.	Decr.	Decr.	Decr.	Decr.	N/A	N/A
	Th(V)															
	Sample	***7157***	***7157***	***7157***	***7157***	***7157***	***7157***	***7157***	***7157***	***7157***	***7157***	***7157***	***7157***	***7157***	***7157***	***7157***
Inclusion ID	Host															
	Chip	8	6		8	8		8	8	8	8	4	4	4	4	4
	Assemblage	FIA31a	FIA31b	FIA31b	FIA31b	FIA31b	FIA31b	FIA31b	FIA31b	FIA31b	FIA31b	FIA4	FIA4	FIA4	FIA4	FIA7

Petrographic character	Type	1a	1b	1b	1b	1b	1b	1b	1b	1c	1c	2	2	1a	1a	1a
	Shape	Sub.	Sub.		Sub.	Sub.		Sub.	Sub.	Sub.	Sub.	Sub.	Sub.	Sub.	Sub.	Sub.
	Size (um)															
	Assemblage	Cl.	Cl.		Cl.	Cl.		Cl.	Cl.	Cl.	Cl.	Cl.	Cl.	Cl.	Cl.	Cl.
Phase proportions	LH2O	95	10	10	10	10	10	10	10			100	100	95	90	95
	LCO2															
	S															
	V	5	90	90	90	90	90	90	90	100	100			5	10	5
Raman Results	H2O		x		x					x		x		x	x	
	CH4		x		x					x						
	CO2		x		x					x						
	N2															
Microthermometry Results	Tm(ice)	-6.9	-63	-61.6	-57.2	-60.4	N/A	-60.9	-61.4			DNF	DNF	DNF	DNF	-26.3
	Tm(s)															
	Tm(calathrate)															
	Th(L)	Decr.														249.2
	Th(V)		11.5		10.2	17.3		5.9	15.8	8.1	17.4			209.2	289	
	Sample	***7157***	***7157***	***7157***	***7157***	***7157***	***7157***	***7157***	***7157***	***7157***	***7157***	***7157***	***7157***	***7157***	***7157***	***7157***
Inclusion ID	Host															
	Chip	4	4	4	4	3	3	3	3	3	3	3	3	3	3	3
	Assemblage	FIA7	FIA7	FIA7	FIA7	FIA8	FIA8	FIA8	FIA8	FIA8	FIA8	FIA8	FIA9	FIA9	FIA9	FIA9
Petrographic character	Type	1a	1a	1a	1a	1a	1a	1a	1a	1a	1a	1a	1a	1a	1a	1a
	Shape	Sub.	Sub.	Sub.	Sub.	An.	An.	An.	An.	An.	An.	An.	Sub.	Sub.	Sub.	Sub.
	Size (um)															
	Assemblage	Cl.	Cl.	Cl.	Cl.	Cl.	Cl.	Cl.	Cl.	Cl.	Cl.	Cl.	Cl.	Cl.	Cl.	Cl.
Phase proportions	LH2O	95	95	95	95	95	95	95	95	95	95	95	95	95	95	95
	LCO2															
	S															
	V	5	5	5	5	5	5	5	5	5	5	5	5	5	5	5
Raman Results	H2O				x		x								x	
	CH4															
	CO2														x	
	N2															
Microthermometry Results	Tm(ice)	-13.1	-10.9	-8.3	-8.2	-21.2	-9	-25.6	-25.6	-9.8	-25.6	N/A	DNF	-27.2	DNF	-27.5
	Tm(s)															
	Tm(calathrate)															
	Th(L)	264.5	Decr.	274.2	233.8	220.8	208.2	202.9	183.5	219.6	PEM	235.9	187	204	225.1	232.9
	Th(V)															
	Sample	***7157***	***7157***	***7157***	***7157***	***7157***	***7157***	***7157***	***7157***							
Inclusion ID	Host															
	Chip	3	3	3	3	3	3	3	3							
	Assemblage	FIA9	FIA9	FIA9	FIA9	FIA9	FIA9	FIA9	FIA9							
Petrographic character	Type	1a	1a	1a	1a	1a	1a	1a	1a							
	Shape	Sub.	Sub.	Sub.	Sub.	Sub.	Sub.	Sub.	Sub.							
	Size (um)															
	Assemblage	Cl.	Cl.	Cl.	Cl.	Cl.	Cl.	Cl.	Cl.							
Phase proportions	LH2O	95	90	95	95	95	95	95	95							
	LCO2															
	S															
	V	5	10	5	5	5	5	5	5							
Raman Results	H2O															
	CH4															
	CO2															
	N2															
Microthermometry Results	Tm(ice)	-27.9	-26.9	-28	-27.6	N/A	N/A	N/A	N/A							
	Tm(s)															
	Tm(calathrate)															
	Th(L)	215.9	*>400*	218.8	275.5	229.3	241	228.8	254.3							
	Th(V)															

Table A1-8 - SEM results of decrepitate mound analyses. All results in wt.% Analyses which did not strike a salt were removed.

	O	*Na*	*Mg*	*Cl*	*K*	*Ca*	*Fe*	*Sb*	*Pb*	*Ti*	*Al*	*As*	*Mn*	*Br*	*Ni*	*Ba*	*P*	*Mo*	*Sc*
LN4-2																			
		54.55		34.59															
		45.17		50.01															
		22.32		27.36		37.13													
		38.35		52.26		7.04													
		26.97		33.8		32.96													
		32.88		48.37		14.68													
		30.13		40.45		22.95													
		6.98		11.8		14.41													
		38.35		52.26		37.13													
		22.32		27.36		7.04													
		8.28		3.13	2.95	62.63	4.17				11.59								
		44.16		55.84															
		41.8		51.52	1.26	2.31													
		39.29		51.25		5.08													
		30.13		42.78		21.71													
		43.9		51.74	1.57														
		30.78		48.13	1	12.98	0.95												
		30.81		42.96	0.89	16.28	2.56												
		33.71		46.06		13.93													
		39.7		47.06		5.25		7.99											
		38.43		44	0.97	5.43		11.18											
		35.71		44.63		8.03		11.63											
		37.49		44.23		5.09		13.19											
		36.33		47.41	3.57	5.11		7.58											
		33.92		53.43	6.16	6.49													
		15.38		37.26		19.55		27.81											
		37.6		49.02		3.96		9.42											
		37.11		47.42	3.08	3.5		8.9											
		34.7		43.27		8.64		13.39											
		34.12		39.8		9.09		17											
		34.41		41.53		8.86		15.19											
		0.41		2.45		0.32		2.55											
		34.14		42.78		10.52		12.56											
		18.12		22.88		17.49		41.52											
		31.95		38.76		8.3		20.99											
		32.25		34.36		7.62		25.77											
		36.83		42.96		4.69		15.51											
		30.66		36.35		9.72		23.27											
		7.28		8.31		4.81		11.4											
		40.91		50.68	2.52			5.89											
		34.47		47.37	4.61	5.9		7.65											
		41.06		49.74	1.29			7.9											
		35.37		50.1	2.35			12.18											
		42.16		51.37	2.16			4.31											
		42.41		43.18	2.24			12.16											
		41.9		45.75	2.54			9.81											
		42.09		50.65	2.61			4.66											
		36.65		48.88	1.64	5.22		7.61											
		37.11		51		3.45		8.43											
		41.88		50.53	1.5	2.27		3.83											
		48.78		32.27				13.04											
		42.49	14.11	24.48	5.42	13.49													
		40.09		55.76	2.09	2.06													
		40.78		54.63	4.59														
		33.39		48.25		6.3		8.4			1.51								
		32.46		44.07		10.37		10.52											
		7.64		4.24		1.4	45.8	2.68											
		6.61		1.22		1.77	46.94												
		15.62		2.46		7.45	34.07								7.95				
		48.33		46.41															
		45.04		53.34															
		44.78		52	1.03														
		46.56		51.5															
		45.77		52.46															
		52.7		42.54															
		49.29		46.05															
		47.51		48.63	1.44														
		36.91	8.82	16.61	1.92	11.39								20.53					
		32.95		41.29		9.53	3.5									5.47			
		36.78		51.3		7.38	1.5												
		40.13		52.68		3.22	1.58												
		37.65		53.69		4.17	1.42												
		52.9		38.19															
		7.18		4.72			50.09												
		5.29		7.13			43.87								8.22				
		40.52		58.55															
		38.39		48.62	2.61	2.24		5.24											
		35.49		51.84		8.02	1.75												
		40.05		44.2	2.61	2.78		6.89											
LN7157		34.26		50.26		9.2						4	0.96						
		32.01		52.14		7.99						6.35	0.99						

	37.53	12.76	15.76	3.1	20.53				8.65							
	26.73		44.62		10.83		10.42			5.3	0.64					
	38.86		54.43		5.38						0.62					
	30.49		53.5		9.07					5.43						
	38.84		54.78	0.67	2.98					2.12						
	36.18		51.17		5.83				1.91	2.87	1.05					
	30.61		57.64	0.66	6.36	0.76				3.17	0.79					
	19.1	12.14	12.54		25.77									30.45		
	23.93		46.42		16.22	1.2				8.42	1.45					
	37.01		53.07		5.13					3.51						
	39.12		52.51		4.73					3.65						
	34.22		53.21	1.08	5.47					3.9	1.12					
	34.82		53.65		4.47	0.63				0.74	0.92	4.16				
	39.65		49.24		5.55					3.75						
	7.23		30.28		19.29	9.92				19.03	10.14					
	29.86		47.51		11.65	1.2				6.28	1.78					
	36.66		54.4	0.79	4.23					2.44	0.84					
	41.32		55.86	0.53	1.86											
	33.99		58.75		2.9					2.99						
64.73	0.36	0.34	0.18		0.34											
	27.94		54.04		10.77					2.26	0.6	3.87				
	24.64		51.87		11.55	0.94				3.96	1.54	4.29				
	25.07		56.17	0.81	12.03					4.6	1.33					
	33.23		50.51		8.4					5.65	1.36					
	22.57		49.16		17.87					7.39	1.52					
	22.21		52.25		16.4					6.29	1.26					
	31.82		52.96		10.34					4.02						
	26.62		51.44		13.9					6.48	0.9					
	27.68		53.84	0.64	10.91	0.74				4.64	0.58					
	30.74		53.8		9.85	0.76				3.34	0.64					
	23.55		46.18	1.43	18.94					7.29	1.15					
	30.62		45.01		14.79					9.58						
	44.17		49.83		3.35											
	47.03		47.39													
	56.35		43.65													
	30.36		50.76	1.12	11.89					4.56						
	37.03		53.53		5.4					3.45						
	27.64		51.41		12.95					5.26	1.12					
	27.44		49.87		12.69					8.12	1.88					
	31.55		47.94		7.8		7.77			4.95						
	30.13		60.44	0.79	4.82					3.2						
	35.49		53.95	0.58	5.73					3.06	0.73					
	35.33		53.7	1.41	3.82					4.3	0.86					
	33.98		55.92	1.48	4.27					3.35						
	43.84		55.15													
	43.1		54							2.01						
	41.79		50.58		1.06		2.52			2.89						
	43.85	3	49.28	1.39	2.49											
	46.91		53.09													
	45.56		51.81													
	33.86		51.18	0.85	5.33	0.75				5.85	1.2					
	36.98		42.2		6.26					9.88						
56.12	1.81		1.57													
	29.8		55.55		8.23					3.04	1.27					
	35.59		55.21		7.99											
	35.6		43.71		5.93		7.06			5.07						
	35.63		53.01		7.05					2.73						
	37.02		51.68		6.76					3.24						
	28.52		46.46		9.03		10.16			3.62	0.65					
	30.96		36.93		9.83		13.71			4.54	1.5					
	32.14		43.82	3.5	6.76		8.11			3.88						
	30.45		44.18		8.65		12.87			2.28						
	43.96		50.54				2.28									
	45.18		48.95													
	48.07		40.47				2.5									
	30.22		18.68	2.7	7.02		21.26			11.24						
41.92	0.99		0.47	0.48		1.43	9.54	21.94								
	32.82		38.13	2.77	4.99		11.24			6.9						
	40.23		47.37	7.58												
	45.27		46.42	3.5												
	34.38		50.88	0.87	4.75		6.01			2.52						
	30.52		55.43		10.26					2.05	0.63					
	32.03		53.32	0.72	9.31					2.62	0.78					
	29.22		54.17		10.76					3.48	1.47					
	35.13		46.33		10.3		6.94									
	37.11		47.66		9.69											
	36.52		50.33		7.42					2.25						
	32.92		46.56	3.97	8.59	0.91				3.77	1.35					
	43.7		52.89													
	42.98		46.37				5.59									
	42.32		54.76	1.05												
	48.24		27.1				13.63									
	25.55		57.43		11.92				1.26	1.06	1.25					0.77
	29.08		59.15		8.62						1.27				1.88	
	33.89		53.67		8.48					2.53	0.83					

32.85		46.76		8.08		10.87					1.43					
34.32		55.31	2.22	7.05												
40.02		53.94	5.42													
42.54		50.27	7.19													
35.5		56.21		6.03	0.62						1.06					
31.64		52.13	0.79	7.42	2.05					2.01	2.37					
39.42		55.07	0.59	4.92												
39.72		56.25	0.91	2.49												
35.81		56.45		6.29							0.92					
40.62		50.21		4.59		4.58										
39.86		53.88	0.5	4.92							0.84					
41.3		58.7														
40.86	2.16	53.87	1.01	2.09												
41.81	7.38	39.77	3.39	7.66												
39.92	6.73	34.67	2.59	7.41					7.12							
32.22		37.14					23.89			1.54						
46.58	23.45	4.45	6.13	19.37												
45.62	22.45	6	7	18.93												
44.42	25.89	4.35	5.93	19.41												
32.96	9.52	12.37	1.35	4.99	31.38	7.43										
40.16	17.79	18.86	6.15	17.04												
34.5	20.42	14.42		20.91												
14.67		4.09			2.08	29.68				3.58						
41.21	19.29	1.45	4.19	18.77					13.02							
41.37	17.64	2.01	4.44	19.94					14.6							
44.84	12.93	31.53		10.69												
21.41	4.8	6.79	2.19	6.26	6.17	16.89	17.86		6.5	1.12						
18.7	4.66	8.19	9.3	9.45	8.04			8.3	18.46					7.44		
40.38		56.53		3.1												
33.35	7.4	10.84	19.49	18.48												
31.59		56.53	0.95	5.94					1.61	2.28	1.11					
32.63		55.2	1.37	6.25						3.16	0.94					
36.5		55.57		4.99	1.86						1.08					
34.01		56.54	0.73	3.58						1.95		3.19				
37.27		46.13	1.07	6.76	1.2					5.04	1.55					
36.68		53.58	1.01	2.6						2.86					3.28	
39.46		53.33		2.15						5.06						
37.16		53.66	1.18	3.23						4.07						
41.05		53.68		2.04						2.59						
42.04		54.46		0.78						2.72						
7.94		44.92	1.61	31.2						5.6	2.63					1.91
21.54		57.49		12.77						3.1	1.07	2.5				
35.4		55.45		9.15												
28.99		57.63		13.38												
37.43		49.94		9.46												
28.97		54		15.1							1.92					
19.93		56.58	1.17	12.09	0.69				1.48	5.38	0.91					1.23
25.62		56.04		13.39						3.09						0.84
27.67		57.04		8.11						2.57	0.65	3.34				0.62
31.1		52.47		9.04						2.18	0.82	3.44				
27.85		41.97		13.88		11.38				3.46						
24.82		59.56		9.28						3.85	1.35					
25.31		44.82		12.3		13.27				3.04						
27.44		56.23		12.83							2.21					
15.83		30.02		15.83		26.18				7.19	2.02					
32.72		39.73		8.95		11.57				3.53						
35.17		40.68		5.03		11.09				4.16						
29.66		36.86		8.29		15.38				6.64						
32.13		35.33		6.43		15.94				5.17						
28.91		51.3		11.71						5.68						

Table A1-9 - Sulfur isotope results from sulfides analyzed at the Lansdowne occurrence

Sample-spot ID	Mineral	$\delta^{34}S$ (‰)	1σ (‰)
7157-Aspy-1	Arsenopyrite	25.1	0.3
7157-Aspy-2	Arsenopyrite	24.6	0.3
7157-Aspy-3	Arsenopyrite	23.0	0.3
7157-Aspy-4	Arsenopyrite	23.4	0.3
7157-Aspy-5	Arsenopyrite	23.7	0.3
LAN2-2-Py-1	Pyrite	15.1	0.3
LAN2-2-Py-2	Pyrite	14.7	0.3
LAN2-2-Py-3	Pyrite	14.7	0.3
LAN2-2-Ccp-1	Chalcopyrite	19.6	0.3
LAN2-2-Ccp-2	Chalcopyrite	18.8	0.3
LAN2-2-Ccp-3	Chalcopyrite	19.4	0.3
LAN2-2-Po-1	Pyrrhotite	15.0	0.3
LAN2-2-Po-2	Pyrrhotite	16.3	0.3
LAN2-2-Po-3	Pyrrhotite	16.1	0.3
LAN2-2-Po-4	Pyrrhotite	15.6	0.3
LAN2-3-Aspy-1	Arsenopyrite	16.1	0.3
LAN2-3-Aspy-2	Arsenopyrite	15.5	0.3
LAN2-3-Aspy-3	Arsenopyrite	14.1	0.3
LAN2-3-Aspy-4	Arsenopyrite	15.2	0.3
LAN2-3-Aspy-5	Arsenopyrite	15.7	0.3
LAN2-3-Aspy-6	Arsenopyrite	14.9	0.3
LAN2-3-Aspy-7	Arsenopyrite	15.1	0.3
LAN2-3-Aspy-8	Arsenopyrite	15.8	0.3
LAN-3-2-Py-7	Pyrite	18.3	0.3
LAN-3-2-Py-8	Pyrite	17.9	0.3
LAN-3-2-Py-9	Pyrite	17.9	0.3
LAN-3-2-Py-4a	Pyrite	22.8	0.3
LAN-3-2-Py-1	Pyrite	18.2	0.3
LAN-3-2-Py-2	Pyrite	17.1	0.3
LAN-3-2-Py-3	Pyrite	23.1	0.3

Table A1-10 - Whole rock geochemistry results of unmineralized samples from Lansdowne

Analyte Symbol	Unit Symbol	Detection Limit	Analysis Method	2020NW LAN 2-10	2020NW LAN 2-13	2020NW LAN 2-14	2020NW LAN 2-15	2020NW LAN 2-16	2020NW LAN 2-17	2020NW LAN 2-18	2020NW LAN 2-19
Co3O4	%	0.005	FUS-XRF	< D.L.	< D.L.	0.006	0.008	< D.L.	< D.L.	< D.L.	0.006
CuO	%	0.005	FUS-XRF	< D.L.	< D.L.	0.007	0.009	< D.L.	< D.L.	< D.L.	0.008
NiO	%	0.003	FUS-XRF	0.011	0.004	0.011	0.045	< D.L.	< D.L.	0.047	0.008
SiO2	%	0.01	FUS-XRF	42.12	37.7	37.78	40.69	63.2	54.15	43.85	58.66
Al2O3	%	0.01	FUS-XRF	17.16	14.38	16.55	10.37	15.85	17.83	15.47	12.2
Fe2O3(T)	%	0.01	FUS-XRF	8.24	11.83	11.46	12.52	8	4.94	11.21	8.6
MnO	%	0.001	FUS-XRF	0.337	0.291	0.148	0.162	0.073	0.259	0.141	0.1
MgO	%	0.01	FUS-XRF	1.83	4.97	5.54	13.75	1.66	1.66	4.52	3.06
CaO	%	0.01	FUS-XRF	12.41	11.61	9.65	7.28	1.49	7.21	7.79	4.8
Na2O	%	0.01	FUS-XRF	1.57	2.12	0.23	1.66	1.38	0.42	4.88	0.08
K2O	%	0.01	FUS-XRF	2.58	0.89	2.63	2.37	2.66	3.72	0.4	2.5
TiO2	%	0.01	FUS-XRF	0.81	4.33	3.86	2.4	0.81	0.79	3.25	3.49
P2O5	%	0.01	FUS-XRF	0.1	0.57	0.46	0.41	0.09	0.1	0.65	0.31
Cr2O3	%	0.01	FUS-XRF	0.03	0.01	0.04	0.1	0.01	0.01	0.04	0.01
V2O5	%	0.003	FUS-XRF	0.011	0.062	0.06	0.037	0.012	0.017	0.044	0.067
LOI	%		GRAV	12.09	11.4	10.75	7.2	3.81	8.46	7.43	4.9
Total	%	0.01	FUS-XRF	99.29	100.2	99.18	99	99.05	99.57	99.74	98.8
B	ppm	20	TD-MS	< D.L.	< D.L.	< D.L.	< D.L.	< D.L.	< D.L.	< D.L.	< D.L.
Li	ppm	0.5	TD-MS	123	112	137	72.9	82.9	71	74.8	78.3
Na	%	0.01	TD-MS	1.22	1.43	0.18	1.14	1.06	0.34	> 3.00	0.07
Mg	%	0.01	TD-MS	1.1	2.71	3.24	7.83	1.07	1.03	2.93	1.75
Al	%	0.01	TD-MS	8.73	6.49	8.44	4.88	7.86	9.61	7.71	6.23
K	%	0.01	TD-MS	2.69	0.89	2.77	2.44	2.72	4	0.43	1.77
Ca	%	0.01	TD-MS	9.25	7.37	6.77	4.78	1	5.34	5.76	3.32
Cd	ppm	0.1	TD-MS	1.4	0.2	0.3	0.1	< D.L.	0.3	0.1	0.3
V	ppm	1	TD-MS	55	84	84	151	74	42	98	165
Cr	ppm	1	TD-MS	59	32	127	316	73	59	37	26
Mn	ppm	1	TD-MS	2600	1960	1160	1200	586	2040	1130	788
Fe	%	0.01	TD-MS	5.66	6.93	7.55	8.1	5.11	3.42	7.8	5.71
Hf	ppm	0.1	TD-MS	2	0.6	1.8	2.8	3.9	2.4	2	1.5
Ni	ppm	0.5	TD-MS	27.8	32.9	101	348	37.6	34.3	26.1	28.5
Er	ppm	0.1	TD-MS	3.3	1.8	2.1	1.5	2.4	2.5	2.2	1.4
Be	ppm	0.1	TD-MS	2.7	1.9	2.8	1.4	2.5	3.4	2.1	2.2
Ho	ppm	0.1	TD-MS	1.1	0.8	0.9	0.6	0.8	0.8	0.9	0.6
Hg	ppb	10	TD-MS	70	90	80	40	50	50	80	90
Ag	ppm	0.05	TD-MS	0.12	< D.L.	0.1	0.11	0.27	0.08	< D.L.	0.11
Cs	ppm	0.05	TD-MS	3.48	0.87	2.34	27.1	3.79	4.21	1.02	2.01
Co	ppm	0.1	TD-MS	15	31.4	48.3	68.6	17.8	15.9	35.9	46.7
Eu	ppm	0.05	TD-MS	1.96	2.7	2.1	1.72	1.52	1.94	2.58	1.67
Bi	ppm	0.02	TD-MS	0.04	< D.L.	0.05	0.03	0.8	0.12	0.02	0.07
Se	ppm	0.1	TD-MS	0.7	0.3	0.6	0.8	0.8	0.4	0.6	0.5
Zn	ppm	0.2	TD-MS	380	177	161	102	103	87.4	106	85.2
Ga	ppm	0.1	TD-MS	22.5	21.4	22.9	15.4	20.5	24.6	25.2	16
As	ppm	0.1	TD-MS	8.8	11.7	19.7	2	3.5	18.3	2.1	15.9
Rb	ppm	0.2	TD-MS	153	33.8	82.4	110	142	189	11.8	73.7
Y	ppm	0.1	TD-MS	30	17.6	22	16.6	22.6	23	21.5	14.1
Zr	ppm	1	TD-MS	73	25	68	117	134	82	118	62
Nb	ppm	0.1	TD-MS	7.1	0.3	0.9	7.3	17.4	4.6	1	0.4
Mo	ppm	0.05	TD-MS	1.79	0.09	0.19	1.28	0.38	0.13	0.2	0.35
In	ppm	0.1	TD-MS	< D.L.	< D.L.	0.1	< D.L.	< D.L.	< D.L.	< D.L.	< D.L.
Sn	ppm	1	TD-MS	2	2	< D.L.	1	3	2	< D.L.	1
Sb	ppm	0.1	TD-MS	18	1.6	10.6	5.5	4	8.6	< D.L.	5.8
Te	ppm	0.1	TD-MS	< D.L.	< D.L.	< D.L.	< D.L.	< D.L.	< D.L.	< D.L.	< D.L.
Ba	ppm	1	TD-MS	551	304	1060	678	548	784	317	644
La	ppm	0.1	TD-MS	49.3	36.2	36.3	25.8	48.5	51.8	38.6	23.3
Ce	ppm	0.1	TD-MS	93.8	77.3	73.7	53.5	95.8	101	80.6	47.4
Pr	ppm	0.1	TD-MS	11	9.5	9.2	6.4	10.5	11.7	9.6	5.8
Nd	ppm	0.1	TD-MS	42	39.6	38.6	27.4	40.5	45.7	39.4	25.4
Sm	ppm	0.1	TD-MS	7.6	8.1	7.4	4.8	7	7.2	8.1	4.7
Gd	ppm	0.1	TD-MS	7.3	7.6	7.1	5.2	6.5	6.6	7.6	4.6
Tb	ppm	0.1	TD-MS	1.1	1	1.1	0.7	0.9	0.9	1.1	0.7
Dy	ppm	0.1	TD-MS	5.7	4.7	5.2	3.8	4.5	4.6	5.4	3.2
Cu	ppm	0.2	TD-MS	5	15.6	63.8	52.3	30.2	13.9	25.8	57.4
Ge	ppm	0.1	TD-MS	0.9	0.1	0.2	0.3	0.2	0.4	0.1	0.5
Tm	ppm	0.1	TD-MS	0.5	0.2	0.2	0.2	0.3	0.3	0.3	0.2
Yb	ppm	0.1	TD-MS	3.4	1.1	1.6	1.1	2.3	2.3	1.5	1.1
Lu	ppm	0.1	TD-MS	0.5	0.2	0.2	0.1	0.4	0.3	0.2	0.2
Ta	ppm	0.1	TD-MS	0.5	< D.L.	< D.L.	0.1	1.3	0.2	< D.L.	< D.L.
Sr	ppm	0.2	TD-MS	209	507	268	637	121	217	1180	175
W	ppm	0.1	TD-MS	0.7	0.3	< D.L.	0.1	1.8	0.2	< D.L.	< D.L.
Re	ppm	0.001	TD-MS	0.014	0.003	0.002	0.003	0.002	0.002	0.003	0.003
Tl	ppm	0.05	TD-MS	1.29	0.12	0.26	0.49	0.64	0.87	< 0.05	0.28

Pb	ppm	0.5	TD-MS	53.5	4	15.5	12	73.8	19.3	9.9	50.9
Th	ppm	0.1	TD-MS	14.7	2.9	4.3	2.7	16	15.5	4.5	2.4
U	ppm	0.1	TD-MS	6.3	0.8	1.7	0.9	3	2.9	1.4	0.7

Table A1-11 - Whole rock geochemistry results of mineralized samples

Analyte Symbol	Unit Symbol	Detection Limit	Analysis Method	2020NW LAN 2-11 (mineralized)	2020NW LAN 2-12 (mineralized)
Sb	%	0.01	FUS-Na2O2	1.18	
Pb	%	0.01	FUS-Na2O2		0.57
Zn	%	0.01	FUS-Na2O2	1.15	
As	%	0.01	FUS-Na2O2		> 10.0
Co3O4	%	0.005	FUS-XRF	< D.L.	0.05
CuO	%	0.005	FUS-XRF	0.081	0.008
NiO	%	0.003	FUS-XRF	0.005	< D.L.
SiO2	%	0.01	FUS-XRF	58.1	24.76
Al2O3	%	0.01	FUS-XRF	5.39	2.41
Fe2O3(T)	%	0.01	FUS-XRF	5.91	29.75
MnO	%	0.001	FUS-XRF	0.178	0.1
MgO	%	0.01	FUS-XRF	2.52	3.66
CaO	%	0.01	FUS-XRF	8.31	4.78
Na2O	%	0.01	FUS-XRF		< D.L.
K2O	%	0.01	FUS-XRF	0.54	0.05
TiO2	%	0.01	FUS-XRF	1.44	0.86
P2O5	%	0.01	FUS-XRF	0.15	0.12
Cr2O3	%	0.01	FUS-XRF	0.01	0.01
V2O5	%	0.003	FUS-XRF	0.027	0.013
LOI	%		GRAV	6.74	22.5
Total	%	0.01	FUS-XRF	89.4	89.09
Al	%	0.01	FUS-Na2O2	2.87	1.28
As	ppm	5	FUS-MS-Na2O2	85	> 10000
B	ppm	10	FUS-MS-Na2O2	< D.L.	< D.L.
Ba	ppm	3	FUS-MS-Na2O2	177	58
Be	ppm	3	FUS-MS-Na2O2	< D.L.	< D.L.
Bi	ppm	2	FUS-MS-Na2O2	< D.L.	< D.L.
Ca	%	0.01	FUS-Na2O2	7.25	3.86
Cd	ppm	2	FUS-MS-Na2O2	409	< D.L.
Ce	ppm	0.8	FUS-MS-Na2O2	21	9.4
Co	ppm	0.2	FUS-MS-Na2O2	12.5	351
Cr	ppm	30	FUS-MS-Na2O2	90	110
Cs	ppm	0.1	FUS-MS-Na2O2	1.1	1
Cu	ppm	2	FUS-MS-Na2O2	689	67
Dy	ppm	0.3	FUS-MS-Na2O2	2.3	1.1
Er	ppm	0.1	FUS-MS-Na2O2	1	0.7
Eu	ppm	0.1	FUS-MS-Na2O2	1.5	0.7
Fe	%	0.05	FUS-Na2O2	4.52	21.9
Ga	ppm	0.2	FUS-MS-Na2O2	10.6	5.5
Gd	ppm	0.1	FUS-MS-Na2O2	3.3	2
Ge	ppm	0.7	FUS-MS-Na2O2	2.1	1.6
Ho	ppm	0.2	FUS-MS-Na2O2	0.4	< D.L.
Hf	ppm	10	FUS-MS-Na2O2	< D.L.	< D.L.
In	ppm	0.2	FUS-MS-Na2O2	0.5	< D.L.
K	%	0.1	FUS-Na2O2	0.5	< D.L.
La	ppm	0.4	FUS-MS-Na2O2	9.3	4
Li	ppm	3	FUS-MS-Na2O2	68	50
Mg	%	0.01	FUS-Na2O2	1.55	0.85
Mn	ppm	3	FUS-MS-Na2O2	1370	728
Mo	ppm	1	FUS-MS-Na2O2	4	6
Nb	ppm	2.4	FUS-MS-Na2O2	14.1	3.1
Nd	ppm	0.4	FUS-MS-Na2O2	12.4	6.1
Ni	ppm	10	FUS-MS-Na2O2	30	50
Pb	ppm	0.8	FUS-MS-Na2O2	> 5000	> 5000
Pr	ppm	0.1	FUS-MS-Na2O2	3	1.2
Rb	ppm	0.4	FUS-MS-Na2O2	16	2.8
S	%	0.01	FUS-Na2O2	1.89	11.2
Sb	ppm	2	FUS-MS-Na2O2	> 5000	2170
Se	ppm	8	FUS-MS-Na2O2	< D.L.	< D.L.
Si	%	0.01	FUS-Na2O2	28.8	11.6
Sm	ppm	0.1	FUS-MS-Na2O2	2.9	1.4
Sn	ppm	0.5	FUS-MS-Na2O2	11.2	3.3
Sr	ppm	3	FUS-MS-Na2O2	205	161
Ta	ppm	0.2	FUS-MS-Na2O2	1	0.5
Tb	ppm	0.1	FUS-MS-Na2O2	0.4	0.3
Te	ppm	6	FUS-MS-Na2O2	6	< D.L.

Th	ppm	0.1	FUS-MS-Na2O2	1.2	0.7
Ti	%	0.01	FUS-Na2O2	0.94	0.45
Tl	ppm	0.1	FUS-MS-Na2O2	0.2	0.2
Tm	ppm	0.1	FUS-MS-Na2O2	0.1	< D.L.
U	ppm	0.1	FUS-MS-Na2O2	0.4	0.3
V	ppm	5	FUS-MS-Na2O2	162	75
W	ppm	0.7	FUS-MS-Na2O2	12.7	12.5
Y	ppm	0.1	FUS-MS-Na2O2	10.6	5.6
Yb	ppm	0.1	FUS-MS-Na2O2	1	0.5
Zn	ppm	30	FUS-MS-Na2O2	> 10000	50

Appendix II

Data related to Chapter 3: Antimony and REE mineralization at the Cape St. Mary's polymetallic (Sb-REE-As-Co-Ni-Au-Ag-Bi-Pb) occurrences, Meguma Terrane, southwest Nova Scotia

Table A2-1 - Samples collected from the Cape St Mary's study area, locations, mineralization, context for collection, and analyses conducted

Sample ID	Year/month collected	Occurrence (easting/northing)	Host Rock [a]	Veining	Mineralization [b]	Context for collection	Analyses [c]
MB12	July/2019	Mavillette Beach (723961/4885617)	WRF	Quartz		Representative barren qtz vein WRF	Pet
CM12	July/2019	Ankerite Breccia (723487/4884960)	BRF	Quartz		Representative barren qtz vein BRF	Pet, EPMA
CM21	July/2019	Ankerite Breccia (723487/4884960)	BRF	Quartz - Ankerite	Flo-Ms-Ap	Qtz-ank with mineralization	Pet, SEM
DSH1	Sept/2019	Galena Occ. (723984/4890000)	BRF			Representative unaltered BRF host rock	Pet
MQ22	Sept/2019	Mavillette Gabbro (725262/4887793)	MG		Pl-Aug-Chl-Ap	Representative Mavillette Gabbro	Pet, SEM, EPMA
B1-92-G011	1992	Deerfoot Trail Sb	BRF	Siderite	Ctsb-Tt-Cpy-Stb-Plg-Sb-Bi	Collected by G. O'Reilly	Pet, SEM
B1-92-G012	1992	Deerfoot Trail Sb	BRF	Siderite	Apy-Flo-Tt-Fr-	Collected by G. O'Reilly	Pet, SEM, SIMS
B1-92-G013	1992	Mavillette Beach	WRF	Quartz	Boul-Jm-Gal-Py	Collected by G. O'Reilly	Pet, SEM
B1-92-G015	1992	Deerfoot Trail Sb	BRF	Siderite	Ctsb-Tt-Cpy-Stb-Sb-Bi	Collected by G. O'Reilly	Pet, SEM, WRG
B1-92-G018	1992	Deerfoot Trail Sb	BRF	Siderite		Collected by G. O'Reilly	
B1-97-G004	1997	Galena Occ.	BRF	Quartz		Collected by G. O'Reilly	Pet, SEM, SIMS
B1-97-G005	1997	Galena Occ.	BRF	Quartz		Collected by G. O'Reilly	Pet, SEM, WRG
B1-97-G010	1997	Mavillette Beach	WRF	Quartz		Collected by G. O'Reilly	Pet, SEM
DS0728 - 2	July/2020	Galena Occ.	BRF			Representative altered mafic sill	WRG
DS0728 - 4	July/2020	Galena Occ.	BRF			Representative least altered mafic sill (still altered)	WRG
DS0728 - 5	July/2020	Galena Occ.	BRF			Botryoidal weathering	WRG
DS0728 - 6	July/2020	Galena Occ.	BRF			Representative altered BRF	WRG

DS0728 - 12	July/2020	Deerfoot Trail Sb	BRF			Representative mafic intrusion	WRG
DS0728 – 13.1	July/2020	Deerfoot Trail Sb	BRF	Siderite	Minor Cpy	Siderite breccia, BRF dominated sample	WRG
DS0728 – 13.2	July/2020	Deerfoot Trail Sb	BRF	Siderite	Minor Cpy	Siderite breccia, siderite dominated sample	WRG

[a] BRF = Bear River Formation, MG = Mavillette Gabbro, WRF = White Rock Formation
[b] Acronyms as defined in the thesis text
[b] Pet = petrography, SEM = scanning electron microscopy (including EDS and/or BSE), EPMA = electron probe microanalysis of chlorite, SI = sulfur isotope analysis via SIMS, WRG = Whole rock geochemical analysis

Table A2-2 - SEM data collected from mineralized samples from the Cape St Mary's occurrences. All data in wt.%

Deerfoot Trail Sb occurrence	**S**	**Fe**	**Co**	**Ni**	**As**	**Sb**	**Cu**	**Pb**	**Bi**	**Ag**	**Zn**
Arsenopyrite	18.55	30.02	2.87	2.98	45.59						
	19.39	35.06			45.55						
	17.34	32.02			39.27						
	19.57	34.57			45.86						
	17.64	26.85	3.34	5.85	44.42	1.25	0.66				
	19.81	17.38	7.07	14.16	41.57						
	17.25	13.86	7.84	14.79	45.16	1.09					
	17.88	12.9	8.21	11.87	49.14						
	16.72	9.88	3.03	20.6	49.77						
	19.81	31.6			47.54	1.04					
	17.95	18.15	5.45	8.58	48.93	0.95					
	19.48	30.59		0.61	48.04	1.28					
	19.62	31.02		0.66	48.7						
	19.55	31.56			48.89						
	19.82	30.92		0.63	48.64						
	19.9	30.32			48.39	1.39					
Chalcostibite	23.38					51.35	25.27				
	23.47					52.02	24.51				
	23.3	0.97				50.89	24.84				
	23.14	1.03				51	24.83				
	23.66					51.73	24.61				
	23.86					51.87	24.27				
	23.79					51.44	24.78				
	23.84					51.82	24.34				
	23.29	0.77				51	24.94				
Tetrahedrite	23.67	5.65				33.18	37.5				
	23.53	5.58				32.86	37.13				0.9
	23.65	5.62				35.29	35.44				
	23.83	6.3				33.46	36.41				
	23.4	6.31				33.53	36.76				
Freibergite	21.59	5.85				31.03	32.78			7.64	1.11
	20.15	5.58				28.54	22.81			21.57	1.35
	24.69	16.18				16.88	28.44			12.74	1.08
Stibnite	25.14	7.33				47.91	8.21		11.41		
	21.34	3.61				44.53	3.74		26.58		
Plagionite	19.01					40.78		40.21			
	19.17					40.38	0.76	39.69			
Chalcopyrite	34.77	29.58					35.65				
	34.99	29.61					35.4				
	34.59	29.92					35.49				
	34.55	29.58					35.86				
Sb-Bi alloy		1.16				86.5	1.71		10.62		
		1.47				88.16	2.13		8.25		
		0.9				82.71	1.97		14.41		
						87.58	0.82		9.14		
						76.14			23.86		
		O	**Al**	**P**	**Ca**	**Fe**	**Sr**	**La**	**Ce**	**Nd**	**Th**
Florencite		47.01	14.4	12.97	1.61	1.81	2.34	5.45	9.68	2.9	1.84
		48.79	15.01	12.92	0.86	0.72	1.95	5.3	10.02	3.51	0.73
		50.04	14.79	12.64	1.51	0.95	2.23	4.97	9.6	3.27	
Ankerite Breccia occurrence											
Florencite		51.8	13.95	12.37	0.23		0.93	4.62	11.34	4.77	0.93
		51.71	13.83	12.36	0.25		0.68	5.35	11.77	4.05	0.68
		40.6	17.47	15.98				5.82	14.06	6.07	
		40.4	17.39	15.83				6.01	14.61	5.76	
		40.4	17.23	15.92				5.97	14.63	5.85	
		39.78	16.88	15.5			0.84	6.56	14.63	5.82	
		40.21	17.36	15.57			0.55	5.65	14.41	5.92	
		40.24	17.15	15.73			0.88	5.65	14.42	5.6	
		O	**P**	**Ca**	**Fe**	**La**	**Ce**	**Nd**	**Sm**	**Gd**	
Monazite		30.15	15.8	2.6	1.62	2.48	11.53	21.57	10.54	3.7	
		O	**P**	**Ca**	**Y**	**Sm**	**Gd**	**Dy**	**F**	**Ti**	
Xenotime		34.06	17.69	0.4	32.11	2.67	6.82	6.24			
Apatite		38.46	19.14	34.44					7.96		

	38.39	19.16	34.17					8.28	
	38.15	19.2	33.48					9.17	
	38.02	18.97	33.88					9.13	
	38.4	19.26	33.91					8.44	
	38.49	19.2	34.29					8.02	
	38.16	19.1	33.8					8.94	
Rutile	40.05								59.95
	40.05								59.95
Galena Occurrence	**S**	**Fe**	**Pb**						
Galena	12.12		87.88						
	12.23		87.77						
Pyrite	54.1	45.9							
	54.15	45.85							
Mavillette Beach occurrence	**O**	**S**	**Fe**	**As**	**Sb**	**Pb**	**Ag**	**Au**	
Boulangerite		20.16			26.95	52.89			
		20.18			27.03	52.78			
		20.26			27.19	52.55			
		20.57			27.03	52.39			
		20.52			27.27	52.21			
		20.04			27.12	52.84			
		20.25			26.71	53.03			
Jamesonite		22.93	3.16		36.54	37.37			
Galena		14.61				85.39			
		14.65				85.35			
Anglesite	25.24	11.38				63.38			
	23.23	11.33				65.44			
	24.18	11.11				64.72			
Pyrite		55.41	44.01	0.58					
		56.06	43.94						
		55.96	44.04						
		53.99	46.01						
		55.95	44.05						
		57.14	42.86						
		56.86	43.14						
		56.53	43.47						
		56.66	43.34						
		56.9	43.1						
Au-Ag alloy	1.45		1.59				12.12	84.84	
	1.47		1.76				12.69	84.07	

Table A2-3 - Sulfur isotope data collected from pyrite, chalcopyrite, and arsenopyrite from the Cape St Mary's occurrences

Occurrence	Sample	Mineral	$\delta^{34}S$ (‰)	1σ (‰)
Galena occurrence	B1-97-G005	Pyrite	11.1	0.3
	B1-97-G005	Pyrite	11.0	0.3
	B1-97-G005	Pyrite	10.7	0.3
	B1-97-G005	Pyrite	11.4	0.3
	B1-97-G005	Pyrite	11.2	0.3
Mavillette Beach occurrence	B1-97-G010	Pyrite	9.3	0.3
	B1-97-G010	Pyrite	8.8	0.3
	B1-97-G010	Pyrite	7.8	0.3
	B1-97-G010	Pyrite	9.0	0.3
	B1-97-G010	Pyrite	8.9	0.3
	B1-97-G010	Pyrite	8.9	0.3
	B1-97-G010	Pyrite	9.9	0.3
Deerfoot Trail Sb occurrence	B1-92-G015	Chalcopyrite	10.8	0.3
	B1-92-G015	Chalcopyrite	10.8	0.3
	B1-92-G015	Chalcopyrite	11.8	0.3
	B1-92-G015	Chalcopyrite	10.9	0.3
	B1-92-G015	Chalcopyrite	11.1	0.3
Deerfoot Trail Sb occurrence	B1-92-G012	Arsenopyrite	12.6	0.3
	B1-92-G012	Arsenopyrite	12.7	0.3
	B1-92-G012	Arsenopyrite	10.6	0.3
	B1-92-G012	Arsenopyrite	12.3	0.3
	B1-92-G012	Arsenopyrite	11.9	0.3
	B1-92-G012	Arsenopyrite	12.2	0.3

Table A2-4 - Whole rock geochemical data of mineralized samples from the Cape St Mary's occurrences

Analyte Symbol	Unit Symbol	L.O.D.	Analysis Method	BI-92-G015	BI-97-G005	BI-97-G010
Au	ppb	0.02	BLEG-MS	< D.L.	1.8	> 1000
Ag	ppb	0.1	BLEG-MS	3.4	202	817
Cu	%	0.005	FUS-Na2O2	3.32		
Mn	%	0.01	FUS-Na2O2	1.03	1.31	
Pb	%	0.01	FUS-Na2O2		7.85	
Si	%	0.01	FUS-Na2O2			37.5
Sb	%	0.01	FUS-Na2O2	5.62		
Co3O4	%	0.005	FUS-XRF	< D.L.	< D.L.	< D.L.
CuO	%	0.005	FUS-XRF	3.96	0.076	0.006
NiO	%	0.003	FUS-XRF	< D.L.	0.01	0.011
SiO2	%	0.01	FUS-XRF	11.18	15.54	93.3
Al2O3	%	0.01	FUS-XRF	3.47	0.53	0.83
Fe2O3(T)	%	0.01	FUS-XRF	39.07	32.98	3.97
MnO	%	0.001	FUS-XRF	1.237	1.592	0.013
MgO	%	0.01	FUS-XRF	4.06	7.92	0.04
CaO	%	0.01	FUS-XRF	0.1	0.65	< D.L.
Na2O	%	0.01	FUS-XRF	< D.L.	0.03	< D.L.
K2O	%	0.01	FUS-XRF	1.03	0.04	0.03
TiO2	%	0.01	FUS-XRF	0.1	0.02	0.19
P2O5	%	0.01	FUS-XRF	0.02	< D.L.	0.04
Cr2O3	%	0.01	FUS-XRF	< D.L.	< D.L.	0.02
V2O5	%	0.003	FUS-XRF	0.007	0.008	0.007
LOI	%		GRAV	24.61	27.62	1.82
Total	%	0.01	FUS-XRF	88.85	87.02	100.3
Al	%	0.01	FUS-Na2O2	2.34	0.29	0.51
As	ppm	5	FUS-MS-Na2O2	26	12	854
B	ppm	10	FUS-MS-Na2O2	40	< D.L.	< D.L.
Ba	ppm	3	FUS-MS-Na2O2	103	7	9
Be	ppm	3	FUS-MS-Na2O2	< D.L.	< D.L.	< D.L.
Bi	ppm	2	FUS-MS-Na2O2	2620	13	13
Ca	%	0.01	FUS-Na2O2	0.16	0.51	0.03
Cd	ppm	2	FUS-MS-Na2O2	< D.L.	5	< D.L.
Ce	ppm	0.8	FUS-MS-Na2O2	11.7	2.1	27.8
Co	ppm	0.2	FUS-MS-Na2O2	3.2	6.4	2.2
Cr	ppm	30	FUS-MS-Na2O2	80	70	70
Cs	ppm	0.1	FUS-MS-Na2O2	1.8	1	0.5
Cu	ppm	2	FUS-MS-Na2O2	> 10000	633	37
Dy	ppm	0.3	FUS-MS-Na2O2	1.2	1	1.6
Er	ppm	0.1	FUS-MS-Na2O2	0.9	0.8	0.7
Eu	ppm	0.1	FUS-MS-Na2O2	0.5	0.1	0.5
Fe	%	0.05	FUS-Na2O2	27.6	25.2	2.65
Ga	ppm	0.2	FUS-MS-Na2O2	5.3	0.7	2.5
Gd	ppm	0.1	FUS-MS-Na2O2	1.2	0.6	2
Ge	ppm	0.7	FUS-MS-Na2O2	0.8	0.7	1.9
Ho	ppm	0.2	FUS-MS-Na2O2	0.3	0.2	0.3
Hf	ppm	10	FUS-MS-Na2O2	< D.L.	< D.L.	< D.L.
In	ppm	0.2	FUS-MS-Na2O2	0.8	2.9	< D.L.
K	%	0.1	FUS-Na2O2	0.9	< D.L.	< D.L.
La	ppm	0.4	FUS-MS-Na2O2	6.2	0.9	12.6
Li	ppm	3	FUS-MS-Na2O2	9	8	17
Mg	%	0.01	FUS-Na2O2	2.45	4.7	0.05
Mn	ppm	3	FUS-MS-Na2O2	> 10000	> 10000	76
Mo	ppm	1	FUS-MS-Na2O2	< D.L.	2	1
Nb	ppm	2.4	FUS-MS-Na2O2	4.2	< D.L.	3.6

Nd	ppm	0.4	FUS-MS-Na2O2	5.7	0.9	12
Ni	ppm	10	FUS-MS-Na2O2	40	70	50
Pb	ppm	0.8	FUS-MS-Na2O2	18.4	> 5000	1420
Pr	ppm	0.1	FUS-MS-Na2O2	1.4	0.3	2.9
Rb	ppm	0.4	FUS-MS-Na2O2	44.9	5.3	2.6
S	%	0.01	FUS-Na2O2	3.32	1.66	2.2
Sb	ppm	2	FUS-MS-Na2O2	> 5000	451	319
Se	ppm	8	FUS-MS-Na2O2	< D.L.	< D.L.	< D.L.
Si	%	0.01	FUS-Na2O2	5.57	7.3	> 30.0
Sm	ppm	0.1	FUS-MS-Na2O2	1.1	0.6	1.5
Sn	ppm	0.5	FUS-MS-Na2O2	1.4	1.2	1.2
Sr	ppm	3	FUS-MS-Na2O2	34	29	22
Ta	ppm	0.2	FUS-MS-Na2O2	0.5	0.3	0.5
Tb	ppm	0.1	FUS-MS-Na2O2	0.2	0.2	0.3
Te	ppm	6	FUS-MS-Na2O2	19	15	14
Th	ppm	0.1	FUS-MS-Na2O2	2.7	0.3	2.2
Ti	%	0.01	FUS-Na2O2	0.1	0.01	0.12
Tl	ppm	0.1	FUS-MS-Na2O2	0.4	< D.L.	< D.L.
Tm	ppm	0.1	FUS-MS-Na2O2	0.1	0.2	0.1
U	ppm	0.1	FUS-MS-Na2O2	0.9	0.2	0.4
V	ppm	5	FUS-MS-Na2O2	28	20	10
W	ppm	0.7	FUS-MS-Na2O2	< D.L.	< D.L.	< D.L.
Y	ppm	0.1	FUS-MS-Na2O2	7	5.4	6.4
Yb	ppm	0.1	FUS-MS-Na2O2	1.2	0.8	0.4
Zn	ppm	30	FUS-MS-Na2O2	50	160	< D.L.

Table A2-5 - Whole rock geochemistry results of unmineralized samples at Cape St. Mary's

Analyte Symbol	Unit Symbol	Detection Limit	Analysis Method	DSH1	CM21	DS0728 - 2	DS0728 - 4	DS0728 - 5	DS0728 - 6	DS0728 - 12	DS0728 - 13.1	DS0728 - 13.2
Co3O4	%	0.005	FUS-XRF	< D.L.	< D.L.	0.006	0.008	< D.L.	< D.L.	0.007	0.009	< D.L.
CuO	%	0.005	FUS-XRF	< D.L.	< D.L.	< D.L.	0.013	< D.L.	< D.L.	0.019	< D.L.	< D.L.
NiO	%	0.003	FUS-XRF	0.004	0.017	0.017	0.021	0.011	< D.L.	0.004	0.01	0.006
SiO2	%	0.01	FUS-XRF	57.44	13.27	50.35	44.91	45.6	58.13	45.8	11.47	53.44
Al2O3	%	0.01	FUS-XRF	22.22	0.59	16.3	14.87	5.31	23.24	17.03	4.37	19.24
Fe2O3(T)	%	0.01	FUS-XRF	8.02	12.87	15.11	14.87	31.28	6.72	17.12	47.83	10.65
MnO	%	0.001	FUS-XRF	0.097	1.827	0.235	0.259	0.097	0.094	0.26	1.588	0.301
MgO	%	0.01	FUS-XRF	2.26	10.34	7.5	6.83	2.7	1.92	7.89	5.1	1.47
CaO	%	0.01	FUS-XRF	0.17	25.07	0.48	10.08	0.11	0.09	0.5	0.18	0.2
Na2O	%	0.01	FUS-XRF	1.08	0.01	0.16	2.1	0.03	0.82	0.23	0.15	0.73
K2O	%	0.01	FUS-XRF	3.51	0.02	0.04	0.06	0.02	4.53	0.13	0.95	4.71
TiO2	%	0.01	FUS-XRF	0.97	0.06	2.67	2.18	0.14	0.94	2.64	0.18	0.81
P2O5	%	0.01	FUS-XRF	0.1	0.04	0.29	0.25	0.04	0.09	0.36	0.03	0.09
Cr2O3	%	0.01	FUS-XRF	0.02	0.01	0.04	0.04	0.02	0.02	0.03	0.01	0.02
V2O5	%	0.003	FUS-XRF	0.02	0.006	0.062	0.055	0.014	0.018	0.066	0.006	0.018
LOI	%		GRAV	4.27	36.08	6.91	3.83	14.6	4.22	8.45	28.16	8.48
Total	%	0.01	FUS-XRF	100.2	100.2	100.2	100.4	99.97	100.8	100.5	100.1	100.2
B	ppm	20	TD-MS	< D.L.	< D.L.	< D.L.	< D.L.	< D.L.	100	< D.L.	< D.L.	< D.L.
Li	ppm	0.5	TD-MS	131	3.7	205	53	83.5	86.6	189	7.4	20.2
Na	%	0.01	TD-MS	0.78	0.03	0.13	1.44	0.03	0.59	0.18	0.1	0.49
Mg	%	0.01	TD-MS	1.31	6.16	4.64	4.14	1.54	1.19	4.73	2.86	0.82
Al	%	0.01	TD-MS	> 10.0	0.25	9.12	8.11	2.51	> 10.0	8.02	1.98	8.25
K	%	0.01	TD-MS	3.38	0.1	0.05	0.06	0.03	2.56	0.14	0.76	3.85
Ca	%	0.01	TD-MS	0.12	16.8	0.34	6.5	0.05	0.06	0.32	0.12	0.13
Cd	ppm	0.1	TD-MS	< D.L.	0.1	0.2	0.2	0.1	< D.L.	0.2	< D.L.	< D.L.
V	ppm	1	TD-MS	45	34	105	172	95	75	102	30	65

Cr	ppm	1	TD-MS	59	12	191	136	42	81	155	28	76
Mn	ppm	1	TD-MS	770	> 10000	2000	1950	758	790	2000	> 10000	2260
Fe	%	0.01	TD-MS	5.58	8.76	10.9	10.1	20.9	4.64	11.8	31.1	6.91
Hf	ppm	0.1	TD-MS	2.1	0.2	0.8	1.7	0.2	2.4	0.9	0.5	1.9
Ni	ppm	0.5	TD-MS	16	10.6	104	93.2	42.9	12.3	78.1	106	44.8
Er	ppm	0.1	TD-MS	2.1	2.4	3.1	2.3	0.7	2	3.1	0.5	1.3
Be	ppm	0.1	TD-MS	2.9	0.2	1.2	1.1	0.3	2.8	2.8	0.6	2.2
Ho	ppm	0.1	TD-MS	0.7	1	1	0.9	0.4	0.7	1.2	0.2	0.5
Hg	ppb	10	TD-MS	60	80	50	60	50	40	40	20	40
Ag	ppm	0.05	TD-MS	0.06	< D.L.	0.36	0.1	0.08	< D.L.	0.23	0.15	0.38
Cs	ppm	0.05	TD-MS	4.99	0.37	0.51	0.42	0.24	6.28	1.33	1.04	4.37
Co	ppm	0.1	TD-MS	7.7	14.8	51.9	61	12.7	4.6	47.7	34.1	24.2
Eu	ppm	0.05	TD-MS	1.29	4.02	1.87	1.59	0.85	0.87	2.18	1.33	1.07
Bi	ppm	0.02	TD-MS	0.48	< D.L.	0.1	0.02	< D.L.	0.21	< D.L.	0.58	0.84
Se	ppm	0.1	TD-MS	0.6	0.7	0.6	0.8	0.5	0.3	0.4	0.4	0.5
Zn	ppm	0.2	TD-MS	81.1	34.6	256	98.4	111	66.1	147	12.2	15.2
Ga	ppm	0.1	TD-MS	27	0.9	24.9	20.4	10.4	25.5	24.2	5.2	22
As	ppm	0.1	TD-MS	6.8	2.6	25.4	2	39	13.3	0.9	533	31.8
Rb	ppm	0.2	TD-MS	153	5.4	2.4	1.9	0.8	149	5.5	42.3	187
Y	ppm	0.1	TD-MS	20.7	30.4	28	23.6	8.5	17.1	31	4.3	11.9
Zr	ppm	1	TD-MS	73	6	26	67	8	79	26	21	54
Nb	ppm	0.1	TD-MS	2	0.9	0.3	1.6	1	11.8	0.2	2.8	3.4
Mo	ppm	0.05	TD-MS	0.08	0.44	0.09	0.37	3.09	0.18	0.07	0.55	0.19
In	ppm	0.1	TD-MS	< D.L.	0.4	< D.L.	< D.L.	< D.L.	< D.L.	< D.L.	0.7	0.1
Sn	ppm	1	TD-MS	< D.L.	< D.L.	< D.L.	< D.L.	< D.L.	< D.L.	1	< D.L.	3
Sb	ppm	0.1	TD-MS	0.2	0.1	0.9	1	19.2	0.2	0.9	17.9	7.6
Te	ppm	0.1	TD-MS	< D.L.	< D.L.	< D.L.	< D.L.	< D.L.	< D.L.	< D.L.	< D.L.	< D.L.
Ba	ppm	1	TD-MS	709	17	12	65	4	757	33	108	505
La	ppm	0.1	TD-MS	41.5	2.1	13.3	13.1	7.8	25	18.3	23.1	36.5
Ce	ppm	0.1	TD-MS	84.8	8.2	30.9	31.2	17.4	54.7	44.4	44.8	75.3
Pr	ppm	0.1	TD-MS	9.6	1.8	4.3	4	2.2	5.8	5.3	4.5	7.9
Nd	ppm	0.1	TD-MS	37.1	14	18.4	19	9.5	24.9	26.9	17.8	33.9
Sm	ppm	0.1	TD-MS	5.7	8.4	4.5	3.8	2.2	3.6	5.9	2.6	5.7
Gd	ppm	0.1	TD-MS	5.5	9.8	5	5.2	2.9	3.8	6.8	1.3	5.2
Tb	ppm	0.1	TD-MS	0.8	1.5	0.9	0.9	0.4	0.5	1.1	0.1	0.6
Dy	ppm	0.1	TD-MS	3.9	6.8	5.2	4.7	2.2	3.4	6.4	0.8	2.7
Cu	ppm	0.2	TD-MS	4.4	1.8	25.2	100	8.1	7.2	152	5.7	12.5
Ge	ppm	0.1	TD-MS	0.3	< D.L.	0.1	0.3	0.2	0.4	0.3	0.1	0.4
Tm	ppm	0.1	TD-MS	0.3	0.3	0.4	0.3	< D.L.	0.3	0.4	0.1	0.2
Yb	ppm	0.1	TD-MS	2.1	1.5	2.1	1.9	0.5	2.2	2.5	1	1.5
Lu	ppm	0.1	TD-MS	0.3	0.2	0.3	0.3	< D.L.	0.3	0.3	0.1	0.3
Ta	ppm	0.1	TD-MS	0.1	< D.L.	< D.L.	< D.L.	< D.L.	0.2	< D.L.	0.2	< D.L.
Sr	ppm	0.2	TD-MS	127	289	9.2	393	4.1	115	6.5	24.3	77.7
W	ppm	0.1	TD-MS	0.2	< D.L.	< D.L.	< D.L.	0.2	0.4	< D.L.	0.5	0.2
Re	ppm	0.001	TD-MS	0.003	0.001	0.003	0.003	0.002	< D.L.	< D.L.	< D.L.	< D.L.
Tl	ppm	0.05	TD-MS	0.67	< D.L.	0.18	< D.L.	0.08	0.98	< D.L.	0.14	0.67
Pb	ppm	0.5	TD-MS	4.1	2.3	121	6.1	24.5	5.3	22.6	1.6	3.2
Th	ppm	0.1	TD-MS	12.2	0.1	1.6	1.3	0.3	11.4	1.6	5.1	10.3
U	ppm	0.1	TD-MS	2.5	< D.L.	0.6	0.4	0.3	2.2	0.5	0.6	2

Appendix III

Data related to Chapter 4: The genetic relationship between Lansdowne, Cape St. Mary's, and Nictaux Falls

Table A3-1 - Sample List of NFDO samples analyzed for this thesis

Sample ID	Year/month collected[a]	Occurrence (easting/northing)[b]	Host Rock[c]	Veining	Mineralization	Context for collection	Analyses[d]
V2-1-M	Sept/2018	339700/4968510	KF	Qtz	Apy-Cobaltite	Representative sulfarsenide mineralization, Main zone 1	Pet, SEM, EPMA
GB-1	Sept/2018	339730/4968730	KF			Representative gabbro sample from gabbro intrusion	Pet, U-Pb in apatite geochronology

[a] Samples collected by Natalie McNeil and Nicole Kennedy
[b] UTM zone 19
[c] KF = Kentville Formation
[d] Pet = petrography, SEM = scanning electron microscopy (including EDS and/or BSE), EPMA = electron probe microanalysis of chlorite

Table A3-2 - EPMA analyses of chlorite from unmineralized samples at Cape St. Mary's and a mineralized sample from NFDO.

All data in wt.%.

Sample Spot	K_2O	SrO	Na_2O	MgO	F	SiO_2	Al_2O_3	FeO	MnO	NiO	Cr_2O_3	Cl	CaO	TiO_2	(OH)	Total
CM12_spot1_center1	< D.L.	< D.L.	0.034	9.757	< D.L.	24.472	25.46	29.189	0.094	< D.L.	< D.L.	0.01	0.008	0.133	10.846	100.003
CM12_spot1_center2	0.036	< D.L.	0.029	9.801	0.021	24.491	25.338	29.25	0.113	0.002	0.008	< D.L.	0.019	0.084	10.819	100.011
CM12_spot1_center3	0.018	< D.L.	0.029	9.699	< D.L.	24.605	25.529	29.307	0.149	0.03	< D.L.	< D.L.	0.018	0.113	10.503	100
CM12_spot1_whispedge1	0.662	< D.L.	0.342	8.682	0.129	26.439	26.656	26.895	0.139	0.014	0.044	0.009	0.025	0.113	9.907	100.056
CM12_spot1_whispedge2	0.213	0.132	0.161	9.035	< D.L.	24.702	25.064	29.161	0.138	0.034	0.01	< D.L.	0.049	0.114	11.187	100
CM12_spot1_center4	0.006	< D.L.	< D.L.	9.53	0.021	24.177	25.524	29.723	0.251	0.012	0.024	0.006	0.027	0.049	10.661	100.011
CM12_spot1.1_vein1	0.006	< D.L.	< D.L.	9.706	< D.L.	24.352	25.225	29.44	0.112	0.013	0.014	0.012	0.037	0.081	11.005	100.003
CM12_spot1.1_vein2	0.006	< D.L.	< D.L.	9.888	0.105	24.673	25.146	29.577	0.144	< D.L.	< D.L.	0.008	0.004	0.065	10.431	100.047
CM12_spot1.1_vein3	< D.L.	< D.L.	0.008	9.658	< D.L.	24.485	25.239	29.744	0.143	< D.L.	0.03	0.015	< D.L.	0.116	10.567	100.005
V2-1-M_spot1_1	0.203	< D.L.	0.208	13.026	0.096	24.859	20.716	20.448	0.235	0.34	0.04	0.032	0.227	0.092	19.527	100.049
V2-1-M_spot1_2	0.047	0.008	0.079	14.573	0.16	26.157	22.077	21.576	0.324	0.059	0.021	0.041	0.184	0.097	14.673	100.076
V2-1-M_spot1_3	0.027	< D.L.	< D.L.	17.058	0.133	28.346	23.476	20.016	0.297	0.005	0.027	0.004	0.071	0.071	10.525	100.056
V2-1-M_spot1_4	0.026	< D.L.	0.067	13.259	0.133	25.647	21.509	25.316	0.51	0.014	0.016	0.027	0.092	0.094	13.352	100.062
V2-1-M_spot1_5	0.063	< D.L.	0.171	11.755	0.025	22.609	19.134	20.789	0.31	< D.L.	< D.L.	0.078	0.364	0.08	24.65	100.028
V2-1-M_spot2_1	0.037	0.015	0.048	16.835	0.154	32.743	23.373	18.632	0.26	< D.L.	0.026	0.007	0.113	0.093	7.731	100.067
V2-1-M_spot2_2	0.145	< D.L.	0.017	16.415	0.157	28.431	23.251	19.789	0.279	0.038	< D.L.	0.026	0.086	0.073	11.365	100.072
V2-1-M_spot2_3	3.339	0.105	0.1	9.923	0.558	36.028	24.805	15.009	0.178	0.024	0.017	< D.L.	0.219	0.215	9.715	100.235
V2-1-M_spot3_1	0.407	< D.L.	0.047	14.359	0.136	29.57	22.899	19.813	0.222	0.046	0.074	0.026	0.23	0.102	12.13	100.061
V2-1-M_spot3_2	9.406	< D.L.	0.125	2.416	0.272	52.237	30.681	2.006	< D.L.	0.027	0.038	0.011	0.094	0.172	2.632	100.117
V2-1-M_spot3_3	1.021	0.031	0.126	14.721	0.206	31.409	23.04	17.343	0.343	0.09	0.017	0.028	0.218	0.053	11.448	100.094
MQ22_spot1_1	0.009	0.023	0.022	9.102	< D.L.	26.354	20.056	33.878	0.236	0.012	< D.L.	< D.L.	0.037	0.051	10.222	100.002
MQ22_spot1_2	< D.L.	< D.L.	< D.L.	8.723	< D.L.	26.292	19.881	34.047	0.251	< D.L.	< D.L.	0.001	0.05	0.098	10.657	100
MQ22_spot1_3	1.416	< D.L.	0.116	3.864	0.022	54.956	6.095	26.111	0.372	< D.L.	< D.L.	< D.L.	0.287	0.136	6.635	100.01
MQ22_spot1_4	0.043	< D.L.	0.043	9.318	< D.L.	26.531	19.094	34.156	0.23	0.018	< D.L.	< D.L.	0.06	0.11	10.398	100.001
MQ22_spot1_5	0.058	< D.L.	0.046	9.366	< D.L.	26.493	19.058	34.122	0.213	0.037	0.012	0.007	0.069	0.08	10.442	100.003
MQ22_spot2_1	0.045	< D.L.	< D.L.	11.217	0.042	29.072	16.112	32.544	0.176	0.028	0.025	0.003	0.127	0.065	10.562	100.018
MQ22_spot2_2	0.858	< D.L.	< D.L.	9.12	< D.L.	28.73	17.757	33.233	0.169	0.022	0.002	0.005	0.177	0.138	9.789	100

MQ22_spot2_3	< D.L.	0.045	0.013	10.941	0.125	28.891	16.573	32.582	0.17	0.034	< D.L.	0.014	0.17	0.067	10.428	100.053
MQ22_spot2_4	0.406	0.083	< D.L.	0.323	0.223	43.556	21.58	12.238	0.065	< D.L.	< D.L.	0.012	19.963	0.091	1.555	100.095
MQ22_spot2_5	2.094	< D.L.	0.058	8.563	< D.L.	31.751	16.563	31.963	0.178	0.013	0.014	< D.L.	0.095	0.237	8.472	100.001
MQ22_spot3_1	< D.L.	< D.L.	0.022	10.41	0.042	28.448	16.796	32.909	0.193	< D.L.	0.049	0.002	0.174	0.126	10.846	100.017
MQ22_spot3_2	0.018	0.015	0.008	10.162	< D.L.	28.228	17.145	32.67	0.2	0.012	0.004	0.009	0.175	0.041	11.316	100.003
MQ22_spot3_3	0.38	< D.L.	< D.L.	9.162	< D.L.	27.694	18.442	33.042	0.196	0.038	< D.L.	< D.L.	0.093	0.074	10.877	99.998
MQ22_spot3_4	2.948	< D.L.	4.377	2.365	0.069	51.533	19.323	12.437	0.085	< D.L.	0.037	< D.L.	3.678	0.062	3.115	100.029

Table A3-3 - Site assignment of elements in chlorite. Temperature (T) based on equation by Cathelineau (1988), as described in section 2.3.3. Sample IDs correspond to grain number and area within the grain analyzed or description of adjacent minerals. Fe# = Fe/(Fe + Mg). Normalized to 14 oxygen. T = tetrahedral site, O = octahedral site, OH = OH anion site.

				CM12_spot1_center1	CM12_spot1_center2	CM12_spot1_center3	CM12_spot1_whispedge2	CM12_spot1_center4	CM12_spot1.1_vein1	CM12_spot1.1_vein2	CM12_spot1.1_vein3	V2-1-M_spot1_3	V2-1-M_spot2_1	V2-1-M_spot2_2	V2-1-M_spot3_1
O	wt.%	cat													
2	60.08	1	SiO2	0.81	0.82	0.82	0.82	0.80	0.81	0.82	0.82	0.94	1.09	0.95	0.98
2	79.88	1	TiO2	0.00	0.00	0.00	0.00	0.00	0.00	0.00	0.00	0.00	0.00	0.00	0.00
3	101.96	2	Al2O3	0.75	0.75	0.75	0.74	0.75	0.74	0.74	0.74	0.69	0.69	0.68	0.67
3	151.99	2	Cr2O3	0.00	0.00	0.00	0.00	0.00	0.00	0.00	0.00	0.00	0.00	0.00	0.00
1	74.692	1	NiO	0.00	0.00	0.00	0.00	0.00	0.00	0.00	0.00	0.00	0.00	0.00	0.00
1	71.844	1	FeO	0.41	0.41	0.41	0.41	0.41	0.41	0.41	0.41	0.28	0.26	0.28	0.28
1	70.94	1	MnO	0.00	0.00	0.00	0.00	0.00	0.00	0.00	0.00	0.00	0.00	0.00	0.00
1	40.3	1	MgO	0.24	0.24	0.24	0.22	0.24	0.24	0.25	0.24	0.42	0.42	0.41	0.36
1	56.08	1	CaO	0.00	0.00	0.00	0.00	0.00	0.00	0.00	0.00	0.00	0.00	0.00	0.00
1	61.98	2	Na2O	0.00	0.00	0.00	0.00	0.00	0.00	0.00	0.00	0.00	0.00	0.00	0.00
1	94.2	2	K2O	0.00	0.00	0.00	0.00	0.00	0.00	0.00	0.00	0.00	0.00	0.00	0.00
1	103.62	1	SrO	0.00	0.00	0.00	0.00	0.00	0.00	0.00	0.00	0.00	0.00	0.00	0.00
1	19	0	F	0.00	0.00	0.00	0.00	0.00	0.00	0.00	0.00	0.00	0.00	0.00	0.00
1	35.45	0	Cl	0.00	0.00	0.00	0.00	0.00	0.00	0.00	0.00	0.00	0.00	0.00	0.00
			Total O:	2.22	2.22	2.23	2.20	2.21	2.21	2.22	2.22	2.35	2.47	2.33	2.31
			CF	6.31	6.32	6.29	6.36	6.33	6.34	6.29	6.31	5.96	5.67	6.02	6.06
			Si	2.57	2.57	2.58	2.61	2.55	2.57	2.58	2.57	2.81	3.09	2.85	2.98
			Ti	0.01	0.01	0.01	0.01	0.00	0.01	0.01	0.01	0.01	0.01	0.01	0.01
			Al	3.15	3.14	3.15	3.13	3.17	3.14	3.10	3.13	2.75	2.60	2.74	2.72
			Cr	0.00	0.00	0.00	0.00	0.00	0.00	0.00	0.00	0.00	0.00	0.00	0.01
			Ni	0.00	0.00	0.00	0.00	0.00	0.00	0.00	0.00	0.00	0.00	0.00	0.00
			Fe	2.56	2.57	2.57	2.58	2.62	2.60	2.59	2.61	1.66	1.47	1.66	1.67
			Mn	0.01	0.01	0.01	0.01	0.02	0.01	0.01	0.01	0.02	0.02	0.02	0.02
			Mg	1.53	1.54	1.51	1.43	1.50	1.53	1.54	1.51	2.52	2.37	2.45	2.16
			Ca	0.00	0.00	0.00	0.01	0.00	0.00	0.00	0.00	0.01	0.01	0.01	0.02
			Na	0.01	0.01	0.01	0.03	0.00	0.00	0.00	0.00	0.00	0.01	0.00	0.01
			K	0.00	0.00	0.00	0.03	0.00	0.00	0.00	0.00	0.00	0.00	0.02	0.05
			Sr	0.00	0.00	0.00	0.01	0.00	0.00	0.00	0.00	0.00	0.00	0.00	0.00
			total	9.84	9.85	9.84	9.85	9.86	9.85	9.84	9.85	9.79	9.58	9.76	9.65
			charge	28.00	27.99	28.00	27.99	27.99	28.00	27.96	28.00	27.96	27.95	27.95	27.95
			F	0.00	0.00	0.00	0.00	0.00	0.00	0.02	0.00	0.02	0.02	0.02	0.02
			Cl	0.00	0.00	0.00	0.00	0.00	0.00	0.00	0.00	0.00	0.00	0.00	0.00
	apfu	T	Si	2.57	2.57	2.58	2.61	2.55	2.57	2.58	2.57	2.81	3.09	2.85	2.98
			Al	1.43	1.43	1.42	1.39	1.45	1.43	1.42	1.43	1.19	0.91	1.15	1.02
			Sum	4.00	4.00	4.00	4.00	4.00	4.00	4.00	4.00	4.00	4.00	4.00	4.00
		O	Al	1.72	1.71	1.73	1.74	1.71	1.71	1.69	1.70	1.56	1.69	1.59	1.70
			Fe	2.56	2.57	2.57	2.58	2.62	2.60	2.59	2.61	1.66	1.47	1.66	1.67
			Mg	1.53	1.54	1.51	1.43	1.50	1.53	1.54	1.51	2.52	2.37	2.45	2.16
			Mn	0.01	0.01	0.01	0.01	0.02	0.01	0.01	0.01	0.02	0.02	0.02	0.02
			sum	5.83	5.83	5.82	5.76	5.85	5.84	5.83	5.84	5.77	5.55	5.72	5.55
			vac	0.17	0.17	0.18	0.24	0.15	0.16	0.17	0.16	0.23	0.45	0.28	0.45
		OH	F	0.02	0.00	0.00	0.00	0.00	0.00	0.00	0.02	0.00	0.02	0.02	0.02
			Cl	0.00	0.00	0.00	0.00	0.00	0.00	0.00	0.00	0.00	0.00	0.00	0.00
			OH	8.00	7.99	8.00	7.99	7.99	8.00	7.95	8.00	7.94	7.93	7.92	7.93
			Fe#	0.63	0.63	0.63	0.64	0.64	0.63	0.63	0.63	0.40	0.38	0.40	0.44
			T	398.05	397.08	396.35	384.45	406.17	398.67	393.98	397.45	320.19	230.90	309.48	266.02

				CM12_spot1_center1	CM12_spot1_center2	CM12_spot1_center3	CM12_spot1_whispedge2	CM12_spot1_center4	CM12_spot1.1_vein1	CM12_spot1.1_vein2	CM12_spot1.1_vein3
O	wt.%	cat									
2	60.08	1	SiO2	0.88	0.88	0.88	0.88	0.97	0.96	0.95	0.94
2	79.88	1	TiO2	0.00	0.00	0.00	0.00	0.00	0.00	0.00	0.00
3	101.96	2	Al2O3	0.59	0.58	0.56	0.56	0.47	0.49	0.49	0.50
3	151.99	2	Cr2O3	0.00	0.00	0.00	0.00	0.00	0.00	0.00	0.00
1	74.692	1	NiO	0.00	0.00	0.00	0.00	0.00	0.00	0.00	0.00
1	71.844	1	FeO	0.47	0.47	0.48	0.47	0.45	0.45	0.46	0.45

1	70.94	1	MnO	0.00	0.00	0.00	0.00	0.00	0.00	0.00	0.00
1	40.3	1	MgO	0.23	0.22	0.23	0.23	0.28	0.27	0.26	0.25
1	56.08	1	CaO	0.00	0.00	0.00	0.00	0.00	0.00	0.00	0.00
1	61.98	2	Na2O	0.00	0.00	0.00	0.00	0.00	0.00	0.00	0.00
1	94.2	2	K2O	0.00	0.00	0.00	0.00	0.00	0.00	0.00	0.00
1	103.62	1	SrO	0.00	0.00	0.00	0.00	0.00	0.00	0.00	0.00
1	19	0	F	0.00	0.00	0.00	0.00	0.00	0.00	0.00	0.00
1	35.45	0	Cl	0.00	0.00	0.00	0.00	0.00	0.00	0.00	0.00
			Total O:	2.17	2.16	2.16	2.16	2.18	2.19	2.17	2.16
			CF	6.45	6.49	6.48	6.49	6.42	6.40	6.45	6.48
			Si	2.83	2.84	2.86	2.86	3.10	3.08	3.06	3.05
			Ti	0.00	0.01	0.01	0.01	0.01	0.01	0.01	0.00
			Al	2.54	2.53	2.43	2.42	2.03	2.08	2.13	2.18
			Cr	0.00	0.00	0.00	0.00	0.00	0.00	0.00	0.00
			Ni	0.00	0.00	0.00	0.00	0.00	0.00	0.00	0.00
			Fe	3.04	3.08	3.08	3.08	2.91	2.90	2.96	2.95
			Mn	0.02	0.02	0.02	0.02	0.02	0.02	0.02	0.02
			Mg	1.46	1.40	1.50	1.51	1.79	1.74	1.67	1.64
			Ca	0.00	0.01	0.01	0.01	0.01	0.02	0.02	0.02
			Na	0.00	0.00	0.01	0.01	0.00	0.00	0.00	0.00
			K	0.00	0.00	0.01	0.01	0.01	0.00	0.00	0.00
			Sr	0.00	0.00	0.00	0.00	0.00	0.00	0.00	0.00
			total	9.90	9.89	9.92	9.93	9.87	9.85	9.86	9.86
			charge	28.00	28.00	28.00	28.00	27.99	27.95	27.99	28.00
			F	0.00	0.00	0.00	0.00	0.01	0.02	0.01	0.00
			Cl	0.00	0.00	0.00	0.00	0.00	0.00	0.00	0.00
	apfu	T	Si	2.83	2.84	2.86	2.86	3.10	3.08	3.06	3.05
			Al	1.17	1.16	1.14	1.14	0.90	0.92	0.94	0.95
			Sum	4.00	4.00	4.00	4.00	4.00	4.00	4.00	4.00
		O	Al	1.37	1.37	1.29	1.28	1.13	1.16	1.18	1.23
			Fe	3.04	3.08	3.08	3.08	2.91	2.90	2.96	2.95
			Mg	1.46	1.40	1.50	1.51	1.79	1.74	1.67	1.64
			Mn	0.02	0.02	0.02	0.02	0.02	0.02	0.02	0.02
			sum	5.88	5.87	5.89	5.89	5.84	5.82	5.82	5.83
			vac	0.12	0.13	0.11	0.11	0.16	0.18	0.18	0.17
			F	0.00	0.00	0.00	0.00	0.01	0.02	0.01	0.00
			Cl	0.00	0.00	0.00	0.00	0.00	0.00	0.00	0.00
			OH	8.00	8.00	8.00	8.00	7.98	7.93	7.98	8.00
			Fe#	0.63	0.63	0.63	0.64	0.64	0.63	0.63	0.63
			T	398.05	397.08	396.35	384.45	406.17	398.67	393.98	397.45

Table A3-4 - U-Pb analyses in apatite by LA-ICP-MS in sample GB-1

Comments	Pb ppm 204	Pb ppm 206	Final 207_235	Final 207_235 Prop2SE	Final 206_238	Final 206_238 Prop2SE	Error Correlation 6_38 vs 7_35	Final 238_206	Final 238_206 Prop2SE	Final 207_206	Final 207_206 Prop2SE	Error Correlation 38_6 vs 7_6	Age Final 206_238	Age Final 206_238 Prop2SE	Age Final 207_235	Age Final 207_235 Prop2SE	Age Final 208_232	Age Final 208_232 Prop2SE
Ap_GB1 - 6	2.61	4.438	3.62	0.16	0.0859	0.0022	0.62632	11.64144	0.298151	0.306	0.011	-0.19449	531.4	13	1542	34	611	22
Ap_GB1 - 4	2.89	3.94	3.94	0.23	0.0882	0.0022	0.10643	11.33787	0.282804	0.32	0.015	-0.038054	544.7	13	1604	40	711	27
Ap_GB1 - 1	2.91	2.679	13.28	0.47	0.1707	0.0056	0.5254	5.858231	0.192186	0.574	0.017	-0.092561	1015	31	2689	33	1207	49
Ap_GB1 - 28	2.29	4.01	3.31	0.22	0.0849	0.0028	0.78735	11.77856	0.388457	0.28	0.013	-0.45281	525	17	1457	50	572	23
Ap_GB1 - 12	2.35	2.662	6.36	0.2	0.11	0.0031	0.17462	9.090909	0.256198	0.414	0.014	0.16339	673	18	2023	27	711	26
Ap_GB1 - 10	3.47	4.48	3.75	0.3	0.0859	0.0028	0.06735	11.64144	0.379465	0.305	0.025	0.17033	531	17	1539	52	685	46
Ap_GB1 - 11	3.33	5.2	2.93	0.25	0.0817	0.0024	0.3558	12.2399	0.359557	0.257	0.019	-0.23696	506	14	1368	60	628	32
Ap_GB1 - 2	1.95	4.81	1.792	0.081	0.0728	0.0018	0.06644	13.73626	0.339633	0.1787	0.0083	0.1712	452.7	11	1029	25	492	17
Ap_GB1 - 5	4.38	2.88	9.08	0.29	0.136	0.0045	0.63053	7.352941	0.243296	0.489	0.016	0.2169	821	25	2337	29	1197	47
Ap_GB1 - 7	2.48	3.601	5.25	0.24	0.1024	0.0033	0.07998	9.765625	0.286102	0.366	0.016	0.1388	628	18	1846	37	699	26
Ap_GB1 - 30	6.2	4.36	8.52	0.37	0.1315	0.0058	0.76614	7.604563	0.335441	0.473	0.018	0.098712	796	33	2282	39	1013	67
Ap_GB1 - 20	2.49	2.066	8.56	0.45	0.1305	0.0047	0.41036	7.662835	0.275988	0.468	0.018	-0.051517	790	27	2296	46	916	40
Ap_GB1 - 32	2.69	5.603	2.297	0.078	0.0781	0.0018	0.35654	12.8041	0.295101	0.2116	0.007	0.093518	484.4	11	1211	25	499.5	16
Ap_GB1 - 33	3.19	3.09	5.53	0.25	0.1061	0.0034	0.45126	9.425071	0.302029	0.376	0.016	0.16155	650	20	1911	39	862	38

Ap_GB1 - 27	3	2.59	7.34	0.37	0.1223	0.0045	0.7255	8.176615	0.300857	0.436	0.017	-0.30619	743	26	2146	45	962	46
Ap_GB1 - 8	6.45	2.87	13.9	1	0.179	0.011	0.54351	5.586592	0.34331	0.565	0.033	0.16944	1060	60	2726	70	1657	96
Ap_GB1 - 25	4.02	3.36	25.6	1.9	0.274	0.018	0.45731	3.649635	0.239757	0.653	0.027	0.17173	1525	73	3258	51	1923	79
Ap_GB1 - 31	4.75	4.119	7.16	0.36	0.1236	0.0048	0.30393	8.090615	0.314199	0.434	0.015	-0.10581	750	27	2124	46	954	36
Ap_GB1 - 29	2.72	2.114	12.4	1.5	0.154	0.0096	0.7046	6.493506	0.40479	0.51	0.034	-0.40024	919	53	2520	110	1149	86
Ap_GB1 - 26	3.09	3.04	13.99	0.67	0.1833	0.0091	0.20112	5.455537	0.270842	0.56	0.023	0.3387	1083	49	2738	45	1432	100
Ap_GB1 - 40	3.79	6.28	7.17	0.81	0.1183	0.0075	0.79169	8.453085	0.53591	0.41	0.027	-0.22311	718	43	2060	110	958	83
Ap_GB1 - 37	6.4	6.51	4.18	0.22	0.0958	0.0031	0.62145	10.43841	0.337778	0.315	0.014	-0.048782	590	18	1658	42	593	25
Ap_GB1 - 39	3.35	4.07	6.38	0.41	0.1139	0.0044	0.77886	8.779631	0.339161	0.397	0.015	-0.34212	695	26	1999	52	1039	51
Ap_GB1 - 34	4	3.24	5.86	0.44	0.111	0.0053	0.7441	9.009009	0.43016	0.383	0.017	-0.25115	677	31	1931	63	743	37
Ap_GB1 - 22	3.37	4.104	5.31	0.22	0.1062	0.0028	0.50016	9.416196	0.248261	0.364	0.014	-0.30525	651	16	1867	35	934	42
Ap_GB1 - 16	2.99	2.668	13.15	0.86	0.1732	0.0079	0.34598	5.773672	0.263349	0.54	0.027	-0.17447	1027	44	2676	62	1219	74
Ap_GB1 - 9	3.4	8.27	2.7	0.46	0.0844	0.0061	0.38133	11.84834	0.856338	0.213	0.025	0.047825	520	36	1193	76	552	48
Ap_GB1 - 3	4.18	3.75	18.1	2.7	0.219	0.025	0.97505	4.56621	0.521257	0.591	0.028	-0.58617	1250	130	2930	140	1590	190
Ap_GB1 - 41	4.36	4.4	6.58	0.34	0.1181	0.0048	0.60423	8.467401	0.344145	0.401	0.016	-0.1431	719	27	2035	46	841	37
Ap_GB1 - 15	4.28	4.24	4.62	0.23	0.1022	0.0032	0.37195	9.784736	0.306371	0.334	0.015	0.12103	627	19	1745	40	833	42
Ap_GB1 - 13	6.81	7.5	3.41	0.31	0.0905	0.0038	0.85437	11.04972	0.463966	0.267	0.017	-0.44808	558	22	1464	63	603	37
Ap_GB1 - 17	6.85	2.71	11.36	0.68	0.1609	0.0075	0.61748	6.21504	0.289701	0.494	0.024	0.026721	959	41	2540	60	1356	63
Ap_GB1 - 23	3.85	4.82	5.4	0.37	0.1103	0.0041	0.44493	9.066183	0.337002	0.35	0.021	0.061528	674	23	1871	57	933	41
Ap_GB1 - 24	2.62	4	4.35	0.34	0.099	0.0036	0.35962	10.10101	0.36731	0.301	0.017	0.017774	608	21	1664	60	620	23
Ap_GB1 - 21	2.78	4.555	3.91	0.11	0.0954	0.0022	0.58747	10.48218	0.241727	0.2968	0.0073	-0.034692	587.3	13	1613	21	696	24
Ap_GB1 - 14	3.49	7.04	2.52	0.12	0.0859	0.0021	0.54705	11.64144	0.284599	0.2155	0.009	-0.23951	531.2	12	1271	32	596	23
Phalaborwa Apatite																		
Phal - 2	4.05	18.15	15.84	0.22	0.4446	0.0084	0.4813	2.249213	0.04249525	0.2615	0.0033	0.0061673	2371	38	2867	13	2196	59
Phal - 3	3.79	20.87	14.09	0.15	0.4279	0.0084	0.52674	2.336995	0.04587697	0.2399	0.0025	0.18931	2296	38	2754	10	2163	59
Phal - 4	4.49	18.53	15.71	0.2	0.4438	0.0087	0.36489	2.253267	0.04417176	0.2569	0.0034	0.37212	2367	39	2861	12	2222	60
Phal - 5	4.02	20.3	13.64	0.16	0.4243	0.0083	0.34011	2.356823	0.0461033	0.2329	0.0026	0.29637	2279	37	2725	11	2177	59
Phal - 6	4.09	18.12	15.62	0.19	0.438	0.0086	0.53447	2.283105	0.04482809	0.2596	0.0029	0.12793	2341	38	2856	11	2220	61
Phal - 7	4.25	17.27	15.92	0.22	0.4454	0.0087	0.60612	2.245173	0.04385497	0.2603	0.003	-0.033531	2381	38	2872	13	2231	60
Phal - 8	4.25	18.29	15.58	0.21	0.4407	0.0087	0.4713	2.269117	0.04479537	0.2564	0.0032	0.18533	2353	39	2850	13	2228	60
Phal - 9	3.82	19.11	15.19	0.2	0.4414	0.0089	0.4549	2.265519	0.04567992	0.248	0.0033	0.13294	2359	39	2827	12	2213	60
Phal - 10	4.08	18.36	16.59	0.2	0.4584	0.0088	0.58311	2.181501	0.04187873	0.2608	0.0025	0.15815	2432	39	2911	12	2227	61
Phal_1	3.8	17.59	16.33	0.21	0.4507	0.0095	-0.097288	2.218771	0.04676797	0.2626	0.0048	0.67381	2398	42	2896	12	2185	61
Standards																		
MAD - 1	1.65	7.453	0.598	0.022	0.07571	0.0015	0.06389	13.20829	0.2616886	0.0568	0.002	0.20868	470.4	9.3	475	14	469.3	13
MAD - 2	1.71	7.427	0.598	0.028	0.07627	0.0016	-0.13453	13.11132	0.2750505	0.0572	0.003	0.3254	473.8	9.3	475	19	468.2	13
MAD - 3	1.71	7.63	0.612	0.028	0.07699	0.0016	-0.11506	12.9887	0.2699301	0.0576	0.0027	0.27107	478.1	9.7	484	18	476.8	13
MAD - 4	1.4	7.23	0.599	0.023	0.07592	0.0016	-0.14859	13.17176	0.2775924	0.0577	0.0024	0.41131	472.3	9.5	476	15	466.3	13

MAD - 5	1.62	7.342	0.606	0.024	0.07644	0.0016	-0.16015	13.08216	0.2738285	0.058	0.0025	0.39596	474.8	9.6	481	16	475.3	13
MAD - 6	1.54	7.383	0.6	0.027	0.07599	0.0015	-0.09079	13.15963	0.2597636	0.0573	0.0026	0.28777	472.1	8.7	476	17	474.6	13
MAD - 7	1.61	7.283	0.595	0.024	0.076	0.0016	-0.22149	13.15789	0.2770083	0.0563	0.0024	0.43029	472.1	9.5	476	15	473.6	13
MAD - 8	1.83	7.553	0.613	0.041	0.07714	0.0015	-0.24753	12.96344	0.2520763	0.0578	0.0041	0.38899	479	9.1	481	26	486.7	14
MAD - 9	1.29	7.298	0.604	0.024	0.07691	0.0016	-0.067753	13.00221	0.270492	0.0567	0.0023	0.32658	477.6	9.4	478	15	473.5	14
MAD - 10	1.34	7.514	0.587	0.025	0.07485	0.0015	-0.075209	13.36005	0.2677365	0.0559	0.0026	0.25982	465.3	8.9	469	16	466.5	13
MAD - 11	1.54	7.272	0.606	0.026	0.07641	0.0015	0.0038213	13.08729	0.2569158	0.0581	0.0026	0.19033	475.1	9.2	478	16	470.8	13
MAD - 12	1.33	7.692	0.599	0.033	0.07648	0.0015	-0.018052	13.07531	0.2564457	0.057	0.0032	0.19538	475.1	9.2	474	21	478.8	14
MAD - 13	1.34	7.846	0.617	0.029	0.0773	0.0016	-0.12377	12.93661	0.2677694	0.058	0.0029	0.33259	480	9.6	484	19	481.6	14
MAD - 14	1.44	7.588	0.598	0.033	0.07553	0.0015	-0.14781	13.23977	0.2629374	0.0576	0.0032	0.24882	469.3	9	471	21	475.2	13
MAD - 15	1.39	7.461	0.597	0.03	0.07606	0.0016	0.16805	13.14752	0.2765714	0.057	0.003	-0.0056419	472.5	9.3	475	19	469.9	13
MAD - 16	1.29	7.562	0.604	0.028	0.07674	0.0015	-0.11725	13.03101	0.254711	0.0572	0.0028	0.27956	476.6	8.8	476	18	470.2	13
MAD - 17	1.76	7.751	0.611	0.028	0.0761	0.0016	-0.037616	13.1406	0.2762808	0.0578	0.0028	0.27689	472.8	9.7	481	18	480.4	14
MAD - 18	1.17	7.316	0.592	0.024	0.07566	0.0016	-0.030521	13.21702	0.2795035	0.0562	0.0025	0.30379	470.1	9.3	474	16	463.4	13
MAD - 19	1.33	7.06	0.596	0.023	0.07537	0.0016	-0.022155	13.26788	0.2816586	0.0574	0.0023	0.2888	468.4	9.4	474	15	468.1	13
MAD - 20	1.28	7.58	0.613	0.032	0.0774	0.0016	0.031222	12.9199	0.267078	0.0574	0.0031	0.21719	480.6	9.8	486	21	479.4	14
NIST610 - 1	436.9	438.5	34.7	0.21	0.2756	0.0051	0.89234	3.628447	0.0671447	0.9145	0.0018	0.29503	1569.2	26	3629.9	6.1	9307	210
NIST610 - 2	411.1	414.5	33.25	0.23	0.2637	0.005	0.90094	3.792188	0.0719345	0.9173	0.0024	0.39575	1508.9	25	3588.2	6.8	9051	210
NIST610 - 3	429.9	428.9	33.87	0.23	0.2699	0.005	0.92955	3.705076	0.06863794	0.9125	0.0017	0.17182	1540.3	25	3605.7	6.6	9275	210
NIST610 - 4	426.7	426.6	33.69	0.21	0.2687	0.005	0.9194	3.721623	0.06925237	0.9093	0.0019	0.32228	1534.2	25	3601.4	6.2	9293	210
NIST610 - 5	426.4	426.4	33.06	0.24	0.2648	0.0049	0.91505	3.776435	0.06988116	0.9058	0.002	0.207	1514.5	25	3581.8	7.1	9206	210
NIST610 - 6	429.2	427.5	32.83	0.21	0.2634	0.0049	0.90543	3.796507	0.07062599	0.9079	0.002	0.31557	1506.9	25	3576.6	6.1	9133	210
NIST610 - 7	431.9	427.4	32.57	0.2	0.2619	0.0048	0.89549	3.818251	0.0699794	0.9045	0.0023	0.32973	1499.5	25	3567.4	6.1	9118	210
NIST610 - 8	426.2	428.3	32.23	0.2	0.2595	0.0048	0.86846	3.853565	0.07127981	0.9017	0.0021	0.2176	1487	24	3557.7	6.2	9017	210
NIST610 - 9	427.5	428.9	33.54	0.22	0.2685	0.005	0.92274	3.724395	0.06935558	0.9028	0.0019	0.37049	1533.3	25	3596.3	6.6	9294	210
NIST610 - 10	420.4	422.6	32.82	0.23	0.2621	0.0049	0.91177	3.815338	0.07132833	0.8999	0.0021	0.19878	1500.6	25	3574.6	7	9044	210

Figure A3-1 - U-Pb Terra-Wasserberg plot of Phalaborwa apatite